Imperial College London

Betatron Radiation from Laser Wakefield Accelerators and its Applications

Jonathan Christopher Wood

September 2016

Submitted in partial fulfilment of the requirements for the degree of Doctor of Philosophy in Physics of Imperial College London and for the Diploma of Imperial College London

Department of Physics
Imperial College London
Prince Consort Road
SW7 2AZ
United Kingdom

Declaration of Originality

I, the author, declare that the material presented in this thesis is my own work. Exceptions to this are acknowledged or referenced within the text.

Copyright Declaration

The copyright of this thesis rests with the author and is made available under a Creative Commons Attribution Non-Commercial No Derivatives licence. Researchers are free to copy, distribute or transmit the thesis on the condition that they attribute it, that they do not use it for commercial purposes and that they do not alter, transform or build upon it. For any reuse or redistribution, researchers must make clear to others the licence terms of this work.

To my parents

Abstract

This thesis will detail experimental research in to laser wakefield acceleration (LWFA), with a particular focus on LWFA's as compact sources of brilliant, hard synchrotron radiation, so-called betatron radiation. The first results presented are from an experiment where a $\sim 10\,\mathrm{TW}$ laser pulse was focussed in to a clustered methane target. The presence of clusters enhanced the stability and tunability of the electron beam while maintaining similar electron beam peak energies and charges to other injection mechanisms. It also produced beams with three times larger transverse momentum in the laser polarisation direction, differentiating this injection mechanism from self- and ionisation-injection as well as hinting at a possible future use as a reliable source of polarised betatron radiation.

The primary result of this thesis follows, which is that a self-injecting, self-guided LWFA driven by a $100 - 200\,\mathrm{TW}$ laser pulse, with a long $f/40$ focussing geometry, showed an increase in betatron brightness to $2.8 \times 10^{24}\,\mathrm{photons/s/mm^2/mrad^2/0.1\%BW}$, the highest brightness betatron source yet reported, along with a source size of approximately $300\,\mathrm{nm}$ inferred from spectral measurements of the almost $2\,\mathrm{GeV}$ electron beams and $\sim 20\,\mathrm{keV}$ critical energy betatron x-ray beams. At longer acceleration lengths an additional, large injection of charge in to the wakefield dramatically increased the photon yield at moderate energies by a factor of $5 - 6$.

The final result is the first demonstration that betatron radiation is suitable for imaging rapidly evolving phenomena. By studying shock propagation in solid density targets it will be shown that it can be used to qualitatively and quantitatively study the properties of the shock. It is shown that with the reported increase in photon number, betatron radiation can produce images of rapidly evolving phenomena of comparable quality to those taken in recent experiments at 3^{rd} and 4^{th} generation light sources.

Contents

Abstract **3**

Contents **4**

List of Figures **8**

List of Tables **12**

Acknowledgements **14**

Role of the Author **15**

1 Introduction **16**
1.1 Particle Acceleration 16
1.2 Particle Accelerators as Light Sources 18
1.2.1 Insertion Devices 18
1.2.2 X-ray Applications 20
1.2.3 Peak X-ray Brightness 22
1.2.4 X-ray Free Electron Lasers 22
1.2.5 Opportunities for Improved X-ray Sources 24
1.3 Laser Wakefield Acceleration 26
1.4 Betatron Radiation from Laser Wakefield Accelerators 29
1.5 Thesis Outline 31

2 Theory **32**
2.1 Electron Motion in Externally Applied Fields 32
2.1.1 Charged Particle Motion in an Electromagnetic Field 33
2.1.2 Electron Motion in a Monochromatic Plane Wave 34
2.1.3 The Ponderomotive Force 36
2.2 Nonlinear Optics in Underdense Plasmas 37
2.2.1 Electromagnetic Waves in Vacuum 38
2.2.2 Creating a Plasma 40
2.2.3 The Plasma Frequency 42

2.2.4 Electromagnetic Waves in Plasmas . . . 42
2.2.5 Nonlinear Refractive Index of a Plasma . . . 43
2.2.6 Pulse Compression . . . 44
2.2.7 Photon Acceleration . . . 45
2.2.8 Transverse Focussing . . . 46
2.2.9 Self-Guiding . . . 47
2.3 Laser Wakefield Acceleration . . . 48
2.3.1 Linear Wakefield Model . . . 48
2.3.2 Nonlinear Wakefields in 1D . . . 50
2.3.3 Nonlinear Wakefields in 3D . . . 53
2.3.4 Trapping . . . 56
2.3.5 Injection Methods . . . 59
2.3.6 Maximum Energy Gain and its Limiting Factors . . . 59
2.4 Radiation Generation . . . 62
2.4.1 Transverse Electron Motion in a Plasma Channel . . . 62
2.4.2 Electron Motion in a Plasma Channel with a Constant Longitudinal Field . . . 64
2.4.3 Electron Motion in an Insertion Device . . . 66
2.4.4 Properties of Synchrotron Radiation and Betatron Radiation . . . 68

3 Experimental Methods 76
3.1 High Power, Short Pulse Laser Systems . . . 76
3.2 Laser Diagnostics . . . 77
3.2.1 Laser Energy Measurement . . . 78
3.2.2 Laser Pulse Duration . . . 78
3.2.3 Focal Spot Characterisation . . . 79
3.3 Gas Targetry . . . 82
3.3.1 Gas Jets . . . 82
3.3.2 Gas Cells . . . 83
3.3.3 Choice of Gas . . . 84
3.3.4 Density Characterisation . . . 85
3.4 Electron Beam Diagnostics . . . 86
3.4.1 Electron Spectrometer Set-up . . . 86
3.4.2 Electron Beam Tracking . . . 87
3.4.3 Electron Beam Profile . . . 89
3.4.4 Charge Calibration . . . 90
3.5 X-ray Diagnostics . . . 92
3.5.1 X-ray Beam Profile . . . 92
3.5.2 X-ray Cameras . . . 92

3.5.3 Dark Field and Flat Field Corrections . . . 94
3.5.4 X-ray Spectral Characterisation . . . 96
3.5.5 Conversion of Camera Counts to Deposited X-ray Energy and Number of Photons . . . 101
3.5.6 X-ray Imaging Resolution and Source Size . . . 106
3.5.7 Measuring Brightness . . . 108
3.5.8 Absorption and Phase Contrast X-ray Imaging . . . 109

4 Electron Acceleration from Clustered Methane 112
4.1 Motivation . . . 112
4.2 Experimental Set-up . . . 115
4.3 Electron Beam Profile Measurements . . . 117
4.4 Simulations of the Electron Beam Profile . . . 124
4.5 Measurements of the Electron Energy Spectrum . . . 129
4.6 Reproducibility . . . 133
4.7 Summary and Outlook . . . 135

5 Enhanced Betatron Radiation from a LWFA with an $f/40$ Focussing Optic 137
5.1 Motivation . . . 137
5.2 Experimental Set-up . . . 138
5.3 Plasma Length Scans . . . 140
5.3.1 Electron Beam and X-ray Montages . . . 140
5.3.2 Study of the Electron Energy Spectrum . . . 142
5.3.3 X-ray Spectral Measurements . . . 146
5.3.4 X-ray Brightness . . . 149
5.4 X-ray Beam Profile . . . 151
5.5 Stability of the Betatron Spectrum . . . 155
5.6 Spatial Variation in the X-ray Spectrum . . . 158
5.7 Measurements of the X-ray Imaging Resolution . . . 161
5.8 Summary and Outlook . . . 162

6 Betatron Imaging of Laser Driven Shock Waves in Solids 164
6.1 Motivation . . . 164
6.2 $f/20$ Experiment Set-up . . . 165
6.3 $f/20$ Experiment X-ray Source Properties . . . 168
6.3.1 Beam Divergence . . . 168
6.3.2 Resolution and Source Size . . . 169
6.3.3 Spectrum . . . 170
6.4 Shock Propagation in a Silicon Target . . . 174

6.5 $f/40$ Experiment Set-up . . . 180
6.5.1 General Set-up . . . 180
6.5.2 Electron Beam Properties . . . 181
6.5.3 Shock Target and Shock Driver . . . 183
6.6 $f/40$ Experiment X-ray Source Properties . . . 184
6.6.1 Beam Divergence . . . 184
6.6.2 Resolution and Source Size . . . 185
6.6.3 Spectrum . . . 185
6.7 Shock Propagation in an Aluminium Target . . . 188
6.8 Summary and Outlook . . . 191

7 Conclusions **194**

8 Appendix **197**
8.1 Maxwell's Equations . . . 197
8.2 Normalised Units . . . 199
8.3 The Relativistic Ponderomotive Force . . . 199
8.4 The Wave Frame . . . 200
8.5 General Equations for Radiation from a Moving Charge . . . 200
8.6 Lanex . . . 202
8.7 Image Plate . . . 204
8.7.1 Spontaneous Decay Rate . . . 205
8.7.2 Conversion of PSL to Electron Number . . . 205
8.7.3 Energy Dependence . . . 206
8.7.4 Saturation of Image Plate . . . 207
8.8 Quantum Efficiency of the X-ray Cameras . . . 208
8.9 X-ray Filter Arrays . . . 208
8.9.1 64 Filter Array . . . 208
8.9.2 16 Filter Arrays . . . 210
8.9.3 Imaging Filter Array . . . 211
8.10 Resolution Targets . . . 212

Bibliography **214**

List of Figures

1.1 Aerial view of the Large Hadron Collider . . . 17
1.2 Diagram of an insertion device . . . 19
1.3 Comparison of absorption and phase contrast imaging . . . 20
1.4 Peak brightness of x-ray sources . . . 23
1.5 Aerial views of LCLS and ESRF . . . 24
1.6 Final amplifier of the Gemini laser system . . . 25
1.7 A PIC simulation demonstrating the bubble regime . . . 26
1.8 A plot of LWFA length vs. energy gain . . . 28

2.1 Electron motion in a plane wave . . . 36
2.2 Electric field of a focussed gaussian laser beam . . . 40
2.3 The geometry for the derivation of the plasma frequency . . . 42
2.4 Density gradients caused by a gaussian laser pulse . . . 44
2.5 Diagram explaining transverse focussing . . . 46
2.6 Electron density oscillation in a linear LWFA . . . 50
2.7 Plasma waves in the 1D nonlinear regime . . . 53
2.8 A 2D PIC simulation output demonstrating the bubble regime . . . 54
2.9 Electron orbits in the γ, ξ phase space in a 1D nonlinear wakefield potential 57
2.10 A longitudinally accelerating electron in a radially symmetric electrostatic field . . . 66
2.11 Demonstration of the searchlight nature of synchrotron radiation . . . 68
2.12 Synchrotron spectral intensity vs. $\gamma\theta$ for three different frequencies . . . 71
2.13 Spectral intensity of the synchrotron spectrum for different observation angles . . . 72
2.14 Spectral intensity of a $K = 10$ wiggler spectrum for different observation angles. . . . 73

3.1 Example $f/40$ focal spot . . . 80
3.2 Demonstration of the focal spot analysis procedure . . . 81
3.3 50% intensity contour of the focal spot overlaid on pixel values > 0.5 . . . 82
3.4 Diagram of the 3mm gas nozzle . . . 83
3.5 Diagram of the gas cell . . . 84

3.6 Typical layout of a two screen electron spectrometer 87
3.7 Output of the electron tracking code 88
3.8 Error analysis of the electron tracking code 89
3.9 Diagram of the electron/ x-ray beam profile diagnostic 90
3.10 Diagram illustrating the charge calibration method 91
3.11 The method of flat-field correction 95
3.12 Example of the x-ray critical energy analysis method 98
3.13 Errors induced by filter thickness variations 99
3.14 Error in measured critical energy induced by a systematic filter thickness offset 100
3.15 Method for determining the random error in the critical energy 101
3.16 Geometry of the disk source problem 103
3.17 Intensity distributions at different distances from a disk source 104
3.18 Data image from the Andor ID camera calibration 105
3.19 Resolution target blurring 107
3.20 Hard edge imaging example 108

4.1 Setup of the clustered methane experiment 115
4.2 Example interferometry image of a methane plasma channel 116
4.3 Hagena parameter Γ^* as a function of electron density for the 3 mm conical nozzle 117
4.4 Comparison of electron beam divergence from helium , helium + 5% CO_2 and methane 118
4.5 Spatial structure in a self-injected beam 119
4.6 Sum of 50 focal spots from the clustered methane experiment 120
4.7 Electron beam profile montage from a methane plasma density scan 120
4.8 Electron beam divergence as a function of electron density for methane . . 121
4.9 Electron beam profile signal as a function of number density from the methane number density scan 122
4.10 Images demonstrating the dual species nature of the electron beams from methane at high density 123
4.11 Long axis and short axis divergence as a function of n_e for electron beams from a pure helium target 124
4.12 The effect of polarisation on the transverse momentum of the accelerated electron beam distribution function 125
4.13 PIC simulations outputs demonstrating bubble oscillations when the laser is polarised in the plane of the simulation 126
4.14 Simulation output showing the position of the bubble and the laser field in the methane experiment 127

4.15 A comparison of dN/dp_y for a y polarised drive laser with a temperature anisotropy in the y and z directions . . . 128
4.16 Comparison of exit mode images taken with a mixed gas target and a cluster target . . . 129
4.17 Example electron spectrometer image from a methane target and a graph of the energy spectrum . . . 130
4.18 Electron spectrometer results from a $P - z$ scan in methane . . . 131
4.19 Peak electron energy from self-injection as a function of density . . . 132
4.20 A comparison of electron spectrometer stability runs between a helium and methane target . . . 133
4.21 Stability of the accelerated electron beam from a methane target . . . 134
4.22 Stability of the accelerated electron beam from a methane target with respect to laser energy fluctuations . . . 135

5.1 Experiment setup with the $f/40$ focussing optic . . . 139
5.2 A montage of the electron spectrometer and x-ray camera images from a gas cell length scan . . . 141
5.3 Comparison of the energy spectra of the first and second injected electron bunches . . . 143
5.4 Comparison of the divergence of the first and second injected electron beams 143
5.5 Peak energies of the first and second injected bunches . . . 144
5.6 Charge contained within the first and second bunches . . . 145
5.7 E_c as a function of accelerator length at $n_e = 2.3 \times 10^{18}$ cm^{-3} . . . 146
5.8 r_β as a function of accelerator length for the first injected bunch . . . 147
5.9 E_c as a function of accelerator length at a range of plasma densities . . . 148
5.10 Total number of photons as a function of accelerator length at $n_e = 2.3 \times 10^{18}$ cm^{-3} . . . 149
5.11 Brightness as a function of accelerator length at $n_e = 2.3 \times 10^{18}$ cm^{-3} . . . 151
5.12 Montage of x-ray profile images showing variation as a function of plasma density . . . 151
5.13 FWHM x-ray beam divergence as a function of plasma density in a 20 mm gas cell . . . 152
5.14 X-ray intensity as a function of plasma density in a 20 mm gas cell . . . 153
5.15 Peak electron energy and total beam charge from the x-ray profile run . . . 153
5.16 Betatron oscillation radius as a function of n_e measured from the x-ray beam divergence . . . 154
5.17 Horizontal and vertical x-ray beam pointing as a function of plasma density 154
5.18 Betatron image of an embryonic mouse . . . 155
5.19 Critical energy as a function of shot number on the 533 shot stability run . 156

5.20 Laser energy and gas cell condition throughout the betatron stability run . 157
5.21 Number of x-ray camera counts vs. shot number for the betatron stability run 158
5.22 Method of analysing the spatial variation in the betatron spectrum 159
5.23 Spatial critical energy variation of the betatron x-ray beam 160
5.24 A comparison of on-axis and off-axis synchrotron spectra 161
5.25 X-ray imaging resolution in the $f/40$ experiment 161

6.1 Experiment setup with the $f/20$ focussing optic 166
6.2 Geometry of the solid shock target interaction point 167
6.3 Spatial profile of the shock driver pulse used to drive a shock in silicon . . 168
6.4 X-ray beam profile from the $f/20$ wakefield driver 169
6.5 X-ray imaging resolution in the $f/20$ setup 169
6.6 LSF and MTF of the x-ray imaging system in the $f/20$ shock physics experiment 170
6.7 Geometry used to calculated the source size 170
6.8 Critical energy measurements from the $f/20$ shock physics experiment . . . 171
6.9 Measurements of the total number of photons from the $f/20$ shock physics experiment 172
6.10 Total number of photons plotted against critical energy 173
6.11 X-ray dI/dE and brightness as a function of photon energy from the $f/20$ shock physics experiment 174
6.12 Betatron images of laser driven shocks in silicon 174
6.13 Shock velocity and laser intensity as a function of transverse position . . . 175
6.14 Time series of shock propagation in untamped silicon 176
6.15 Shock propagation distance as a function of time in silicon 176
6.16 Lineout of shock propagation in untamped silicon 177
6.17 Pressure output from HELIOS 5.2 ns after the start of the interaction . . . 179
6.18 Mass density output from HELIOS 1.0 ns after the start of the interaction 179
6.19 Shock physics experiment setup with the $f/40$ focussing optic 181
6.20 Example electron energy spectrum from the $f/40$ shock physics experiment 182
6.21 Histogram of peak electron energies from the $f/40$ shock physics experiment 182
6.22 Peak electron energy plotted against wakefield driver laser energy for the $f/40$ shock experiment 183
6.23 Design of the grooved aluminium shock target 183
6.24 Temporal profile of the shock drive pulse in the $f/40$ shock experiment . . 184
6.25 22.5 times magnified image of the gold resolution target 185
6.26 Critical energy as a function of shot number and laser energy for the aluminium shock imaging run 186

6.27 Critical energy as a function of electron number density 186
6.28 Number of photons and peak brightness as a function of number density . 187
6.29 Comparison of mean peak brightness between the $f/20$ and $f/40$ shock physics experiments 188
6.30 Betatron x-ray images of shocks travelling through aluminium taken at a range of delays 189
6.31 Enlarged image of the shock in aluminium when the betatron delay was 30 ns 190
6.32 Diagram depicting the analysis method for the shocked aluminium 30 ns after the start of the interaction 191
6.33 Transmission of the betatron beam through thicknesses of aluminium relevant to gas gun experiments 192
6.34 Photons per eV from the betatron source 193

8.1 Electron energy deposition in Lanex 203
8.2 Spontaneous decay in Image Plate 206
8.3 Energy deposition in Image Plate vs. incident electron energy 207
8.4 X-ray camera quantum efficiencies 208
8.5 Diagram of the 64 filter array 209
8.6 Transmission of the filters of the 64 filter array 210
8.7 Diagram of the 16 filter array 210
8.8 Diagram of the imaging filter array 211
8.9 Transmission of the filters of the imaging filter array 212
8.10 Diagram of the JIMA resolution target 212
8.11 Optical image of the gold resolution target 213

List of Tables

2.1 Dephasing length, depletion length and maximum energy gain for the linear, 1D nonlinear and 3D nonlinear regimes 62

3.1 X-ray camera technical details 93
3.2 Photon emission from Fe-55 decay 103
3.3 X-ray camera calibration results 106

4.1 Comparison of beam divergence for He, He + 5% CO_2 and methane 118
4.2 Comparison of the angle between the long axis of the beam profile ellipse and the x axis for He, He + 5% CO_2 and methane 118
4.3 Injection threshold density with a methane target. 129
4.4 Electron beam parameters from a methane stability run. 134

8.1 Summary of normalised units 199
8.2 Summary of the properties of different types of Lanex screen. 203
8.3 Composition of Image Plates 204

Acknowledgements

As many people have told me, the acknowledgements section of a thesis is the only place where you get to be yourself, and, I hope, refer to what others have said without attribution. I hope that many people will read this section and come to understand what an important part they have played in me getting to this stage in life, and also that they will carry on and read at least some of this thesis. I also hope to express myself in a way that was formally barred in the rest of the thesis. But we will get to supervisors later. I am compelled to start with the people who encouraged me to study physics in the first place. Most notable amongst this crowd is my father Chris who, while I was thinking of applying to study at university, suggested that my poor aptitude at fixing bicycle tyre punctures might preclude the possibility of me successfully completing an engineering degree. This is the story of how a will to study physics was born over an awkward Friday night roast. He, my mother Margaret and my brothers Simon and Adam have consistently encouraged me, supported me and provided a welcome distraction from physics on so many occasions. Thank you. While the bookishness continued in to my degree I found that I took an increasing liking to the lab. Without doubt I must thank my long term undergrad lab partner Matilda, whose excellent company and strong views on practicality ensured that I exited my student career, M6 Allen key held aloft, ready to plunge in to the world of physics research. Or so I wished to believe at the time. In this regard I owe my utmost thanks to my regular lab junkies Kristjan, Jason and Nelson, without whose excellent teaching skills I would not be where I am today, and without whose fine company I would have gone crazy on all of those late nights. Without the huge efforts put in by my colleagues none of the data presented in this thesis would have ever been taken. In this light, I also extend special thanks to our shock physics regulars Dan, Dave, Michael and Tom, and to the CLF staff without whom none of these experiments could have happened. Finally I would like to thank my supervisors Stuart Mangles and Zulfikar Najmudin. I have learnt a lot over the four years of this PhD and I am tremendously grateful for that. I have learnt via direct supervision, but also via the many opportunities that they have provided to work at world class facilities. I particularly thank Zulfikar for the intense interest he has shown in the results presented in this thesis, helping me to develop them to the stage that they are at now. I also extend my thanks to Bucker Dangor, for the incredibly pleasant and encouraging chats that have lead me here.

Role of the Author

High power laser experiments are necessarily collaborative, so in this section the contributions of the author to the work presented in this thesis will be briefly described. The author was responsible for the analysis of all of the data presented in this thesis.

For the data presented in chapter 4 the author was involved in setting up the main beamline, the electron beam diagnostics, and the probe beam line and interferometry diagnostic. The author was also involved in the daily alignment of the beamlines. The particle-in-cell simulations were run by the author, who gratefully acknowledges the assistance of Kristjan Poder for his initial help with this.

The chapter 5 data was taken during a Gemini experiment on which the author acted jointly as a target area operator and was responsible for alignment of the beamlines and, in particular, all of the x-ray diagnostics. It was a similar case for the data presented in chapter 6, although in the second experiment discussed in this chapter the author was was target area operator for only the final week. The shock targets were designed by Michael Rutherford.

Chapter 1

Introduction

1.1 Particle Acceleration

With the recent discovery of the Higgs boson [1][2] at the Large Hadron Collider (LHC) [3], these are auspicious times to be working in the field of particle acceleration. Almost since their inception particle accelerators have been one of our primary routes to probing the universe at its smallest scale: that of the fundamental particles. The high centre of mass energies achievable at the collision points of these accelerators facilitate interactions that only occur naturally in the most violent events such as supernova explosions or even the Big Bang itself. The advantage of the particle accelerator, of course, is that very sensitive detectors can be placed in close proximity to these interactions allowing for careful measurements of vast numbers of events. It is clear from the flurry of press coverage that greets each hint of a new particle discovery that a significant portion of the general public, in addition to the scientific community, place a high value on these advancements in our collective knowledge. Politicians clearly agree with these sentiments as, between its member nations, an estimated $13.25 billion was spent on the discovery of the Higgs Boson, including the LHC's operating costs of around $1 billion per year [4].

Unfortunately there are a number of basic physical principles driving these high costs. For high energy particle physics experiments, we would ideally like to accelerate long lifetime fundamental particles. It is important that these particles are long lived so that they do not decay before they interact. It is desirable to have interactions between fundamental particles because this allows the maximum energy to be available in a collision. In the example of proton collisions at the LHC, while each proton has an energy of 7 TeV, this is shared amongst its constituent parts: the quarks and gluons. Therefore much of this 7 TeV energy is not available for a fundamental particle interaction. Based purely on these arguments electron and positron acceleration are prime candidates, but problems arise when it comes to building a practical and economical accelerator. In a circular de-

vice such as a synchrotron, energy can be stored in the particle beams for a long period of time and each of the particles will have many chances to be involved in a collision. This seems to be an attractive option on efficiency grounds, until one considers energy losses due to synchrotron radiation; this is the radiation emitted by charged particles in circular orbits. The power P emitted by a single particle in a synchrotron is given in equation 1.1, where q, m and $\mathcal{E}$ are the particle's charge, mass and energy, and B is the magnetic field it is in.

$$P = \frac{1}{6\pi\epsilon_0 c^5}\left(\frac{q}{m}\right)^4 \mathcal{E}^2 B^2 \tag{1.1}$$

The strong $\mathcal{E}^2 m^{-4}$ scaling is prohibitive for high energy circular electron/ positron accelerators, although it does explain the attraction of proton acceleration. Considering the inverse proportionality of B to the radius of the machine, the only way to limit synchrotron losses are to build bigger machines, meaning that circular colliders are necessarily very large and therefore expensive.



Figure 1.1: Aerial view of CERN [5]. The large ring is the 27 km circumference LHC. Accelerator physicists are already discussing a potential successor, dubbed the Future Circular Collider (FCC), which could accelerate protons to 100 TeV in a ring of around 100 km circumference [6] or electrons and positrons to at most 0.5 TeV [7].

Linear particle accelerators (linacs) do not have the problem of large synchrotron losses so using linacs and dumping the beam after the collision point is more efficient than it sounds, relatively speaking at least. And yet conventional linear accelerators are also very large machines that are expensive to build. This is because the maximum acceleration gradient they can support is of order 100 MeV/m [8]. Even this gradient has only been shown in prototype devices so far: the accelerating gradient of the SLAC linac is

20 MeV/m for example [9]. This limit is imposed by the breakdown of the cavity wall of the accelerator. The reduction in potential felt by electrons in the wall due to the large radio-frequency (RF) fields in the cavity allows electrons to tunnel out of the wall in a process called field emission. This is enhanced by imperfections and non-uniformities in the wall. The field emission current can be so large (of order 10^8 A/cm^2) that melting of a small part the wall occurs over a time-scale of 10's of nanoseconds, permanently damaging the accelerating structure [10]. The breakdown-limited accelerating gradient puts the full length of a TeV linear collider in to tens of kilometres. As an example, the International Linear Collider (ILC) will collide electrons and positrons with a centre of mass energy of 200-500 GeV, with a possible future extension to 1 TeV, from two main linacs each 11 km in length [11].

The large international collaborations required to fund the latest generation of conventional high energy particle accelerators suggest that these machines are approaching the limits of what societies might be willing to support. Large synchrotron power losses necessitate the construction of large circumference circular machines. Synchrotron losses are mitigated with linear colliders, but the limited acceleration gradients achievable mean that these too must be very large and costly machines. This is strong encouragement to study alternative methods of particle acceleration.

1.2 Particle Accelerators as Light Sources

To paraphrase, one scientist's trash is another scientist's treasure. With appropriate design much of the synchrotron radiation emitted can be in the x-ray (>1 keV) region of the electromagnetic spectrum. These sources are in demand for a wide range of applications, evidenced by the 47 operational and planned synchrotron light sources around the world, each of which has multiple beamlines [12]. In this section the working of these light sources will be briefly described followed by an overview of their applications. The concepts of average and peak brightness will be elucidated; these will show the advantage these sources have over conventional x-ray tube technology. The physics of and results from hard x-ray free electron lasers (X-FELs), the forefront of modern x-ray technology, will be briefly discussed. This section will conclude with some thoughts on the limitations of these devices.

1.2.1 Insertion Devices

While some beamlines use the synchrotron radiation coming from bending magnets, many use an insertion device consisting of a sequence of dipole magnets of alternating polarity (figure 1.2). The advantage of an insertion device is that radiation from multiple oscilla-

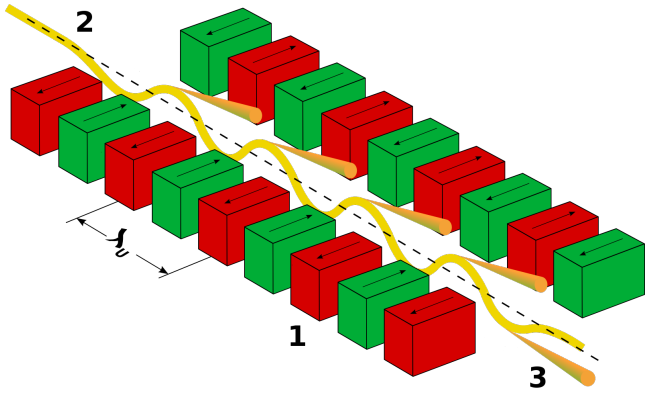


Figure 1.2: Diagram of an insertion device [13]. Alternating polarity dipole magnets (1), spacing λ_u, wiggle a relativistic electron beam (2) to produce a bright beam of x-rays (3).

tions of the electrons is emitted in the forward direction resulting in a brighter source than a single bending magnet. Insertion devices are often characterised by the dimensionless undulator or wiggler parameter K, where

$$K = \frac{eB_0\lambda_u}{2\pi m_e c} \tag{1.2}$$

B_0 is the peak magnetic field in the device and λ_u is the dipole magnet spacing. For $K \ll 1$ the device is known as an undulator, and it emits monochromatic radiation because the cones of emitted light overlap and interfere. In this way an undulator behaves like a diffraction grating where light emitted from spatially separate sources (points on the electron beam trajectory) constructively interferes only when the source positions are separated by an integer number of wavelengths. For an undulator the wavelength of radiation emitted on-axis is given by the equation

$$\lambda = \frac{\lambda_u}{2{\gamma_e}^2}\left(1 + \frac{K^2}{2}\right) \tag{1.3}$$

γ_e is the electron relativistic factor. The high γ_e available in modern particle accelerators (typically a few thousand) creates short wavelength radiation that is also concentrated within a narrow cone of opening angle $\sim 1/\gamma_e$ making this a very useful x-ray source. For example parameters of $K = 1$, $\lambda_u = 10$ mm and an electron energy of 3 GeV the photon energy is 5.7 keV. For $K \sim 1$ many harmonics are emitted, and for very large K a white light continuum is produced and the insertion device is referred to as a wiggler. X-ray sources such as these based on relativistic electron beams interacting with insertion devices are referred to as 3$^{\text{rd}}$ generation light sources.

1.2.2 X-ray Applications

Since the production and detection of x-ray radiation by Röntgen, a feat that won him the Nobel prize, advances in x-ray technology have transformed multiple fields of study. X-ray imaging is immensely popular for the simple reason that it allows the user to observe what is inside a usually opaque object. Differences in absorption between different elements in the material provide contrast to produce a useful image. Alternatively if one starts with a spatially coherent x-ray beam, slight differences in the real part of the refractive index of the material distort the wavefront. X-rays are, therefore, refracted away from gradients in refractive index which enhances the edges of features in an object, such as the edges of a fly's wings as shown on the right hand side of figure 1.3. This effect can be especially useful when examining biological tissue samples [14]. For example, it can highlight the edges of a tumour which may have a very similar level of absorption to the surrounding tissue. This technique is called phase contrast imaging (PCI), and is described further in section 3.5.8. X-ray PCI has since been applied to multiple fields, even including reading scrolls burnt by the eruption of Mount Vesuvius in 79 AD[1] [15].

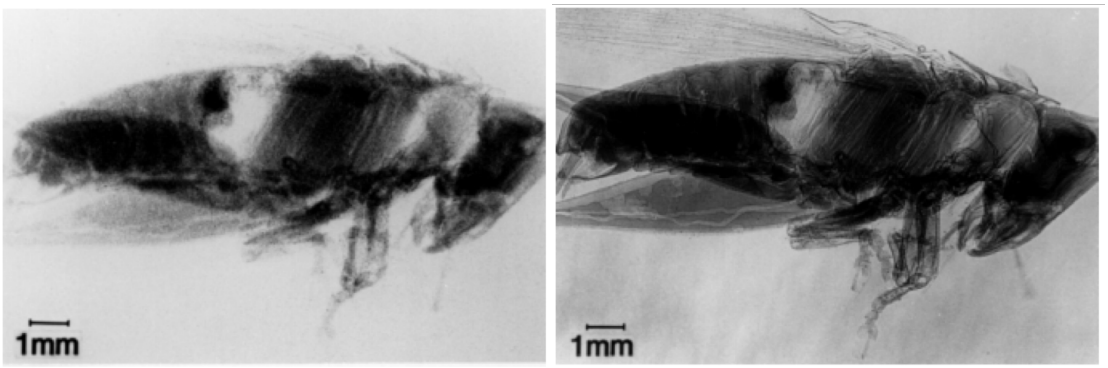


Figure 1.3: Comparison of an absorption contrast image (left) and phase contrast image (right) of a locust [14]. Note that the wings, for example, are seen clearly in phase contrast but are virtually invisible in absorption contrast.

Typically much absorption contrast imaging of static objects is done with a setup based on x-ray tubes where electrons emitted from a cathode are accelerated across a potential difference of $\lesssim 100$ kV and into an anode which then emits x-rays from line emission and bremsstrahlung. Magnetic optics acting on the electron beam focus it to a small (sub-mm scale) spot on the anode to enable high resolution imaging. Commercial systems with focal spot sizes as low as $5\,\mu$m are now available [16]. In the last few decades the field of computed tomography (CT) has taken off and it is now a very common application of these sources. It is also now possible to perform phase contrast imaging with

[1]For the enthusiastic historians in the x-ray imaging field, at one time these scrolls formed part of Napoléon Bonaparte's private collection.

these sources: this can be propagation based PCI [17] or methods based on high aspect ratio gratings [18] [19].

Despite their multiple capabilities, sources based on x-ray tubes are limited in scope because of their low brightness. Brightness B, sometimes referred to as brilliance, is a common figure of merit for x-ray sources. B is measured in photons/s/mm^2/mrad^2/0.1%BW i.e. it is the number of photons produced per second within a bandwidth of 0.1% of some central energy divided by the cross sectional area and divergence of the beam. X-ray tube sources typically have brightnesses of 10^8 - 10^{10} photons/s/mm^2/mrad^2/0.1%BW [20]. Synchrotron sources meanwhile meanwhile have average brightnesses as high as 10^{20} photons/s/mm^2/mrad^2/0.1%BW [21]. This huge increase is a product of two physical factors: radiation from relativistic electrons is highly directional and the photon flux is higher[2]. An obvious use of this higher brightness is that both phase and absorption contrast tomographies can be performed very quickly at high resolution. TOMCAT, a bending magnet beamline at the Swiss Light Source, has been built for tomographic purposes and can acquire a tomography with a 3D resolution of 200 nm in a matter of minutes, or can acquire a lower resolution tomography in less than 1 s [23]. With x-ray optics such as Fresnel zone plates imaging resolution at synchrotrons can be pushed to 40-60 nm [24] [25]. However the wavelength of the light itself is sub-nm and thus it is possible to probe matter at the level of atomic spacings in solids. Determination of crystal structure by diffraction has produced thousands of scientific papers, a nice example being the determination of charge density in variants of buckminsterfullerene (C_{60}) [26]. Further information about correlations in the positions of ions in a material can be obtained using spectroscopic techniques such as Extended X-ray Fine Structure (EXAFS) and X-ray Absorption Near Edge Structure (XANES). In both of these techniques the absorption coefficient of a material is measured close to one of the absorption edges, usually the k-edge. The operating principle is that an x-ray photon is absorbed by an atom, which ejects a core photoelectron that has the energy of the photon minus the binding energy of its initial state. This photoelectron has a wave-like nature, and this wave interferes with the waves of other core electrons that have not been excited. This interference effect causes a modulation in the absorption spectrum of the bulk material, which can be used to determine which elements are present in the material and details of the atomic positions i.e. the lattice structure. Arguably both diffraction and spectroscopic techniques reveal the most interesting physics when looking at short-lived excited states which have become accessible with the short flashes of light synchrotrons emit, which we will now discuss.

[2]The photon flux is limited in x-ray tubes by the melting of the anode, although liquid metal anodes have recently pushed the brightness up by an order of magnitude [22].

1.2.3 Peak X-ray Brightness

The high brightness afforded by synchrotron radiation sources facilitates x-ray probing of transient events. Specifically this requires high peak, rather than average, brightness. Fortunately synchrotron based sources typically accelerate short duration bunches of electrons, typically 10's to 100's ps long. The radiation emitted by these bunches is on a similar time-scale, giving these sources a high peak brightness approaching 10^{24} photons/s/mm^2/ mrad^2/0.1%BW. This is the brightness produced by a single bunch of electrons whereas average brightness is the time average over a large number of bunches. Without such sources, it is difficult to envisage how x-ray techniques could be applied to fields that study transient behaviours such as high-energy-density physics (HEDP). To study HEDP is to study the behaviour of materials under extreme conditions of pressure and temperature. These conditions can only be created over short temporal and spatial scales in the laboratory. Synchrotron light sources have enabled absorption and phase contrast imaging of dynamic shock physics experiments in medium to high atomic number materials, all with a temporal resolution of <100 ps and a spatial resolution of a few μm [27] [28] [29]. Diffraction experiments reveal dynamic phase changes. An example use of this technique is the determination of the phase diagram of iron up to 130 GPa [30].

1.2.4 X-ray Free Electron Lasers

In 2009 the world's first hard x-ray free electron laser (X-FEL), LCLS, began lasing. An FEL consists of an electron accelerator followed by a long undulator, and is often referred to as a 4$^{\text{th}}$ generation light source. Over time, as the electrons oscillate in the magnetic field of the undulator, the radiation they emit acts to modulate the electron beam which causes it to microbunch at the wavelength of the emitted radiation. Once this microbunching has developed the electron bunches oscillate in phase emitting radiation that experiences gain from the electrons. This instability requires seeding. This seed can be provided by random shot noise and the radiation is amplified in a process called Self-Amplified Spontaneous Emission (SASE), which is used in the standard operation mode of LCLS. This produces an extremely bright source of hard x-rays: the peak brightness of LCLS is 10^{33} photons/s/mm^2/mrad^2/0.1%BW. Since the beam grows from noise it has poor temporal coherence and a relatively 'large' bandwidth ($\sim$ 20 eV). The bandwidth can be improved to 0.4 eV, along with an order of magnitude increase in brightness, by a self-seeding set-up [31]. In this set-up the x-rays from the first half of the undulator are monochromated and recombined with the electron beam, which is delayed in a magnetic chicane, to seed the FEL process in the second half of the undulator. A graph of peak x-ray brightness for a selection of 3$^{\text{rd}}$ and 4$^{\text{th}}$ generation light sources is shown in figure 1.4 emphasising the huge ($\sim 10^9$) increase in brightness due to lasing. LCLS x-ray pulses can be tuned to have energies of 0.25-10.5 keV and durations of 5-500 fs,

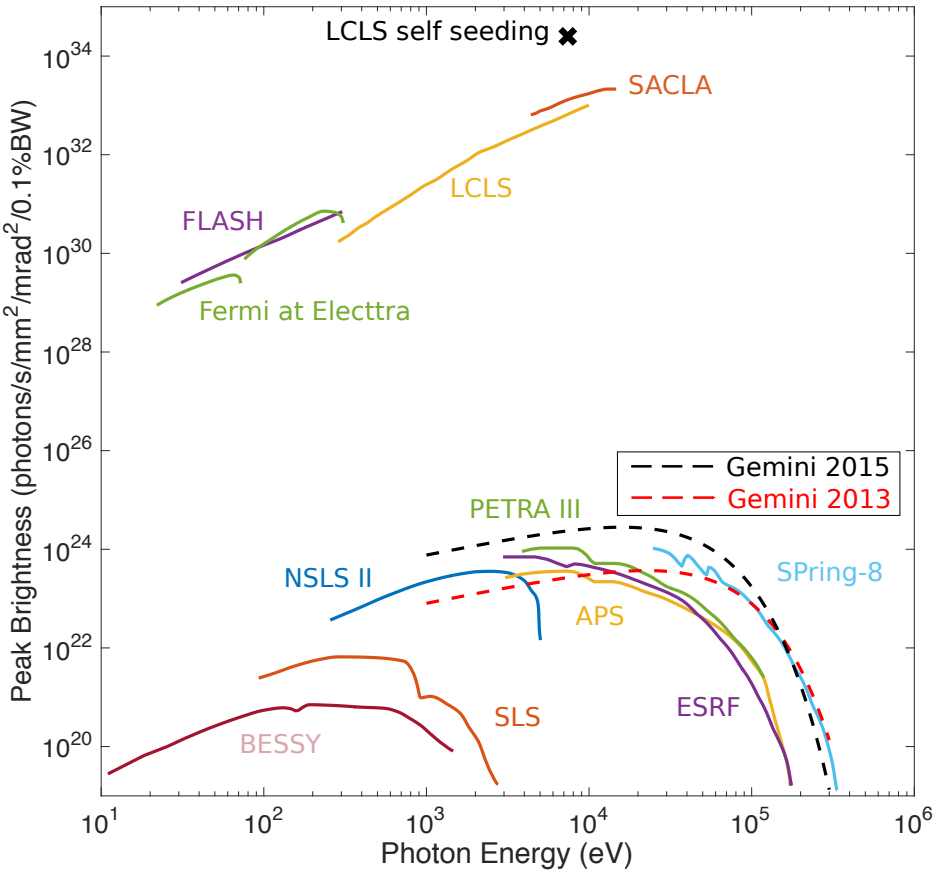


Figure 1.4: Peak brightness of a number of third and fourth generation light sources from around the world, adapted from [32]. The dashed lines show the brightness of betatron radiation produced at the Gemini laser facility in an experiment carried out in 2013, in a short focal length geometry [33], and in a 2015 experiment in a long focal length geometry, which is reported in chapter 5 of this thesis.

with 10^{12}-10^{13} photons/pulse [34]. This has been made possible by the availability of very high quality electron beams, which typically have energy 2.4-15.4 GeV, beam charge 250-300 pC , energy spread $\sigma_E/E < 10^{-3}$ and an emittance close to 1π mm-mrad [34] [35].

The extremely high brightness available at XFELs coupled with the fs duration of the x-ray pulse allows matter to be investigated not only at atomic length scales but at atomic time scales as well. Studies carried out at LCLS have advanced multiple fields of science including: x-ray absorption and emission of materials on a fs time-scale [36], femtosecond crystallography [37], dynamics of superfluids [38], studies of high temperature superconductors [39] and femtosecond chemistry [40].

1.2.5 Opportunities for Improved X-ray Sources

Both 3rd and 4th generation light sources have had a huge impact on multiple scientific fields. However, due to the previously mentioned issues of limited acceleration gradient and synchrotron power losses (section 1.1), these devices are both large (see figure 1.5) and very expensive. ESRF, for example, has annual operating costs of €86M and is currently undergoing a €150M upgrade to improve energy efficiency and to reduce beam emittance and thus increase brightness by a factor of 30 [41]. LCLS has operating costs of $50-60M per year [42] and the upgrade to LCLS-II will cost close to $1 billion [43]. During the upgrade a superconducting linac will be built producing electron bunches of 4 GeV energies at a 1 MHz repetition rate. These electrons will be delivered to two new undulators covering photon energy ranges 0.2-1.2 keV and 1-5 keV while LCLS will continue to operate at 120 Hz providing harder photons [44]. In a way these figures highlight the perceived importance of bright sources of x-rays to the scientific community and indeed citizens in general. There are applications which require all of the features of these sources: hard, short pulse x-ray beams of extremely high brightness with high repetition rate. However if the constraint of the high repetition rate can be relaxed one might consider the use of a different source of bright x-rays. Much of this thesis will argue that betatron radiation from laser wakefield accelerators (introduced in sections 1.3 and 1.4) has become a useful and viable source in this regard where repetition rates of 0.1-1 Hz can be tolerated. An example application demonstrated in this thesis will be imaging of shock waves in solids.

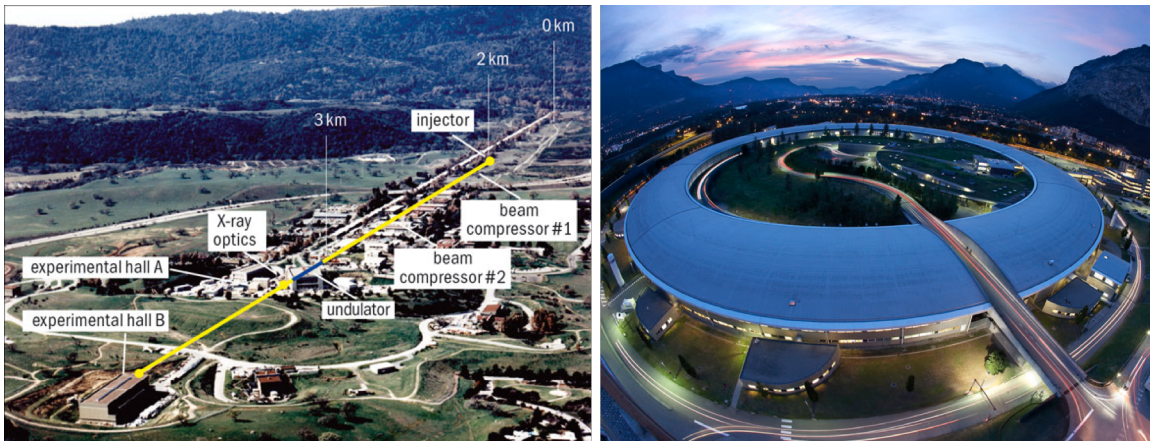


Figure 1.5: Left: Aerial view of LCLS [45]. Note the length of the accelerator section of 1 km. Right: Aerial view of ESRF [46]. The diameter of the storage ring is $\sim$ 280 m [47].



Figure 1.6: Final amplifier of the Gemini laser system [48]. The picture shows the final amplifier and compressor. The room is approximately double the size shown here. The other half houses the pump lasers. Note the modest scale compared to conventional particle accelerator structures.

The relative advantages of 3rd and 4th generation light sources, and betatron radiation, will now be briefly summarised. Synchrotron based light sources produce a large number of hard x-ray photons, but in a relatively long (10's to 100 ps) pulse. Depending on the type of insertion device (an undulator or a wiggler) the radiation can be monochromatic or broadband. X-FELs produce ultrashort (10's femtosecond) bursts of monochromatic radiation, although the x-ray energy can be tuned. They also generate a large number of photons, which combined with the short x-ray pulse duration, make them the brightest source of x-ray radiation currently available. Betatron radiation, as we will soon discover, also has a pulse duration on the order of 10's fs, although since there is no lasing, each pulse contains fewer photons than an X-FEL pulse. It is also broadband, meaning that it is currently a unique x-ray source in that it can provide ultrashort pulses of broadband hard x-ray radiation. As figure 1.4 showed it has a brightness higher than modern synchrotron sources such as ESRF, especially in the 10's keV region of the spectrum. The figure also demonstrates that this is a relatively hard source of synchrotron-like radiation. In addition betatron sources have a significant cost advantage, with a Gemini style (several hundred TW) laser costing of order £5 million. Currently such lasers have a significantly lower repetition rates than sources driven by conventional accelerator technology. Progress is being made in this area however, and it seems likely that within the next few years lasers with a power of several hundred TW will be operating at 10 Hz repetition rates.

1.3 Laser Wakefield Acceleration

Electric fields in the focus of high-power short-pulse optical laser beams can exceed 100 TV/m, which suggests that a compact accelerator might be achievable based on laser technology. The method of Laser Wakefield Acceleration (LWFA) proposed by Tajima and Dawson [49] has emerged as one of the most promising candidates. While their proposal involved driving a linear plasma wave, in most current experiments an intense, focussed laser pulse travelling through an underdense plasma drives a nonlinear plasma wave in its wake, known as a wakefield. Here 'intense' refers to a pulse with a normalised vector potential $a_0 = 0.856 \left(I_{18}\lambda_{\mu m}{}^2\right)^{0.5} \gtrsim 1$. I_{18} is the laser intensity in units of 10^{18} W/cm^2 and $\lambda_{\mu m}$ is the laser wavelength in microns. For efficient wakefield generation, the requirement on the laser pulse length $\tau_{pulse} \approx {\omega_p}^{-1}$ should be fulfilled, where ω_p is the plasma frequency. These targets are well within the reach of many modern short pulse laser systems which typically have $\tau_{pulse} \approx 40$ fs and focussed intensities $I \gtrsim 10^{18}$ W/cm^2 of ~ 1 μm light. For $a_0 > 4$, a target that can often be reached by a lower intensity pulse that self-focusses and self-compresses in the plasma [50] [51] [52] [53], the plasma wave takes the form of a near-spherical bubble with the driving laser sitting at the front [54] [55]. This is demonstrated in the simulation output in figure 1.7. The fields in this

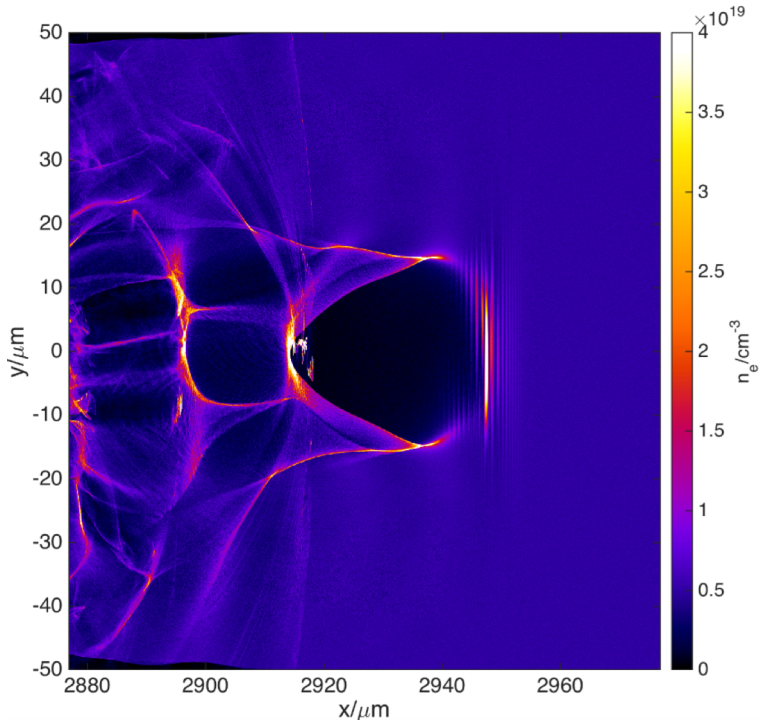


Figure 1.7: A 2D-3V Particle-in-Cell simulation demonstrating the bubble regime. The laser is propagating from left to right. The electron density as a function of x-y is plotted. We see a fully cavitated bubble in the wake of the laser pulse and the beginnings of electron acceleration at the rear of the bubble.

bubble can have accelerating gradients in excess of 100 GeV/m. A number of groups have reported acceleration to the GeV level and beyond in cm scale plasmas [56][57][58][59][60]. The largest energy gain recorded to date is 4.2 GeV [61]. It is important to note that everywhere inside the cavitated bubble is focussing for electron beams and rear half is accelerating for electrons.

Electron beams accelerated via the LWFA mechanism have been shown to have bunch durations as low as a few femtoseconds [62] and have low emittance of order 1π mm-mrad [63], and it has been known since 2004 that low energy spread electron bunches (σ_E/E of a few %) can be accelerated [64][65][66]. The highest energy electron linac ever built was the 3 km SLAC linac that could reach a maximum energy of approximately 50 GeV. Considering this figure, it is hard to deny that energy gains beyond 1 GeV achieved via LWFA in a facility that, even if it wouldn't quite fit on a tabletop, is very much 'university scale', is an impressive advance in compact accelerator technology.

Of course the large acceleration gradients are only part of the story here. A method of injecting electrons in to the accelerating region of the bubble is required. In the most commonly used method, self-injection, the plasma wake is driven to large amplitudes and some electrons take trajectories that result in their injection in to the accelerating region of the bubble. In GeV class experiments the total accelerated charge can be up to 0.5 nC with 10's pC in the high energy peak [56][57][60]. Relying on a nonlinear process such as this for injection can lead to large shot-to-shot fluctuations in the amount of charge injected, although it has been shown that, near to the injection threshold [67], the maximum energy fluctuations can be below 10% [68]. These fluctuations have, in part, led to the development of alternative injection techniques. A popular method is ionisation injection where a high Z gas such as nitrogen is added to the primary gas, usually hydrogen or helium, at the few % level. The operating principle is that all electrons apart from the inner shell electrons of the high Z gas are ionised before the peak of the laser pulse and make up the plasma wakefield. The inner shell electrons are ionised at the peak of the pulse and are 'born' inside the bubble. Experiments have shown large amounts of charge injected compared to self-injected electrons with some quasi-monoenergetic features [69][70][58]. Alternative methods such as down-ramp injection [71], shock injection [72] and colliding pulse injection [73] have all been shown to produce electron beams with small absolute energy spreads. In the LWFA bubble the focussing forces acting on the beam are linear which preserves emittance, meaning that the emittance is controlled via the injection mechanism. Simulations have suggested that a beam with a normalised emittance of 50 nm could be injected via ionisation injection that is localised by a tightly focussed injection laser [74].

The route to the TeV scale is not simple. The energy gain from a single stage LWFA $\Delta E \propto n_e^{-1}$ where n_e is the plasma electron number density. The length over which this acceleration takes place is is known as the dephasing length. This is the length over which the relativistic electron beam outruns the accelerating field of the wakefield, which travels at the group velocity of the drive laser. This length scales as $L_d \propto n_e^{-3/2}$ meaning that the length required for a defined energy gain $\frac{L}{\Delta E} \propto n_e^{-1/2}$, which is unsatisfactory for a compact high energy machine. To demonstrate this figure 1.8 shows a graph of the length of a single stage LWFA versus the maximum energy gain assuming a linear wakefield model. We see that 1 TeV gain would require a 1 km stage. The practicalities of creating a uniform plasma of this length aside, this has partially dented the argument of compact acceleration. It is proposed that this long length problem could be avoided by accelerating through multiple 'high' density stages, allowing the electron bunch to be re-phased into an accelerating region of the bubble between stages [75] [76]. While coupling of electrons between two LWFA stages has been shown recently [77] the coupling efficiency was only 3.5% which is prohibitively small for a staged accelerator.

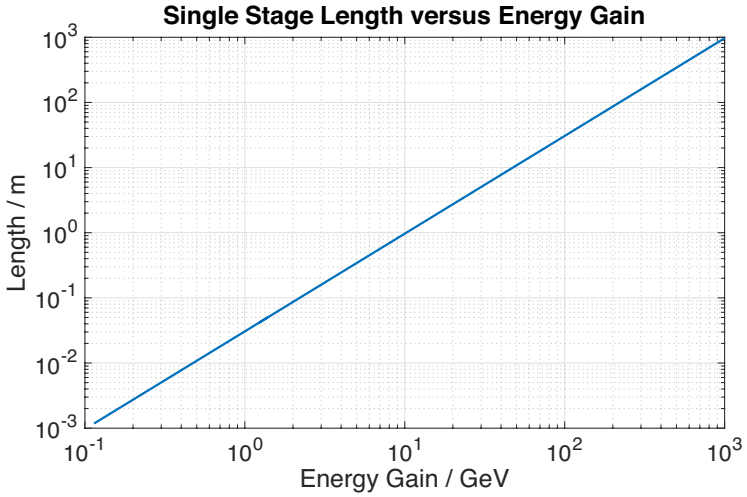


Figure 1.8: Graph of the length of LWFA required as a function of energy gain. This assumes a linear wakefield and that the acceleration length is the dephasing length.

It should not be forgotten that the observed energy gains coming from these compact LWFA experiments are still very respectable. This means that LWFA could be a very disruptive technology in the medium term, especially in the field of light sources, where it is believed that a LWFA could be used to drive a free-electron laser [78]. However it is known that a bubble regime LWFA acts as a wiggler to the electrons it accelerates producing a short burst of bright, hard x-rays called betatron radiation [79], which is the topic of the next section. It is indeed the topic of this thesis that betatron radiation is a useful source for x-ray applications and can provide an immediate application of LWFA

technology.

LWFA is not the only compact particle acceleration mechanism. As discussed, the electric field in a focussed laser pulse can be significantly larger than 100 TV/m [3]. However it is very difficult to utilise these large fields for particle acceleration as discussed in detail in [80]. Experiments on vacuum acceleration report total energy gains of only a few MeV [81] with laser parameters that one would expect to produce multi-hundred MeV electrons from a LWFA. So-called 'acceleration on a chip' has demonstrated acceleration gradients in excess of 250 MV/m with relatively modest laser power required and a high transfer of laser energy to the electrons [82]. However energy gains of only 100 keV were reported in this paper. These results shed light on the advantage of laser wakefield acceleration: it creates a strong accelerating field travelling at close to the speed of light in the laser propagation direction which allows for acceleration over relatively long lengths. As a final note, it is possible to drive a wakefield with a high energy particle beam instead of a laser. These experiments have had great successes showing energy doubling from 42 to 84 GeV in a metre length plasma [83] and quasi-monoenergetic acceleration of a beam with a gradient of 4.4 GeV/m [84]. The drawback here is that a large conventional accelerator is required to drive the wakefield although it is thought of as a useful compact 'afterburner' to boost the final particle beam energy from such a machine. So for the near future at least the LWFA seems a promising candidate for a compact particle accelerator to multi-GeV energies.

1.4 Betatron Radiation from Laser Wakefield Accelerators

While the talk of LWFA driven FEL sources is somewhat speculative for now, LWFA's operating in the bubble regime are already known to act as a source of bright x-ray radiation, termed 'betatron radiation' [85] [79], which is emitted by electrons oscillating transversely in the fields of the bubble while they are being accelerated. This oscillation occurs at the betatron frequency $\omega_\beta = \omega_p/\sqrt{2\gamma_e}$. Much like undulator radiation this is frequency upshifted by a factor of $2\gamma_e^2$ in the lab frame. For GeV electrons this radiation is in the hard x-ray (10's keV) region of the spectrum. The undulator parameter describing this system $K > 1$ meaning that the radiation is broadband. The shape of this spectrum is predicted to be the on-axis synchrotron spectrum [86]. The characteristic energy of this spectrum is called the critical energy which is the energy above and below which exactly half of the energy in the angularly integrated spectrum is contained. One might

[3] As an example a 1 J, 40 fs FWHM pulse focussed to a spot of 10 μm FWHM has a peak electric field of 340 TV/m.

expect the spectrum produced in experiments to more complicated for reasons such as the presence of an intense laser pulse in the bubble, the electrons generally not being monochromatic, and electron longitudinal acceleration and oscillation happening at the same time. Nevertheless good agreement with a synchrotron spectrum has been found [87]. This is not too surprising because the intensity of the radiation scales with γ_e^2 so most of the radiation is emitted when the electrons are close to their maximum energy.

There are a number of publications which state a measured brightness of betatron sources as $5 \times 10^{21} - 1 \times 10^{22}$ photons/s/mm^2/mrad^2/0.1%BW [88] [89] [79] with critical energies around 5 keV, x-ray divergence of approximately 10 mrad and with $10^7 - 10^8$ x-ray photons detected per shot. This has been improved on in recent times with the use of a higher power laser driver such that the number of photons with energies above 1 keV was of order 10^9 with a critical energy of 33 keV [33]. Betatron x-rays are emitted from a micron scale source [90] [79] which permits high resolution imaging in a compact geometry [33] and means that this source can be used for propagation based phase contrast imaging [91] [92] [93]. The electron bunch and therefore x-ray duration is simplistically estimated to be of order $\lambda_p/(2c) \approx 30$ fs. Measurements of the electron bunch length from transmission radiation suggest that x-ray pulses of few fs duration can be expected under optimum conditions [62]. These values indicate that betatron radiation is comparable in brightness to 3$^{\text{rd}}$ generation light sources. However it is important to remember that part of this is coming from the significantly shorter x-ray pulse length and that it is has only recently become possible to obtain high quality images of moderate Z materials [33] which is the bread and butter of synchrotron sources. It could be argued that an important step for betatron radiation is to increase the number of photons significantly to really allow the field of betatron imaging to take off. This would also be beneficial for other potential applications such as ultrafast probing of materials via Laue diffraction or x-ray absorption, a conclusion that agrees with other current views on potential applications of betatron radiation [94].

So far we have seen that betatron radiation is a bright x-ray source operating in the few to tens of keV part of the spectrum. Other applications of electron beams from LWFA's as light source drivers have been explored. 17 nm UV light has been produced by coupling a wakefield accelerator to a conventional magnetic undulator [95]. It has also been shown that the electron beam from a LWFA can be used for Compton scattering of optical photons up to the MeV energy scale [96] [97] [98] [99].

1.5 Thesis Outline

The rest of this thesis will proceed as follows:

Chapter 2 will cover the theory of charged particle interaction with electromagnetic fields and then the collective response of a plasma to an intense laser pulse. This will lead to a theoretical description of the LWFA mechanism. Finally the topic of synchrotron radiation will be covered as the theoretical basis for betatron radiation.

Chapter 3 will discuss the experimental methods used to obtain the data in this thesis, with a particular focus on electron beam and x-ray diagnosis.

Chapter 4 is going to present results from a 10 TW LWFA experiment which used a clustered methane target, as opposed to a more conventional gas monomer target. By comparing the properties of the electron beams to those produced by self-injection and ionisation injection some unique aspects of this method will be elucidated.

Chapter 5 will show that by moving to a longer focal length geometry the brightness of betatron radiation from a LWFA can be increased by an order of magnitude. This chapter will detail the brightest betatron source yet measured, produced from a self-guided, self-injecting LWFA driven by a multi-hundred TW laser pulse.

Chapter 6 will show that betatron radiation is a suitable x-ray source for studying transient phenomena in solid density matter, with the example of shock waves travelling through solid targets. A significant increase in the imaging quality with the improved brightness and number of photons presented in chapter 5 will be demonstrated.

Chapter 2

Theory

This chapter is concerned with the theory behind the mechanism of laser wakefield acceleration and the generation of betatron radiation. Studying the motion of an electron in a laser field will lead to an understanding of the ponderomotive force, and we will see that this is the force driving the wakefield. The propagation of intense laser pulses in an underdense plasma will be discussed. The form of 1D linear and nonlinear, and 3D nonlinear wakefields will be mathematically described, from which the anticipated properties of LWFA electron beams will be found. By considering the transverse motion of an electron in a wakefield we will discover that it is similar to electron motion in a conventional insertion device. Armed with this knowledge the expected properties of betatron radiation will be found.

2.1 Electron Motion in Externally Applied Fields

In laser wakefield acceleration experiments a very intense laser pulse interacts with an initially neutral plasma. As they are much lighter than the ions, the electrons dominate the plasma response to the laser. To begin this chapter, therefore, the behaviour of an electron in an electromagnetic field will be mathematically described. This will be in a Lagrangian/ Hamiltonian formalism so this will be introduced first. For values of the normalised vector potential $a_0 \sim 1$ the motion of the electrons in the transverse laser field becomes relativistic, which will be accounted for. From the Lagrangian the equations of motion of an electron in the simplest case, the monochromatic plane wave, will be found. Then as a more realistic model the effect of gradients in the pulse intensity, as are found in any laser pulse, will be examined. This will give rise to a derivation of the ponderomotive force, which as we will see when discussing wakefield excitation, is what drives the wakefield.

2.1.1 Charged Particle Motion in an Electromagnetic Field

Throughout much of this chapter physical systems will be dealt with in a Lagrangian or Hamiltonian formalism. The Lagrangian for a system of particles with charge Q and mass m in a prescribed electric field $\boldsymbol{E}$ and magnetic field $\boldsymbol{B}$ is given by [100]

$$L = -mc^2\sqrt{1-\beta^2} - Q\phi + Q\boldsymbol{v}.\boldsymbol{A} \tag{2.1}$$

where $\boldsymbol{\beta} = \boldsymbol{v}/c$ is the velocity of the particle normalised to the speed of light c. ϕ and $\boldsymbol{A}$ are the scalar and vector potentials associated with the $\boldsymbol{E}$ and $\boldsymbol{B}$ fields. They are related via the equations

$$\boldsymbol{B} = \boldsymbol{\nabla} \times \boldsymbol{A} \tag{2.2}$$

$$\boldsymbol{E} = -\boldsymbol{\nabla}\phi - \frac{\partial \boldsymbol{A}}{\partial t} \tag{2.3}$$

Electric and magnetic fields are governed by Maxwell's equations. These equations, and more details on the potentials, can be found in appendix 8.1.

In general the Lagrangian is related to physics via Hamilton's principle which in effect states that the dynamics of a physical system can be determined by minimising the action A

$$A = \int_{t_1}^{t_2} L dt \tag{2.4}$$

The minimisation of the action yields the Euler-Lagrange equations:

$$\frac{d}{dt}\frac{\partial L}{\partial \dot{q}_i} = \frac{\partial L}{\partial q_i} \tag{2.5}$$

The solution to these equations gives the equations of motion for each of the N particles denoted i in a system with coordinates q_i. In 3D cartesian coordinates the motion of each particle would be described by three Euler-Lagrange equations, one each for $q = (x(t), y(t), z(t))$. The Euler-Lagrange equations physically show that the time rate of change of a generalised (canonical) momentum $u_i = \frac{\partial L}{\partial \dot{q}_i}$ is equal to a generalised force $F = \frac{\partial L}{\partial q}$. For example setting $(\phi, \boldsymbol{A}) = 0$ and solving the Euler-Lagrange equations for the Lagrangian in equation 2.1 results in the conservation of linear momentum i.e. $\frac{d}{dt}(\gamma m \boldsymbol{v}) = 0$, where γ is the Lorentz factor of the particle. For non-zero values of the potentials application of the Euler-Lagrange equations, along with use of the convective derivative $\frac{d}{dt} = \frac{\partial}{\partial t} + \boldsymbol{v}.\boldsymbol{\nabla}$, the Lorentz force law is recovered in its familiar form

$$\frac{d\boldsymbol{p}}{dt} = Q\left(\boldsymbol{E} + \boldsymbol{v} \times \boldsymbol{B}\right) \tag{2.6}$$

Finally the Hamiltonian for any system, which gives the total system energy, is constructed

as

$$H = \sum_i u_i \dot{q}_i - L \tag{2.7}$$

For a single particle of charge Q in potentials $(\phi, \boldsymbol{A})$ the generalised momentum $u = \gamma m \dot{q} + QA$ and the Hamiltonian is given by

$$H = \gamma m c^2 + Q\phi \tag{2.8}$$

2.1.2 Electron Motion in a Monochromatic Plane Wave

As seen in appendix 8.1 Maxwell's equations are invariant under a gauge transformation, which is a more general version of the principle that adding a constant to the scalar potential ϕ of the universe does not affect the motion of any of the charged particles in it. One choice of gauge is the Coulomb gauge where one sets $\boldsymbol{\nabla}.\boldsymbol{A} = 0$, the result of which is that $\phi = 0$ in a vacuum. An infinite plane wave travelling at speed c in the $+z$ direction is described by $\boldsymbol{A} = \boldsymbol{A}(z - ct)$ where $\boldsymbol{A} = (A_x, A_y, 0)$ is some twice-differentiable function. The Lagrangian for a single electron in this wave is given by

$$L = -m_e c^2 \sqrt{1 - \beta^2} - e\boldsymbol{v}.\boldsymbol{A} \tag{2.9}$$

where m_e is the electron mass, e is the charge of the electron and $\boldsymbol{v}$ is the electron velocity. This Lagrangian has no spatial dependence in x or y i.e. $\frac{\partial L}{\partial x}$ and $\frac{\partial L}{\partial y}$ from equation 2.5 are both equal to zero. Therefore the generalised momenta $u_x = p_x - eA_x$ and $u_y = p_y - eA_y$, where p denotes linear momentum, do not change in time: they are conserved. The Euler Lagrange equations give the equation of motion in the z direction as

$$\frac{dp_z}{dt} = -e\boldsymbol{v}.\frac{\partial \boldsymbol{A}}{\partial z} \tag{2.10}$$

Insight in to how this affects the z motion of the electron can be gained by incorporating this result in to the equation for the time rate of change of the total energy i.e. the Hamiltonian

$$\frac{dH}{dt} = -\frac{\partial L}{\partial t} = e\boldsymbol{v}.\frac{\partial \boldsymbol{A}}{\partial t} = -ec\boldsymbol{v}.\frac{\partial \boldsymbol{A}}{\partial z} = c\frac{dp_z}{dt} \tag{2.11}$$

The first equality is a standard property of Hamiltonian mechanics. The second is found by partially differentiating the Lagrangian with respect to time, and then the substitution $z = ct$ is made for light waves. The final equality has simply used the result of equation 2.10. From the previous equation and the definition of the Hamiltonian the following conserved quantity is identified

$$\frac{d}{dt}\left(\gamma m_e c^2 - c p_z\right) = 0 \tag{2.12}$$

Before summarising the equations of motion for an electron in a plane wave from what we have learned here, the variables will be converted to normalised units. Normalised (mechanical) momentum $\tilde{\boldsymbol{p}} = \gamma\boldsymbol{\beta}$ and $\boldsymbol{a} = e\boldsymbol{A}/m_e c$ are used here. A full reference of all the normalised units used in this work are detailed in appendix 8.2. The relationships between the transverse momentum of the electron and the laser field are simply a restating of the conservation of generalised momentum:

$$\tilde{p}_x = a_x \tag{2.13}$$

$$\tilde{p}_y = a_y \tag{2.14}$$

These equations describe an electron oscillating transversely in an electromagnetic wave. In the normalised units it becomes clear that for $a \sim 1$ the motion becomes relativistic. For an electron starting at rest equation 2.12 implies that

$$(\gamma - 1) = \tilde{p}_z \tag{2.15}$$

Inserting this and equations 2.13 and 2.14 in to the energy equation $E^2 = p^2c^2 + {m_e}^2c^4$ produces the equation for $\tilde{p}_z$

$$\tilde{p}_z = \frac{1}{2}a^2 \tag{2.16}$$

This has used the identity $a^2 = a_x^2 + a_y^2$. A useful result from combining equations equations 2.15 and 2.16 is

$$\gamma = 1 + \tilde{p}_z = 1 + \frac{1}{2}a^2 \tag{2.17}$$

Gaining momentum in the direction of wave propagation is unfamiliar from solving linearised equations in the low velocity limit. This motion comes from the $\boldsymbol{v} \times \boldsymbol{B}$ term in the Lorentz force law and is only comparable in magnitude to the $\boldsymbol{E}$ field term at high velocities i.e. where large amplitude electromagnetic fields are present.

To examine this motion in more detail it is useful to solve the equations of motion for this system. Describing the wave in the lab frame as $\boldsymbol{a} = a_0 \cos(kz - \omega t)\ \hat{\boldsymbol{x}} = a_0 \cos\theta\ \hat{\boldsymbol{x}}$ then the equations of motion, from equations 2.13 and 2.16, are

$$\frac{\gamma}{c}\frac{dx}{dt} = a_0 \cos\theta \tag{2.18}$$

$$\frac{\gamma}{c}\frac{dz}{dt} = \frac{1}{2}{a_0}^2 \cos^2\theta \tag{2.19}$$

where the y component has been ignored since there is no electric field in this direction. To integrate these equations the identity $\frac{d\theta}{dt} = \omega/\gamma$ was used, which can be derived using the definition of the total derivative and equation 2.15. Integrating equations 2.18 and

2.19 with respect to the variable $\theta = (kz - \omega t)$ produces the electron trajectories

$$x = \frac{a_0}{k} \sin\theta \tag{2.20}$$

$$z = \frac{1}{4}\frac{{a_0}^2}{k}\left(\theta + \frac{1}{2}\sin(2\theta)\right) \tag{2.21}$$

These trajectories are plotted on the left hand side of figure 2.1.

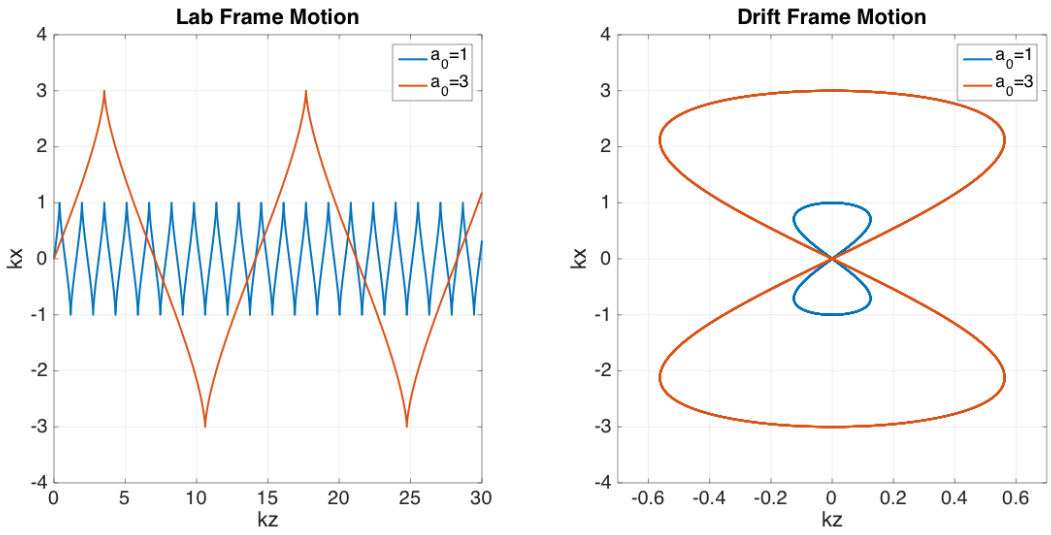


Figure 2.1: The motion of a relativistic test electron in a monochromatic plane wave in the lab frame (left) and drift frame (right).

Taking the time average of equations 2.18 and 2.19 and writing γ in terms of $\boldsymbol{a}$ reveals that there is an average drift velocity in the lab frame $v_d = c{a_0}^2/(4 + {a_0}^2)$. This suggests that electrons could be accelerated in a vacuum via this mechanism. High intensity laser systems can produce focal intensities of order 10^{21} W/cm^2 which corresponds to $a_0 \sim 22$. Issues confining electrons to the focal spot of the laser beam aside, this produces a drift momentum of only ~ 60 MeV/c, which is significantly below what can be achieved with the same laser systems via the LWFA mechanism. The time-averaged electron momentum in the lab frame is $\tilde{p}_D = \frac{1}{4}{a_0}^2$. Moving to the average rest frame of the electron, i.e. a frame moving at $v_d = c{a_0}^2/(4 + {a_0}^2)$, the motion is a figure of 8 as plotted on the right hand side of figure 2.1. This is most easily done by finding the equation of motion from the momentum $\tilde{p}'_z = \tilde{p}_z - \tilde{p}_D = \frac{1}{2}a^2 - \frac{1}{4}{a_0}^2$.

2.1.3 The Ponderomotive Force

The previous section dealt with electron motion in a rapidly oscillating electromagnetic field using a plane wave as the simplest example. This is not, however, representative of

a typical laser pulse used in a high intensity experiment. These are short, focussed pulses with spatial and temporal envelopes with significant gradients. We will now look at the effects these gradients have on electron motion over time periods much longer than the oscillation period of the wave. Considering first electron motion in the non-relativistic ($a_0 \ll 1$) limit and assuming that $\boldsymbol{a} = a_0 \cos(kz - \omega t)\hat{\boldsymbol{x}}$, equation 2.13 can be re-written as

$$v_x = c a_0 \cos(kz - \omega t) \tag{2.22}$$

The z motion can be ignored because $v_z \propto {a_0}^2$ and is therefore negligible. The velocity from equation 2.22 is known as the quiver velocity and has an associated quiver energy E_q,

$$E_q = \frac{1}{2} m_e c^2 \left\langle a^2 \right\rangle \tag{2.23}$$

The angled brackets denote that the quantity is time averaged i.e. we are only interested in the effects of the 'slowly' varying pulse envelope and not the fast oscillations. Treating this quantity like a potential the ponderomotive force is derived as

$$\boldsymbol{F_p} = \left\langle \frac{d\boldsymbol{p}}{dt} \right\rangle = -\frac{1}{2} m_e c^2 \boldsymbol{\nabla} \left\langle a^2 \right\rangle . \tag{2.24}$$

This equation can be generalised to relativistic electron motion as derived in appendix 8.3:

$$\left\langle \frac{d\tilde{\boldsymbol{u}}}{dt} \right\rangle = -\frac{1}{2} c \left\langle \frac{1}{\gamma} \boldsymbol{\nabla} a^2 \right\rangle \tag{2.25}$$

$\tilde{\boldsymbol{u}} = \boldsymbol{u}/m_e c$ is the normalised generalised momentum of the electron.

The ponderomotive force pushes charged particles away from regions of high intensity. It has the interesting property that the force is in the same direction for both positive and negative charges. To examine the effect on the ion species in a plasma the electron mass m_e in equation 2.24 should simply be replaced by the ion mass m_i, remembering to perform the same replacement in the definition of a. The significantly larger mass of the ion species means that on time-scales of order $1/\omega_p$ (see section 2.2.3) the ion motion can be ignored compared to the electron motion. Therefore a laser pulse in a plasma will excite a collective electron oscillation in its wake as a result of its ponderomotive force. This is the basis of laser wakefield acceleration, the theory behind which will be discussed further in 2.3.

2.2 Nonlinear Optics in Underdense Plasmas

Moving on from descriptions of single electrons, this section will look at the response of an underdense plasma as it is perturbed by electromagnetic fields. First the propagation

of electromagnetic waves in a vacuum will be examined. A brief description will follow on how plasmas are created by a laser pulse interacting with matter. Studying the propagation of electromagnetic waves in a plasma will lead to an expression for the plasma refractive index. This refractive index becomes nonlinear for intense radiation leading to effects such as pulse compression, photon acceleration and self-focussing of the pulse in the plasma which will be described for a pulse of moderate intensity i.e. $a_0 < 1$, following the work of Mori [50]. References to other works showing that similar effects exist in the high intensity $a_0 > 1$ regime will be provided.

2.2.1 Electromagnetic Waves in Vacuum

Electromagnetic waves in a vacuum are described by the equation

$$\left(\nabla^2 - \frac{1}{c^2}\frac{\partial^2}{\partial t^2}\right)\boldsymbol{E} = 0 \tag{2.26}$$

where $c^2 = 1/(\mu_0\epsilon_0)$. The $\boldsymbol{B}$ field can then be calculated from Faraday's law (equation 8.3). This equation was found by taking the curl of Faraday's law (equation 8.3) and inserting Ampere's law (equation 8.4) in to the resulting equation, and it describes a wave propagating at speed c. The simplest non-trivial solution to this equation is the infinite plane wave which takes the form $\boldsymbol{E} = \boldsymbol{E_0}\exp(i(\boldsymbol{k}.\boldsymbol{r} - \omega t))$. However this is not the only solution. This equation may be solved more generally via the method of separation of variables. Defining $\boldsymbol{E} = \boldsymbol{E}(\boldsymbol{r}, t) = \boldsymbol{u}(\boldsymbol{r})v(t)$, where $\boldsymbol{u}$ is only a function of space and v is only a function of time, equation 2.26 becomes

$$v\nabla^2\boldsymbol{u} - \boldsymbol{u}\frac{\partial^2 v}{\partial t^2} = 0 \tag{2.27}$$

This equation can only hold in general if both terms in this equation are equal to some constant k^2, meaning that one can write

$$\nabla^2\boldsymbol{u} = -k^2\boldsymbol{u} \tag{2.28}$$

$$\frac{\partial^2 v}{\partial t^2} = -k^2 v \tag{2.29}$$

The spatial part of this equation is the Helmholtz equation

$$\left(\nabla^2 + k^2\right)\boldsymbol{u} = 0 \tag{2.30}$$

Inserting the trial solution $\boldsymbol{u}(\boldsymbol{r}) = \boldsymbol{u}_0(\boldsymbol{r})\exp(ikz)$, i.e. a plane wave that is spatially modulated by some function $\boldsymbol{u}_0(\boldsymbol{r})$, the Helmholtz equation becomes

$$\left(\frac{\partial^2 \boldsymbol{u}_0}{\partial x^2} + \frac{\partial^2 \boldsymbol{u}_0}{\partial y^2} + \frac{\partial^2 \boldsymbol{u}_0}{\partial z^2}\right)\exp(ikz) + ik\frac{\partial \boldsymbol{u}_0}{\partial z}\exp(ikz) + k^2\boldsymbol{u} = 0 \tag{2.31}$$

For a slowly focussing beam one can use the paraxial approximation, which is to say $\left|\frac{\partial^2 \boldsymbol{u}}{\partial z^2}\right| \ll \left|k\frac{\partial \boldsymbol{u}}{\partial z}\right|$. This allows for the simplification of the Helmholtz equation to

$${\nabla_\perp}^2\boldsymbol{u}_0 + ik\frac{\partial \boldsymbol{u}_0}{\partial z} + k^2\boldsymbol{u}_0 = 0 \tag{2.32}$$

Where the short-hand ${\nabla_\perp}^2 = \frac{\partial^2}{\partial x^2} + \frac{\partial^2}{\partial y^2}$ has been used. For an electric field polarised along the x direction the lowest order solution (i.e. the TEM_{00} mode) to this equation is a gaussian beam of the form [101]

$$\boldsymbol{E}(\boldsymbol{r},t) = E_0\hat{\boldsymbol{x}}\frac{w_0}{w(z)}\exp\left(\frac{-r^2}{w^2(z)}\right)\exp\left[-i\left((kz-\omega t) + k\,\frac{r^2}{2R(z)} - \psi(z)\right)\right] \tag{2.33}$$

where w_0 is the $1/e$ radius of the electric field at focus. $w(z)$ is the width of the beam at position z, defined as

$$w(z) = w_0\sqrt{1 + \frac{z^2}{{z_R}^2}} \tag{2.34}$$

which makes use of the Rayleigh length

$$z_R = \frac{\pi {w_0}^2}{\lambda} \tag{2.35}$$

The Rayleigh length is the distance over which the width of the beam increases by a factor of $\sqrt{2}$. $R(z)$ is the radius of curvature of the beam which is given by

$$R(z) = z\left[1 + \left(\frac{z_R}{z}\right)^2\right] \tag{2.36}$$

Finally $\psi(z) = \tan^{-1}\left(\frac{z}{z_R}\right)$ is the Gouy phase, which is an extra phase shift picked up by a gaussian beam moving through focus. The electric field around focus is visualised in figure 2.2. The intensity of the beam I is

$$I = I_0\left(\frac{w_0}{w(z)}\right)^2\exp\left(-\frac{2r^2}{w^2(z)}\right) \tag{2.37}$$

where $I_0 = \frac{1}{2}c\epsilon_0{E_0}^2$. It is emphasised that w_0 is the $1/e$ width for the field and $1/e^2$ width for intensity.

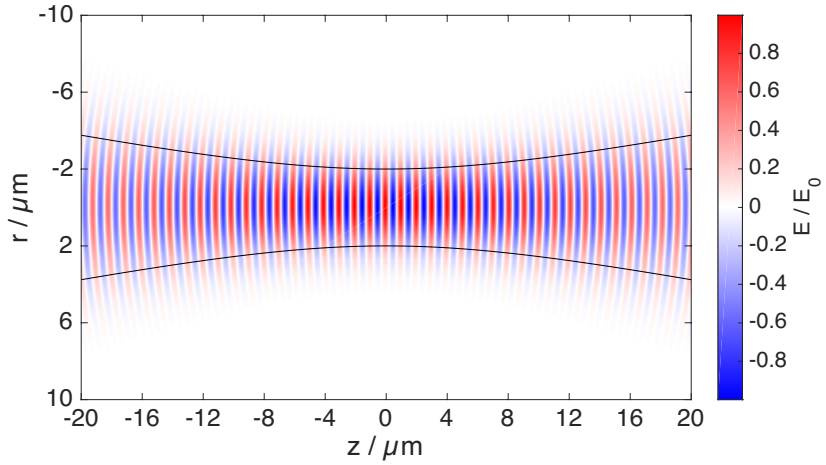


Figure 2.2: Electric field of a focussed gaussian laser beam normalised to E_0. $\lambda = 1$ μm and $w_0 = 2$ μm. This is plotting the real part of the electric field. The black lines show the $1/e$ field width.

In this section we have seen a solution to Maxwell's equations that is more representative of focussed laser beams than the infinite plane wave. This has been derived by solving the Helmholtz equation using the paraxial approximation. The intensity profile is gaussian, and as the beam goes in and out of focus the peak intensity drops by a factor of 2 over a characteristic length, the Rayleigh length (equation 2.35), because of the increase in the beam width. This is an important quantity to keep in mind when high intensities are required, as the target should generally be placed within a Rayleigh length of the focus.

2.2.2 Creating a Plasma

Focussed laser intensities in LWFA experiments usually exceed 10^{18} W/cm^2 meaning that the leading edge of the laser pulse, or a prepulse, will be sufficiently intense to fully ionise a low Z gas such as hydrogen or helium. For this reason it is not necessary to use preformed plasmas for LWFA. At high intensity the ponderomotive potential of the laser, which is related to the laser electric field E_L and the laser frequency ω_L by

$$\Phi_{pond} = \frac{e^2 {E_L}^2}{4 m_e {\omega_L}^2} \tag{2.38}$$

becomes comparable in magnitude to the binding potential of the ion $\mathcal{E}_{ion}$. This means that the atomic binding potential felt by an electron is significantly distorted by the laser field. In a simple 1D model [102] [103] where a static electric field E is applied to an atom

of charge Ze, the potential $V(x)$ is given by

$$V(x) = -\frac{Ze^2}{4\pi\epsilon_0 x} - eEx \tag{2.39}$$

Minimising this equation with respect to the position x gives the position of the potential maximum i.e. the position of the potential barrier that must be overcome for ionisation to occur. The position of the potential maximum is

$$x_{max} = \left(\frac{Ze}{4\pi\epsilon_0 E}\right)^{\frac{1}{2}} \tag{2.40}$$

By setting the height of the potential barrier $V\left(x_{max}\right) = \mathcal{E}_{ion}$ a threshold electric field E_t, where

$$E_t = \frac{\pi\epsilon_0 {\mathcal{E}_{ion}}^2}{Ze^3} \tag{2.41}$$

is found. If the applied electric field exceeds this threshold field the potential barrier will be fully suppressed, giving rise to so-called over-the-barrier or above-threshold ionisation. Written in terms of laser intensity this condition is given by

$$I > I_t = \frac{\pi^2 {\epsilon_0}^3 c}{2e^6}\frac{{\mathcal{E}_{ion}}^4}{Z^2} \approx 4 \times 10^9 \left(\frac{\mathcal{E}_{ion}}{\mathrm{eV}}\right)^4 Z^{-2}\ \mathrm{W/cm^2} \tag{2.42}$$

$\mathcal{E}_{ion}$ is the ionisation potential of an ion with charge $(Z-1)$. For example, this equation predicts that hydrogen will be ionised at an intensity of $1.4 \times 10^{14}\,\mathrm{W/cm^2}$, and helium will be fully ionised at an intensity of $8.8 \times 10^{15}\,\mathrm{W/cm^2}$. Both of these values are significantly less than the peak laser intensity used in LWFA experiments, which verifies the earlier claim that preformed plasmas are not required.

At slightly lower intensities the atomic binding potential felt by the electron will be greatly reduced, making tunnelling out of the potential much more likely. This was explored by Ammosov, Delone and Krainov [104]. At even lower intensities of $10^{10} - 10^{13}$ W/cm^2 ionisation occurs via multiphoton ionisation [102]. The multiphoton and tunnelling regimes are distinguished by the Keldysh parameter

$$\gamma_K = \omega_L \sqrt{\frac{2\mathcal{E}_{ion}}{I_L}} \tag{2.43}$$

Here ω_L and I_L are the laser frequency and intensity respectively. The tunnelling regime has $\gamma < 1$ and the multiphoton regime has $\gamma > 1$.

2.2.3 The Plasma Frequency

Electromagnetic wave propagation is governed primarily by the plasma electrons, which are driven to oscillate by the incoming light. These electrons have a natural oscillation frequency called the plasma frequency, which will now be derived in the geometry shown in figure 2.3.

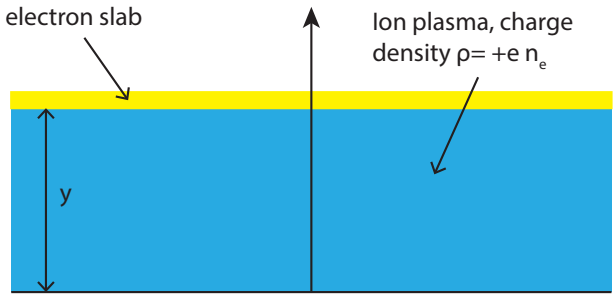


Figure 2.3: The geometry for the derivation of the plasma frequency.

We consider the displacement of a slab of plasma electrons along a single axis y leaving behind a charge density $\rho = en_e$, where n_e is the density of displaced electrons. Poisson's equation gives the potential that is produced by this displacement as

$$\phi = -\frac{en_e}{2\epsilon_0}y^2 \tag{2.44}$$

This can be inserted in to the Lagrangian (equation 2.1) with $\boldsymbol{A} = 0$. Solving the Euler-Lagrange equations and assuming that we are in a non-relativistic regime ($\gamma = 1$) yields the equation of motion

$$\ddot{y} = -\frac{e^2 n_e}{\epsilon_0 m_e}y = -{\omega_p}^2 y \tag{2.45}$$

This is the equation for a simple harmonic oscillator at the plasma frequency ω_p, where

$$\omega_p = \sqrt{\frac{e^2 n_e}{\epsilon_0 m_e}} \tag{2.46}$$

The ions have been assumed to be stationary because of their larger mass. When relativistic effects become important equation 2.45 becomes $c\dot{\tilde{p}}_y = -{\omega_p}^2 y$. This is usually dealt with by replacing m_e with $\langle\gamma\rangle\, m_e$ in the expression for the plasma frequency, where the angled brackets denote the time average.

2.2.4 Electromagnetic Waves in Plasmas

To understand how a laser can produce a wakefield in an underdense plasma, it is critical to understand the behaviour of electromagnetic waves in plasmas. Maxwell's equations

with charge density $\rho = 0$ for a quasi-neutral plasma and current density $\boldsymbol{J} = -en_e\boldsymbol{v}$ can be used to produce a wave equation for the electric field $\boldsymbol{E}$:

$$\nabla^2\boldsymbol{E} = -\mu_0 e n_e \frac{\partial \boldsymbol{v}}{\partial t} + \frac{1}{c^2}\frac{\partial^2 \boldsymbol{E}}{\partial t^2} \tag{2.47}$$

$\boldsymbol{v}$ is the velocity of plasma electrons and n_e is the electron number density. The non-relativistic limit of equation 2.13 can be used to write $\boldsymbol{v} = -ie\boldsymbol{E}/(m_e\omega)$ where i is the imaginary unit and ω is the frequency of the light. Inserting this in to equation 2.47 results in a wave equation in terms of $\boldsymbol{E}$ only

$$\nabla^2\boldsymbol{E} = \frac{i{\omega_p}^2}{\omega c^2}\frac{\partial \boldsymbol{E}}{\partial t} + \frac{1}{c^2}\frac{\partial^2 \boldsymbol{E}}{\partial t^2} \tag{2.48}$$

Inserting a plane wave solution of the form $\boldsymbol{E} = \boldsymbol{E_0}\exp\left[i\left(\boldsymbol{k}.\boldsymbol{r} - \omega t\right)\right]$ results in the dispersion relation

$$\omega^2 = {\omega_p}^2 + c^2k^2 \tag{2.49}$$

The phase velocity $v_p = \omega/k$ and group velocity $v_g = \frac{\partial\omega}{\partial k}$ are derived as

$$v_p = \frac{c}{\sqrt{1 - \frac{{\omega_p}^2}{\omega^2}}} \tag{2.50}$$

$$v_g = c\sqrt{1 - \frac{{\omega_p}^2}{\omega^2}} \tag{2.51}$$

The refractive index $\eta = c/v_p$ is then defined as

$$\eta = \sqrt{1 - \frac{{\omega_p}^2}{\omega^2}} = \sqrt{1 - \frac{n_e}{n_c}} \tag{2.52}$$

In the second equality $n_c = m_e\epsilon_0\omega^2/e^2$ is the critical density of the plasma: the density above which light of frequency ω does not propagate in the plasma. This allows for a definition of 'underdense' i.e. a density conforming to the inequality $n_e < n_c$.

2.2.5 Nonlinear Refractive Index of a Plasma

As discussed at the end of section 2.2.3, for an intense electromagnetic wave the plasma frequency is altered because of the relativistic mass increase of the electrons oscillating in the wave, which have a relativistic factor $\gamma = 1 + \frac{1}{2}a^2$ as seen in equation 2.17. To account for this the substitution ${\omega_p}^2 \rightarrow {\omega_p}^2/\langle\gamma\rangle$ is made where $\langle\gamma\rangle = 1 + {a_0}^2/4$ for a sinusoidal field. This leads to a relativistic expression for the refractive index η

$$\eta \approx 1 - \frac{1}{2}\frac{{\omega_p}^2}{\omega^2}\left(1 - \frac{{a_0}^2}{4}\right) \tag{2.53}$$

This is valid for $\frac{1}{4}{a_0}^2 \ll 1$ and ${\omega_p}^2/\omega^2 \ll 1$ because of the binomial expansions that have been performed. An intense laser pulse can additionally cause changes in n_e, for example by the ponderomotive force acting to push electrons away from regions of high intensity. This can produce longitudinal gradients in refractive index which in turn can change the frequency of the driving laser, as we will see in section 2.2.7. To account for this we set number density $n_e = n_0 + \delta n_e$ and laser frequency $\omega = \omega_0 + \delta\omega$ in equation 2.53. n_0 and ω_0 are constants, δn_e and $\delta\omega$ are perturbations to these, and for simplicity we demand that $\delta n_e/n_0 \ll 1$ and $\delta\omega/\omega_0 \ll 1$. Ignoring all terms that are a product of two or more small quantities the nonlinear refractive index can be written as

$$\eta = 1 - \frac{1}{2}\frac{{\omega_{p0}}^2}{{\omega_0}^2}\left(1 + \frac{\delta n_e}{n_0} - \frac{2\delta\omega}{\omega_0} - \frac{{a_0}^2}{4}\right) \tag{2.54}$$

where ${\omega_{p0}}^2 = \frac{e^2 n_0}{\epsilon_0 m_e}$. In the coming sections the consequences of this modified refractive index will be examined.

2.2.6 Pulse Compression

A longitudinal gradient in refractive index causes a gradient in the group velocity of the pulse. Consider two points in the pulse z_1 and z_2, with $z_2 - z_1 = l$, which move with group velocities v_{g1} and v_{g2}. The change in l, Δl, in time Δt is given by

$$\Delta l = (v_{g2} - v_{g1})\,\Delta t = \Delta v_g \Delta t = c\Delta\eta\Delta t \tag{2.55}$$

Writing $\Delta v_g \approx \frac{\partial v_g}{\partial z} l$ the rate of change of the pulse length l with respect to time is

$$\frac{1}{l}\frac{\partial l}{\partial \tau} \approx c\frac{\partial \eta}{\partial \xi} \tag{2.56}$$

This is given in the wave frame coordinates $\xi = (z - ct)$ and $\tau = t$ (see appendix 8.4) because this problem is more naturally considered when the gradients are co-moving with the pulse.

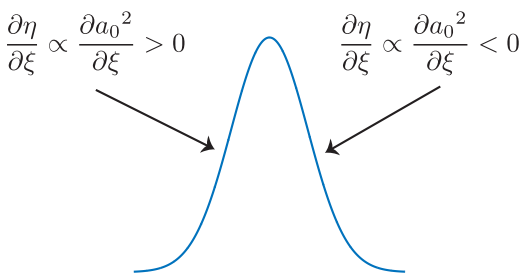


Figure 2.4: Density gradients caused by a gaussian laser pulse.

Equation 2.54 shows that the refractive index increases with a_0. For a gaussian pulse $\frac{\partial \eta}{\partial \xi}$ will be negative at the front of the pulse and positive at the rear of the pulse, as figure 2.4 shows. This will cause the front half of the pulse to compress or steepen. This increases the ponderomotive force $\boldsymbol{F_p} \propto \boldsymbol{\nabla} {a_0}^2$ which will drive a stronger wakefield. This is one of the reasons that a pulse with a vacuum $a_0 < 2$ can drive a bubble regime LWFA, even to the point where self-injection occurs. Experimental results showing self-injection from LWFA's driven by such pulses will be presented in chapters 4 and 5 of this thesis. Pulse compression in a nonlinear LWFA has been measured experimentally, Faure et al. [53] saw compression from 38 ± 2 fs to $(10 - 14) \pm 2$ fs with a compression efficiency of around 20%. The rest of the energy went in to driving the wakefield. Schreiber et. al. [105] also measured pulse compression, from 45 to (18 ± 3) fs. We conclude that pulse compression is a large and important effect in LWFA's.

2.2.7 Photon Acceleration

From Fourier theory, it is clear that for a pulse to be compressed temporally there must be a corresponding increase in its bandwidth. It is possible to find the equation that describes how the frequencies in the pulse change with time by considering the separation between two wavefronts in the presence of a longitudinal refractive index gradient. Letting the initial positions of two wavefronts be z_{10} and z_{20} and velocities be $v_{\phi 1}$ and $v_{\phi 2}$, their positions after time Δt are $z_1 = z_{10} + v_{\phi 1}\Delta t$ and $z_2 = z_{20} + v_{\phi 2}\Delta t$. The change in their separation $(z_2 - z_1) - (z_{20} - z_{10}) = \Delta\lambda = \Delta v_\phi \Delta t$. Working in the wave frame and using $v_\phi = c/\eta$ and $\Delta v_\phi \approx \lambda \frac{\partial v_\phi}{\partial z}$, the change in wavelength, which has initial value λ_0, with time follows the equation

$$\frac{\Delta\lambda}{\Delta\tau} \approx \lambda \frac{\partial}{\partial \xi}\left(\frac{c}{\eta}\right) = -\frac{\lambda c}{\eta^2}\frac{\partial \eta}{\partial \xi} \tag{2.57}$$

Written in terms of angular frequency ω this becomes

$$\frac{\partial \omega}{\partial \tau} = \frac{c\omega}{\eta^2}\frac{\partial \eta}{\partial \xi} \tag{2.58}$$

Referring back to the form of η in equation 2.54 we see that going up a density ramp $\frac{\partial \eta}{\partial \xi} < 0$ and the frequency of light decreases with time. This agrees with intuition of light propagating more slowly in higher density material and shows that the cause of this is the photons red-shifting. From this fact and figure 2.4 it is clear that for a gaussian pulse the front of the pulse will red shift and the back will blue shift, so the back of the pulse will catch up with the front of the pulse, causing it to compress. This is in agreement with what we saw when discussing pulse compression. A more thorough description of photon acceleration can be found in [106]. Evidence of photon acceleration in wakefield experiments has been seen experimentally [107] and has been suggested as a diagnostic for probing wakefield dynamics [108].

2.2.8 Transverse Focussing

As well as longitudinal gradients in the refractive index of the plasma there may also be transverse gradients. A transverse gradient will cause two points along a wavefront to propagate at different phase velocities leading to a tilted wavefront at angle θ. This is demonstrated in figure 2.5. For a small tilt $\theta \approx \Delta v_\phi \Delta\tau / w$ where w is the spot radius.

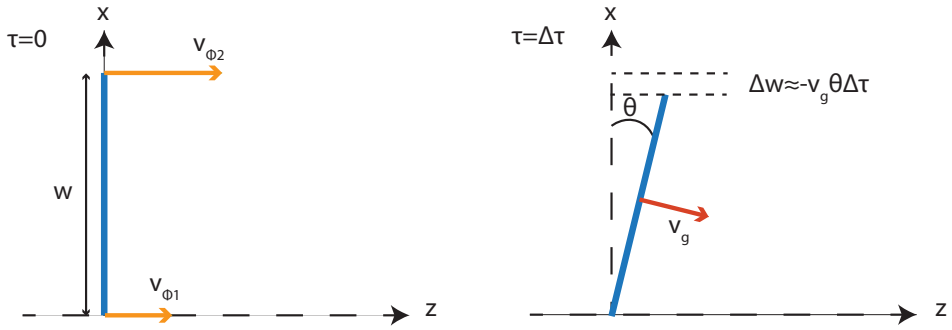


Figure 2.5: Left: A transverse density gradient causes two points on a wavefront, separated by distance w, to propagate with different phase velocities. Right: After some time $\Delta\tau$ the wavefront becomes tilted and the spot size w decreases.

Energy flows perpendicularly to the wavefront so the tilted wavefront will make w change with time as described by the equation

$$\Delta w \approx -v_g \theta \Delta\tau \Rightarrow \frac{\Delta w}{\Delta\tau} \approx -\eta c \frac{\Delta v_\phi \Delta\tau}{w} \tag{2.59}$$

Using $\Delta v_\phi \approx \frac{\partial v_\phi}{\partial r} w$ the acceleration of the focal spot is calculated as

$$\frac{\partial^2 w}{\partial \tau^2} = -\eta c \frac{\partial v_\phi}{\partial r} = \frac{c^2}{\eta} \frac{\partial \eta}{\partial r} \tag{2.60}$$

Therefore the spot will accelerate inwards if $\frac{\partial \eta}{\partial r} < 0$ which can be caused by n_e being lowest on-axis. This has encouraged the study of laser guiding and laser wakefield acceleration in a preformed plasma channel with a radial density profile. The guiding has been studied theoretically [109] and over the years experiments have shown acceleration of high quality electron beams from channel-guided LWFA's to the 100 MeV [65], 1 GeV [56] and now 4 GeV [61] levels. The laser focal spot will also accelerate inwards if the laser intensity profile is greatest on-axis, which is usually the case, as a result of the relativistic increase in refractive index. This will be examined in the next section. Along with pulse compression, self-focussing increases a_0 within the plasma, meaning that the laser drives a stronger wakefield, which can increase the energy gain of the injected electron beam or encourage self-injection.

2.2.9 Self-Guiding

A gaussian beam propagating in free space has a beam waist (the radius at which its intensity drops to $1/e^2$ of the maximum) given in equation 2.34, where $z_R = \pi {w_0}^2/\lambda$ is the Rayleigh length. Making the substitution $z = c\tau$ and differentiating this equation twice with respect to τ results in an equation for the acceleration of the focal spot due to diffraction. Assuming that we are close to the laser focus this equation simplifies to

$$\frac{\partial^2 w}{\partial \tau^2} \approx w_0 \frac{c^2}{{z_R}^2} = \frac{4c^2}{{k_0}^2 {w_0}^3} \tag{2.61}$$

$k_0 = 2\pi/\lambda_0$ is the spatial frequency of the laser. In a LWFA it would be preferable to accelerate an electron beam over distances much longer than the Rayleigh length z_R leading to the question of whether it is possible to have the focal spot acceleration from a transverse density gradient (equation 2.60) cancel out the acceleration from diffraction (equation 2.61). Using only the relativistic part of the refractive index i.e. using equation 2.53 and setting equation 2.60 equal to 2.61 produces the condition

$$\frac{4c^2}{{k_0}^2 {w_0}^3} = \frac{c^2}{\eta} \frac{{\omega_{p0}}^2}{8{\omega_0}^2} \frac{\partial {a_0}^2}{\partial r} \tag{2.62}$$

Assuming that ${a_0}^2$ is not too large we can say $1/\eta \approx 1$. We also have $\frac{\partial}{\partial r}{a_0}^2 \approx -{a_0}^2/w_0$. This results in the condition for a self-guided spot

$${w_0}^2 {a_0}^2 = 32 \frac{c^2}{{\omega_{p0}}^2} \tag{2.63}$$

Noting that the right hand side has units of power a critical power for self guiding is found as [110]

$$P_c \approx 17 \frac{{\omega_L}^2}{{\omega_p}^2} \mathrm{GW} \tag{2.64}$$

Thomas et. al. [51] showed that short pulses ($c\tau < \lambda_p$) could be guided over long distances when a large F number optic was used, producing a vacuum spot size $w_0 > \lambda_p$. In this case the pulse self focussed slowly in the plasma allowing a significant fraction of the pulse energy to be guided along a single filament. Self-guided LWFA experiments are commonly performed and GeV-level electrons have been accelerated in this regime, for example in [57]. In fact, self-guiding is critical for the success of LWFA's that don't employ a preformed plasma channel because it allows electrons to be accelerated for the full dephasing length (see section 2.3.6) which can be significantly longer than the Rayleigh length.

2.3 Laser Wakefield Acceleration

This section will mathematically explore the properties of laser driven plasma wakefields. Firstly, by modelling the plasma as an electron fluid with a fixed ion background in the low intensity limit, we will see that a wakefield can be described by a driven oscillator equation, where the driver is the ponderomotive force of the laser. The theory will be extended in to the relativistically nonlinear regime ($a_0 \gtrapprox 1$) in 1D, and with reference to the literature the 3D nonlinear 'bubble' regime will be described. It is important to know the structure of the wakefield so that methods of injecting charge in to its accelerating field can be understood, and the motion of an electron beam trapped within the wakefield can be calculated. This will result in the derivation of formulae for the maximum energy gain of the electron beam at the end of this section, and a description of the characteristics of the betatron x-ray spectrum which will be done in section 2.4.

2.3.1 Linear Wakefield Model

A model for a LWFA can be built up from Gauss' law, the continuity equation and the momentum equation for a plasma fluid element:

$$\nabla . \boldsymbol{E} = \frac{e(n_i - n_e)}{\epsilon_0} \tag{2.65}$$

$$\frac{\partial n}{\partial t} + \nabla(n\boldsymbol{v}) = 0 \tag{2.66}$$

$$m_e \left(\frac{\partial \boldsymbol{v}}{\partial t} + (\boldsymbol{v}.\nabla)\boldsymbol{v} \right) = -e\left(\boldsymbol{E} + \boldsymbol{v} \times \boldsymbol{B}\right) \tag{2.67}$$

$\boldsymbol{E}$ is the electric field, n_i and n_e are the ion and electron number densities respectively, $\boldsymbol{v}$ is the velocity of the fluid element and $\boldsymbol{B}$ is the magnetic field. For small a_0 one can write $v_i \approx ca_i$ from equation 2.13 where i denotes an axis perpendicular to the direction of laser propagation. Using this fact and $\boldsymbol{B} = \frac{m_e c}{e}(\nabla \times \boldsymbol{a})$ equation 2.67 becomes

$$m_e \frac{\partial \boldsymbol{v}}{\partial t} + e\boldsymbol{E} = -m_e c^2 \nabla a^2 \tag{2.68}$$

This system of equations can be linearised with the assumptions $a_0 \ll 1$, $n_i = n_{e0}$ and $n_e = n_{e0} + n_1$ where n_{e0} is a constant background density and n_1 is a small perturbation to this. Ignoring any terms that are the product of two small perturbations, and simplifying the problem so that there is only variation in the z direction, Gauss' law and the continuity equation become

$$\frac{\partial E}{\partial z} = -\frac{e n_1}{\epsilon_0} \tag{2.69}$$

$$\frac{\partial n_1}{\partial t} + n_{e0}\frac{\partial v}{\partial z} = 0 \tag{2.70}$$

Taking the partial derivative of equation 2.70 with respect to time, and replacing the $\frac{\partial v}{\partial t}$ term using equation 2.68 yields

$$\frac{\partial^2 n_1}{\partial t^2} + {\omega_p}^2 n_1 = \frac{1}{2} n_0 c^2 \frac{\partial^2 a^2}{\partial z^2} \tag{2.71}$$

This equation describes a plasma density wave driven by the ponderomotive force. It can be trivially generalised to 3D by making the substitution $\frac{\partial^2}{\partial z^2} \rightarrow \nabla^2$. The factor of $\frac{1}{2}$ has come from time averaging over the rapidly oscillating component of a. This can be written as a function of a single independent variable in the wave frame $\xi = z - ct$ by using the quasi-static approximation to set time derivatives to 0 (see section 8.4 for more details). This produces the equation

$$\frac{\partial^2 n_1}{\partial \xi^2} + {k_p}^2 n_1 = \frac{1}{2} n_0 \frac{\partial^2 a^2}{\partial \xi^2} \tag{2.72}$$

Using $\nabla . \boldsymbol{E} = -\nabla^2 \phi = -\frac{e n_1}{\epsilon_0}$ this equation can also be used to describe $\boldsymbol{E}$ and the scalar potential ϕ

$$\frac{\partial^2 E}{\partial \xi^2} + {k_p}^2 E = -\frac{1}{2} {k_p}^2 \left(\frac{m_e c^2}{e} \right) \frac{\partial a^2}{\partial \xi} \tag{2.73}$$

$$\frac{\partial^2 \phi}{\partial \xi^2} + {k_p}^2 \phi = \frac{1}{2} {k_p}^2 \left(\frac{m_e c^2}{e} \right) a^2 \tag{2.74}$$

Figure 2.6 plots the solution of equation 2.72 for a laser envelope described by $a = a_0 \exp\left(-\frac{\xi^2}{2L^2}\right)$. $a_0 = 0.05$ was chosen and the pulse length was set so that $2L = \lambda_p$. In the lab frame the laser travels from right to left and leaves a sinusoidal plasma oscillation in its wake: a wakefield. The wakefield has a phase velocity equal to the laser group velocity, and zero group velocity. It can be shown that plasma waves are most efficiently excited when the length of the laser pulse envelope is close to the plasma wavelength [111]. This can be seen in the figure: the plasma wave is excited by the ponderomotive force of the front of the pulse, and the oscillation is re-enforced by the change in sign of the ponderomotive force at the back of the pulse.

From a particle acceleration point of view, it is of particular interest to find the maximum possible electric field strength that can be produced inside the wakefield. It is possible to drive a wave to such a large amplitude that the particles (electrons in this case) in it lose coherence: their trajectories cross and the entire coherent wave structure breaks down in a process called wavebreaking. The maximum electric field that can be supported by a 1D linear wake is given by the wavebreaking limit [112]. For a sinusoidal oscillation Gauss' law is

$$\frac{\partial E}{\partial \xi} = -\frac{e n_e}{\epsilon_0} \sin(k_p \xi) \tag{2.75}$$

The maximum attainable field is achieved when $n_e = n_0$ because there is no more charge

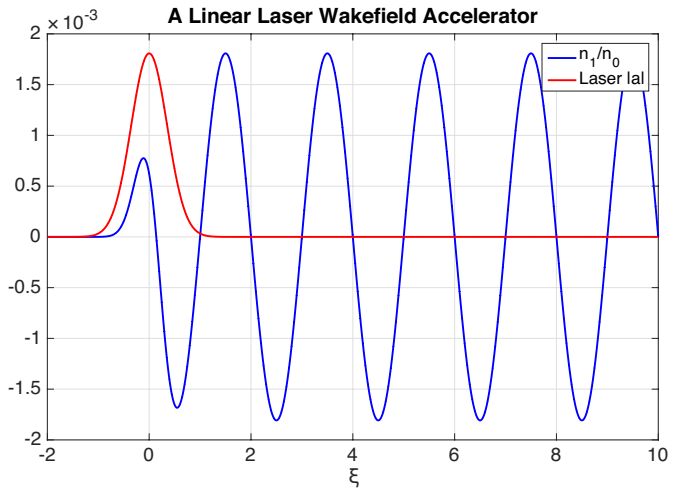


Figure 2.6: Electron density oscillation in a linear LWFA. The laser $|a|$ has been scaled to fit the window. The simulated laser had $a_0 = 0.05$ and is moving from right to left.

to separate. Using this condition and integrating the equation above gives the maximum field strength E_0 which is often referred to as the cold wavebreaking limit,

$$E_0 = \frac{m_e c \omega_p}{e} \tag{2.76}$$

It is, however, not possible to achieve fields of this strength with a low intensity ($a_0 \ll 1$) pulse. For a low amplitude gaussian wave packet of the form $|a(\xi)|^2 = {a_0}^2 \exp(-\xi^2/2L^2)$ the electric field inside the wake was calculated in [113] as

$$\frac{E}{E_0} = \sqrt{\pi}\, \frac{{a_0}^2}{2} k_p L \exp\left(-\frac{{k_p}^2 L^2}{4}\right) \tag{2.77}$$

Despite this, we see that the cold wavebreaking limit E_0 sets the scale of the electric field in a wakefield. For a plasma number density of $10^{19}\,\mathrm{cm}^3$, $E_0 \approx 300\,\mathrm{GV}$. This is more than one thousand times higher than the limit to electric field amplitude in conventional RF accelerators, which is what makes LWFA's such a good prospect for next generation accelerators.

2.3.2 Nonlinear Wakefields in 1D

Considering linear wakefields was instructive but ultimately not representative of what happens in LWFA experiments where pulses with a_0 of order 1 are routinely used. The primary difference is that the quiver velocity of the electrons in the wakefield becomes relativistic. To explore this we start with the definition of the Hamiltonian on the left hand side of equation 2.7. In the lab frame, constraining ourselves to the z direction only

(for 1D wakefields), the Hamiltonian for a relativistic electron in a plasma wave is

$$H = p_z\dot{z} + \frac{m_e c^2}{\gamma} - e\phi \tag{2.78}$$

The wakefield wave frame has a velocity which is the phase velocity of the wakefield $v_{ph} = c\beta_{ph}$. Performing a Galilean transformation of Hamiltonian from the lab frame coordinates to the wave frame coordinates $H(p_z, z) \rightarrow H(p_z, \xi)$ yields the wave frame Hamiltonian [114]

$$H(p_z, \xi) = \gamma m_e c^2 \left(1 - \beta_z \beta_{ph}\right) - e\phi \tag{2.79}$$

Note that p_z and γ are unchanged by this transformation, we merely replace the explicit coordinate $\dot{z} \rightarrow \dot{\xi} = (\beta_z - \beta_{ph})\, c$. $\beta_z c$ is the electron velocity.

The time rate of change of the Hamiltonian is zero because the Lagrangian has no explicit time dependence i.e. $\frac{dH}{dt} = -\frac{\partial L}{\partial t} = 0$. If the initial conditions for the wakefield electron are $\gamma_0 = 1$, $\beta_{z0} = 0$ and $\phi_0 = 0$ then the following equality is always true, where the approximation $\beta_{ph} = 1$ has been made.

$$\gamma - \tilde{p}_z = 1 + \frac{e\phi}{m_e c^2} = 1 + \tilde{\phi} \tag{2.80}$$

$\tilde{\phi} = e\phi/(m_e c^2)$ is the normalised scalar potential. By writing $\gamma - \tilde{p}_z = \gamma(1-\beta_z) = \frac{\tilde{p}_z}{\beta_z}(1-\beta_z)$ this equation can be used to show that

$$\frac{\tilde{p}_z}{1+\tilde{\phi}} = \frac{\beta_z}{1-\beta_z} \tag{2.81}$$

This equation tells us how the electron momentum and velocity are related to the scalar potential of the wakefield, however it says nothing about how these relate to the driving laser field a. To find such a relationship we begin by squaring equation 2.80 to give

$$\gamma^2 = \left(1+\tilde{\phi}\right)^2 + 2\left(1+\tilde{\phi}\right)\tilde{p_z} + {p_z}^2 \tag{2.82}$$

and we compare this γ^2 to that of an electron in a laser field

$$\gamma^2 = 1 + a^2 + {p_z}^2 \tag{2.83}$$

to produce the relation

$$\frac{\tilde{p_z}}{1+\tilde{\phi}} = \frac{1}{2}\left[\frac{1+a^2}{\left(1+\tilde{\phi}\right)^2} - 1\right] = \frac{\beta_z}{1-\beta_z} \tag{2.84}$$

This equation plays the role of the momentum equation from the linear wakefield section. The second equality is restating equation 2.81. Once again the other two equations that describe this system are Gauss' law and the continuity equation. As we are dealing with the potential $\tilde{\phi}$ we use Poisson's equation to describe the field

$$\frac{\partial^2 \phi}{\partial \xi^2} = \frac{e n_0}{\epsilon_0}\left(\frac{n_e}{n_0} - 1\right) \tag{2.85}$$

The integral form of the continuity equation in the wave frame is

$$n_e v_{ph} - n_e v_z = n_0 v_{ph} \implies \frac{n_e}{n_0} = \frac{v_{ph}}{(v_{ph} - v_z)} \approx \frac{1}{1 - \beta_z} \tag{2.86}$$

From this and Gauss' law it is clear that

$$\frac{n_e}{n_0} = \frac{1}{{k_p}^2}\frac{\partial^2 \tilde{\phi}}{\partial \xi^2} + 1 = \frac{1}{1 - \beta_z} \implies \frac{1}{{k_p}^2}\frac{\partial^2 \tilde{\phi}}{\partial \xi^2} = \frac{\beta_z}{1 - \beta_z} \tag{2.87}$$

By comparing this to equation 2.84 the differential equation describing the wake potential $\tilde{\phi}$ resulting from the interaction with the drive laser potential a is found as

$$\frac{1}{{k_p}^2}\frac{\partial^2 \tilde{\phi}}{\partial \xi^2} = \frac{1}{2}\left[\frac{1 + a^2}{\left(1 + \tilde{\phi}\right)^2} - 1\right] \tag{2.88}$$

The equation is valid for sufficiently underdense plasmas ($\beta_{ph} \sim 1$) and for laser pulses with a slowly evolving envelope ($\frac{d}{d\tau} \sim 0$). A slightly more sophisticated version of this equation can be found in [115] where the assumption that $\beta_{ph} = 1$ has not been made. The numerical solution to equation 2.88, expressed in terms of the electron density perturbation which is linked to $\tilde{\phi}$ by Gauss' law, is plotted in figure 2.7 for a_0 of 0.1, 1 and 3 along with the electric field of the wake for $a_0 = 3$. The laser was described by the function $a = a_0 \exp(-\xi^2/2L^2)$ with $L = \lambda_p/4$, where λ_p is the linear plasma wavelength. The graphs show that for high a_0 the plasma wavelength increases and the electron rich part of the wake becomes a narrow spike, leaving most of the plasma wave available for electron beam focussing and almost half for electron acceleration. Thus in the relativistically nonlinear regime the distance over which acceleration happens is increased by two factors: the increase in the plasma wavelength and the increase in the fraction of the plasma wavelength that is accelerating and focussing for electrons. The electric field takes the form of a sawtooth, and can be larger than the cold wavebreaking limit E_0 as seen in the bottom right graph. This is another reason that it is beneficial to use a relativistically intense drive laser for LWFA. In fact the wavebreaking limit is increased in the nonlinear regime [116] to

$$E_{0,NL} = \frac{m_e c \omega_p}{e}\sqrt{2}\left(\gamma_{ph} - 1\right)^{\frac{1}{2}} \tag{2.89}$$

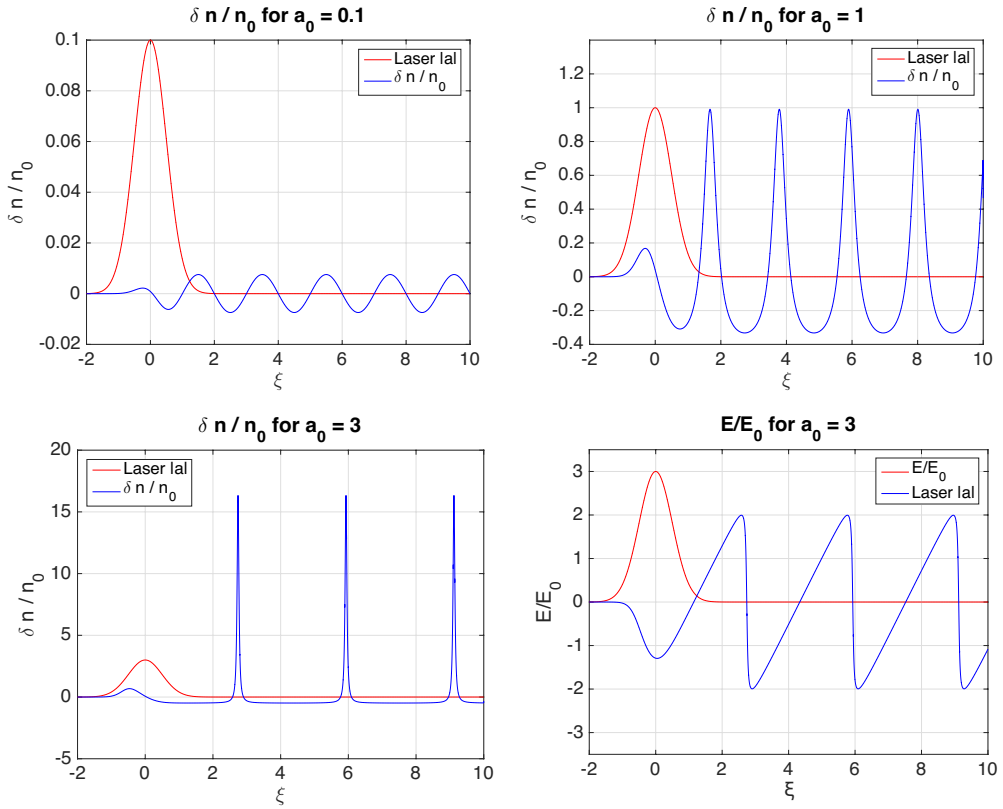


Figure 2.7: Plasma waves in the 1D nonlinear regime. The top left and right graphs show the electron density wave for $a_0 = 0.1$ and $a_0 = 1$. The bottom left graph shows the electron density wave for $a_0 = 3$ and the bottom right graph shows the electric field resulting from this.

where $\gamma_{ph} = \left(1 - {\beta_{ph}}^2\right)^{-\frac{1}{2}} = \omega/\omega_p$. For $n_e/n_c = 0.01$ this increases the wavebreaking limit by a factor of 14. However this wavebreaking limit is reduced for a warm plasma [117].

From equation 2.88 it is possible to compute the electric field from the numerical solution for $\tilde{\phi}$, although it is not possible to do this analytically for any laser pulse shape. For a top hat pulse it was shown [118] that the maximum electric field in a 1D nonlinear wake is

$$\frac{E_{max}}{E_0} = \frac{{a_0}^2}{\sqrt{1 + {a_0}^2}} \tag{2.90}$$

where once again E_0 is the cold wavebreaking limit. Note that this is slightly larger than for the gaussian drive pulse case in figure 2.7, although it remains a reasonable approximation.

2.3.3 Nonlinear Wakefields in 3D

Three dimensional PIC simulations have demonstrated that for an a_0 of approximately 2 or more [119] that the wake takes the form of a single, approximately spherical, bubble that

is completely cavitated of electrons [54]. This bubble has a radius r_b that is commonly referred to as the blowout radius. This is demonstrated in figure 2.8. The motion of

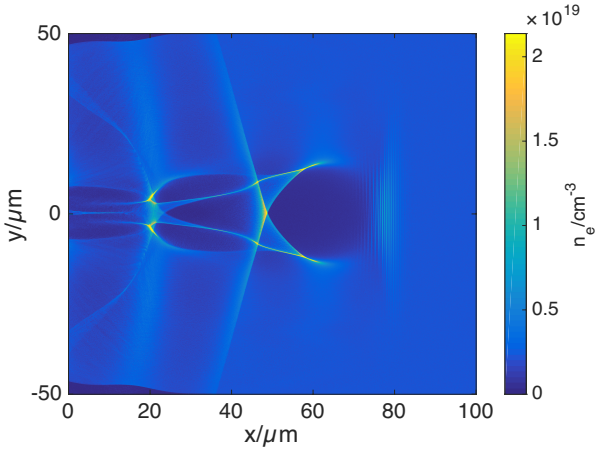


Figure 2.8: A 2D PIC simulation output demonstrating the bubble regime. The laser, propagating from left to right, leaves an almost spherical bubble in its wake that is completely devoid of electrons. A narrow high density sheath of electrons surrounds the cavitated region.

an electron in the 3D nonlinear regime is under the influence of three forces: a radial electrostatic force ($E \propto r$), the laser ponderomotive force and radial plasma currents. In the ultra-relativistic regime ($a_0 \gg 1$), where the width of the electron sheath $\Delta \ll r_b$, the blowout radius can be described by the equation [120]

$$r_b \frac{d^2 r_b}{d\xi^2} + 2\left(\frac{dr_b}{d\xi}\right)^2 + 1 = -\frac{d|a|^2}{dr}\frac{1}{(1+\beta {r_b}^2/4)^2} \tag{2.91}$$

where $\beta = \ln(1+\Delta/r_b)^2 - 1$. This is clearly a nonlinear equation however it retains the familiar feature of being a plasma oscillation driven by a slightly modified ponderomotive force. The solution to this equation agrees well with the bubble shape found in PIC simulations apart from at the back of the bubble where it is no longer the case that $\Delta \ll r_b$. Behind the driver equation 2.91 simplifies to

$$r_b \frac{d^2 r_b}{d\xi^2} + 2\left(\frac{dr_b}{d\xi}\right)^2 + 1 = 0 \tag{2.92}$$

This equation [55] [121] describes a sphere. There is no simple physical argument to explain why the bubble formation is spherical. The plasma acts to confine the laser pulse to a spot size close to the (nonlinear) plasma wavelength, as we will see very shortly when discussing the 'matched spot size'. Similar to the 1D case, the laser excites a wake longitudinally via its ponderomotive force in the longitudinal direction, which also has a wavelength of the nonlinear plasma wavelength. Therefore a 3D wakefield has a similar spatial scale in both transverse directions and the axial direction, although this

does not mean that the wake must be spherical. Lu et al. [121] presented a nonlinear, kinetic theory describing multidimensional wakefields being driven by either a particle bunch or a high intensity laser. Equation 2.91 is a simplification of their equation describing the evolution of the bubble radius, which is valid in the ultra-relativistic (i.e. high drive intensity) regime. After the driver has passed this equation simplifies to 2.92, an equation describing a sphere. PIC simulations demonstrating a near-spherical bubble are ubiquitous in the modern literature. As the laser typically sits towards the front of the bubble this means that the accelerating electron beam can be considered to be under the influence of the fields of a sphere of positive charge with constant charge density $\rho_0 = en_0$.

As discussed in section 2.2.9, a laser pulse will guide in a plasma due to relativistic corrections to the refractive index. This happens if the laser power is greater than the critical power $P_c = 17\frac{{\omega_L}^2}{{\omega_p}^2}$ GW. A similar condition can be found in the bubble regime by balancing the bubble electric field acting on a wakefield electron with the ponderomotive force of the driving laser i.e.

$$\frac{1}{3}\ \frac{e^2 n_e}{\epsilon_0}\ r_b = \frac{1}{2\left\langle\gamma\right\rangle} m_e c^2 \nabla a^2 \approx \frac{1}{2\left\langle\gamma\right\rangle}\ m_e c^2\ \frac{a_0}{r_b} \tag{2.93}$$

For moderate a_0, $\left\langle\gamma\right\rangle\ \sim 1$ and equation 2.93 produces the relation $k_p r_b \propto \sqrt{a_0}$ for good guiding i.e. where the focal spot size oscillations are minimal. Through simulation Lu et. al. [119] found the so called 'matched spot size'

$$k_p r_b \approx k_p w_0 = 2\sqrt{a_0} \tag{2.94}$$

The matched spot size sets the radius of the bubble which should additionally be matched to the laser pulse length through $r_b \sim c\tau$.

In the bubble regime the maximum electric field is

$$E_{z,max} = \frac{m_e c \omega_p}{e}\ \sqrt{a_0} \tag{2.95}$$

where the factor of $\sqrt{a_0}$ has been introduced via the nonlinear increase in the plasma wavelength [121]. From Gauss' law the on-axis electric field $E_z \propto \xi$ and has a sawtooth profile. The bubble regime is ideal for electron acceleration. Almost all of the plasma wavelength is focussing for electrons and close to half of the nonlinear plasma wavelength is accelerating. This shows that the advantages we found for accelerating in nonlinear wakes compared to linear wakes in 1D also applies in 3D, confirming that a relativistic drive pulse ($a_0 > 1$) is necessary for LWFA. The transverse electric field $E_r \propto r$, therefore any off-axis electrons experience a linear restoring force pointing towards the axis.

2.3.4 Trapping

So far the generation of large amplitude wakefields has been discussed and they have been shown to have large accelerating electric fields. However to be a useful accelerator an electron beam must be injected in to and trapped in the accelerating region of the wakefield. A trapped electron experiences the accelerating field of the wakefield for a long period of time. The initial condition for an electron to be trapped is that, in the frame of the wake, the kinetic energy of the electron $(\gamma_e{}' - 1)\, m_e c^2$ must be less than its potential energy of the wakefield $e\phi'$. In 1D this condition is

$$e\phi' > (\gamma_e{}' - 1)\, m_e c^2 \tag{2.96}$$

Lorentz transforming this in to the lab frame produces the inequality

$$e\phi > \gamma_e m_e c^2 - \beta c p_z - \frac{m_e c^2}{\gamma_{ph}} = \left[\gamma_e \left(1 - \beta_e \beta_{ph}\right) - \frac{1}{\gamma_{ph}}\right] m_e c^2 \tag{2.97}$$

where $\gamma_{ph} = \omega/\omega_p = (1 - {\beta_{ph}}^2)^{\frac{1}{2}}$ is the relativistic factor associated with the wakefield velocity $c\beta_{ph}$. Note that the potential transforms as $\phi' = \gamma_{ph}\phi$. In a very underdense plasma $\beta_{ph} \sim 1$, and if the plasma electrons are cold $\beta_e \sim 0$ and $\gamma_e \sim 1$. In this case the trapping threshold becomes $\tilde{\phi} \gtrsim (1 - 1/\gamma_{ph})$. For large γ_{ph} this can be written in terms of the electric field as $E_{trap} \gtrsim E_0 = m_e c\omega_p/e$. Therefore in this simplified 1D case if the wave breaks then the wake has a large enough amplitude to trap electrons. This argument is often used to describe self-injection.

A more complete approach is to examine the behaviour of single electrons with different initial conditions in the wake [114]. For any electron the wave frame Hamiltonian $H(p_z, \xi)$ from equation 2.79 is constant along its trajectory. Re-writing this as the normalised Hamiltonian $\tilde{H} = H/(m_e c^2)$, we can write that for any electron trajectory

$$\left(\tilde{H} + \tilde{\phi}\right) = \gamma - \tilde{p_z}\beta_{ph} = \sqrt{1 + {\tilde{p_z}}^2} - \tilde{p_z}\beta_{ph} \tag{2.98}$$

Note that this analysis is also in 1D, where only motion in the z direction is permitted. Rearranging equation 2.98 to put this in terms of the electron momentum $\tilde{p_z}$ yields the equation

$$-\frac{1}{{\gamma_{ph}}^2}{\tilde{p_z}}^2 + 2\tilde{p_z}\beta_{ph}\left(\tilde{H} + \tilde{\phi}\right) + \left(\tilde{H} + \tilde{\phi}\right)^2 - 1 = 0 \tag{2.99}$$

Solving this quadratic formula leaves an expression for $\tilde{p_z}$ as

$$\tilde{p_z} = \beta_{ph}{\gamma_{ph}}^2\left(\tilde{H} + \tilde{\phi}\right) \pm \gamma_{ph}\sqrt{{\gamma_{ph}}^2\left(\tilde{H} + \tilde{\phi}\right)^2 - 1} \tag{2.100}$$

$\gamma = \sqrt{1+\tilde{p}_z^2}$ is plotted vs. position ξ in the wake for electrons with various initial γ factors in figure 2.9, using equation 2.100. The laser $a = 0.2\exp\left(\xi^2/2L^2\right)$ is centred around $\xi = 0$ with $L = \lambda_p/4$. The potential ϕ was found via numerical integration of equation 2.88.

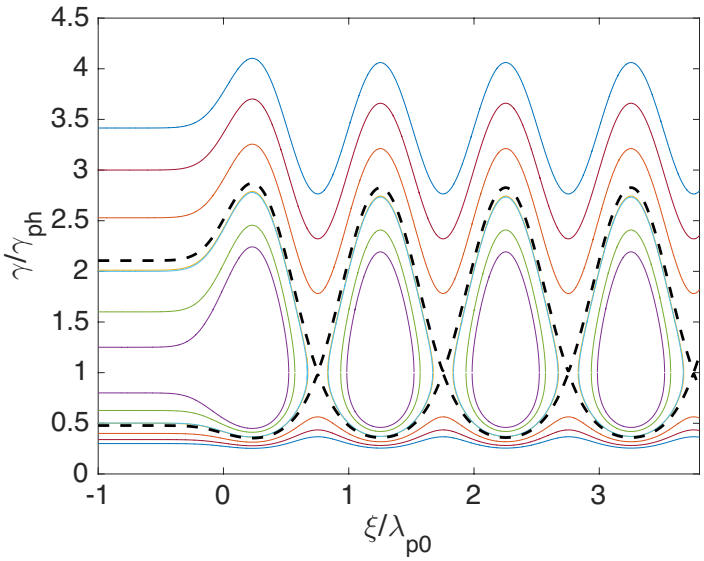


Figure 2.9: Electron orbits in the γ, ξ phase space in a 1D nonlinear wakefield potential. The black dashed line shows the separatrix.

What this figure shows is that, for a reasonably low amplitude wake, electrons with low initial momentum, i.e. $\beta < \beta_{ph}$, exhibit an oscillation induced by the laser: these are the electrons that make up the wakefield. As we have already seen for large amplitude wakes $\left(\tilde{\phi} \gtrsim 1\right)$ even stationary electrons are trapped. Electrons with large initial momenta are accelerated and decelerated by the wakefield as they pass through it but the wakefield potential well is not deep enough to contain them. Between these limits electrons undergo closed orbits in the (ξ, γ) phase space. These are the trapped electrons: they stay within a single plasma bucket at all times. An electron starting at the 'bottom' of the bucket as shown in the diagram will be accelerated by the potential, outrun the accelerating field (because it has $\beta_e > \beta_{ph}$) and be decelerated. This motion plots out the closed orbit in phase space. The boundary between the open and closed orbits, plotted as the dashed black line, is the separatrix. As this separates two different behaviours it is found at the stationary points of the Hamiltonian $\tilde{H}$ i.e. where $\frac{\partial \tilde{H}}{\partial \tilde{p}_z} = \frac{\partial \tilde{H}}{\partial \xi} = 0$. The separatrix Hamiltonian $\tilde{H}_s = \gamma_{ph}^{-1} - \tilde{\phi}_{min}$ and inserting this in to equation 2.100 produces the separatrix orbit. Electrons with $\tilde{H} < \tilde{H}_s$ are trapped, and electrons with $\tilde{H} > \tilde{H}_s$ are not. It can be shown [114] that the minimum and maximum γ along the separatrix orbit are

$$\gamma_{min} \approx \frac{\Delta\tilde{\phi}}{(1+\beta_{ph})} + \frac{\beta_{ph}}{2\Delta\tilde{\phi}} \tag{2.101}$$

$$\gamma_{max} \approx (1 + \beta_{ph})\, {\gamma_{ph}}^2 \Delta\tilde{\phi} \tag{2.102}$$

$\Delta\tilde{\phi}$ is the difference between the maximum and minimum values of the potential experienced by the electron. γ_{min} is the minimum γ required for electrons to be trapped in a wake. $(\gamma_{max} - \gamma_{min})\, m_e c^2$ is the maximum energy gain from a wakefield.

Moving to the 3D bubble, there are two conditions for an electron to become trapped. The first is that in the lab frame the axial electron velocity v_z must exceed the phase velocity of the plasma wave v_{ph}. The second is that the electron must take a trajectory that crosses with the trajectory of a plasma electron that is not part of the sheath, which will cause the electron to arrive on-axis before the bulk of the sheath electrons [122]. It is then, by definition, inside the accelerating phase of the wakefield. Electrons that take such a trajectory begin inside a cylindrical shell of some radius r_0 [122] [123]. PIC simulations have estimated this radius [124], assuming that plasma electrons are initially cold and are stationary in the lab frame, as

$$k_p r_0 \approx -2.0 + 1.4 a_0 - 0.05 a_0^2 \tag{2.103}$$

To obey both trapping conditions usually requires a large amplitude wakefield i.e. a large $\tilde{\phi}$, as we saw in the 1D case. It is also useful to have a reasonably high plasma density so that the wakefield phase velocity is slower and the first trapping condition is more easily met. This results in a trapping threshold that is dependent on a_0 and n_e. Thomas [125] derived a condition for trapping in the bubble regime that required

$$\frac{c\sqrt{\ln(2{\gamma_{ph}}^2 - 1)}}{\omega_p r_b} \lesssim \frac{1}{2} \tag{2.104}$$

This depends on n_e through the ${\gamma_{ph}}^2$ and ω_p terms and on a_0 through the matched condition with the bubble radius r_b. This was found to be in agreement with experimental results from Mangles et. al. [67] who re-wrote equation 2.104 as

$$\frac{\alpha P}{P_c} > \frac{1}{16}\left[\ln\left(\frac{2n_c}{3n_e}\right) - 1\right]^3 \tag{2.105}$$

Here α is the energy in the FWHM laser focal spot and P is the laser power.

Work in recent times has suggested that electron injection and trapping can be strongly influenced by the evolution of the wakefield. Recall from sections 2.2.6 and 2.2.8 that a_0 changes as the laser propagates through the plasma due to pulse compression and self-focussing. These effects cause the bubble to expand. Bubble expansion causes a negative change in the Hamiltonian for the electrons which can be large enough to move them from untrapped to trapped orbits. This has been shown theoretically [126] [127], albeit

in the absence of a laser at the front of the bubble deflecting incoming electrons. However 3D PIC simulations in these papers demonstrate that injection does occur during periods of bubble expansion. These theories also show that bubble contraction causes a positive change in the Hamiltonian which can terminate trapping and produce quasi-monoenergetic electron bunches.

2.3.5 Injection Methods

In the last section we saw how electrons within a certain range of initial conditions can be trapped in a wakefield bucket and accelerated. The first model used showed that in 1D if the plasma wave is driven to wavebreaking amplitudes then the electrons will be trapped in the wake potential. For this reason wavebreaking is often used to describe self-injection. In practice (which typically means being in the 3D bubble regime), and indeed in simulation, plasma electrons can be injected in to the bubble without a catastrophic wavebreaking event i.e. the coherent bubble structure remains, in the first wake period at least. Perhaps the best explanation comes from Tsung [122], who describes how an electron starting at an optimum distance off-axis will trajectory cross with a plasma electron, causing it to return to the axis early (i.e. it has effectively broken from the wave) where it can be trapped.

With ionisation injection inner shell electrons ionised close to the peak of the laser pulse are 'born' in to the bubble close to the axis and with minimal initial momentum. If the wake potential is large enough these stationary electrons will be trapped, which has been shown to occur for $a_0 \gtrsim 1.7$ for a resonant gaussian drive laser [128].

2.3.6 Maximum Energy Gain and its Limiting Factors

As we saw in figure 2.9 electrons trapped in the wakefield potential have an upper limit to the energy they can gain. The physics behind this limitation will be discussed in more detail in this section, along with the limits in the linear and 3D nonlinear regimes. Energy gain in laser wakefield accelerators is limited by two major factors: dephasing and pump depletion. Dephasing occurs because the relativistic electron beam travels at very close to c whereas the driving laser travels at the group velocity. In the linear regime, the time t_d it takes for the electron beam to outrun the accelerating field is

$$t_d = \frac{\frac{1}{4}\lambda_p}{c - v_\phi} \tag{2.106}$$

v_ϕ is the phase velocity of the plasma wave which is equal to the group velocity of the laser pulse. In the linear regime the accelerating and focussing regions of the wakefield

only overlap for $\lambda_p/4$. Using $v_\phi = v_{g,laser} = c\sqrt{1-{\omega_p}^2/\omega^2} \approx c\left(1-\frac{1}{2}\frac{{\omega_p}^2}{\omega^2}\right)$ the dephasing length is given by

$$L_d = \frac{1}{2}\frac{\omega^2}{{\omega_p}^2}\lambda_p = \frac{1}{2}{\gamma_{ph}}^2\lambda_p \propto {n_e}^{-\frac{3}{2}} \tag{2.107}$$

In the 1D nonlinear regime it is not so trivial to calculate the dephasing length because the plasma wavelength comes from the solution of a nonlinear equation (equation 2.88). The 1D nonlinear dephasing has been found in other works [119] to be

$$L_{d,NL} = \frac{2}{\pi}{a_0}^2\frac{\omega^2}{{\omega_p}^2}\lambda_p \tag{2.108}$$

λ_p in this equation is the linear plasma wavelength. Finally in the 3D bubble regime the dephasing length is [119]

$$L_{d,3D} = \frac{2}{3}\frac{\omega^2}{{\omega_p}^2}r_b = \frac{4}{3}\frac{\omega^2}{{\omega_p}^2}\frac{\sqrt{a_0}}{k_p} \tag{2.109}$$

where the second part of the inequality has made use of the matched condition. This is of a very similar form to the 1D linear dephasing length where λ_p has been replaced by the bubble radius. The factor of $\frac{2}{3}$ arose because of a phenomenon known as etching depletion, discussed later in this section, which reduces the effective group velocity of the laser pulse.

Pump depletion refers to the fact that by driving a plasma wave the laser is constantly losing energy to the wave, meaning that eventually it will drop significantly in intensity and stop driving a strong wakefield. This also places a limit on the energy gain in LWFA's, and was not taken in to account in the calculations for figure 2.9, which assumed a laser potential that did not evolve in time. The length over which pump depletion occurs can be estimated by equating the energy in the laser pulse to the electromagnetic energy stored in the wakefield. The laser field has energy density $U_L = \epsilon_0{E_L}^2$ and volume $V_L = \pi{w_0}^2c\tau$. It is assumed that we are operating in optimal conditions so $c\tau = \lambda_p/2$. The plasma wave has energy density $U_p = \frac{1}{2}\epsilon_0{E_z}^2$ and volume $V_p = \pi{w_0}^2L_{pd}$ where L_{pd} is the pump depletion length. For $a_0 \ll 1$ the electric field $E_z \approx {a_0}^2E_0$. Equating these two energies, i.e. setting $U_LV_L = U_pV_p$ and using $a_0 = \frac{e}{m_ec}\frac{|E_L|}{\omega}$ produces the depletion length for a linear wakefield accelerator

$$L_{pd} = \frac{\lambda_p}{{a_0}^2}\frac{\omega^2}{{\omega_p}^2} = \frac{2L_d}{{a_0}^2} \tag{2.110}$$

Therefore in the linear ($a_0 < 1$) regime dephasing limits the energy gain, not depletion. This exercise can be repeated for a flat top pulse in the 1D nonlinear regime using the wakefield electric field from equation 2.90. This gives the pump depletion length as

$$L_{pd,NL} = \frac{1}{2}\frac{\omega^2}{{\omega_p}^2}\left(\frac{1+{a_0}^2}{{a_0}^2}\right)c\tau \tag{2.111}$$

This features the laser pulse length because now there is no simple correspondence between

the plasma wavelength and the ideal pulse length, because the plasma wavelength depends on the pulse amplitude. For $a_0 \gg 1$ this expression is independent of a_0 and significantly shorter than the dephasing length (equation 2.108). Therefore in the 1D nonlinear regime the depletion length limits the energy gain. This estimate of the depletion length is quite simple because it has assumed that the wakefield electric field is constant at its maximum value. A more careful analysis [129] [119] gives the depletion length at a slightly reduced

$$L_{pd,NL} = \frac{1}{3} \frac{\omega^2}{{\omega_p}^2} \frac{\omega_p}{k_p} \tau \tag{2.112}$$

A more physical depletion model, the etching model, was described by Decker et. al. [130]. In short, the photons in the pulse that have driven the wakefield are red shifted and consequently slow down (section 2.2.7). This moves the front of the pulse backwards at the etching velocity $v_{etch} = c\ {\omega_p}^2/\omega^2$. Therefore the wakefield phase velocity is less than the (linear) laser group velocity and is given by $v_{ph} = v_g - v_{etch} \approx c\left(1 - \frac{3}{2}\frac{{\omega_p}^2}{\omega^2}\right)$. This is the origin of the factor of 2/3 in the bubble regime dephasing length in equation 2.109. The depletion length in the bubble regime [119] is

$$L_{dp,3D} = \frac{\omega^2}{{\omega_p}^2} \frac{\omega_p}{k_p} \tau \tag{2.113}$$

This is of a similar order to the dephasing length in 3D. This is in contrast to the 1D linear case where energy gain is limited by dephasing, and the 1D nonlinear case where it is limited by pulse depletion. In the 3D case both processes are important. It also means that in the 3D nonlinear case the electrons should attain energies close to the dephasing limited energy, which is large thanks to the large electric fields of the bubble.

The maximum attainable energy gain is usually expressed as

$$W_{max} = -e \int_0^{L_d} E_z(z) dz \tag{2.114}$$

In the linear case the energy gain is $W_{lin} = \langle E \rangle\, L_{d,lin}$. $\langle E \rangle = 2E_{max}/\pi$ is the electric field averaged over the $\lambda_p/4$ part of the wave which is both focusing and accelerating. Making the same assumption as Tajima and Dawson [49] that $E_{max} = E_0$ (the cold wavebreaking limit) the maximum energy gain is given by the familiar equation

$$W_{max} = 2\frac{\omega^2}{{\omega_p}^2} m_e c^2 = 2{\gamma_{ph}}^2 m_e c^2 \tag{2.115}$$

However we know that the linear regime only applies for $a_0 \ll 1$ and that in this regime equation 2.77 showed that $E_{max} \propto {a_0}^2 E_0$. Therefore the actual energy gain $W_{max} \propto {a_0}^2 {\gamma_{ph}}^2$ which is strongly prohibitive for electron acceleration in the linear regime

because the small ${a_0}^2$ factor heavily reduces the energy gain. This is why it is essential to have a relativistic drive pulse for laser wakefield acceleration.

In the bubble regime $\langle E_z \rangle = E_0\sqrt{a_0}/2$. Combining this with the dephasing length from equation 2.109 and the matched condition $k_p r_b = 2\sqrt{a_0}$ the maximum energy gain is

$$W_{max,3D} = \frac{2}{3} a_0 \frac{\omega^2}{{\omega_p}^2} m_e c^2 \tag{2.116}$$

A summary of the dephasing lengths, depletion lengths and the maximum energy gains from the regimes covered here is provided in the table below.

Regime	Dephasing Length	Depletion Length	W_{max}
Linear	$\frac{1}{2}\lambda_p \frac{\omega^2}{{\omega_p}^2}$	$\frac{\lambda_p}{{a_0}^2}\frac{\omega^2}{{\omega_p}^2}$	$2{a_0}^2\frac{\omega^2}{{\omega_p}^2} m_e c^2$
1D Nonlinear	$\frac{2}{\pi}{a_0}^2\lambda_p\frac{\omega^2}{{\omega_p}^2}$	$\frac{1}{3}\frac{\omega^2}{{\omega_p}^2}\frac{\omega_p}{k_p}\tau$	$4{a_0}^2\frac{\omega^2}{{\omega_p}^2} m_e c^2$
3D Nonlinear	$\frac{4}{3}\frac{\omega^2}{{\omega_p}^2}\frac{\sqrt{a_0}}{k_p}$	$\frac{\omega^2}{{\omega_p}^2}\frac{\omega_p}{k_p}\tau$	$\frac{2}{3}a_0\frac{\omega^2}{{\omega_p}^2} m_e c^2$

Table 2.1: Dephasing length, depletion length and maximum energy gain for the linear, 1D nonlinear and 3D nonlinear regimes.

2.4 Radiation Generation

It is a basic physical principle that accelerating charges emit radiation. This radiation can be calculated from a solution to Maxwell's equations called the Liénard-Wiechert fields, provided that the equation of motion of the accelerating charge is known. With this in mind, this section will begin with the calculations of the transverse equations of motion of an electron in a LWFA. This will start by approximating the motion as that of a relativistic electron in an ion channel with a radially symmetric electric field. Then a constant longitudinal field will be added to see how this affects the motion. The first case will be compared to the motion of an electron in a conventional insertion device. This analogy, along with the equations describing the radiation generated by electrons undertaking such trajectories, will lead to an understanding of the properties of 'betatron radiation', which is the synchrotron-like radiation produced by transverse oscillations of electrons in a LWFA.

2.4.1 Transverse Electron Motion in a Plasma Channel

Much of this thesis will cover the topic of betatron radiation, which is radiation emitted by electrons oscillating in the wakefield while they are being accelerated. To understand

this motion a simple physical model will be examined. This will begin by deriving the equation of motion of an electron in a cylindrically symmetric plasma channel. Although a nonlinear wakefield takes the shape of a near-spherical bubble [54] [55] the problem is not spherically symmetric because the bubble is moving at $v_{g,laser}$ in the axial direction so the electron beam oscillates (dephases, rephases) very slowly in the axial direction compared to the transverse direction. Therefore a simplified version of the problem is usually tackled in a cylindrical geometry [86] [131]. This section will deal with an off-axis relativistic electron oscillating in a cylindrically symmetric potential. In the next section a constant axial accelerating field will be added to iterate the model to something closer to a real LWFA.

The Lagrangian for a test electron with velocity βc in an electrostatic field described by the scalar potential ϕ is

$$L = -m_e c^2 \sqrt{1-\beta^2} + e\phi \tag{2.117}$$

The potential ϕ is the solution to Poisson's equation for a cylindrical plasma channel

$$\frac{1}{r}\frac{\partial}{\partial r}\left(r\frac{\partial \phi}{\partial r}\right) = \frac{-e\left(n_0 - n_e\right)}{\epsilon_0} \tag{2.118}$$

which has been written explicitly in terms of the radial coordinate r. n_0 is the (static) ion number density in the plasma, n_e is the remaining (unperturbed) electron number density and ϵ_0 is the permittivity of free space. The solution to this equation assuming $n_e = 0$ i.e. in the 'blowout' or fully-cavitated regime is

$$\phi = -\frac{n_0 e r^2}{4\epsilon_0} \tag{2.119}$$

The radial equation of motion given by the Euler-Lagrange equations is

$$\frac{d}{dt}\left(\gamma m_e \dot{r}\right) = -\frac{e^2 n_0}{2\epsilon_0} r \tag{2.120}$$

In the absence of an axial accelerating field and assuming that the radial velocity is small compared to c (with the axial velocity $v_z \sim c$) then $\dot{\gamma} \approx 0$ and the test electron in this field follows the oscillator equation

$$\ddot{r} = -{\omega_\beta}^2 \, r \tag{2.121}$$

The dot notation has been used to denote a total time derivative. This is the equation for an electron oscillating at the betatron frequency $\omega_\beta = \omega_p/\sqrt{2\gamma_{z0}}$ where γ_{z0} is the initial relativistic factor of the electron due to its longitudinal motion. The radial equation has

the solution

$$r = r_\beta \cos(\omega_\beta t) \tag{2.122}$$

where r_β is the amplitude of the betatron oscillation. The initial conditions were $r(t = 0) = r_\beta$ and $\dot{r}(t = 0) = 0$.

The fact that the electron is oscillating means that the equation of motion in the axial (z) direction is modified. This can be explored perturbatively beginning with the assumption $\dot{\gamma} = 0$, meaning that the square of the electron speed $\beta^2 = {\beta_r}^2 + {\beta_z}^2$ is constant. From this the motion in z can be calculated as in [86]. Using the expansion $\beta_z = \left(\beta^2 - {\beta_r}^2\right)^{\frac{1}{2}} \approx \beta\left(1 - \frac{{\beta_r}^2}{2}\right)$, where $\beta \approx 1$ has been used in the final denominator, the z component of velocity is found to be

$$\beta_z \approx \beta\left(1 - \frac{{r_\beta}^2{\omega_\beta}^2}{4c^2}\right) + \beta\frac{{r_\beta}^2{\omega_\beta}^2}{4c^2}\cos\left(2\omega_\beta t\right) \tag{2.123}$$

Upon integration, with initial condition $z(t = 0) = z_0$, the z equation of motion is

$$\frac{z}{c} \approx \frac{z_0}{c} + \beta\left(1 - \frac{{r_\beta}^2{\omega_\beta}^2}{4c^2}\right)t + \beta\frac{{r_\beta}^2\omega_\beta}{8c^2}\sin\left(2\omega_\beta t\right) \tag{2.124}$$

There is a drift velocity $\beta c\left(1 - \frac{{r_\beta}^2{\omega_\beta}^2}{4c^2}\right)$, and in the moving frame there is a familiar figure of 8 motion as we first saw for an electron in a plane electromagnetic wave (section 2.1.2). The implication of this is that in the electron rest frame the fields of the plasma channel are an electromagnetic wave, which is exactly what one would expect from the properties of the Lorentz transformation.

2.4.2 Electron Motion in a Plasma Channel with a Constant Longitudinal Field

As a more realistic approximation to how an electron behaves in a laser driven wakefield a constant axial electric field E_z is introduced. This can be done in the Lagrangian formulation by the inclusion of an extra term in ϕ such that $\frac{\partial\phi}{\partial z} = -E_z$. In this case the Euler-Lagrange equations give the equations of motion as

$$\frac{d}{dt}\left(\gamma m_e\dot{r}\right) = -\frac{e^2 n_0}{2\epsilon_0}r \tag{2.125}$$

$$\frac{d}{dt}\left(\gamma m_e\dot{z}\right) = eE_z \tag{2.126}$$

It can no longer be assumed that $\dot{\gamma} \approx 0$ because of the longitudinal field meaning that equation 2.125 must be written as

$$\dot{\gamma}\beta_r + \gamma\dot{\beta}_r = -\frac{e^2 n_0}{2\epsilon_0 m_e c} r \tag{2.127}$$

Equation 2.126 is trivially solved as

$$\gamma\beta_z = -\frac{e}{m_e c} E_z t + \gamma_0\beta_0 \tag{2.128}$$

where γ_0 and β_0 are the initial relativistic factor and normalised velocity of the test electron respectively. For relativistic electrons in this scenario we have $\beta_z \approx 1$ and therefore $\dot{\gamma} = eE_z/m_e c$. Inserting this result in to the radial equation of motion 2.127 and keeping the assumption that $\beta_z \approx 1$ in 2.128 the following equation of motion is produced

$$\left(eE_z t + \gamma_0\beta_0 m_e c\right)\ddot{r} + eE_z\dot{r} + \frac{e^2 n_0 c}{2\epsilon_0} r = 0 \tag{2.129}$$

This is recast to

$$\left(At + B\right)\ddot{r} + A\dot{r} + Cr = 0 \tag{2.130}$$

This can be solved analytically [132] resulting in the equation

$$r(t) = \frac{\pi\sqrt{CB}}{A} r_{\beta 0} \Big[\mathrm{J}_1\left(2\sqrt{CB}/A\right) \mathrm{Y}_0\left(2\sqrt{C\left(B + At\right)}/A\right) - \mathrm{Y}_1\left(2\sqrt{CB}/A\right) \mathrm{J}_0\left(2\sqrt{C\left(B + At\right)}/A\right) \Big] \tag{2.131}$$

The initial conditions were $r(t = 0) = r_{\beta 0}$ and $\dot{r}(t = 0) = 0$. J_0 and J_1 are Bessel functions of the first kind of order 0 and 1. Y_0 and Y_1 are Bessel functions of the second kind of order 0 and 1. This trajectory is plotted in figure 2.10 for the initial conditions $\gamma_0 = 10$ and $r_\beta = 4$ μm, and a constant longitudinal electric field of $E_z = 100$ GV/m. As the electron is accelerated its oscillation wavelength increases and its amplitude decreases. Higher energy electrons emit harder and more intense radiation. Therefore the highest energy electrons in a LWFA emit the the most x-rays from the smallest source size.

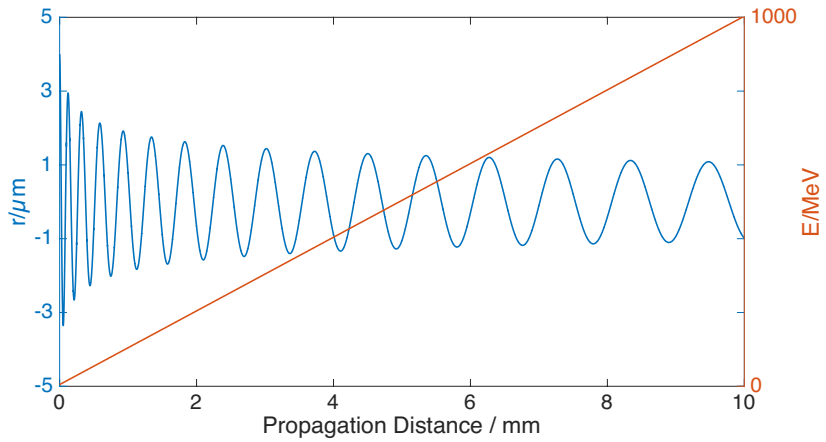


Figure 2.10: The motion of a longitudinally accelerating electron in a radially symmetric electrostatic field. The radial displacement r is plotted in blue and the total electron energy is plotted in red.

2.4.3 Electron Motion in an Insertion Device

Classical insertion devices, i.e. undulators and wigglers, are common sources of synchrotron x-ray light. The motion of electrons in them will now be discussed and compared to the motion of electrons in a LWFA. We consider a planar wiggler in Cartesian geometry. This is the type of wiggler shown in figure 1.2. z is the wiggler axis and the magnets are orientated with their poles lying along the y axis. Near to the axis the magnetic field can be approximated as

$$B_x = 0 \tag{2.132}$$

$$B_y = B_0 \cos\left(k_u z\right) \tag{2.133}$$

$$B_z \approx 0 \tag{2.134}$$

B_0 is the peak magnetic field strength and $k_u = 2\pi/\lambda_u$ is the wavenumber of the insertion device [133]. The motion will be the solution to the equation $\gamma m_e \dot{\boldsymbol{v}} = -e\ \boldsymbol{v} \times \boldsymbol{B}$. This gives rise to the differential equations

$$\gamma m_e \ddot{x} = e B_y \dot{z} \tag{2.135}$$

$$\gamma m_e \ddot{z} = -e B_y \dot{x} \tag{2.136}$$

To remain close to the axis, we have set $y = 0$. The (x, z) motion will once again be found using a perturbative method. To first order $\dot{z}$ is constant implying that

$$z = \beta c t \tag{2.137}$$

Using this fact and integrating equation 2.135 twice, the x (transverse) displacement as a function of time is found to be

$$x = -\frac{K}{\gamma\beta k_u}\cos\left(k_u\beta ct\right) \tag{2.138}$$

The undulator parameter K is defined as

$$K = \frac{eB_0}{m_e c k_u} = \frac{eB_0\lambda_u}{2\pi m_e c} \tag{2.139}$$

The initial conditions used were $x(t=0)=0$ and $\dot{x}(t=0)=0$. A helical undulator, one with $\boldsymbol{B}=(B_x, B_y, 0)$, has undulator parameters $K_x = eB_x/(m_e c k_u)$ and $K_y = eB_y/(m_e c k_u)$ [134]. K is a convenient parameter to use because the normalised transverse momentum $\tilde{p}_x = K\sin(k_u\beta ct)$. It is interesting to compare this to equation 2.18 for an electron in an infinite plane wave, which reveals that the undulator parameter in such a wave is simply a_0.

The second order motion is studied using the same method that was used in section 2.4.1 i.e. calculating β_z by assuming that the total velocity β is constant and using $\beta_z \approx \beta\left(1-\frac{{\beta_x}^2}{2}\right)$. This results in the equation for the z displacement of the electron as a function of time

$$\frac{z}{c} = \frac{z_0}{c} + \beta\left(1-\frac{K^2}{4\gamma^2}\right)t + \frac{1}{c}\frac{K^2}{8\gamma^2 k_u}\sin(2k_u\beta ct) \tag{2.140}$$

Similar to the example of an electron in a radial electrostatic field (section 2.4.1) this is a figure of 8 motion, imposed on a constant drift velocity of $\beta c\left(1-\frac{K^2}{4\gamma^2}\right)$. It is these similarities in the electron motion that mean we can consider the LWFA plasma bubble to be a plasma wiggler. Comparing the form of equations 2.122 and 2.138 we can write down the wakefield undulator parameter K_β as

$$K_\beta = \gamma k_\beta r_\beta \tag{2.141}$$

It is interesting to compare this to the form of the conventional undulator parameter in equation 2.139. The conventional K relies only on the properties of the externally applied magnetic field: it is proportional to its magnitude and inversely proportional to its wavenumber. K_β depends entirely on the electron beam parameters: its energy, the wavenumber of its oscillation and the oscillation amplitude. However this is perhaps unsurprising as in the conventional case the electrons only oscillate because of the applied field whereas in the betatron case the oscillation required the electrons to have some initial transverse momentum (or displacement), and then that oscillation is supported by the strong electric field inside the wakefield bubble.

2.4.4 Properties of Synchrotron Radiation and Betatron Radiation

The general equations that describe the electric and magnetic fields and the angular distribution of power from a moving charge are give in appendix 8.5. The electric field is the sum of two components: one proportional to the velocity of the particle called the velocity field, which is a generalisation of Coulomb's law for a relativistic moving charge, and one proportional to the acceleration of the charge called the acceleration field which is associated with radiation. For very relativistic particles the electric field from the acceleration field (i.e. from perpendicular forces acting on the charge) dominates over that from the velocity field.

A very relativistic charge under the influence of a perpendicular force travels, at any instant, along an arc of a circle of radius

$$\rho = \frac{v^2}{\dot{v}_\perp} \approx \frac{c^2}{\dot{v}_\perp} \tag{2.142}$$

where $\dot{v}_\perp$ is the perpendicular acceleration. The radiation emitted by a single electron will have an angular width of approximately $1/\gamma$ and this will pass by an observer in a very short time, much like a searchlight, as demonstrated in figure 2.11. The distance the

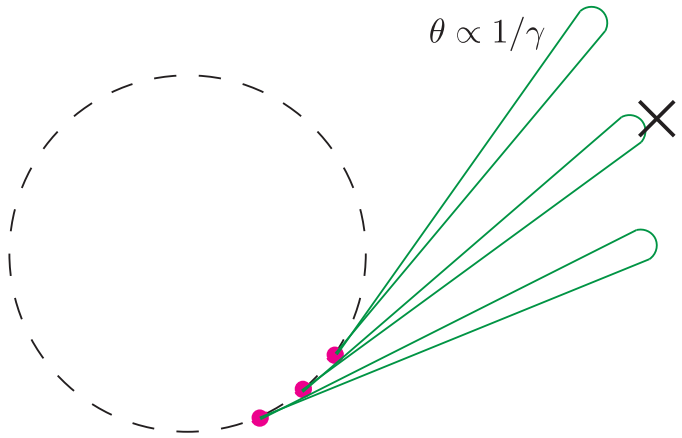


Figure 2.11: Demonstration of the searchlight nature of synchrotron radiation. Electrons (pink) emit synchrotron light in to narrow cones of angular width $\theta \sim 1/\gamma$. As the electrons continue their circular trajectory these cones rapidly sweep over the observer at X. Fourier theory means that the observed radiation must be broadband.

particle moves during the observation $d = \rho/\gamma$ because the angular width of the beam is approximately γ^{-1}. This corresponds to a time of

$$\Delta t = \frac{\rho}{\gamma v} \tag{2.143}$$

For any kind of light source based on conventional accelerators γ is many thousands and ρ is on the order of $10-100\,\mathrm{m}$, meaning that Δt is very small. Fourier theory means that the radiation will be broadband, which is exactly what is observed for bending magnet radiation. The time Δt is small but finite meaning that there will be some 'maximum' frequency above which there will be no substantial frequency components. In time Δt the pulse travels a distance $D = c\Delta t = \rho/(\gamma\beta)$. The electron beam moves a distance $d = \rho/\gamma$ in the approximately the same direction and so the pulse length is

$$L = D - d = \frac{\rho}{\gamma}\left(\frac{1}{\beta} - 1\right) \approx \frac{\rho}{2\gamma^3} \tag{2.144}$$

Another way of looking at this is that in the frame of the electron the x-ray pulse length is $\Delta t = \rho/(\gamma v)$ as in equation 2.143, but due to relativistic time dilation this is contracted in the lab frame by a factor of $2\gamma^2$. Therefore the pulse will contain significant frequency components up to the critical frequency

$$\omega_c \sim \frac{c}{L} = 2\gamma^3\frac{c}{\rho} \tag{2.145}$$

which has been up-shifted by the same factor of $2\gamma^2$ in the lab frame i.e. it has been Doppler up-shifted.

Undulators (which have wiggler parameters $K \ll 1$) are a special case. As we saw in section 2.4.3, electrons in an insertion device have maximum transverse momentum $\tilde{p}_x = K$ and longitudinal momentum $\tilde{p}_z \sim \gamma\beta$. Therefore the maximum angle which electrons are deflected by the magnetic field is $\sim K/\gamma$. For an undulator this is less than the $1/\gamma$ width of the emitted x-ray beam, which means that all of the emitted radiation cones overlap and interfere. Consider an electron on a sinusoidal trajectory through an undulator. It emits light towards an observer at angle θ to the z axis. The electron takes time $t_e = \lambda_u/c\,\langle\beta_z\rangle$ to travel one undulator period, where it emits once again. Recall from equation 2.140 that $\langle\beta_z\rangle = \beta\,[1 - K^2/(4\gamma^2)]$. In this time the wavefront has travelled a longitudinal distance of $d_w = \lambda_u\cos\theta \implies t_w = \lambda_u\cos\theta/c$. The wavefronts of the emitted light are, therefore, separated by distance $d = c\Delta t = \lambda_u/\langle\beta_z\rangle - \lambda_u\cos\theta$. Therefore the condition for constructive interference is

$$n\lambda = \frac{\lambda_u}{\langle\beta_z\rangle} - \lambda_u\cos\theta \tag{2.146}$$

For small angles $\cos\theta \approx 1 - \theta^2/2$. Writing $\beta = \sqrt{1 - 1/\gamma^2}$, and assuming that γ is large, one can write that $[\beta\,(1 - K^2/4\gamma^2)]^{-1} \approx 1 + (1 + K^2/2)/(2\gamma^2)$. Combining all of this with the condition for constructive interference above, the wavelength of the harmonics from

an undulator are given by

$$\lambda = \frac{\lambda_u}{2n\gamma^2}\left(1 + \frac{K^2}{2} + \gamma^2\theta^2\right) \tag{2.147}$$

This equation shows that an undulator emits harmonics of a single wavelength, and not a continuous spectrum like a bending magnet or a wiggler, where the radiation cones do not overlap. For an electron beam this light is incoherent because there is no fixed phase relationship between the electrons in the beam. In a free-electron laser, which in essence is a very long undulator at the end of an electron accelerator, the emitted radiation causes the electron beam to modulate at the wavelength of the light. In this scenario the light is coherent and also experiences gain from the electron beam.

We now move to a more formal description of synchrotron radiation. From appendix 8.5, the power emitted per unit solid angle can be written in terms of the observer's time t as

$$\frac{dP(t)}{d\Omega} = R^2\left[\boldsymbol{S}.\hat{\boldsymbol{n}}\right]_{ret} \tag{2.148}$$

This can be used to derive the intensity per unit solid angle per unit frequency interval [100]

$$\frac{d^2I}{d\omega d\Omega} = \frac{e^2\omega^2}{16\pi^3 c\epsilon_0}\left|\int_{-\infty}^{\infty}\hat{\boldsymbol{n}}\times\left(\hat{\boldsymbol{n}}\times\boldsymbol{\beta}\right)e^{i\omega(t'-\hat{\boldsymbol{n}}.\boldsymbol{r}(t')/c)}dt\right|^2 \tag{2.149}$$

where t' is the charge's own time. Definitions of all of the other variables are contained in appendix 8.5, although in essence this relates the x-ray intensity I to the time varying position $\boldsymbol{r}(t')$ and normalised velocity $\boldsymbol{\beta}(t')$ of the electron along with the unit vector $\hat{\boldsymbol{n}}$ pointing from the electron to the observer. By inserting $\boldsymbol{\beta}$ and $\boldsymbol{r}$ from the equation of motion for the charge the equation above can be solved, although this is not simple. For a relativistic charged particle undergoing instantaneous circular motion, the spectrum can be found [100] as

$$\frac{d^2I}{d\omega d\Omega} = \frac{e^2}{12\pi^3 c\epsilon_0}\left(\frac{\omega\rho}{c}\right)^2\left(\frac{1}{\gamma^2}+\theta^2\right)^2\left[K_{2/3}^2\left(\psi\right) + \frac{\theta^2}{(1/\gamma^2)+\theta^2}K_{1/3}^2(\psi)\right] \tag{2.150}$$

This equation applies for both a bending magnet (synchrotron) and a high K wiggler where interference effects can be ignored. θ is the off-axis angle, ρ is the bending radius, ω is the angular frequency of radiation and Ω denotes solid angle.. $K_{2/3}$ and $K_{1/3}$ are modified Bessel functions of the second kind. ψ is defined as

$$\psi = \frac{\omega\rho}{3c}\left(\frac{1}{\gamma^2}+\theta^2\right)^{3/2} \tag{2.151}$$

The properties of Bessel functions mean that for $\psi \gg 1$ the intensity becomes very small.

The critical frequency is therefore defined as the frequency for which $\psi = 1/2$ at $\theta = 0$

$$\omega_c = \frac{3}{2}\gamma^3 \frac{c}{\rho} \tag{2.152}$$

This agrees well with the earlier simple estimate. The form of equation 2.150 hints that γ^{-1} is the natural unit for angles. Taking $\rho = 130$ m and $\gamma = 12,000$, similar to the ESRF machine, the synchrotron spectrum is plotted as a function of $\gamma\theta$ for $\omega = 0.3\omega_c$, ω_c and $3\omega_c$ in figure 2.12. High frequency light has an intensity that is peaked in a narrow

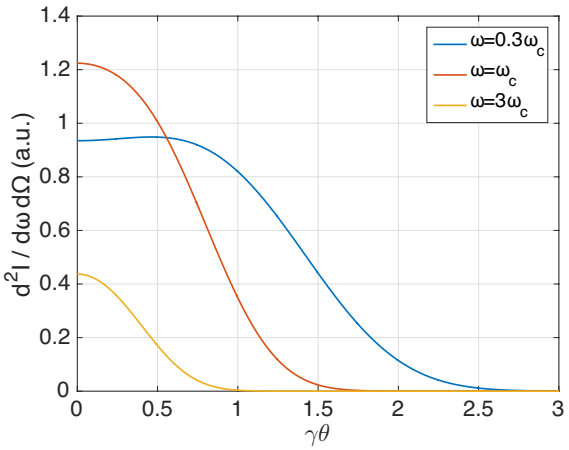


Figure 2.12: Synchrotron spectral intensity vs. $\gamma\theta$ for $\omega = 0.3\omega_c$, $\omega = \omega_c$ and $\omega = 3\omega_c$.

angular range around the axis, but above the critical frequency the intensity is reduced by the shape of the Bessel functions. It is important to note that there is little radiation for $\gamma\theta$ larger than a few times unity. With the γ factor used, $\gamma\theta \sim 1$ for $\theta \sim 0.1$ mrad, which is a very narrow divergence.

The spectral content of the beam can be found [100] by integrating over all angles to find

$$\frac{dI}{d\omega} = \frac{\sqrt{3}}{4}\frac{e^2}{\pi c \epsilon_0}\gamma\frac{\omega}{\omega_c}\int_{\omega/\omega_c}^{\infty} K_{5/3}(x)dx \tag{2.153}$$

where $x = \omega/\omega_c$. In the low frequency and high frequency limits this integral can be approximated as

$$\frac{dI}{d\omega} \sim \begin{cases} \frac{e^2}{4\pi\epsilon_0 c}\left(\frac{\omega\rho}{c}\right)^{1/3} & \text{if } \omega \ll \omega_c \\ \sqrt{\frac{3\pi}{2}}\frac{e^2}{4\pi\epsilon_0 c}\gamma\left(\frac{\omega}{\omega_c}\right)^{1/2} e^{-\omega/\omega_c} & \text{if } \omega \gg \omega_c \end{cases} \tag{2.154}$$

So for small frequencies the intensity increases slowly with an $\omega^{1/3}$ scaling and for high frequencies there is a rapid exponential fall-off in intensity. This helps to explain the shape of brightness curves, for example in figure 1.4.

The intensity spectrum (equation 2.150) can be re-written in the useful form

$$\frac{d^2I}{dEd\Omega} = \frac{3e^2}{16\pi^3\hbar c\epsilon_0}\gamma^2\frac{E^2}{{E_c}^2}\left(1+\gamma^2\theta^2\right)^2\left[K^2_{2/3}(\psi)+\frac{\gamma^2\theta^2}{1+\gamma^2\theta^2}K^2_{1/3}(\psi)\right] \tag{2.155}$$

where ψ is now given as

$$\psi = \frac{E}{2E_c}\left(1+\gamma^2\theta^2\right)^{3/2} \tag{2.156}$$

E is the photon energy and $E_c = \hbar\omega_c$ is the critical energy. The intensity spectrum for a 1 GeV electron, assumed to be undertaking an orbit such that $E_c = 20$ keV, is plotted for a range of angles in figure 2.13. This shows a very rapid fall-off in the spectral intensity of high frequency light with the observation angle θ. This result is at odds with reports that

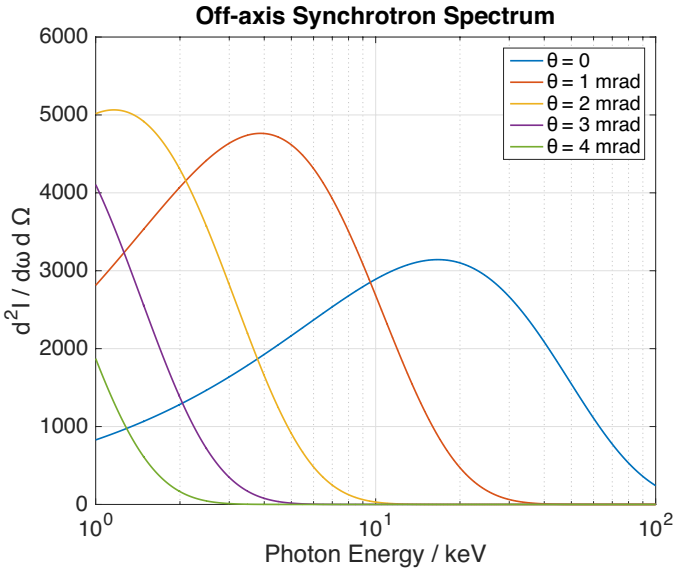


Figure 2.13: Spectral intensity of the synchrotron spectrum for different observation angles.

a betatron spectrum is well approximated by the on-axis synchrotron spectrum ($\theta = 0$) [87]. The reason this approximation can be made lies in the trajectory of electrons in a high K wiggler. From equation 2.140 the mean particle velocity in the z direction is

$$\langle\beta_z\rangle = \beta\left(1-\frac{K^2}{4\gamma^2}\right) \tag{2.157}$$

Writing $\langle\gamma\rangle^{-2} = 1-\langle\beta\rangle^2$ produces a mean Lorentz factor $\langle\gamma\rangle$ in a wiggler of

$$\langle\gamma\rangle \approx \frac{\gamma}{\sqrt{1+\frac{1}{2}K^2}} \tag{2.158}$$

provided that β stays close to unity. Taking this in to account and re-plotting figure 2.13 for a $K = 10$ wiggler, representative of a LWFA, produces the graph in figure 2.14. In our

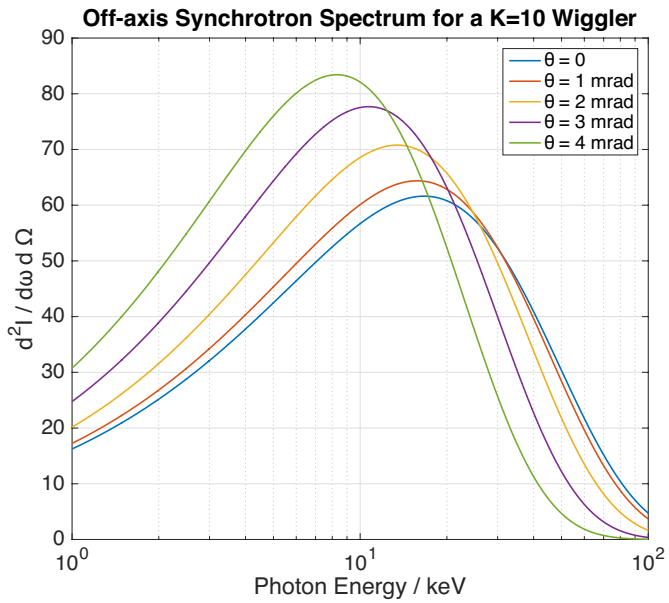


Figure 2.14: Spectral intensity of a $K = 10$ wiggler spectrum for different observation angles.

angular range of interest there is significantly less variation in energy spectrum with θ, which is one reason that the betatron spectrum appears to be close to an on-axis spectrum.

Since these results were derived for a particle in instantaneous circular motion, they apply for any particle trajectory. For a wiggler the only difference is that ω_c is altered by replacing the synchrotron radius of curvature ρ with the effective radius of curvature of an electron on a wiggler trajectory. The most radiation is emitted at the points on the trajectory with the greatest acceleration and therefore the smallest radius of curvature. It can be shown that for the wiggler trajectory (equation 2.138) that

$$\rho_{min} = \frac{\gamma}{K\ k_u} \tag{2.159}$$

Inserting this in to equation 2.152 for the critical frequency gives[1]

$$\omega_c \sim \frac{3}{2}\gamma^2 K\ k_u c \tag{2.160}$$

If we were to instead consider the motion of an electron inside a plasma wiggler, i.e. a LWFA, and use the wakefield wiggler parameter (equation 2.141) the LWFA critical frequency is found as

$$\omega_c \sim \frac{3}{2}\gamma^3 {k_\beta}^2 r_\beta c = \frac{3}{4c}\gamma^2 {\omega_p}^2 r_\beta \tag{2.161}$$

[1]It should be noted that this will be larger than the measured 'effective' critical energy because we have ignored all radiation emitted at all other points on the trajectory.

This, combined with the intensity spectra, is in line with the results of [86], where an alternative to equation 2.150 was explicitly derived by inserting the equation of motion for an electron in a wakefield, or strictly speaking a plasma channel (section 2.4.1), in to equation 2.149.

Finally we come to the energy emitted by an electron in a wiggler, be it conventional or plasma. From appendix 8.5 the power emitted by a single accelerating electron takes the general form

$$P = \frac{e^2}{6\pi c\epsilon_0}\gamma^6 \left[\left| \dot{\boldsymbol{\beta}} \right|^2 - \left| \boldsymbol{\beta} \times \dot{\boldsymbol{\beta}} \right|^2 \right] \tag{2.162}$$

Assuming that $\dot{\boldsymbol{\beta}} \perp \boldsymbol{\beta}$ then $|\boldsymbol{\beta} \times \dot{\boldsymbol{\beta}}|^2 = |\beta\dot{\beta}|^2$. Then the total radiated power simplifies to

$$P = \frac{e^2}{6\pi\epsilon_0 c}\gamma^6 \left[|\dot{\boldsymbol{\beta}}|^2 \left(1 - \beta^2\right) \right] = \frac{e^2}{6\pi\epsilon_0 c}\gamma^4 |\dot{\boldsymbol{\beta}}|^2 \tag{2.163}$$

As we have seen the transverse momentum of an electron in a wiggler is $\tilde{p}_x = \gamma\beta_x = K\sin(k_u\beta ct)$. Therefore $\dot{\beta}_x = (K/\gamma)\ k_u\beta c\cos(k_u\beta ct)$ assuming that $\dot{\gamma} = 0$. Inserting this in to the simplified power equation above, and averaging over a full cycle, the average power is found to be

$$\langle P \rangle = \frac{e^2 c}{12\pi\epsilon_0}\gamma^2 K^2 k_u^2 \tag{2.164}$$

The total energy emitted per cycle $W_c = \langle P \rangle \Delta t = \langle P \rangle \lambda_u/c$, which becomes

$$W_c = \frac{e^2}{6\epsilon_0}\gamma^2 K^2 k_u \tag{2.165}$$

For a LWFA with N_e electrons undertaking N_β oscillations the total energy emitted is

$$W_{tot} = \frac{e^2}{6\epsilon_0} N_e N_\beta \gamma^2 K_\beta^2 k_\beta \tag{2.166}$$

The derivation of this equation has assumed that each of the N_e electrons has the same energy and oscillation radius. This means that this formula may not be valid for electron populations where there is a large spread in either of these factors, although it does highlight that the most energetic electrons undergoing large oscillations contribute the most to the total emitted energy.

In this section we have seen that the motion of an electron in a LWFA, approximating it as a cylindrically symmetric plasma channel, is analogous to the motion of an electron in a conventional insertion device i.e. a wiggler. By comparing this motion to the general equations for x-ray intensity from a relativistic charge in instantaneous circular motion, an approximate form of the x-ray spectrum has been derived. The spectrum is broadband and

is described by a characteristic frequency called the critical frequency. Finally equations estimating the total power emitted by an electron undergoing betatron motion in a LWFA were found.

Chapter 3

Experimental Methods

This section will briefly discuss high power laser systems and detail those which were used in this work. Their characterisation will be described. The plasma targets that were deployed are shown next. The bulk of this section is dedicated to the set-up of the electron and x-ray beam diagnostics, their usage and calibrations. This chapter makes frequent reference to appendices 8.6-8.9.

3.1 High Power, Short Pulse Laser Systems

Much of the last chapter discussed relativistically nonlinear plasma phenomena i.e. a laser pulse with $a_0 \sim 1$ interacting with electrons. Considering that $a_0 \approx 0.856 \left(I_{18}\lambda_{\mu m}{}^2\right)^{\frac{1}{2}}$ a focussed 1 μm laser pulse of at least 10^{18} W/cm^2 is required to reach this regime, and the ${I_{18}}^{\frac{1}{2}}$ scaling is not favourable for progression to larger a_0's. To reach such high intensities LWFA experiments need lasers with powers of 10's-100's TW. This necessitates the use of a short (10's fs) laser pulse, which is also exactly what is required for efficient wakefield generation.

A typical short pulse laser system starts off with an oscillator: one highly reflective mirror, one 'leaky' mirror and a gain medium in between which is usually pumped with a CW laser. In this configuration a train of pulses are transmitted though the leaky mirror separated by time $T = 2L/c$ where L is the cavity length. Ultrashort pulses require a significant bandwidth to respect the uncertainty principle. For this reason Ti:sapphire is a very common gain medium in short pulse laser systems because of its large gain bandwidth. This large bandwidth is necessary but not sufficient for ultrashort pulse generation: mode-locking is required for this.

A laser cavity can support a large number of modes. If each of these modes has a random phase then the sum of their electric fields i.e. the total electric field in the cavity will be a low intensity 'mess', and not very short at all. Instead if these modes are locked

in phase they sum to an intense, short pulse. Mode-locking can be achieved by putting a device such as a saturable absorber or a Kerr lens and an aperture in to the cavity. These devices act as ultrafast switches that only transmit high intensity light i.e. the modes that are synchronised in time. After a number of cavity round trips only mode locked pulses remain.

There is a limit to how much a pulse can be amplified where it becomes so intense it starts to cause material damage to components in the laser system through nonlinear effects. This can be mitigated somewhat by using a larger beam and larger components. However it is the technology of chirped pulse amplification (CPA) [135] that has revolutionised laser amplification and is the technology on which virtually all high power systems are based. A short pulse from a mode-locked cavity is stretched in time by a large factor by chirping it. This is then amplified, often in a multipass arrangement, and then recompressed using gratings resulting in a very high power short pulse.

The lasers used for the work presented here are all part of the Astra Gemini system at the CLF at the Rutherford Appleton Laboratory. The Astra system employs a Femtolasers Compact Pro oscillator [136] [137]. Pulses are selected from this with a Pockels cell plus polariser setup to form a 10 Hz pulse train which seeds the amplification system. The first part of this system is a grating stretcher followed by three multipass amplifiers based on the design in [138], except since this publication all of the pump lasers have been replaced by Spectra-Physics Quanta Ray lasers. A rotating waveplate plus a polariser alternately sends each pulse either to the TA2 target area or to the Gemini amplifier. The pulse going to TA2 has up to 1 J of energy before compression and a nominal beam size of 55 mm. The shortest pulse length available is ~ 37 fs full width at half maximum (FWHM). The Gemini amplifier, as stargazers and those of a fatalist disposition may have guessed, is actually two amplifiers. The 5 Hz pulse is split in to two and sent through two separate 4 pass Ti:sapphire amplifiers. Each of the beams is independently compressed and delivered in to the TA3 target chamber. The maximum beam energy is approximately 20 J before the compressor. The compressor throughput is 60-70% meaning that $12-14$ J is delivered to the target area in each beam. The beam size is ~ 15 cm and the shortest pulse duration is ~ 47 fs FWHM.

3.2 Laser Diagnostics

We have seen that a LWFA is driven by gradients in the normalised vector potential $\boldsymbol{a}$ of the driving laser. Therefore it is important to measure this quantity to aid understanding, for use in simulation and for comparison to other works. We have $a_0 \propto I_0\lambda^2$ where a_0 and I_0 are the peak values of $\boldsymbol{a}$ and intensity respectively. All of the laser systems used in this

work were titanium sapphire systems operating at a central wavelength of 800 nm. To determine the intensity I, the laser pulse energy, pulse duration and the focal spot size must be measured.

In this work it is simply assumed that the pulse is gaussian in both space and time. The intensity I as a function of the radial coordinate r and time t is given by

$$I = I_0 \exp\left(-\frac{2r^2}{{d_0}^2}\right) \exp\left(-\frac{2t^2}{\tau^2}\right) \tag{3.1}$$

d_0 and τ are the radius and time at which the intensity falls to $1/e^2$ of the peak intensity respectively.

Integrating this equation over all of space gives the power P of the pulse. Integrating again over all of time gives the total pulse energy E_L. I_0 can then be written as a function of total energy

$$I_0 = \frac{E_L}{\left(\frac{\pi}{2}\right)^{\frac{3}{2}} {d_0}^2 \, \tau} \tag{3.2}$$

For a pulse with radii $d_1, d_2, d_1 \neq d_2$ one can substitute ${d_0}^2 \rightarrow d_1 d_2$. Often in this thesis FWHM values will be given. These are related to the $1/e^2$ widths as $d_{FWHM} = \sqrt{2\ln 2}\, d_0$ and $\tau_{FWHM} = \sqrt{2\ln 2}\, \tau$.

3.2.1 Laser Energy Measurement

On Gemini (TA3) the laser energy was measured every shot by a CLF set-up and recorded for the user via their online eCat system [139]. To do this the near field of the pulse that leaked through a highly-reflective (HR) coated mirror was projected on to a CCD camera. A calibration of CCD counts to laser energy was performed by CLF staff using a Gentec laser energy meter. The energy was measured after the final amplifier and before the compressor. The compressor efficiency reduced the energy delivered to the target area. To account for this the compressor throughput was found by comparing measurements of the laser energy before the compressor and in the target chamber. A similar system was fielded on the Astra laser (TA2) except the system was set up by the user.

3.2.2 Laser Pulse Duration

Femtosecond laser pulses are amongst the temporally shortest events ever created, meaning that to measure them one usually has to use a copy of the pulse itself. One method of pulse length measurement involves splitting the laser pulse using a beamsplitter, and then recombining the two copies of the pulse in a nonlinear optical medium to produce a second

harmonic signal. An autocorrelator measures the intensity of the second harmonic light as a function of delay between the pulses to estimate the pulse length. This is using the pulse to gate itself. The whole measurement can be made in a single shot by focussing the two pulses to a line focus in the nonlinear medium, and crossing them at an angle, producing a varying delay between the two pulses along the length of the line focus. In a FROG (frequency resolved optical gating) [140] [141] the detector is replaced with a spectrometer, so that the spectral phase of the pulse can also be measured. A single shot FROG produces a 2D image of intensity as a function of delay and frequency, and the pulse shape is found from this using a relatively complicated phase-retrieval algorithm. An alternative method of pulse measurement, relying on spectral interferometry, is known as SPIDER (spectral phase interferometry for direct electric-field reconstruction). In spectral interferometry a known reference pulse is combined with the unknown pulse with some time delay, which when measured on a spectrometer produces spectral fringes. The overall fringe spacing is due to the delay, but the spacing is locally modified by the difference in spectral phase between the reference and unknown pulses. As the reference pulse is well characterised, the spectral phase and electric field amplitude of the unknown pulse can be easily found. Similarly, the spectral phase can be retrieved from two unknown pulses that have a known difference in central frequency. This is the operating principle of a SPIDER [142] [143]. The laser pulse is first split in to two, with one pulse being strongly chirped and the other being split further by a mismatched Michelson interferometer, creating two temporally separated pulses. These two short pulses are then combined with the chirped pulse in a nonlinear crystal and undergo sum frequency generation, creating two short pulses with different central wavelengths, owing to them interacting (via the medium) with different frequencies in the chirped pulse. The two short high frequency pulses are interfered in a spectrometer to create spectral fringes, from which the amplitude and spectral phase of the original pulse can be reconstructed [144]. The analysis of SPIDER spectrograms is simpler than those from a FROG, although it is not well suited to measuring longer pulses and it is, arguably, a more difficult diagnostic to build.

The Gemini laser pulse duration was measured with a FROG set up by the CLF. Typically the optimally compressed pulse has a FWHM duration of $\tau_{FWHM} \sim 47$ fs which was measured multiple times during each experiment. The Astra laser pulse duration was measured with a SPIDER at the start of the experiment detailed in chapter 4 and at best had $\tau_{FWHM} \sim 37$ fs.

3.2.3 Focal Spot Characterisation

The laser focal spot was imaged on to a CCD camera using an apochromatic microscope objective lens. A typical image of the focal spot from the F40 focussing optic is shown

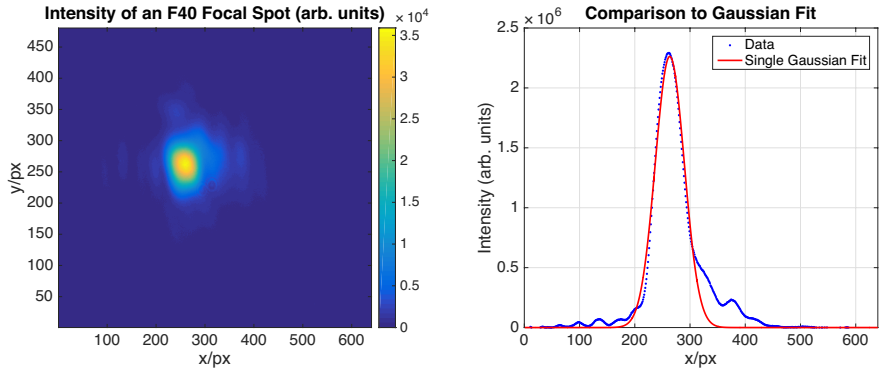


Figure 3.1: Left: raw image of the low power focal spot from the $f/40$ optic. Right: in blue is the summation over all of the rows of the background subtracted focal spot image. In red is a fit of a single gaussian to this. We see that the gaussian beam approximation is quite good near the centre of the spot but does not account for the wings of the pulse.

in figure 3.1. This was taken in the Gemini 'low power' mode, which is an attenuated version of the pulse coming from Astra with the final Gemini amplifier turned off.

The first step in determining the focal spot size was to spatially calibrate the camera i.e. to answer the question: what distance does one camera pixel correspond to? This was done by inserting a grating with separation $d = 15$ mm in to the collimated beam upstream of the focussing optic (focal length f). This produces multiple orders of the spot with angular separation θ determined by the equation $\sin\theta = m\lambda/d$. In the focal plane these will be physically separated by a distance $x = mf\tan\theta$. For small θ we can then write $x \approx f\lambda/d$. Comparison of this number to the spot spacing on the image provides the calibration.

The focal spot analysis procedure will now be described with reference to figure 3.2. The top left image is the raw image of the focal spot. The green rectangles surround regions far away from the peak of the pulse that were used for background subtraction. The mean pixel value from the areas within these rectangles was subtracted from the entire image. This camera had a few burnt pixels which are surrounded by red rectangles in this image. All pixels within the red rectangles had their values set to 0. To remove any other 'hot' pixels the image was median filtered with a 3×3 pixel neighbourhood size. The top right image shows the saturated image of the spot which highlights the extent of the wings of the pulse. To find the FWHM size of the spot a contour was fitted[1] to 50% of the maximum pixel value. In case not all of the hot-spots had been removed all points along the contour lying further than two standard deviations from the mean were eliminated. Inspection of the results revealed this to be an effective method. An

[1]Using the inbuilt contour.m function in MATLAB

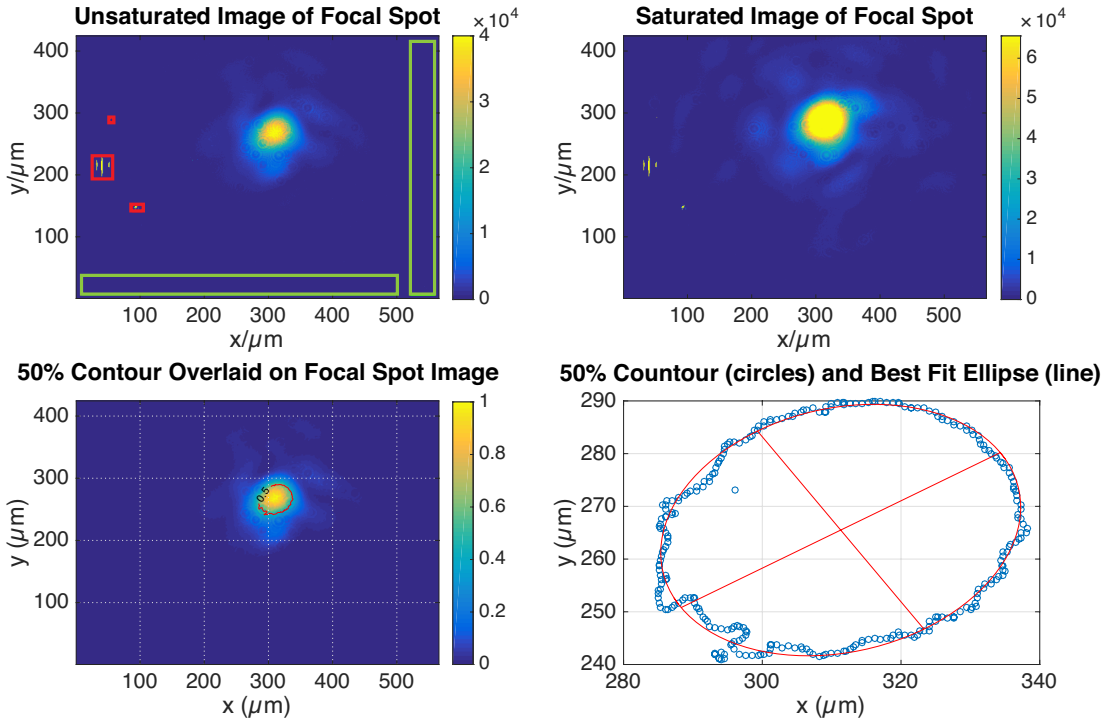


Figure 3.2: Demonstration of the focal spot analysis procedure.

ellipse was fitted to the remaining points[2]. This function returned the lengths of the long and short axes of the ellipse, i.e. the FWHM beam size, in microns thanks to the spatial calibration. It also returned the rotation of the ellipse with respect to the x, y axes and the coordinates of the centre of the ellipse which allowed the pointing fluctuations to be characterised. The final parameter that was calculated was the energy within the FWHM which has a maximum value of 50% for a gaussian beam. This was done by finding the sum of all of the pixel values with a value greater than half of the maximum pixel value, and dividing this by the sum of all of the pixel values in the image. This seems to be a simplistic analysis, but an image of the values greater than half of the maximum with the 50% contour overlaid (figure 3.3) confirms that this is in fact an accurate method.

Typically 50-200 images were taken of the focal spot each day after the focal spot optimisation using the adaptive optic (in Gemini TA3 only) and shortly before taking full power shots. The large number of images allowed for averaging and an estimation of the fluctuations in the properties of the spot.

[2]Using the code fit_ellipse.m which is available from the Mathworks File Exchange [145]

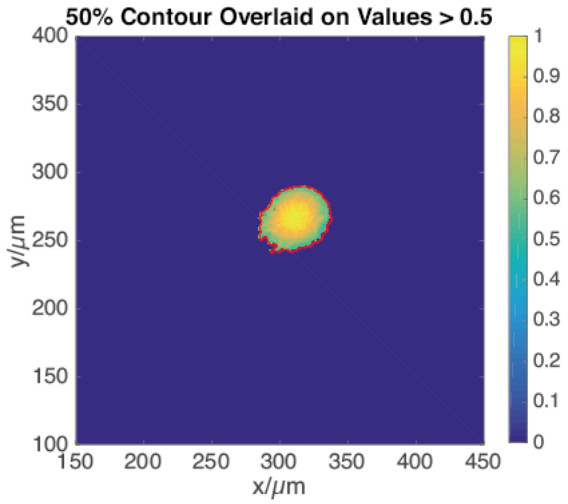


Figure 3.3: 50% Intensity contour of the focal spot overlaid on pixel values greater than 0.5 (maximum value is 1). This verifies the method of calculating the energy inside the FWHM spot

3.3 Gas Targetry

This section will detail the plasma targets used in this thesis. All targets employed neutral gas which was ionised by the wakefield driver laser, which was more than two orders of magnitude above the ionisation threshold intensity for both electrons of helium. Therefore it was not necessary to pre-ionise the gas via another method, such as an additional laser pulse or a high voltage discharge. For the plasma number densities studied in each experiment presented in this thesis the laser power was higher than the critical power for self-guiding. This meant that it was not necessary to use a preformed plasma channel, as described in [146] [147] [56], to guide a significant fraction of the laser energy over many Rayleigh lengths, justifying the use of neutral gas targets. Such an approach is not uncommon; multiple GeV scale LWFA experiments have been performed in this self-guided configuration [57] [58] [59] [60].

3.3.1 Gas Jets

Conical gas jets (nozzles) have historically been the most popular target for LWFA experiments. They were used in the TA2 experiment here (chapter 4). The reason for their popularity is that these supersonic conical nozzles give a density profile with a constant density plateau with reasonably short density ramps at the edge. Additionally they are relatively easy to use and align. The optimal design is a trade-off between wanting a high Mach number to give a flat-top profile and a small Mach number to give a reasonably high gas density. This problem was explored in [148]. The 3 mm nozzle used in the TA2 experiment, a diagram of which is shown in figure 3.4, was designed according to the

optimum parameters for a 3 mm length nozzle from this publication. The gas was stored in a reservoir at high pressure and released through the nozzle by a Peter Paul solenoid valve[3] which was typically opened 10 ms before the laser-gas interaction took place.

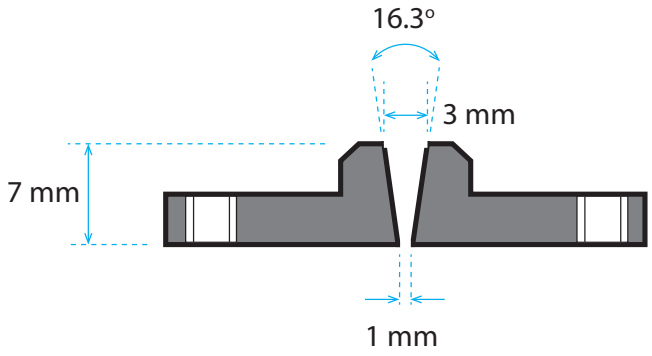


Figure 3.4: Diagram of the 3 mm gas nozzle.

3.3.2 Gas Cells

For most of the work in this thesis the plasma target was a gas cell, an example of which is shown in figure 3.5. The precise design differed between experiments although the operating principle was the same. The total length of the accelerator L_{acc} was adjustable by moving the cones which were typically made of brass or plastic. The starting diameter of the laser entry and exit holes in the cones was 300 μm although this could increase significantly over many shots due to laser ablation. The gas pressure in each of the compartments could be independently controlled. The cell was filled with gas for $\sim$ 20 ms starting 60 ms before a laser shot was fired. The divider wall permitted the use of a different gas in each compartment to have an initial injector stage followed by a lower density accelerator stage similar to [149]. The 100 μm diameter hole in the divider wall meant that relatively short scale length density gradients could be created between the two compartments to investigate density down-ramp injection [71]. However the most common mode of operation was to have both compartments set to an identical pressure or in some experiments to remove the dividing wall entirely. While the plasma density could be characterised on shot (section 3.3.4) the opaque nature of the cones prevented the determination of the plasma density inside them. This has been numerically modelled using OpenFOAM [150]. After the hole in the cone the distance over which the gas density drops from 90% to 10% was found to be on the order of 1 mm for 300 μm holes.

[3]Peter Paul Series 20, model EH22, orifice 1/32".

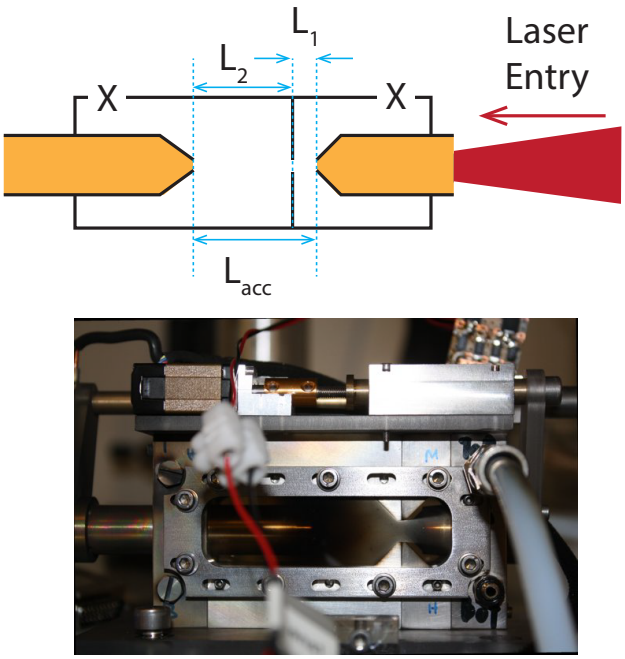


Figure 3.5: Diagram of the gas cell (top) and image of the gas cell (bottom). The laser enters the cell from the right-hand side in both images. Gas enters from the inlets marked X and fills both compartments of the cell.

3.3.3 Choice of Gas

For self-injection runs pure helium gas was used. Helium becomes fully ionised at 8.8×10^{15} W/cm^2 assuming that ionisation happens at total barrier suppression i.e. when the electric field of the laser is great enough to reduce the atomic potential to zero. This is much lower than the intensities above 10^{18} W/cm^2 of the wakefield driver laser meaning that the gas will be fully ionised well in advance of the peak of the laser pulse.

For ionisation injection the gas was helium plus some dopant gas at the few per cent level. The dopant gas was chosen so that its outer shell electrons would be ionised easily and contribute to the background plasma and its inner shell electrons would be ionised only near the peak of the laser pulse. Typical dopant gases were nitrogen and CO_2. Five electrons of nitrogen are ionised at intensities below 1.5×10^{16} W/cm^2 and the remaining two are ionised at 1.0 and 1.6×10^{19} W/cm^2 respectively, corresponding to a_0 values of 2.2 and 2.8. CO_2 has 10 electrons ionised below 4.1×10^{16} W/cm^2 and then additional ionisations at a_0's of 1.3 and 1.7 for carbon and 3.4 and 4.1 for oxygen.

From gas jets it is possible to produce clusters which are bundles of 10's to many tens of thousands of atoms held together by van der Waals forces. A clustering system can be described by the empirically found Hagena parameter Γ^* [151] [152],

$$\Gamma^* = k \frac{(d/\tan\alpha)^{0.85}}{T_0^{2.29}} P_0 \tag{3.3}$$

d is the nozzle diameter in mm, α is the expansion half angle, P_0 is the gas backing pressure in mbar, T_0 is the initial gas temperature in Kelvin and k is a gas dependent constant related to how easily inter-atomic bonds are formed. Clustering begins for $\Gamma^* > 100 - 300$ and the number of atoms per cluster scales as $N_c \propto (\Gamma^*)^{2.0-2.5}$ [151] [153] [154]. For helium $k = 3.85$ whereas for methane (CH_4) $k = 2360$ [152]. For the nozzle shown in figure 3.4 $\Gamma^*_{He} \approx 1.1$ and $\Gamma^*_{CH4} \approx 670$ for 10 bar backing pressure and $T_0 = 300$ K. Therefore one would expect to produce methane clusters but not helium clusters using this nozzle with gas parameters similar to these.

3.3.4 Density Characterisation

Plasma density characterisation was done on shot using a ~ 40 fs probe pulse timed to arrive just after the wakefield driver pulse had exited the plasma. The probe pulse was propagated through the gas target and then through a modified Mach-Zehnder interferometer. A Mach-Zehnder interferometer usually has the plasma target in one of its arms. In a modified Mach-Zehnder the target is before the interferometer and the interferometer is purposefully misaligned so that the part of the beam that passed through the plasma is overlapped with part of the beam that did not from the other arm. The phase shift of the light due to the plasma $\Delta\phi(y, z)$ can be retrieved from an interferogram and is related to the refractive index $\eta(r, z)$ by the equation

$$\Delta\phi(y, z) = \frac{2\pi}{\lambda} \int_{-\infty}^{\infty} (\eta(r, z) - 1)\, dx \tag{3.4}$$

For plasmas with electron number density $n_e \ll n_c$ equation 3.4 can be simplified using the expression $\eta \approx 1 - n_e/(2n_c)$. Note that at this stage the observed phase shift is integrated along a Cartesian coordinate through what is assumed to be a cylinder of plasma. Enforcing this assumption mathematically an Abel transformation [155] can be performed to equation 3.4 to give the plasma density $n_e(r, z)$ from the measured $\Delta\phi(y, z)$. The density analysis in this thesis was done using an algorithm developed by Jason Cole [156]. Alternatively a method based on moiré deflectometry [157] [158] [159] was used. Again the analysis was done by Jason Cole. A moiré pattern, a series of light and dark fringes, is produced when a collimated light source is used to back-light two Ronchi gratings, with one rotated by a small angle with respect to the other. If a transparent object (such as an underdense plasma) is placed in the collimated beam then the wavefront of the beam will be altered, causing a change in the observed moiré fringe pattern. The phase shift can be found by comparing the fringe pattern to the reference pattern, taken with no object in the beam. The plasma density can then be calculated using equation 3.4 and the Abel transformation.

3.4 Electron Beam Diagnostics

There are many properties of an electron beam that one might wish to measure such as its energy, the number of electrons it contains, its divergence, its temporal duration and its emittance. Here only the first three of these parameters are measured directly. The temporal duration of the beam and its emittance will first be discussed briefly with reference to the literature.

Measurements of coherent transition radiation have shown that electron bunches as short as 4.4 fs FWHM can be produced [62]. The duration has been indirectly inferred from measurements of beam loading as 4 fs [160]. However both experiments employed a two-beam colliding pulse injection method similar to [73]. It is not clear that these low values can be produced in experiments reliant on self-injection or ionisation injection, especially where a large energy spread beam is observed. Measurements of THz coherent transition radiation from a self-injected bunch have previously suggested a bunch duration below 38 fs [161].

Direct measurements of the normalised transverse emittance of a LWFA beam have been made using the pepper-pot technique [162] and found it to be at best 1.1π mm-mrad [63], although the mean values were $(2.2 \pm 0.7)\pi$ mm-mrad and $(2.3 \pm 0.6)\pi$ mm-mrad in the (x, x') and (y, y') phase spaces. This is in line with earlier measurements of of $(2.7 \pm 0.9)\pi$ mm-mrad [163]. Betatron radiation measurements suggest that within the bubble the normalised transverse emittance is < 0.57-0.81π mm-mrad [164] (from the x-ray beam divergence and an assumption of a Maxwell-Boltzmann electron beam distribution) or $< 0.5\pi$ mm-mrad [165] (combination of betatron source size and electron beam divergence measurements). Both of these betatron-based measurements will be an underestimate of the emittance of the beam outside the plasma because it ignores the effect of the plasma-vacuum boundary and the growth of emittance during free space propagation due to finite energy spread. None of the methods discussed so far are spectrally resolved whereas for a number of proposed applications of these beams (e.g. colliders, FEL's) would require a monochromatic, or monochromated, electron beam. To this end, Weingartner et al. [166] measured a normalised transverse emittance of 0.21π mm-mrad at 245 MeV using a quadrupole scan method.

3.4.1 Electron Spectrometer Set-up

The energy spectra of the electron beams were characterised using a set-up based on that shown in figure 3.6. The electrons coming from the source pass through one or more dipole magnets. Travelling through the dipole magnet electrons of different momenta travel along an arc of a cyclotron orbit with radius $r_c = \gamma m_e v_\perp/(eB)$ where $v_\perp$ is the

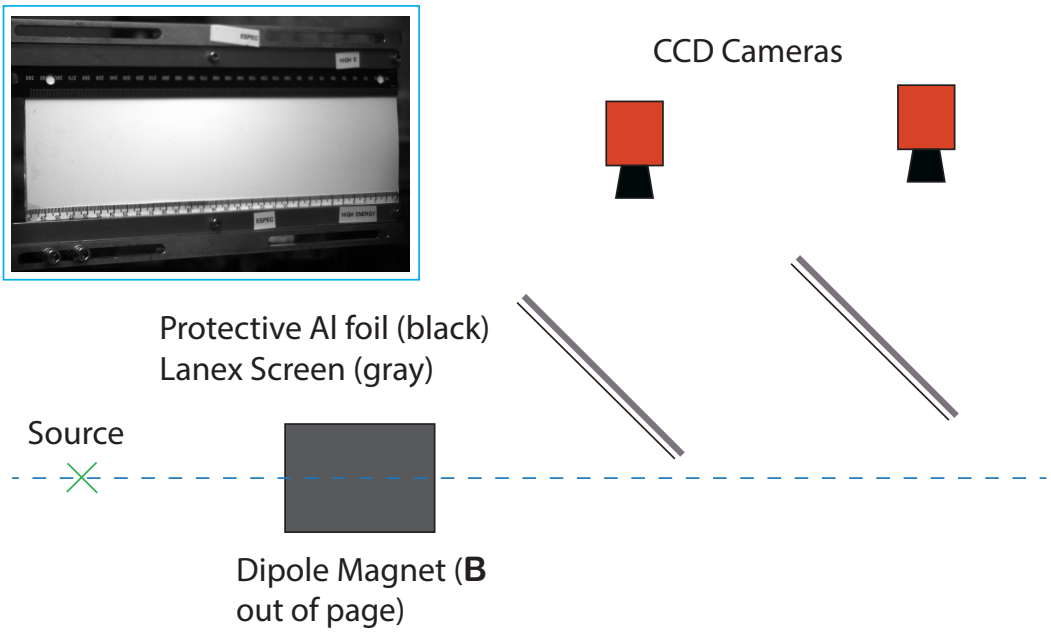


Figure 3.6: Typical layout of a two screen electron spectrometer. Inset top left is a reference image of an electron spectrometer screen. The Lanex screen (white) was spatially calibrated using the rulers running along its edges.

velocity perpendicular to the magnetic field, which is close to c for the electron energies considered. When these electrons exit the magnet they are dispersed by their momenta. The dispersed beam is detected on two Lanex (see appendix 8.6 for details on Lanex) screens angled at 45° to the vertical which are then imaged on to a CCD camera with a TV lens, sometimes via an arrangement of mirrors. Calculations of the electron trajectories as a function of energy, careful measurement of the Lanex screen positions and a spatial calibration were used to convert pixel number in the images to electron energy. Two screens are used because in principle this allows features to be tracked backwards through the magnetic field to the source revealing the angle at which they exited the source. Using this the electron energy can be corrected. This is an iterative process to find the true electron energy.

3.4.2 Electron Beam Tracking

For a rectangular magnet as depicted in figure 3.6 with constant field strength the electron beam tracking problem, and the intersection of the electrons trajectories with the Lanex screens, can be solved analytically. This is also true of electrons travelling at some angle to the laser axis although this becomes a little involved. Real dipole magnets do not have a spatially invariant magnetic field within the magnet 'box'. This necessitates the use of a particle tracking code. Electron tracks used in this thesis were produced by a code

written by the author, an example output of which can be seen in figure 3.7. While all

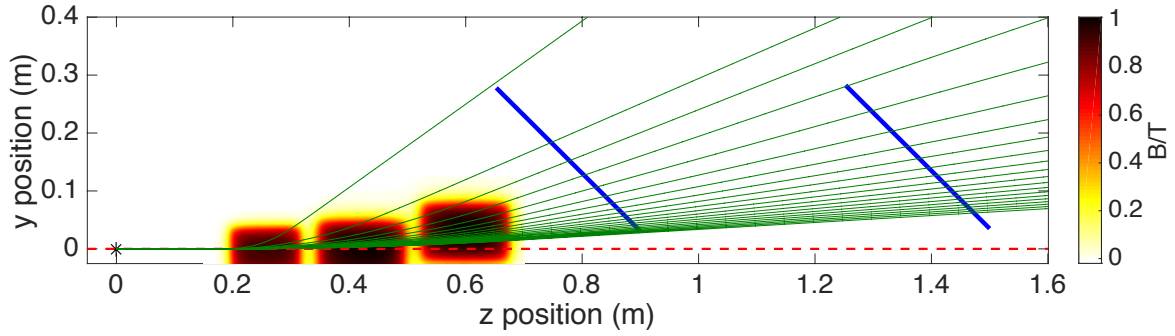


Figure 3.7: Example output of the electron tracking code. Electrons from the source (black star at (0,0)) are tracked through three dipole magnets and intersect the Lanex screens (blue). The electrons (green tracks) were initiated with energies between 50 and 2,050 MeV spaced by 100 MeV. We see that energy resolution is worse at high energy, which is unsurprising considering that in a $\boldsymbol{B}$ field the acceleration $\ddot{\boldsymbol{r}} \propto 1/\gamma$.

calculations are done in 3D the electron trajectories were confined to the $y-z$ plane for simplicity. Electrons are initiated with a user defined range of kinetic energies. There is the option to track all of these energies at multiple initial angles which can shed light on the effect of beam divergence or correct for a constant angular offset. The time step of the simulation is not adaptive but it is set to $10^{-3} \times 1/\omega_{c,max}$ where $\omega_{c,max} = eB_0/m_e$ is the maximum cyclotron frequency an electron of momentum $\gamma m_e \boldsymbol{v}$ will experience anywhere in the simulation (i.e. in the region of highest $\boldsymbol{B}$ field). At each time step the local $\boldsymbol{B}$ field is determined from the electron position and the magnetic field map that was input in to the simulation. This subjects the electron to a force $\boldsymbol{F} = -e(\boldsymbol{v} \times \boldsymbol{B})$ which is used to update the velocity via the leapfrog method using the fact that $\dot{\gamma} = 0$ in a magnetic field. The leapfrog method was chosen because it is simple to implement, fast and conditionally stable for oscillatory solutions [167]. The position was updated from the velocity via the leapfrog method also. Once they have left the magnetic field the electrons travel in a straight line. An equation of the form $y = mz + c$ was fitted to this line and its intersections with the equations defining the Lanex screen positions were found. From these coordinates a distance to the high energy end of the Lanex screen was calculated for each electron energy for comparison with the experimental data. To produce the magnetic field map, the field of the dipole magnets was measured using a Gauss meter at regular intervals in (y, z) space. For the map shown in figure 3.7 a 1 mm grid spacing was used. Care was taken to ensure that the field was sampled far enough away from the magnets to capture the fringe fields. This map was then input in to the simulation, ensuring that fringe fields were properly accounted for.

A simple error analysis was performed to check the correct working of this code. A relativistic electron was tracked in a spatially uniform 1.0 T magnetic field with time step $10^{-3}/\omega_c$. This has a simple solution of the electron travelling in a circle with the aforementioned cyclotron radius r_c. The fractional error was defined as $(r_c - r_c')/r_c$ where r_c' is the cyclotron radius as calculated by the code. This is plotted as a function of time in figure 3.8. A maximum fractional error of 1.5×10^{-6} is observed independent of initial electron energy and it is noted that the code is stable for at least 15 electron orbits. Stable means that the error oscillates and does not increase exponentially with time.

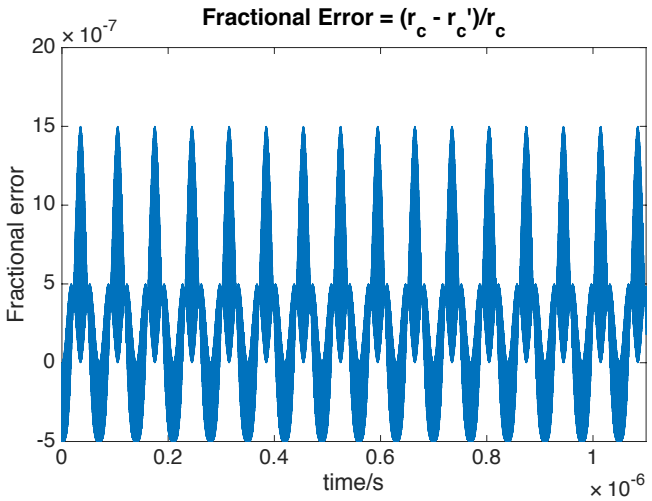


Figure 3.8: Error and stability analysis of the electron tracking code. The fractional error is defined as the difference between the physical and simulated cyclotron radii r_c and r_c' divided by r_c.

3.4.3 Electron Beam Profile

The electron beam profile was measured as shown in figure 3.9, employing as much shielding from stray light as was practical. An on-axis Lanex screen, protected by aluminium foil on the laser side, was typically placed 1-2 m after the LWFA source. The electron spectrometer dipole magnets (section 3.4.1) were moved off-axis for these measurements. The reason for the relatively large distance from source to screen was to ensure that the size of the beam was significantly larger than the minimum feature size that could be resolved by the detection system. The properties of Lanex, including its intrinsic resolution, are discussed in appendix 8.6. The screen was then imaged on to a CCD camera, typically an AVT Pike or Andor iXon camera. Before analysis, the background was removed by subtraction of the camera dark field (section 3.5.3). A laser beam aligned along the principle (wakefield driver) laser axis was used to determine the coordinates of this axis on the image: thus the electron beam pointing could be determined. A grid of known spacing was stuck on to the Lanex so that the image could be spatially calibrated. This grid was

removed before taking shots with the electron beam. The known size of the screen could also be used as a spatial calibration. The FWHM electron beam size was found by fitting an ellipse to the 50% contour of the intensity pattern on the image. This is the same method that was used to characterise the laser focal spot (section 3.2.3). Measurements of the distance from source to detector allowed this beam diameter to be converted in to a divergence angle.

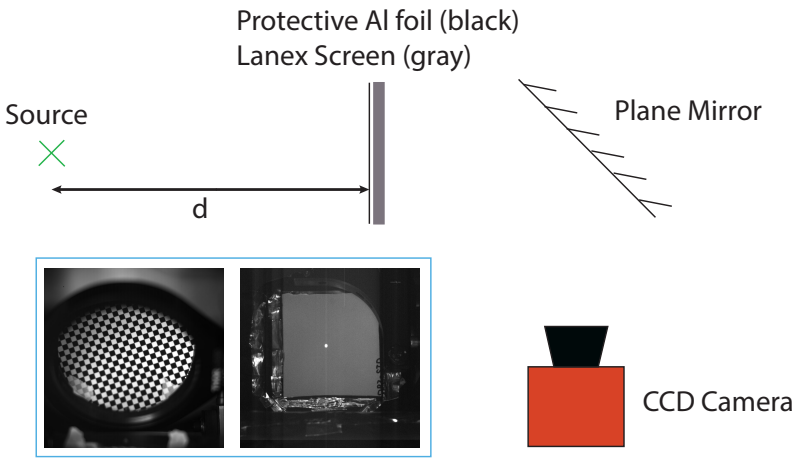


Figure 3.9: Representative layout of the electron beam profile diagnostic (not to scale). Typically $d \approx 1 - 2$ m. Inset bottom left are reference images of a spatial calibration grid and the laser dot that shows where the beam axis is.

3.4.4 Charge Calibration

The Lanex screens for the electron spectrometer and the electron beam profile were calibrated so that the number of CCD camera counts from the scintillation light could be converted to electron beam charge in pC. Crucially the number of scintillation photons are proportional to the electron beam charge and the energy deposited by one electron is approximately constant with electron energy above ~ 1 MeV as discussed in appendix 8.6. This allows for a meaningful calibration. The fact that deposited energy is not constant with electron energy below 1 MeV may affect the charge calibration of the electron profile screen but not the electron spectrometer screens which had a low energy cut-off of many MeV. A calibration can be done entirely from the properties of Lanex and careful knowledge of the imaging system [168]. However this is not trivial and the set-up changes significantly between experiments. Therefore the calibration is done by placing Image Plate (IP) in front of each Lanex screen. The properties of IP are detailed in appendix 8.7. For the charge calibration the conversion of PSL, the photo-stimulated luminescence that is stored on the IP, to electron charge was done assuming a constant energy deposition per electron as a function of electron energy (meaning that PSL is directly proportional to the the number of electrons that passed through the IP). More information on the val-

ues used for this can be found in appendix 8.7.2. Only unsaturated IP regions from the first scan were used. The effects of spontaneous PSL decay were corrected using figure 8.2.

Figure 3.10 outlines the charge calibration method. The IP QL image was first converted in to PSL using equation 8.35. QL, quantum level, is how image plate data is stored on a computer. A background subtraction was then performed. All of the points inside the red rectangles were used to interpolate the background intensity over the charge region bounded by the green rectangle. This was done using the MATLAB griddata function with the 'natural' method specified. This background was then subtracted and the total PSL found by summing over all of the charge region. This could then be converted directly to a number of electrons (section 8.7.2). On the right of this figure is an image of the Lanex electron spectrometer screen from the same shot with the corresponding charge and background regions highlighted. A background subtraction was done using the same method and the total Lanex counts in the charge region were summed. Comparison to the electron beam charge from the IP gave a conversion from Lanex counts to charge.

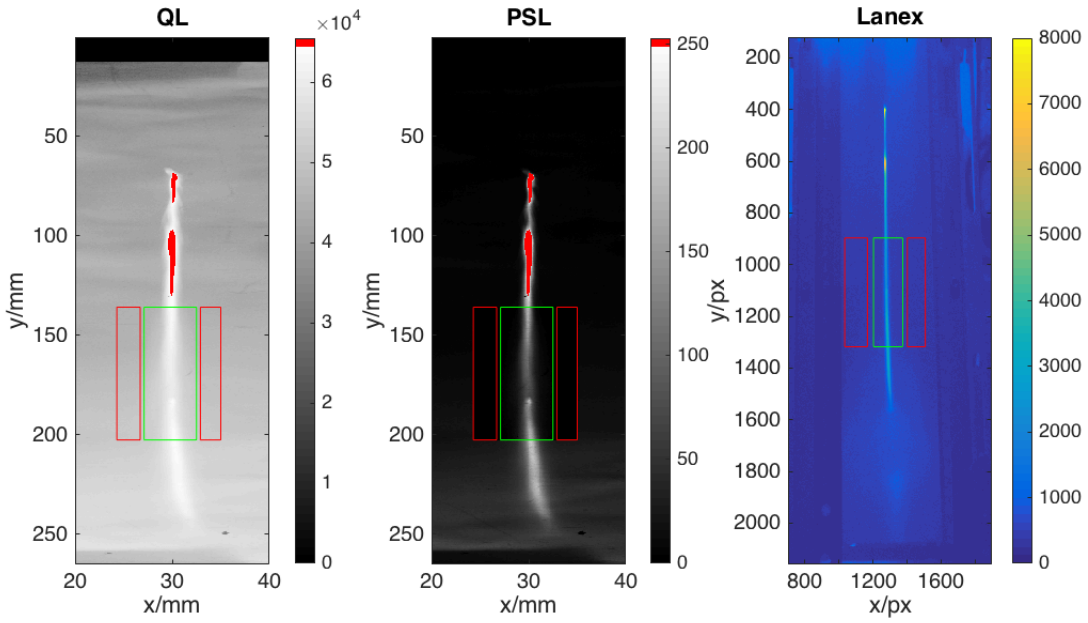


Figure 3.10: Diagram illustrating the charge calibration method. The IP QL image is shown on the far left and is converted to PSL in the centre. The red indicates areas where the IP image was saturated. The image of the first Lanex screen from the same shot is on the right. Green rectangles were the regions in which the charge was found and the red rectangles show regions used for background subtraction.

3.5 X-ray Diagnostics

As discussed earlier (section 1.2) a key figure of merit for x-ray sources is brightness. To measure this the amplitude and shape of the x-ray spectrum must be known along with its divergence, source size and temporal duration. Naturally this also requires the x-ray diagnostics to be well understood. In this section the x-ray beam profile (beam divergence) diagnostic will first be discussed. All other measurements used an x-ray camera of some form so these are described next along with dark-field and flat-field corrections which are necessary x-ray image corrections. The method of characterising the x-ray spectrum will be delineated followed by a description the x-ray camera calibration method which allowed for a conversion of camera counts to deposited x-ray energy. This in turn permits the number of x-ray photons to be estimated. Finally methods of characterising the resolution of the x-ray imaging system will be detailed. These also produced a measurement of the x-ray source size. Where peak brightness values of the betatron source are given a flat-top temporal duration of 30 fs has been assumed. This is approximately a plasma wavelength at the plasma densities used in most of the experiments detailed here (approximately 2-5$\times 10^{18}$ cm^{-3}). This could be an overestimate of the real x-ray pulse length provided that electron injection occurs only in the first wakefield bucket. However if electrons are being continually injected in to the wakefield and dephased, or if there is injection in to multiple wakefield buckets, then the x-ray pulse duration could be longer than 30 fs. The 30 fs figure is in broad agreement with measured electron bunch durations from other experiments (see section 3.4) and is a figure that has been used in previous works on the characterisation of betatron radiation [85] [79]. In the absence of further knowledge this estimate will be retained.

3.5.1 X-ray Beam Profile

The x-ray beam profile diagnostic was almost identical to the electron beam profile diagnostic, which was detailed in section 3.4.3. The only difference was that the amount scintillation light was significantly lower in the x-ray case. To detect a signal an Andor iXon EMCCD (electron-multiplying CCD) camera was used with significant EM gain. The Lanex screen was replaced either by DRZ-HIGH scintillator (appendix 8.6) or a structured caesium iodide (CsI) scintillator which will be discussed in the next section. The analysis method was identical to the one used for the electron beam profile.

3.5.2 X-ray Cameras

All high resolution x-ray cameras on the market today are based on silicon CCD technology. They broadly lie in two categories: direct detection (DD) and indirect detection (ID). DD cameras have an exposed silicon chip with is illuminated directly by the x-rays, which

are absorbed by the silicon and produce electron-hole pairs. The number of electron-hole pairs is directly proportional to the energy of the incident photon [169]. This is a very sensitive method of x-ray detection but only up to ~ 10 keV, above which very few x-rays are absorbed in the depletion region of the CCD. ID cameras image a scintillator which converts x-ray photons in to visible light photons which are then detected by the camera. This can be a lossy process but scintillators can have a reasonable quantum efficiency (QE) at energies up to ~ 100 keV.

Three x-ray cameras were used in the experiments here: one DD camera (Andor iKon-M 934 BR-DD [170], 'Andor DD camera') and two ID cameras (Princeton Instruments PIXIS-XF 2048B [171], 'Princeton camera', and an Andor iKon-L 936 BV [172], 'Andor ID camera'). Their key features are highlighted in table 3.1. Regarding illumination, front illuminated CCDs have the electrode structure for the readout electronics on the front (outward facing) surface. This is easier to manufacture and therefore cheaper but reduces the QE of the camera. Back illuminated CCDs have the electrode structure behind the depletion region and therefore have a higher QE. Deep Depletion CCDs have a thicker depletion region which improves the QE at higher x-ray energies and can push the detection limit of direct detection cameras a little beyond 10 keV. Quantum efficiency curves for these three cameras can be found in appendix 8.8.

Camera Name	Andor DD Camera	Princeton Camera	Andor ID Camera
Detection Type	Direct	Indirect	Indirect
Active Pixels	1024×1024	2048×2048	2048×2048
Pixel Size	13×13 μm	13.5×13.5 μm	13.5×13.5 μm
Chip Area	13.3×13.3 mm	27.6×27.6 mm	27.6×27.6 mm
Illumination	Back Illuminated	Back Illuminated	Back Illuminated
Deep Depletion	Yes	No	No
Bit Depth	16	16	16

Table 3.1: X-ray camera technical details.

The ID cameras both had 1:1 optical fibre face-plates with a scintillator held against the front surface. The most commonly used scintillator was a structured (columnar) caesium iodide (CsI) scintillator doped with thallium. Specifically this was a Hamamatsu J6677-01 HR [173], which is a 150 μm thick structured CsI(Tl) scintillator on a 3 mm fibre optic plate. Columnar scintillators are used because they give the high QE benefits of a thick scintillator while preserving good spatial resolution. CsI(Tl) is a good choice of scintillator in general because it is sensitive to very hard x-rays (see appendix 8.8), has a relatively high light output at 54 photons per keV of deposited energy and emits at 550 nm [174], which is in the region of highest QE for silicon CCDs.

3.5.3 Dark Field and Flat Field Corrections

Noise in images is a combination of read noise, dark noise and shot noise. Only the last of these is related to the x-ray source. Therefore it is imperative to minimise both read and dark noise to maximise image quality. Read noise is any noise introduced while the pixels are being read out by the camera electronics. It is typically minimised by choosing the slowest readout rate that is acceptable in the experiment. Dark noise comes from the thermal excitation of electron hole pairs and can be minimised by cooling the CCD. Read noise plus dark noise produces what is called a dark field (DF) image. A DF image taken with identical camera settings should be subtracted from every x-ray image to remove the bulk of the read and dark noise. Usually an average of multiple DF's was used. This should be a pixel-by-pixel subtraction because every CCD has a unique pattern of dark charge [175]. Knowing this the total number of dark counts is of little concern. It is the standard deviation of the mean dark counts per pixel over multiple images that should be minimised to find the optimum camera settings. For the Andor ID camera this was optimised for readout rate, CCD temperature and exposure time individually, holding the other two parameters constant. The optimum settings were found to be 1 MHz readout rate (surprisingly not 50 kHz), 25 ms exposure time and a temperature of either -25 °C or -30 °C [4]; there was no significant difference between the two. For the Princeton camera the standard deviation of dark noise counts in a single image was minimised at a temperature of ~ -25 °C [5].

Upon identical illumination by x-ray radiation not every camera pixel will have the same response due to non-uniformities in the scintillator, the optical fibres or even the pixels themselves. This degrades the image quality. This can be corrected with a flat-field (FF) image. The 'true' x-ray image I_t is related to the recorded x-ray image I_r by the equation

$$I_t = \frac{I_r - DF}{FF - DF} \tag{3.5}$$

where the division operates pixel-by-pixel. $(FF - DF)$ is normalised so that its mean pixel value is 1. This method should be applied to an image taken by any camera: it does not only apply to x-rays!

Practically speaking it is non-trivial to uniformly illuminate every pixel of an x-ray camera. Synthetic flat fields were created as outlined in figure 3.11. First the camera was exposed to the betatron beam for some number of shots: 25 in this case. Each of these

[4] For the Andor ID camera the readout rate scan was at -20 °C, 100 ms exposure and rates 0.05, 1, 3 and 5 MHz were trialled. For the exposure time scan the temperature was -20 °C, the readout rate was 1 MHz and exposure times 10, 25, 50, 75 and 100 ms were trialled. For the temperature scan the readout rate was 1 MHz, the exposure time was 100 ms and temperatures -10, -15, -20, -25 and -30 °C were trialled.

[5] For the Princeton Camera CCD temperatures between -30 °C and +20 °C were trialled in increments of 5 °C.

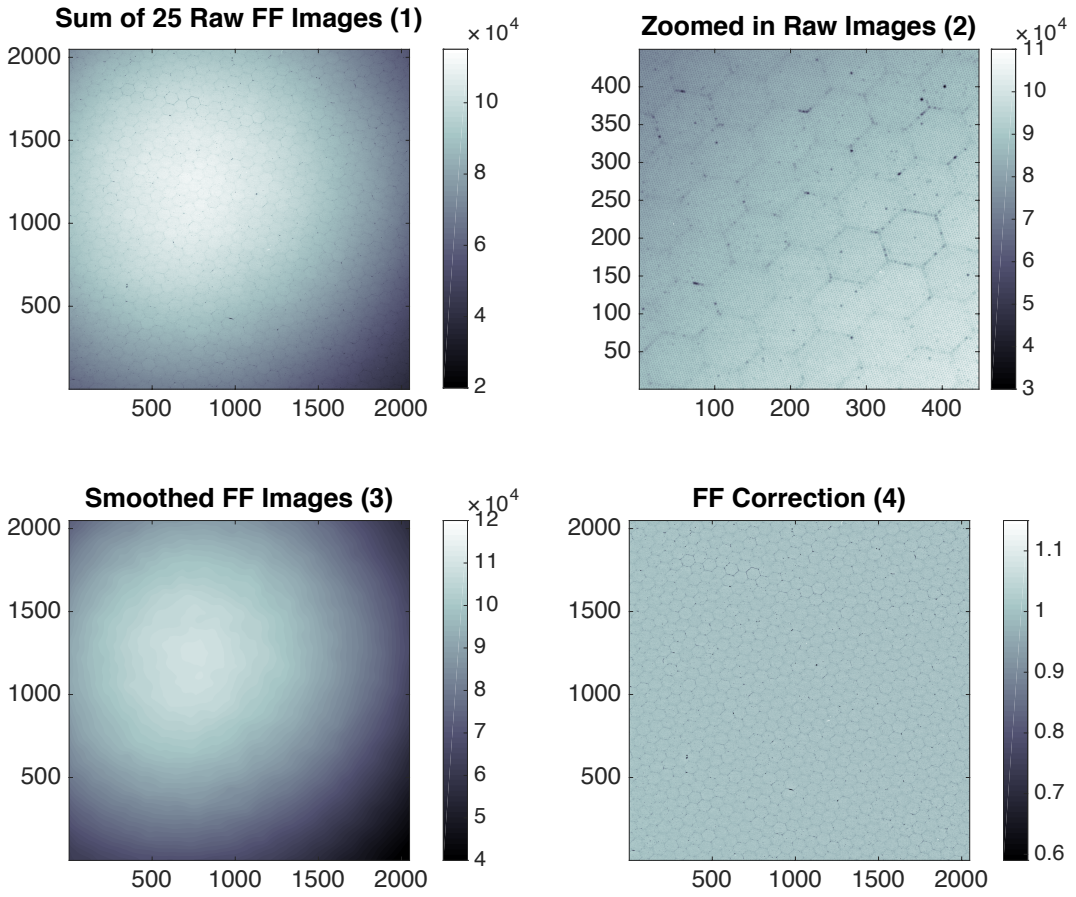


Figure 3.11: The method of flat-field correction. Synthetic flat-fields (4) were created by summing a number of betatron images (1) and dividing it by its spline (3).

raw FF images have the DF subtracted from them and then they are summed producing the image in the top left (1). Zooming in on part of this image in the top right (2) we see that there is structure on multiple spatial scales being introduced by the imaging system. This is exactly what we wish to correct with the FF. A cubic smoothing spline was fitted to (1) and is plotted in the bottom left (3). This was using the MATLAB function csaps with $p = 10^{-5}$. We see that in this fit there is no sign of the hexagons, which were the largest feature we wished to remove. (3) is then an approximation of the betatron beam spatial profile. Dividing (1) by (3) on a pixel-by-pixel basis gives the flat field correction FF in the bottom right (4), which has a mean value of 1. It is important to note that a FF must be done for every camera configuration, especially if there is a chance that the scintillator has moved.

3.5.4 X-ray Spectral Characterisation

The method of spectrally characterising the betatron x-ray beam was partly constrained by the total number of $photons/eV$ which was simply far too high for single photon counting. The spectrum has been characterised in other works with a crystal spectroscopy method [176], although the limited spectral range of the measurement meant that the full spectrum could not be characterised on a single shot. It is desirable to have broad range single shot diagnostics on high power laser experiments because the jitter in the laser parameters can be significant. A method based on measuring the x-ray transmission through an array of different filters similar to [79] was employed. The filter arrays that were used are detailed in appendix 8.9. An example x-ray image of the 64 filter array can be seen in the top left of figure 3.12.

The transmission as a function of photon energy of a filter i, $T_i'(E)$, is given by

$$T_i'(E) = exp(-\mu_i(E)d) \tag{3.6}$$

where μ_i is the mass attenuation coefficient of the material (interpolated from [177]) and d is the material thickness. This is just the familiar Beer-Lambert law. The x-rays transmitted through a filter were recorded on an x-ray camera. The estimated signal level on the camera image of filter i, Y_i, is given by the equation

$$Y_i = A \int_{E_{min}}^{E_{max}} E\ S(E)\ Q(E)\ T_i(E)\ dE \tag{3.7}$$

A is a constant of proportionality, $Q(E)$ is the quantum efficiency of the camera, $S(E)$ is the x-ray number spectrum dN/dE, and $T_i(E)$ is the transmission of the filter i and any other materials in the path between the x-ray source and the detector. The integration limits E_{min} and E_{max} reflect the difficulty of integrating this function numerically from 0 to ∞. Typically the values $E_{min} = 1$ keV and $E_{max} = 300$ keV were used. 1 keV is the minimum energy provided in the NIST data[6] [177] and a betatron spectrum with an E_c of a few 10's keV contains very few photons above 300 keV.

The spectrum $S(E)$ was assumed to be an on-axis synchrotron spectrum with a critical energy E_c that was to be determined. To reflect this we now write $S = S(E, E_c)$. To find the E_c that best fit the data the quantity Δ in equation 3.8 was minimised, where

$$\Delta = \sum_i (Y_{m,i} - Y_i)^2 \tag{3.8}$$

This is to say that the trial E_c with the smallest Δ parameter was taken to be the true

[6]Transmission at energies <1 keV can be calculated using the XOP code [178] although none of these x-rays would have made it through the laser beam dump so this was not necessary here.

E_c.

$Y_{m,i}$ is proportional to the measured counts through filter i. To make this a one parameter fit, i.e. a fit of E_c only, the data and the calculated Y's were normalised so that the mean transmission through all of the filters was unity.

The workings of the analysis code are illustrated in figure 3.12. Top left (1) is an x-ray image of the 64 filter array which has been DF subtracted and FF corrected. The user then defines which filters should be included in the processing. In this example the chosen filter regions are highlighted by the green rectangles in (2). It is clear from (1) and (2) that the filter pack is not being uniformly illuminated by the betatron beam. To correct for this effect it is necessary to estimate what the x-ray intensity profile is. The red rectangles around the filters in (2) highlight the regions that are used for this. In previous works such as [79] the mean x-ray counts in the background regions around a filter was computed and the mean counts transmitted through the filter was divided by this background average. In this work a slightly more sophisticated approach is used which can deal with variations in x-ray intensity across a single filter. The mean counts in each of the background rectangles is computed and placed on a grid at the coordinates of the centre of that rectangle. A smooth surface is fitted to these points using the MATLAB griddata function[7] which is plotted in (3), where the colour scale has been exaggerated slightly compared to the other images. Because the surface is fitted to values which are a mean of many pixel values this method is robust even for noisy images. (3) is then normalised so that the mean pixel value is one and then (1) is divided by this, pixel by pixel, to produce (4) where the background is no longer spatially varying. Of course this only applies in regions close to the red rectangles: this can be seen in the top left corner of (4). For any further calculations such as the number of photons in the beam, or brightness, points far away from the red rectangles should be ignored. A region of 'good' pixel values is defined which for this example is shown as the blue rectangle in (4). As a method of background flattening this appears to work well. It gives comparable E_c values to the previously used method (typically within 1 keV) and is able to estimate E_c at lower signal levels.

Close inspection of (1) reveals a number of hard hits in the x-ray image. While some of these may come from the source, some may also come from bremsstrahlung x-rays from the electron beam colliding with materials in the target area. These are dealt with using a 2 mm lead sheet stuck to the bottom of the filter array. The mean counts in this region (specifically inside the yellow rectangle in (2)) are subtracted from the whole image. This assumes that only bremsstrahlung x-rays, and no betatron x-rays, are transmitted through the lead region. This does make a considerable difference to the measured critical energy:

[7]The method used is 'v4' which is a biharmonic spline interpolation.

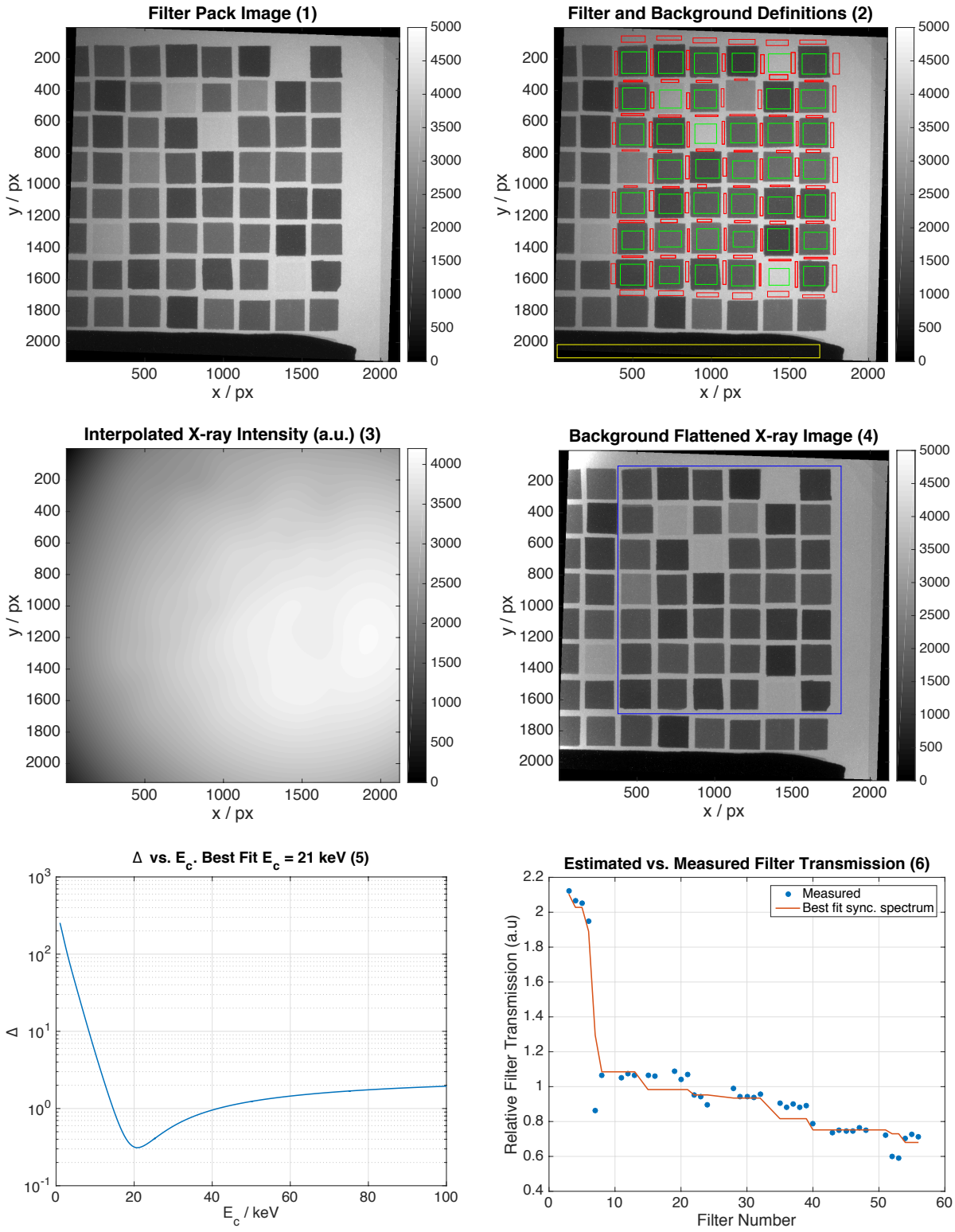


Figure 3.12: Example of the x-ray critical energy analysis method.

if no bremsstrahlung subtraction is done the measured E_c for this shot would be 25.5 keV, with the subtraction it would be 21.0 keV. A downside of this method is that it can be argued that it introduces an arbitrary high-energy cut-off in the betatron spectrum. We now examine this claim. Assuming that the spectrum is an on-axis synchrotron spectrum with $E_c = 25.5$ keV, then in the energy range $1 - 500$ keV an estimated fraction of 1.1×10^{-4} of the total beam energy is expected to be transmitted through the lead and be absorbed by the scintillator. Comparing the measured x-ray counts inside the lead region to those outside then 6.5×10^{-2} of the energy appears to be transmitted. It is clear that almost all of this is from a source of radiation that is not accounted for in the model of betatron radiation, with bremsstrahlung being a likely candidate. This provides good evidence that the subtraction of the background from this region is important to correctly determine E_c.

As it is such an involved process to estimate E_c it is not trivial to put an error on the result. The most obvious source of systematic error is in the thickness of the foils on the filter array. The tolerance on the thickness of each of the filters, as stated by the manufacturer, was $\pm 15\%$ [179]. To estimate the magnitude of this effect on the critical energy retrieval the transmission through the filters in the array (the 64 filter array in this example) was calculated for a 20 keV critical energy spectrum. The thickness of each filter material was then varied at random between -15 and +15% and then the modified critical energy was measured from this. This process was repeated 1000 times and the standard deviation was 0.7 keV. Repeating this process for 'real' E_c's from 6 to 50 keV in 2 keV steps produced the graph in figure 3.13. No E_c value can be confidently reported with an error smaller than the one in this graph. This represents a fractional error that increases from $\sim 3\%$ to $\sim 6\%$ between 5 and 50 keV.

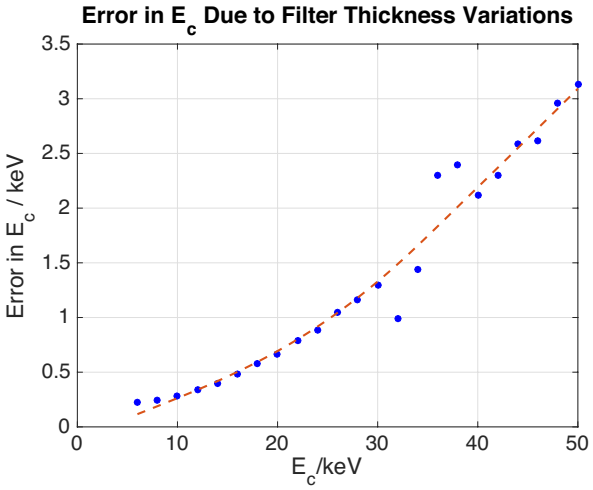


Figure 3.13: Errors induced by filter thickness variations.

The worst case scenario is that there was a systematic offset of 15% in the thickness of each of the filters. The effect of this was simulated numerically by passing on-axis synchrotron spectra with critical energies between 6 and 50 keV through two modified versions of the 64 filter array: one where all of the filters were 15% thicker and one where all of the filters were 15% thinner than the stated value. The critical energy was then 'measured' using the standard routine, assuming the filter thickness were as stated by the manufacturer. The difference between the measured and real critical energies is plotted as a function of real critical energy in figure 3.14. The graph shows, as expected, that if

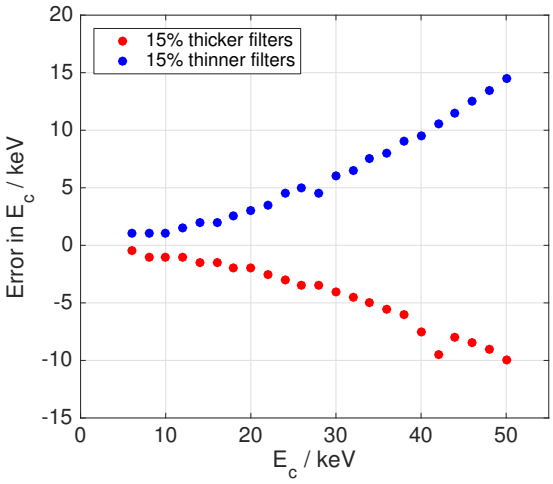


Figure 3.14: Error in measured critical energy induced by a systematic filter thickness offset.

the filters were 15% thinner than stated then the critical energy would have been overestimated, and conversely if the filters were 15% thicker then the critical energy would have been underestimated. Around 20 keV, a common value of critical energy found in the experiments presented in this thesis, this analysis gives an error on this value of $(-2, +3)$ keV. There is no reason to expect that this is the case, but it is reassuring to know that in the worst case the systematic error was not larger than 10-15% on most measurements. Nevertheless, in future this situation could be improved by determing the thickness by measuring the mass of each filter and measuring its transverse dimensions using a calibrated microscope, which would be accurate to the few micron level over 2.5 mm. High precision scales can measure mass to micro-gram precision [180]. Most of the filters on the array had a mass on the order of milligrams, therefore the mean thickness could be estimated via this method to a accuracy of significantly better than 1%.

To estimate the random error we start with the definition of Δ from equation 3.8: $\Delta = \sum_i (Y_{m,i} - Y_i)^2 = \sum_i {\delta_i}^2 = N \left\langle {\delta_i}^2 \right\rangle = \left\langle {\delta_i'}^2 \right\rangle$ where N is the number of filters and the angled brackets denote the mean. For each trial critical energy one could plot a graph

of ${\delta_i}'^2$ vs. filter number i to see a distribution with some mean and variance because even the best fit doesn't perfectly match the observed filter transmission for every filter. This distribution has a mean value $\langle {\delta_i}'^2 \rangle$ with some error $\epsilon = \sigma_{{\delta_i}'^2}/\sqrt{N}$, where $\sigma_{{\delta_i}'^2}$ is the standard deviation of the distribution. This is the error on Δ for a single trial critical energy. Plotting the errors on top of the Δ vs. E_c curve produces figure 3.15. The error on the critical energy (green line) is found at the positions where the lower red curve ($\Delta = \langle {\delta_i}'^2 \rangle - \sigma_{{\delta_i}'^2}$) is equal to the minimum value of Δ plus the error on this value. If the red curves were plotted as error bars, outside these bounds the error bars would not overlap with the error bar at the minimum. For the shot analysed for this figure the critical energy was $20.5^{+1.3}_{-0.9}$ keV. Combining this error in quadrature with the error due to filter thickness variations, which is 0.7 keV at this critical energy, the critical energy with the total errors was $20.5^{+1.5}_{-1.1}$ keV.

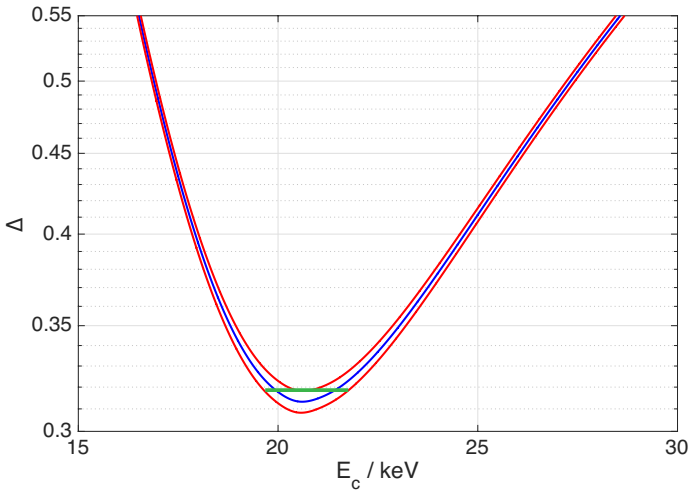


Figure 3.15: Method for determining the random error in the critical energy. The blue line is Δ and the red lines show the uncertainty on this due to discrepancies between the estimated and observed filter transmission. The green line shows the range of E_c values that fall within the error bounds.

3.5.5 Conversion of Camera Counts to Deposited X-ray Energy and Number of Photons

Scintillators emit a number of scintillation photons that is directly proportional to the energy deposited in the scintillator. The constant of proportionality is known for many scintillation materials but what is not known in our set-up is how many of these scintillation photons are detected by the CCD. Some will be lost because they do not travel in that direction, others will be lost in the optical fibre bundles and more because of the QE of the CCD. Furthermore, what is read out in the image is some number of counts that is proportional to the number of detected scintillation photons. As a result of all of

these factors it is necessary to calibrate the camera with a well characterised source so that the number of counts in the image can be converted to x-ray energy deposited in the scintillator. The number of photons N_p between energies E_{min} and E_{max} is related to the number of camera counts C by the equation

$$C = \alpha N_p \int_{E_{min}}^{E_{max}} E\ S(E, E_{c,m})\ T(E)\ Q(E)\ dE \tag{3.9}$$

α is the x-ray counts per keV deposited in the scintillator. All x-ray energies are measured in keV. $E_{c,m}$ is the measured critical energy from the filter array. The spectrum S has been normalised such that $\int_{E_{min}}^{E_{max}} S(E, E_{c,m})dE = 1$. T is the transmission of any materials between the source and the detector and Q is the quantum efficiency of the detector. C was found by summing over all of the pixels in part (3) of figure 3.12 bounded by the blue rectangle shown in part (4), which denotes the area over which the intensity interpolation is considered to be good. The total number of photons in the x-ray beam can be found by comparing the number of photons going in to this area with the beam profile (section 3.5.1) provided that the peak of the profile can be found.

The Andor ID camera and the Princeton camera were calibrated using a radioactive iron-55 source of activity $A_{Fe} = 23.6$ MBq. This is a suitable source because it has a long half life of 2.737 years so the activity of the source can be assumed constant over the length of the experiment and it emits moderate energy x-rays mostly at 5.9 keV. From [181] [182] one can calculate that a moderate energy x-ray is emitted in 27.25% of decays with the energies and relative probabilities given in table 3.2 [8]. The rest of the decays happen via an Auger process. The source activity implies that 6.49×10^6 x-rays are emitted per second in to 4π steradians. We will return to the issue of geometry shortly. The average energy absorbed in the scintillator per incident x-ray photon $\langle E_{dep} \rangle$ is calculated using

$$\langle E_{dep} \rangle = \frac{\sum_i E_i\ p_i\ T(E_i)\ Q(E_i)}{\sum_i p_i} \tag{3.10}$$

E_i is the photon energy, p_i is the probability of emission, $Q(E_i)$ is the quantum efficiency of the camera from figure 8.4 and $T(E_i)$ is the fractional transmission of photons of energy E_i through all materials between the source and the scintillator including the air and the 40 μm inorganic parylene layer that protects the scintillator [183]. For the Andor indirect detection camera $\langle E_{dep} \rangle = 5.56$ keV, and for the Princeton indirect detection camera $\langle E_{dep} \rangle = 5.01$ keV.

[8] X-rays at 0.64 keV have been omitted as they would have been absorbed before the scintillating layer and are emitted relatively infrequently. This is why $\sum_i p_i$ is slightly less than 1.

Photon Energy E_i/keV	Relative Probability
5.888	0.30
5.899	0.59
6.49	0.104

Table 3.2: Photon emission from Fe-55 decay from [182].

Concerning the geometry of the calibration setup. The source was a 12.5 mm diameter disk in a holder with an 11 mm circular aperture. This was placed close to the scintillator at the front of the camera. It was difficult to measure this distance accurately because of radiological safety issues. Near to an extended source the dose delivered to the scintillator does not fall off as $1/r^2$. For a circular source the fall off is instead described in [184]. The geometry used in the calculation is shown in figure 3.16. The dose D delivered to a

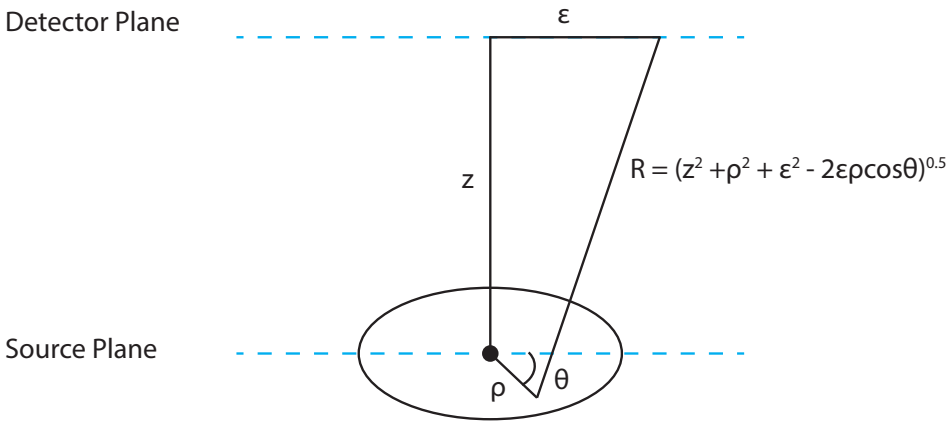


Figure 3.16: Geometry of the disk source problem.

point of distance ϵ from the centre of the detector is described by the equation

$$D(z,\epsilon) = \int_0^a \int_0^{2\pi} G(R)\ S(\rho)\ \rho\ d\rho\ d\theta \tag{3.11}$$

ρ and θ are the radial and azimuthal coordinates on the disk respectively and z is the distance from the plane of the disk to the plane of the detector. From figure 3.16 $R = [z^2 + \rho^2 + \epsilon^2 - 2\epsilon\rho\cos\theta]^{\frac{1}{2}}$. $S(\rho)$ is the source strength per unit area which is assumed to be constant here. The detector response $G(R) = \cos\psi/(4\pi R^2)$ where ψ is the angle between the detector surface and R, therefore $\cos\psi = z/R$. Because the source is close to the detector it cannot be assumed that it is a point source so a form factor for the source must be taken in to account. This is the integral over the surface of the source in equation 3.11. Another consequence of the source being close to the detector is that rays from the source subtend a significant angle ψ to the detector which is the reason for the

$\cos\psi$ term. Far from the source $\cos\psi \to 1$. The validity of equation 3.11 can be checked by testing what happens in the limit of small and large displacement z from the source. Far from the source ($z \gg a$) the source should look like a point source. To simplify the workings we observe the source with a small detector placed on axis such that $\epsilon = 0$. For large z, $R \approx z$ and $cos\psi = z/R \approx 1$, so the equation simplifies to

$$D(R,0) = \frac{1}{4\pi R^2} S_0 \pi a^2 \tag{3.12}$$

where $S_0\pi a^2$ is the total activity of the source (assuming a constant source activity) and z has been explicitly replaced by R. This is exactly what would be expected from a point source. It can be shown [185] that as $z \to 0$ equation 3.11 tends to $D = \frac{1}{2}S(\rho)$ as expected from elementary considerations.

Equation 3.11 was numerically integrated for a 27.6 mm side length square detector (see table 3.1) for trial z values in the range of 1 to 20 mm in 1 mm increments. This was a little computationally expensive so the mock detector had only 200×200 pixels. Examples of the calculated intensity distributions at 5, 10 and 15 mm from the source are shown in figure 3.17.

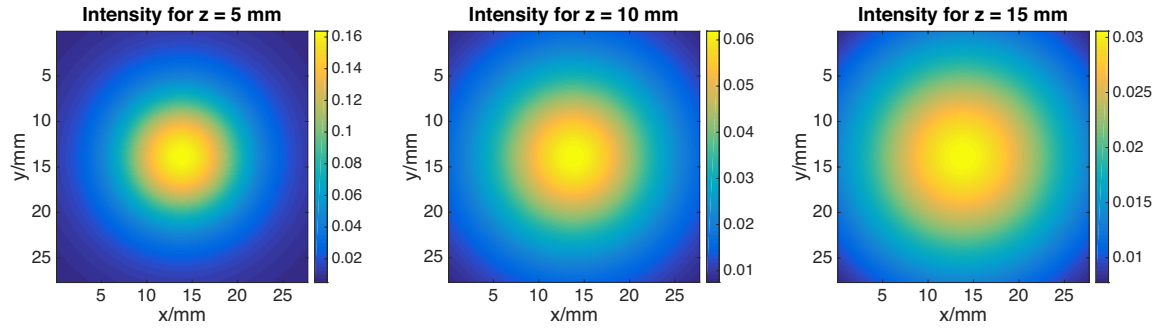


Figure 3.17: Intensity distributions at different distances from a disk source.

An experimental image taken with the Andor ID camera along with the horizontal and vertical lineouts through its centre are shown in figure 3.18. A cubic smoothing spline s was fitted to these lineouts and the FWHM of the intensity pattern was found from this. The small difference in the widths is attributed to a slight misalignment of the source with respect to the detector. The average of these values was taken as the real width. This width was compared to the calculated FWHM widths from the range of trial z's. Minimising the difference between the two revealed that for the Andor ID camera $z = 7.6$ mm and for the Princeton camera $z = 3.0$ mm. The sub-mm resolution was possible by interpolating the widths of the trial patterns on to a finer spatial scale.

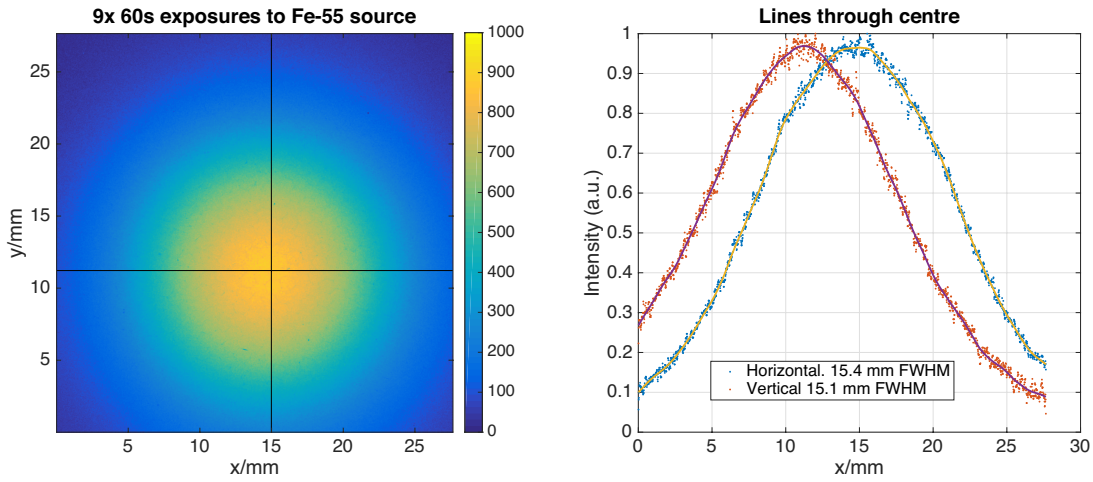


Figure 3.18: Data image from the Andor ID camera calibration with the Fe-55 source. 9 exposures of 60 s duration were taken. The black lines go through the centre of the intensity pattern. The lineouts were taken along these lines.

The total energy deposited in to the scintillator E_s is

$$E_s = B \int_{\epsilon_{x,min}}^{\epsilon_{x,max}} \int_{\epsilon_{y,min}}^{\epsilon_{y,max}} D(z, \epsilon_x, \epsilon_y)\, d\epsilon_x\, d\epsilon_y \tag{3.13}$$

where ϵ_x, ϵ_y are the (cartesian) coordinates on the detector. B, defined below, is the energy emitted by the source per unit area over the full camera acquisition time τ_{aq}.

$$B = \frac{0.2725 \times A_{Fe} \langle E_{dep} \rangle \tau_{aq}}{\pi a^2} \tag{3.14}$$

The factor of 0.2725 is the probability of x-ray emission during a decay. The integration in equation 3.13 was done numerically on an image constructed from equation 3.16 with the measured z for each camera. Again this was done on a reduced 200×200 grid. The total deposited energy from this calculation was compared to the total number of counts in the image and the results are tabulated in 3.3. The final result is given in units of x-ray camera counts per keV of deposited x-ray energy.

Camera Name	Gain	$\langle E_{dep} \rangle$/keV	τ_{aq}	Counts/keV
Andor ID	1×	5.56	9 × 60 s	0.24
Princeton	Low	5.01	300 s	0.056
Princeton	Medium	5.01	300 s	0.11
Princeton	High	5.01	300 s	0.84

Table 3.3: X-ray camera calibration results. $\langle E_{dep} \rangle$, the energy deposited per photon emitted, differs between the two cameras because for the Andor ID camera the x-rays travelled through 7.6 mm of air whereas for the Princeton Camera x-rays travelled through 2.75 mm of air and 0.25 mm of beryllium.

3.5.6 X-ray Imaging Resolution and Source Size

The simplest way to characterise the resolution of an imaging system is to use a resolution target which consists of a number of bars of different widths and spacings. The resolution targets used in the experiments can be seen in appendix 8.10. For explanatory purposes we will first deal with a mock up of a resolution target as can be seen at the top left of figure 3.19. For a perfect imaging system, as the lineout on the top right of this figure shows, the contrast made by the bars $C = (I_{max} - I_{min})/(I_{max} + I_{min}) = 1$ independent of the bar spacing. This is the equivalent to saying that the contrast is 1 for all spatial frequencies. Plotting contrast against spatial frequency (usually given in units of line pairs/mm) gives the Modulation Transfer Function (MTF).

In the bottom left of figure 3.19 the mocked up resolution target has been convolved with a gaussian Point Spread Function (PSF) with a FWHM of 17 pixels. In conventional optics the PSF is the response of an imaging system to a point source. Without x-ray optics, we are not strictly speaking imaging (we are taking point-projection images), so the PSF is best defined as the response of the system to a point object. It includes the effects of the detector and the finite source size. The effect of the PSF on the MTF can be inferred from the lineout in the bottom right of the figure. We now see the 50 pixel features with a contrast of 97.5% and the 25 pixel features with a contrast of 58%. If we were to put some real world units on this such as 100 pixels = 1 mm we would say that the MTF is 58% at 2 lp/mm. Therefore imaging resolution targets is a direct measurement of the MTF of a system. The resolution targets were imaged at high magnification so that the effect of the finite source size on the MTF was closer in magnitude to that of the scintillator plus camera. The MTF of the whole system is the product of the MTF of each of its components.

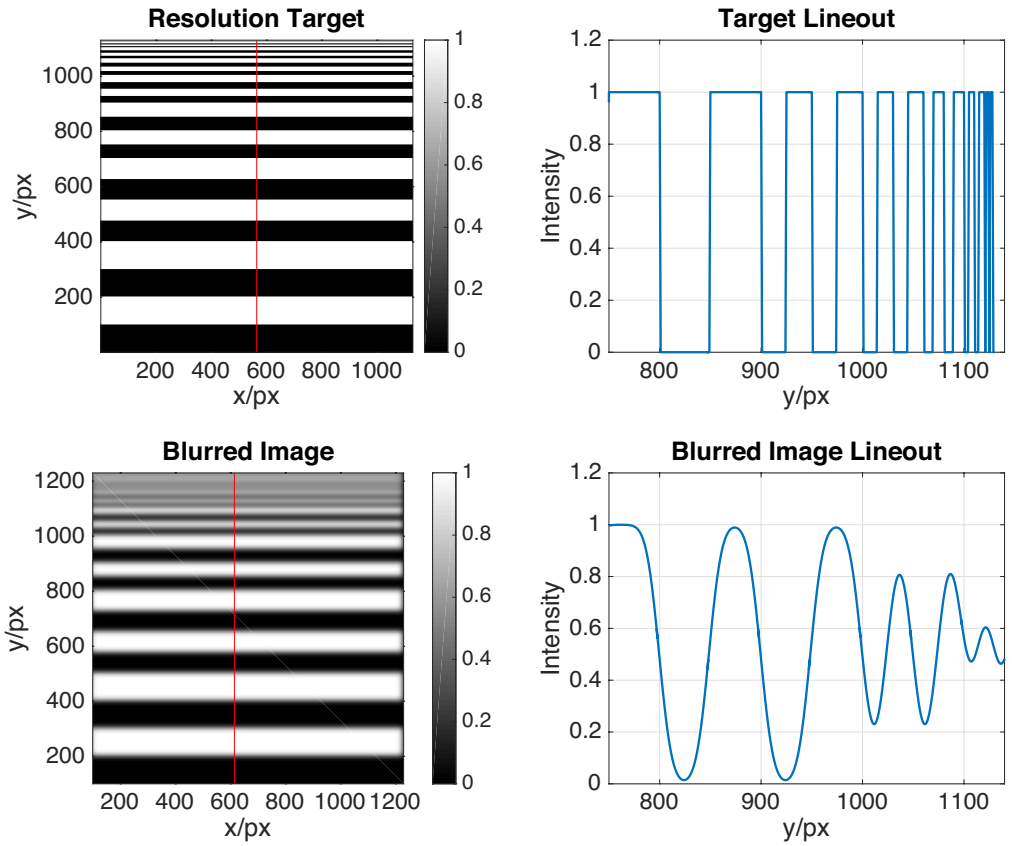


Figure 3.19: Example of the blurring of a resolution target due to the PSF of an imaging system. Top left is a mocked up resolution target with bar size and spacing of 100, 75, 50, 25, 15, 10, 5 and 2 pixels. An intensity of 1 is perfect transmission and 0 perfect attenuation. A lineout along the red line is in the top right where the x axis has been cropped so that the largest features are 50 pixel bars. This was convolved with a gaussian PSF with a FWHM of 16.7 pixels to produce the image in the bottom left. The equivalent lineout is shown in the bottom right.

A different method of measuring the MTF is to image a hard edge such as the edge of a cleaved crystal as in the top left of figure 3.20. A horizontal lineout of this gives the Edge Spread Function (ESF). Due to the noisy data the image was summed over several hundred rows to produce the ESF. Differentiating the ESF gives the Line Spread Function (LSF) which is the system response an infinitesimally thin line. Differentiating noisy data gives a very noisy result so this data was smoothed and had a gaussian fitted to it as shown in the bottom left of figure 3.20. The LSF on this shot had a FWHM width of 102 μm taken at the camera plane which is 7.6 pixels. The Fourier transform of the LSF is the MTF plotted in the bottom right of the figure. Taking the MTF calculated from the gaussian fit as the real MTF then it is clear that it is almost impossible to resolve features smaller than 50 μm at the detector plane. This is why a reasonably large

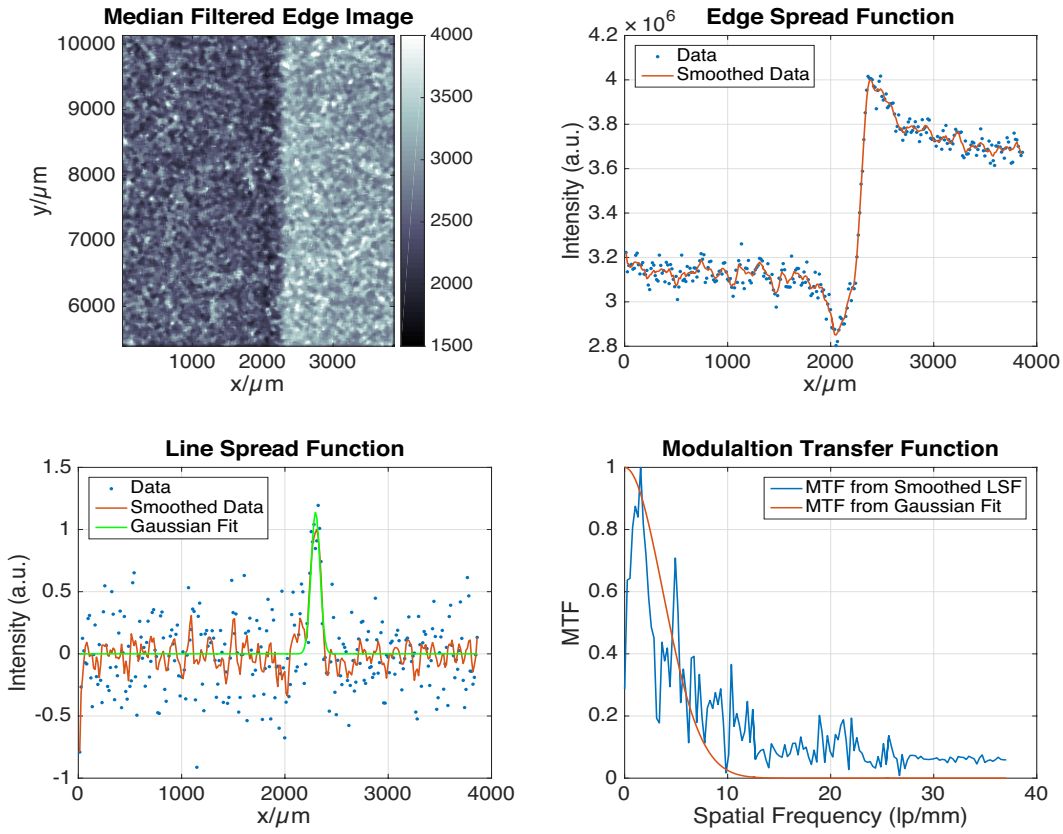


Figure 3.20: Top left: betatron x-ray image of the edge of a cleaved silicon crystal. Top right: the ESF which is the summation of the hard edge over many rows. The derivative of the ESF is the LSF shown in the bottom left. Taking the Fourier transform of the LSF yields the MTF plotted in the bottom right.

magnification was usually used for imaging. To improve resolution a thinner scintillator could be used, however this reduces the amount of light collected and hence the signal to noise ratio. Therefore one route to improving the resolution of hard betatron x-ray imaging is to significantly increase the number of photons to enable a switch to a thinner scintillator.

3.5.7 Measuring Brightness

Brightness B is calculated using the equation

$$B = \frac{N_{p,0.1}}{\tau_x A_s \theta_x \theta_y} \tag{3.15}$$

$N_{p,0.1}$ is the number of photons in a window of width $10^{-3}E'$ around some energy E'. For peak brightness the value of E that maximised the brightness curve was chosen to be E'. The amplitude of the on-axis synchrotron spectrum at $E = E_c$ is 0.987 of the maximum

amplitude. It can be shown that the peak of the intensity spectrum $dI/dE \propto EdN/dE$ is at approximately the same energy (E_p) as the peak of the brightness curve by writing

$$B = C\int_{E_p-\Delta E}^{E_p+\Delta E}\frac{dN}{dE}dE = N(E_p+\Delta E) - N(E_p-\Delta E) \approx C\Delta E\frac{dN}{dE} \propto E\frac{dN}{dE} \quad (3.16)$$

$C = 1/(\tau_x A_s \theta_x \theta_y)$ and when a 0.1% bandwidth is specified $\Delta E = 0.5 \times 10^{-3} E_p$, meaning that the approximation to the derivative is very good. The total number of photons in the beam is calculated as described in section 3.5.5. When peak brightness is calculated the highest pixel value from the beam profile in part (3) of figure 3.12 is taken. The pixel size and distance from the source gives θ_x and θ_y. A photon number spectrum is constructed using the on-axis synchrotron spectrum, the measured E_c from the filter array and is normalised so that the integral over all photon energies gives the number of photons hitting the brightest pixel. $N_{p,0.1}$ is found by integrating this spectrum over the 0.1% energy bin width around E'. The assumption $\tau_x = 30$ fs is made. A_s is the source area. The main sources of error are the uncertainty in the spectral shape due to the error on E_c and the source area. The errors in $\theta_{x,y}$ come from the uncertainty in the distance from the source to the camera which is below 1%. The error in the camera calibration, which gives the number of photons from the number of camera counts, is assumed to be small because a large number of photons from the Fe-55 source were detected.

3.5.8 Absorption and Phase Contrast X-ray Imaging

The refractive index η in a medium can generally be written as $\eta = 1-\delta+i\beta$. δ is the real part of the refractive index and is associated with effects such as refraction. The imaginary part $i\beta$ results in attenuation of the electric field in the medium and an exponential decrease in its amplitude with distance in to the material. Most x-ray radiography images, such as familiar medical x-rays showing bone, are based on this attenuation. Contrast in the image is provided by some parts of the object, e.g. bones in an arm, having a different level of absorption (different β) to the surrounding material. However it is also possible to use gradients in δ to produce intensity variations in an x-ray beam, which provides the image contrast. This is called phase contrast imaging, something which will now be explored in more depth.

Consider an initially spatially coherent x-ray beam, i.e. one with flat wavefronts, travelling in the z direction. We now imagine a material with a spatially varying $\delta(x)$ that, for simplicity, is uniform in the y direction. Ignoring absorption effects (β can be orders of magnitude smaller than δ for hard x-rays) the electric field of the x-ray beam can be written as

$$E(x,z) = E_0 \exp(ikz + i\phi(x)) \quad (3.17)$$

where E_0 is the electric field amplitude, k is the initial wavenumber and $\phi(x)$ is the spatially varying phase picked up by the wavefronts as they passed through the material due to variations in δ integrated along the path of the x-rays. The wavevector in the direction of propagation is then [186]

$$\boldsymbol{k}'(x) \approx \frac{\partial \phi(x)}{\partial x}\hat{\boldsymbol{x}} + k\hat{\boldsymbol{z}} \tag{3.18}$$

where $\hat{\boldsymbol{x}}$ and $\hat{\boldsymbol{z}}$ are unit vectors in the x and z directions. If the gradient in the phase change is small then the angle of light propagation relative to the initial direction is given by

$$\Delta\theta \approx \frac{1}{k}\frac{\partial \phi(x)}{\partial x} \tag{3.19}$$

This has shown that gradients in the refractive index, which produce gradients in the phase picked up by a wavefront passing through them, refracts the beam by a small angle. In early phase contrast imaging experiments [186] [187] the x-ray beam, encoded with the phase information from the object, was reflected from an analyser crystal on to a detector. The crystal was rotated slightly from the Bragg angle for normally incident light so that only refracted light was reflected on to the detector (note that this required monochromatic x-rays). This ensured that an image of only the refractive index gradients in the object was taken.

It is, however, not necessary to have an analyser crystal to see this effect [188]. If the light is propagated some distance after the object the refraction of light produces features on the detector. For example, in a region of a sample with a strong gradient in refractive index, such as the edge of a plastic wire, light is refracted away from this part of the image leaving a dark feature. The angle that light is refracted at is again given by equation 3.19. This is called propagation based phase contrast imaging. It has the advantage that it is experimentally much simpler and can be performed with broadband light sources [189]. However, unlike the case of monochromatic light and an analyser crystal, there is no way to discard the rest of the image meaning that the image formed on the detector is a mixture of absorption and phase contrast. This is not an issue when the absorption is negligible however.

While betatron radiation is not initially spatially coherent, it can become partially spatially coherent after propagation over some distance u. This is due to the van Cittert-Zernicke theorem [190] which states that, for uncorrelated emitters with a gaussian intensity distribution, the transverse coherence length of light L_c is given by

$$L_c = \frac{\lambda u}{2\pi w_{x,y}} \tag{3.20}$$

where λ is the wavelength and $w_{x,y}$ is the source size in the x or y direction. This, combined with the hard x-ray energies available, has encouraged the use of betatron radiation from laser wakefield accelerators for propagation based phase contrast imaging [91] [92] [93] because of the micron scale source size.

Chapter 4

Electron Acceleration from Clustered Methane

4.1 Motivation

LWFA experiments relying on self-injection have enjoyed many successes such as the production of quasi-monoenergetic electron beams [64] [65] [66], the acceleration of electrons to multiple GeV [59] [60] [61] and they are also known to be a source of bright betatron x-rays [79]. However to drive wakefields to the amplitudes required for self trapping, many current laser systems rely on the nonlinear processes of self-focussing and self-compression of the driving laser pulse. Self-trapping itself is a strongly nonlinear process. This means that these experiments tend to have issues with shot-to-shot stability. It is not that all of these processes are intrinsically unstable or chaotic, but it does mean that shot-to-shot fluctuations in the laser parameters can drive significant fluctuations in the electron beam parameters. Reports of significant shot-to-shot variations in laser parameters are ubiquitous in the literature on high intensity laser-matter experiments. These fluctuations are multifaceted and have several sources: there are beam pointing fluctuations due to mechanical vibrations and thermal effects in optical media [191], the phase of the beam can be subject to random noise [192] which will ultimately affect the quality of the focal spot, there can be variations in the spectrum and therefore temporal duration of the pulse [193] and finally there can be fluctuations in the energy of the pulse, especially in flash lamp pumped systems [194] (the pump lasers for the Astra and Gemini systems are pumped by flash lamps) which have poor shot-to-shot repeatability. Pulse energy variations can, however, be partially mitigated by saturating the gain media.

These fluctuations have encouraged many groups to study controlled injection mechanisms such as density down-ramp injection [195] [196] [72] or colliding pulse injection [73]. However the simplest form of controlled injection is ionisation injection [197] [69]

[70]. This is where the plasma is doped with a small percentage of high Z gas such as nitrogen or CO_2. The inner shell electrons of the dopant gas are only ionised close to the peak of the wakefield driver pulse and are therefore 'born' inside the wakefield bubble and trapped. It has been suggested that ionisation injection produces higher charge electron beams than self-injection [69] [198]. The trapping threshold has been shown to be lower than it is for self-injection at $a_0 \sim 1.7$ [70]. More exotic schemes based on localising this injection have been proposed to reduce the energy spread and/ or emittance of these beams such as two-pulse ionisation injection [199], similar to the Trojan Horse scheme for beam driven wakefields [200], or two-colour ionisation injection [201]. Other groups have experimented with confining the doped gas to a fraction of the accelerator to produce quasi-monoenergetic electrons beams [202] [203]. Additionally it has been shown that this can be achieved by using a large, mismatched laser focal spot [204] [205]. As the pulse is mismatched, and has a power greater than the critical power, it self-focusses strongly in the plasma as well as compressing. Before the pulse has evolved significantly, electrons from the dopant gas are ionised close to the centre of the pulse, which is towards the centre of the wake, meaning that the difference in wake potential between the position of this electron and the potential minimum in the wake (located at the back of the bubble) is large enough for the electron to become trapped. After self-focussing and self-compression have occurred, the front of the laser pulse is intense enough to ionise electrons from the dopant gas. However since this now occurs very close to the front of the wakefield, the potential difference between this position and the minimum is significantly reduced and trapping no longer occurs. Therefore trapping has been truncated as a result of pulse evolution, yielding a low energy spread electron beam. This is similar to the result found in [206].

As discussed in section 3.3.3 clusters can be formed when a high k (a gas dependent constant related to polarisability) gas expands in a supersonic nozzle. Such nozzles are routinely used in wakefield acceleration experiments but using gases with low k values that do not cluster easily, such as hydrogen, helium or doped helium. Clusters are collections of solid density material which expand when heated by the laser. When their density falls to the critical density the imaginary part of their refractive index increases and laser light is efficiently absorbed, heating the material significantly. For this reason laser-cluster interactions have been studied in their own right as a source of energetic electrons and ions [207], with ion kinetic energies up to 20 MeV per nucleon [208], and as a source of hard x-rays [209] [210]. Cluster media have also been shown to self-focus laser pulses [211] allowing guiding over approximately 40 Rayleigh lengths with a coupling efficiency of 50% [212].

Of particular interest here is the work on LWFA from clustered media driven by a sin-

gle relativistic laser pulse. A 4 TW laser interacting with argon clusters showed a factor of 3 improvement in beam pointing stability and divergence compared to a helium monomer target, although the maximum energy was lower in the argon case: (8.5 ± 0.7) MeV compared to (24.8 ± 3.6) MeV [213]. This paper does not mention clusters although their presence seems likely for a supersonic nozzle with 4 bar of backing pressure. Moving to an 18 TW system wakefield acceleration up to 58 MeV was reported by Fukuda et. al. [214] from a clustered argon medium. This was using an $f/3.5$ focussing geometry and the plasma electron number density of 9.1×10^{19} cm^{-3}. Interestingly when a prepulse with intensity greater than 10^{16} W/cm^2 was used to break up the clusters before the arrival of the main pulse no electron acceleration was observed, which suggests that the clusters play an important role in electron injection in to the wakefield. It should be noted that electron acceleration up to 600 MeV with a total beam charge in excess of 3 nC has been reported from a 100 fs, 10 TW laser pulse focussed with an $f/3$ optic on to a clustered argon target, with an average electron number density of 5.5×10^{19} cm^{-3} [215]. However it seems likely that the electron beam charge and energy figures are exaggerated as the laser to electron beam energy conversion efficiency would be 10's of per-cent, which would be by far the highest efficiency ever reported for a LWFA. Additionally this electron energy is a factor of approximately 25 higher than the Lu scaling [119], assuming the a_0 in the plasma is the same as the vacuum a_0 from this publication.

The field of LWFA from clustered media has yielded a small number of positive results. However this has not been in a geometry considered optimal for most LWFA experiments. The high electron number densities and short focal lengths limit, unnecessarily, the maximum electron energy. By moving to a larger F-number focussing optic, and hence increasing the spot size, the laser will be closer to the matched spot size at lower plasma densities, which can potentially provide a large increase in maximum electron energy through the inverse scaling of energy gain with plasma density n_e. This is explored in [216] who find that electron bunches with energy of ~ 80 MeV can be produced with a 15.8% energy spread from a low density (5×10^{18} cm^{-3}) jet with a $17 - 50$ TW laser pulse. The low energy spread is attributed in this publication to localised ionisation injection from a mismatched laser spot.

In this chapter LWFA in a clustered gas, methane in this case, will be studied in a long focal length geometry. This will be compared to self-injection (in pure helium gas) and ionisation injection (in helium doped with 5% CO_2) in the same experimental set-up for the first time. This will elucidate unique aspects of LWFA in clustered media.

4.2 Experimental Set-up

Figure 4.1 is a diagram of the set-up. The laser energy was measured before the compressor and was found to be (0.62 ± 0.03) J. Taking in to account the 62.5% compressor

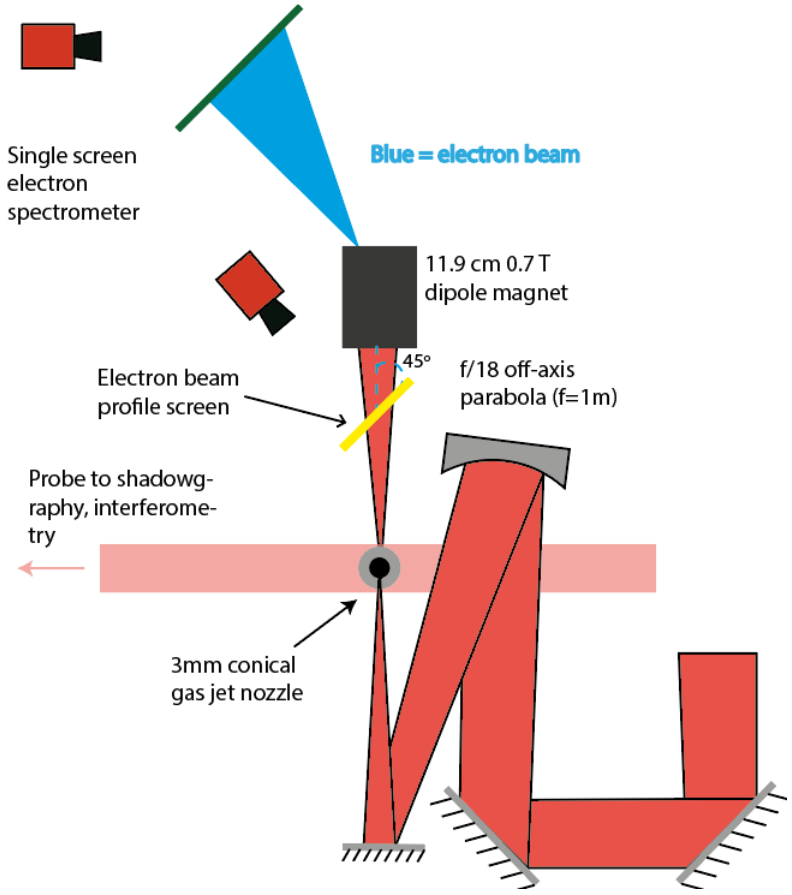


Figure 4.1: Diagram of the experimental set-up of the clustered methane experiment.

efficiency the energy on target was (0.39 ± 0.02) J. The error quoted is the standard deviation from 20 shots. After the compressor the laser pulse had a FWHM duration of approximately 37 fs, meaning the laser power was close to 10 TW. It was focussed on to the gas jet with an $f/18$ off-axis parabolic mirror with a 1 m focal length. This produced a FWHM spot size, in optimal conditions (i.e. those with the highest a_0), of (27 ± 2) μm by (20.2 ± 0.5) μm with (27 ± 2)% of the energy contained in the FWHM. The vacuum a_0 was 0.63 ± 0.03. This calculation has assumed that the 'interesting' part of the laser is a single gaussian mode containing $2 \times 27 = 54$% of the total laser energy and that the rest of the energy is contained in the wings of the pulse. The 1σ pointing fluctuation was below 5 μm. The laser was polarised in the plane of the page as drawn.

After the interaction the transmitted laser beam would either be dumped on an alu-

minium foil on the front of the electron beam profile screen or reflected off a glass wedge placed after the magnet and collimated by a spherical mirror. It was then transported to diagnostics to image the laser mode as it exited the plasma ('exit mode') and determine its spectrum ('forward spectrometer'). These are not shown in the figure for simplicity and because they will not be discussed in depth.

The probe beam was a collimated 800 nm pulse of approximately 40 fs FWHM duration. The backlit plasma channel was imaged with a lens on to a CCD camera (not shown) for the shadowgraphy diagnostic. After this lens was a beamsplitter so that 50% of the light could be sent through a modified Mach-Zehnder interferometer to characterise the plasma density, as discussed in section 3.3.4.

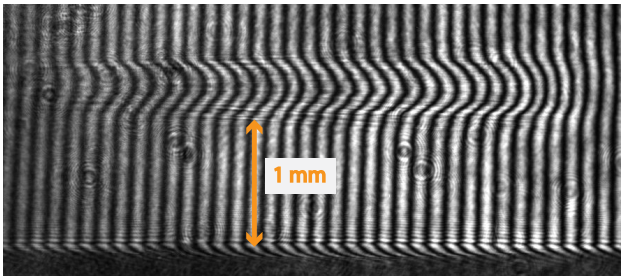


Figure 4.2: Example interferometry image of a methane plasma channel.

An example interferometry image is shown in figure 4.2. Scans of backing pressure for each gas allowed a fit to be made between backing pressure and plasma number density. This was done with the probe timed to arrive just after the wakefield driver had exited the plasma. This fit allowed the backing pressure to be converted to number density on any shot. The error on the fit provided the error on the density. The gases used were pure helium, helium with 5% CO_2 and methane (CH_4). The nozzle used is drawn in figure 3.4. The Hagena parameter for CH_4 expanding from this nozzle is plotted as a function of density in figure 4.3. The magnitude of the Hagena parameter means that the gas will have been clustering, although the fact that Γ^* is relatively small implies that the mean cluster size will have been at the few atom level.

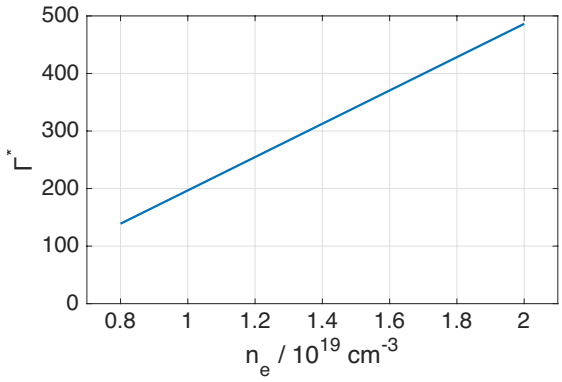


Figure 4.3: Hagena parameter Γ^* as a function of electron density for the 3 mm conical nozzle.

The electron beam profile screen was 0.40 m away from the gas jet and was angled at $\sim 45°$ to the laser beam axis. It could be driven on and off the laser axis. The front of the magnet was 0.60 m after the gas jet. It was 11.9 cm long and had a peak magnetic field of 0.7 T. The electron spectrometer screen was angled at 45° to the laser axis and the high energy end was 1.05 m from the gas jet in z and 12 ± 1 mm from the laser axis in x. In this configuration the diagnostic could detect electrons in the energy range $43 - 620$ MeV.

4.3 Electron Beam Profile Measurements

Figure 4.4 shows a comparison of electron beam profile data taken with pure helium in the density range $(0.98 - 1.15) \times 10^{19}$ cm^{-3}, helium mixed with 5% CO_2 at a density of $(0.94 \pm 0.04) \times 10^{19}$ cm^{-3} and methane at a density of $(1.22 \pm 0.05) \times 10^{19}$ cm^{-3}. These were the experimentally deduced optimum densities for electron stability. It is noted immediately that in the self-injection case (pure He), the beam charge is prone to large fluctuations. Often it produces beams with a lot of spatial structure that is not present in the ionisation injection (mixed gas) or methane cases. This provides good evidence, that with these laser parameters at least, self-injection is not the optimal injection mechanism if reproducibility or beam quality is required. The issue of reproducibility will be covered in more depth in section 4.6.

There is a striking difference between the mixed gas and methane beam profiles which is that the electron beams from methane are elongated horizontally, which was the direction in which the laser was polarised. The mean FWHM divergence of these methane beams was $(13.8 \pm 0.6) \times (4.4 \pm 0.4)$ mrad, where the error given is the standard error. For He + 5% CO_2 it was $(6.3 \pm 0.2) \times (3.5 \pm 0.1)$ mrad. The divergence along the major and minor axes for He, He + 5% CO_2 and CH_4 are summarised in table 4.1.

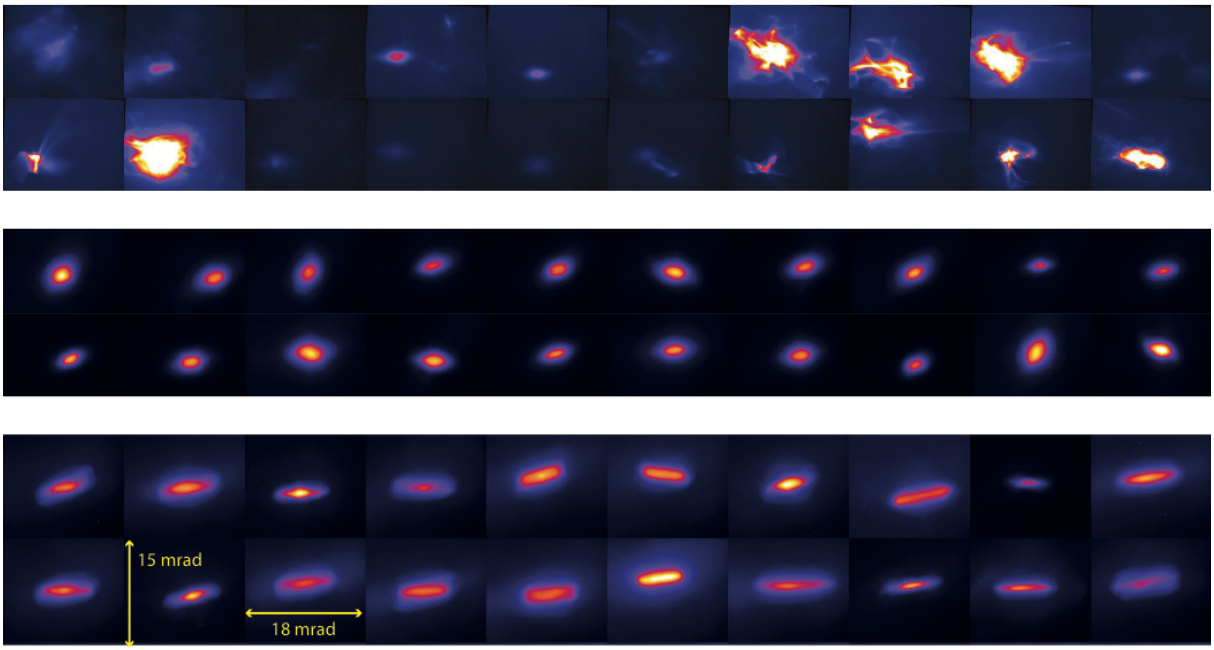


Figure 4.4: Montage comparing the electron beam divergence from helium (top), helium + 5% CO_2 (middle), and methane (bottom).

Gas	He	He + 5% CO_2	Methane
Major axis divergence (mrad)	(7.1 ± 0.9)	(6.3 ± 0.2)	(13.8 ± 0.6)
Minor axis divergence (mrad)	(5.1 ± 0.2)	(3.5 ± 0.3)	(4.4 ± 0.4)

Table 4.1: Comparison of beam divergence for He, He + 5% CO_2 and methane.

The electron beams from ionisation injection had a tendency to be elliptical, although, as we saw in figure 4.4, there was not a strongly preferred direction for this. The angle between the major axis and the x axis is summarised for each plasma species in table 4.2. The errors are the standard deviation over multiple shots to give a better idea of the shot-to-shot fluctuations.

Gas	He	He + 5% CO_2	Methane
θ_x (degrees)	(2 ± 28)	(-10 ± 23)	(-10 ± 10)

Table 4.2: Comparison of the angle between the long axis of the beam profile ellipse and the x axis for He, He + 5% CO_2 and methane.

This shows that, as well as being more elongated, the long axis of the methane beam profiles stays closer to the polarisation axis. However it is noted that electron beams from each type of plasma target tend to be elongated in the polarisation direction.

Both self-injection and ionisation injection produced slightly elliptical beams, with a ratio of long axis to short axis divergence of 1.5 and 1.8 respectively, along with a slight preference for being oriented along the polarisation (x) axis. However only 3 shots of the self-injection data could be analysed because some of the images saturated the CCD camera, and others had such unusual shapes that a FWHM value could not be used to describe them. Figure 4.5 shows such a beam in more detail, re-enforcing the point that II and methane produce smoother electron beams for the range of laser and plasma parameters studied. Methane produces highly elliptical beams with a long to short axis divergence ratio of 3:1, with a clearer preferential orientation along the polarisation-axis. This demonstrates that injection in the methane target is not simply the standard ionisation injection due to ionisation of ions.

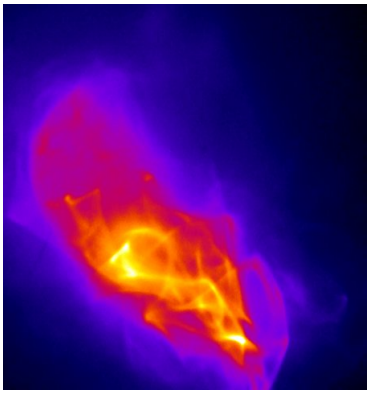


Figure 4.5: Spatial structure in a self-injected beam.

The focal spot exhibited some asymmetry in this experiment. For the methane run the FWHM focal spot was $(32.3 \pm 0.6) \times (20.5 \pm 0.1)$ μm, a ratio of 1.6, although as figure 4.6 demonstrates this was at an angle of approximately 27° to the x axis, something that was not reflected in the electron beam profile data.

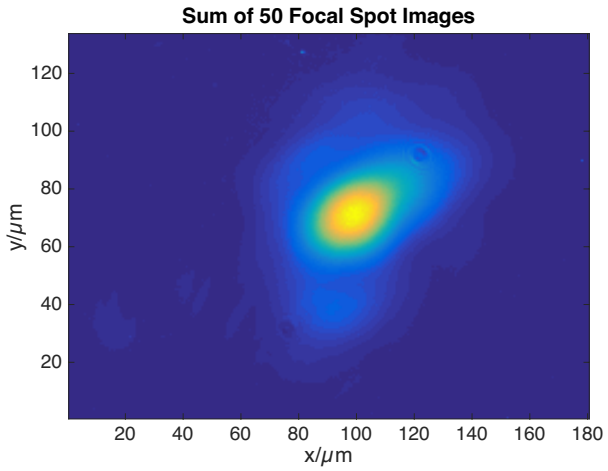


Figure 4.6: Sum of 50 focal spots demonstrating the asymmetry in the focus.

The ellipticity of the beams from methane was additionally found to vary as a function of plasma density. As demonstrated in figure 4.7, the ellipticity of the beam reduces as the number density increases.

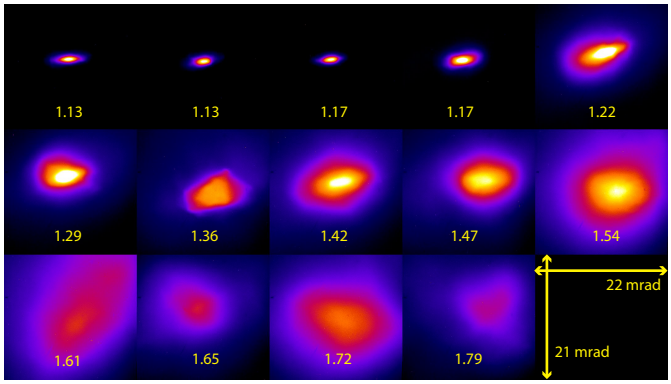


Figure 4.7: Electron beam profile montage from a methane plasma density scan. The yellow numbers indicate the plasma electron density in units of 10^{19} cm^{-3}. The error on these values is approximately 4%.

A graph of this effect can be seen in figure 4.8. The ratio of long axis to short axis divergence decreases as a function of electron density. For densities above approximately 1.4×10^{19} cm^{-3} the ratio is roughly constant between 1.1 and 1.7, close to that of the II and SI injected beams. SI beams have a ratio of 1.5 at both 0.9 and 1.3×10^{19} cm^{-3}. This points to a different injection mechanism occurring in methane which is only apparent at lower densities.

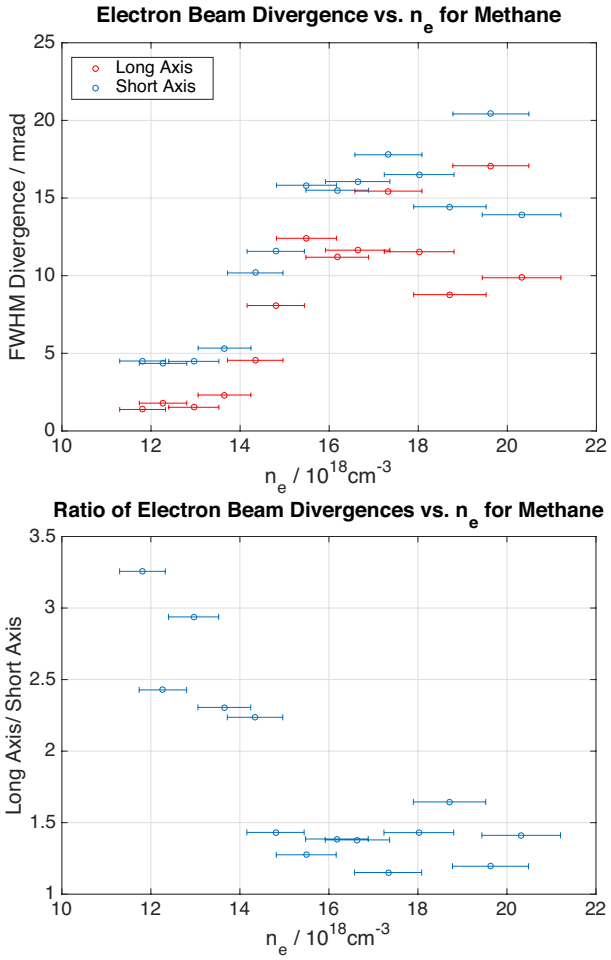


Figure 4.8: Top: Electron beam divergence in x, y as a function of electron density for methane. Bottom: Ratio of long axis to short axis divergence.

The total signal on the beam profile screen as a function of electron density for methane is plotted in figure 4.9. Unfortunately a good charge calibration was not available for these shots. However what this graph does show is a more than doubling of detected electron beam charge at around 1.3×10^{19} cm^{-3}. This aligns well with the drop in the long to short axis divergence ratio from figure 4.8. To summarise: from the shape of the electron beam it is clear that at low density electrons are being injected with more transverse momentum in the laser polarisation direction than in the transverse direction. At higher densities this beam shape has similar properties to those from SI and II. At the density where this happens there is a large increase in injected charge.

Taking all of this in to account it seems that a large self-injection or ionisation injection event must be happening at this density. In light of this it is particularly noteworthy that the self-injection threshold for this system is at a density of $\sim 1.35 \times 10^{19}$ cm^{-3} with laser parameters $\alpha = 0.54$, $\mathcal{E} = 0.39$ J and $\tau = 37$ fs. This was calculated using equation 2.105. Figure 4.4 shows that some self-injection is happening at densities of around

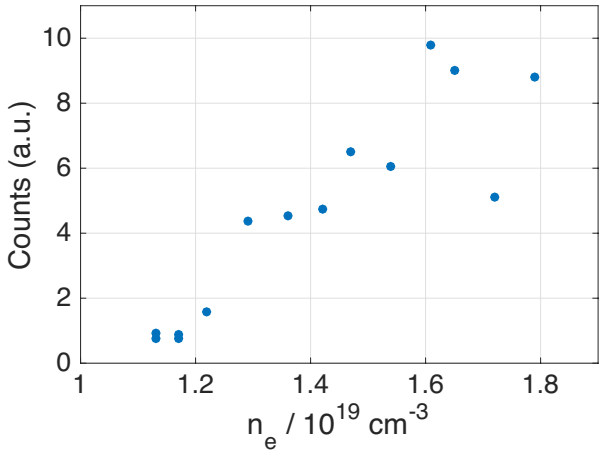


Figure 4.9: Electron beam profile signal as a function of number density from the methane number density scan.

1.1×10^{19} cm^{-3} although on most shots this is a very small amount of charge - close to the detection limit of the diagnostic. This, then, does not rule out a large self-injection event happening near to the theoretical self injection threshold.

This raises the question: is self-injection turning off 'methane injection' or is so much self-injection happening that the cluster injected beam no longer contributes significantly to the overall beam profile? To answer this the raw image was first rotated by a small angle so that the long axis of the ellipse was parallel to the x axis. The data was summed along the columns of the image and a double gaussian fit was made to the resulting curve. This was clearer than summing along the rows of the image because the intensity profile of the methane beams was more strongly peaked in the y direction. The result of this exercise for densities $(1.13\pm0.04)\times10^{19}$ cm^{-3} and $(1.47\pm0.05)\times10^{19}$ cm^{-3} is shown in figure 4.10. In the top line of the image we see that when the density is below the theoretical SI threshold a single gaussian fit works well. In the bottom line where the density is above this threshold there are two distinct populations: one with a relatively narrow 7.7 mrad FWHM divergence and one with a 27.1 mrad FWHM divergence. These could be attributed to the 'cluster injected' and self-injected beams respectively. Integrating over both of these gaussians reveals that the SI beam has approximately 3.5 times the charge of the cluster injected beam. This is in line with the values in figure 4.9. We conclude that neither self injection nor the higher densities turns off methane injection. Instead the methane produced electron beam persists and there is an additional injection of a higher charge beam which is thought to be from self-injection. The additional injection is apparent from both measurements of the beam charge and the beam shape.

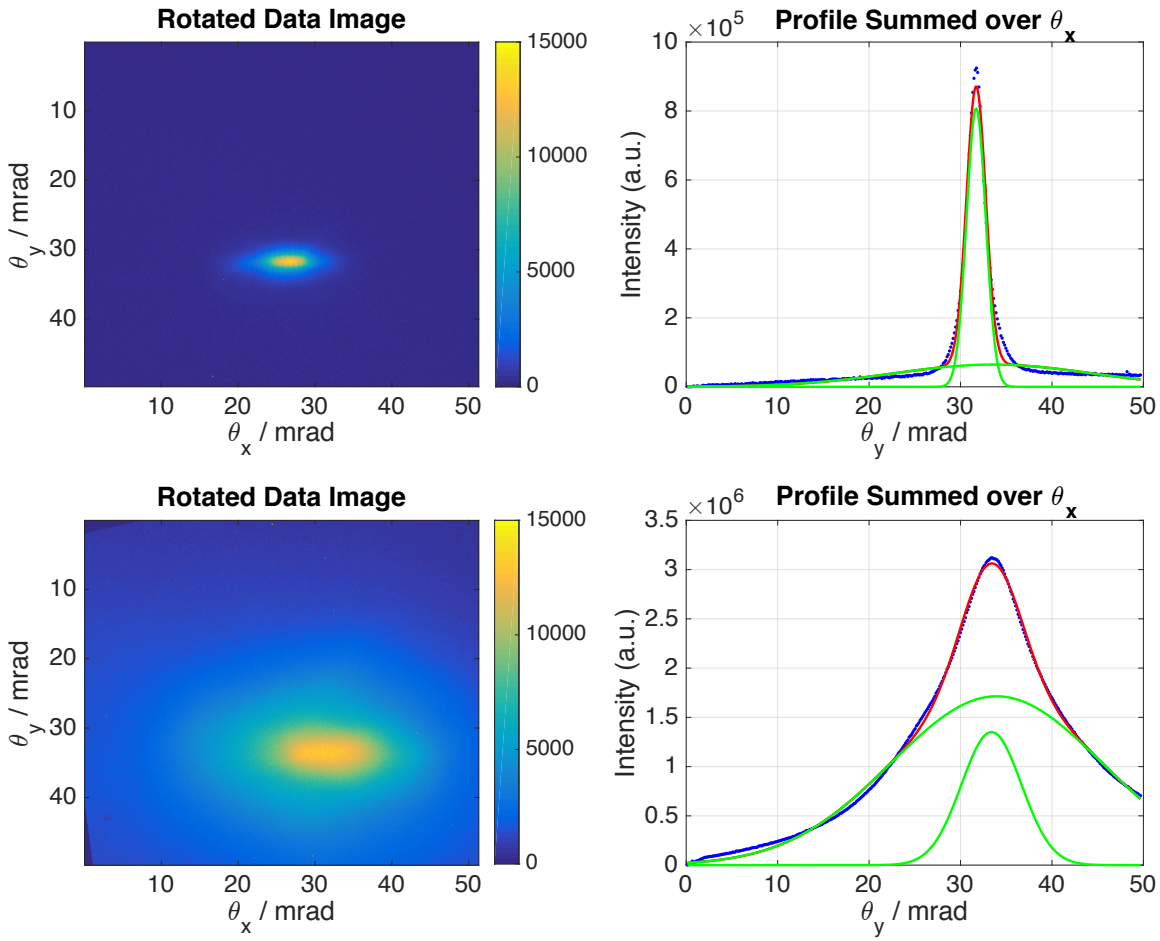


Figure 4.10: Images demonstrating the dual species nature of the electron beams from methane at high density. Top left is the electron beam profile from a 'low' density, $n_e = (1.13 \pm 0.04) \times 10^{19}$ cm^{-3}, shot. Summing the image along the x direction produces the blue curve in the top right graph. A double gaussian (red line) is fitted to this curve. This double gaussian is deconstructed in to two single gaussians in the green curves. In this case the profile is well described by a single gaussian fit. Bottom left shows an electron beam profile from a 'high' density shot at a density of $(1.47 \pm 0.05) \times 10^{19}$ cm^{-3}. In the bottom right this image is summed along the x axis (blue), and fitted with a double gaussian (red) which is the sum of the two distinct gaussians (green), demonstrating a dual species nature of the electron beam.

Yet further justification for the double injection comes from figure 4.11, which shows the long axis and short axis divergence of self-injected beams from a pure helium target as a function of number density. The vertical error bars are the standard error from multiple shots. The asymmetry between x and y divergence remains relatively small as a function of density, in stark contrast to what happens in methane. The y divergence around $1.4 - 1.5 \times 10^{19}$ cm^{-3} is slightly smaller than that found by the double gaussian fit in figure 4.10 but is still significantly larger than the methane divergence. These findings

lend further weight to the double injection hypothesis.

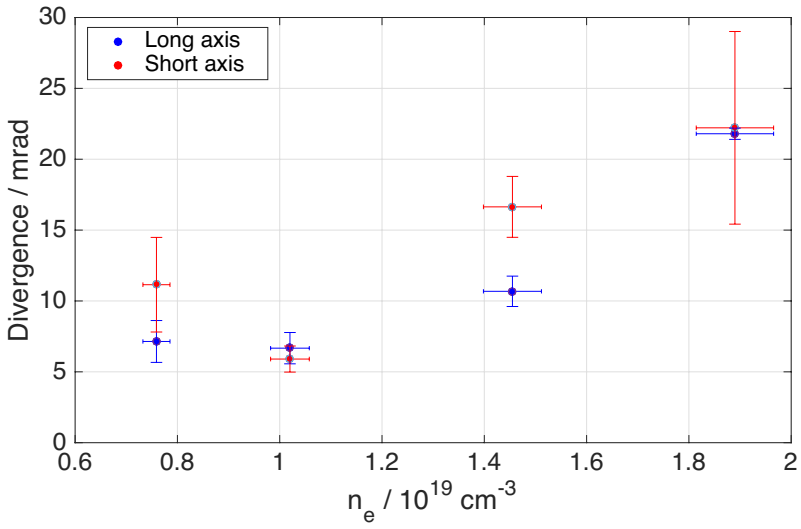


Figure 4.11: Long axis and short axis divergence as a function of n_e for electron beams from a pure helium target.

4.4 Simulations of the Electron Beam Profile

The one observation that has not yet been explained is the shape of the beam profile. Self-injection (SI) and ionisation injection (II) beam profiles showed a slight elongation in the polarisation direction of the laser and methane, at low densities, showed a large elongation in this direction. First, to understand the SI and II cases, 2D PIC simulations were run in the EPOCH code [217]. A gaussian laser pulse with a peak a_0 of 1.3 and a FWHM waist of 23 μm at focus, with a FWHM pulse duration of 37 fs, was focussed in to a plasma with a trapezoidal density profile. The value of a_0 was increased in the simulations compared to the experiment because the simulations were performed in 2D. Self-focussing of the pulse happens more slowly in 2D, meaning that 2D simulations do not reach the same peak a_0 in the wakefield as 3D simulations, or experiments. Self-focussing was important in these simulations because the pulse was mismatched to the plasma (its width was larger than the plasma wavelength) and the initial a_0 was much lower than 4, which is required for self-injection. Therefore, to see the same physics as the experiment, i.e. self-trapping and acceleration of an electron beam, the initial laser energy had to be increased in 2D. After increasing a_0 to 1.3 the simulations showed self-injection of electrons and acceleration to above 100 MeV. This was in line with the experimental results, justifying the increase in a_0. Simulations at a_0 values of 0.63 and 0.88 showed no self-injection in to the wakefield, and so were clearly not representative of the experiment.

The plasma profile had 0.5 mm density ramps at either end with a 2 mm plateau in the

middle. The laser was focussed at the top of the density up ramp. The geometry was set up such that x was the laser propagation direction, y was the axis orthogonal to this in the plane of the simulation, and z was perpendicular to the simulation plane. The simulations had 30 cells per laser wavelength in the x direction and 12 cells per laser wavelength in the y direction, with four particles per cell. For the SI simulations the initial plasma electron number density in the plateau region was 1.3×10^{19} cm^{-3}. For ionisation injection a C^{4+} impurity was added with a density of 1% of the electron species. To simulate the effect of polarisation on the beam profile simulations were run, for both SI and II, with the laser polarised in the y and z directions respectively and the (p_x, p_y) distribution function was output from the simulation. Integrating out the p_x component reveals the effect of laser polarisation on the y momentum of accelerated electrons. Electrons with $p_x < 10$ MeV were excluded so that no electrons in the plasma wave were included in this integration. One can imagine that the y polarised simulation gives the horizontal component of the beam profile images shown in this section, and the z polarised simulation gives the vertical component. With this scenario in mind the electron beam was sampled just after it exited the plasma.

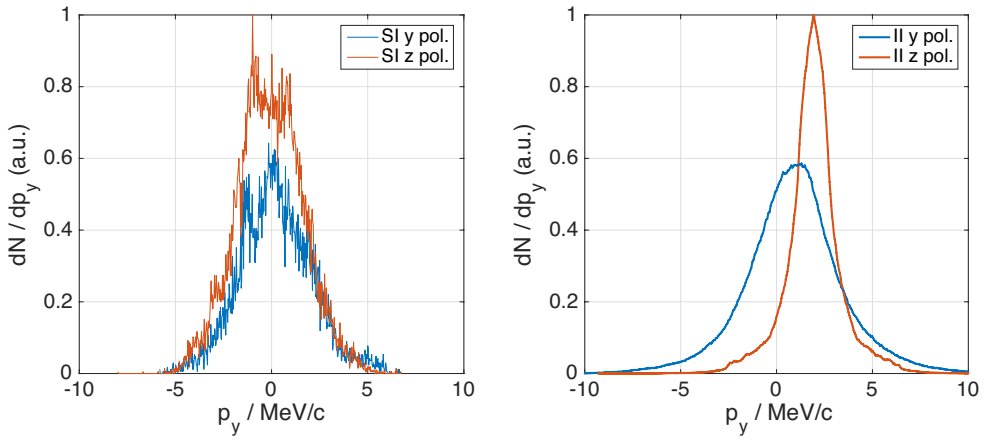


Figure 4.12: The effect of polarisation on the transverse momentum of the accelerated electron beam distribution function. Left: for self injected electrons. Right: for ionisation injected electrons i.e. the sum of the fifth and sixth ionised electrons from carbon. Significantly less total charge was injected in the SI case, explaining the large amount of noise in the dN/dp_y curve.

Figure 4.12 shows the effect of laser polarisation on the p_y distribution of injected electrons in both the SI and II cases. The left hand side of the figure shows that slightly more charge is self-injected when the laser is polarised in the plane of the simulation. The simulation showed that the electron sheath near the back of the bubble underwent large oscillations when the laser was y polarised which coincided with electron injection

in to the second wakefield bucket. This bubble oscillation also caused beam centroid os-

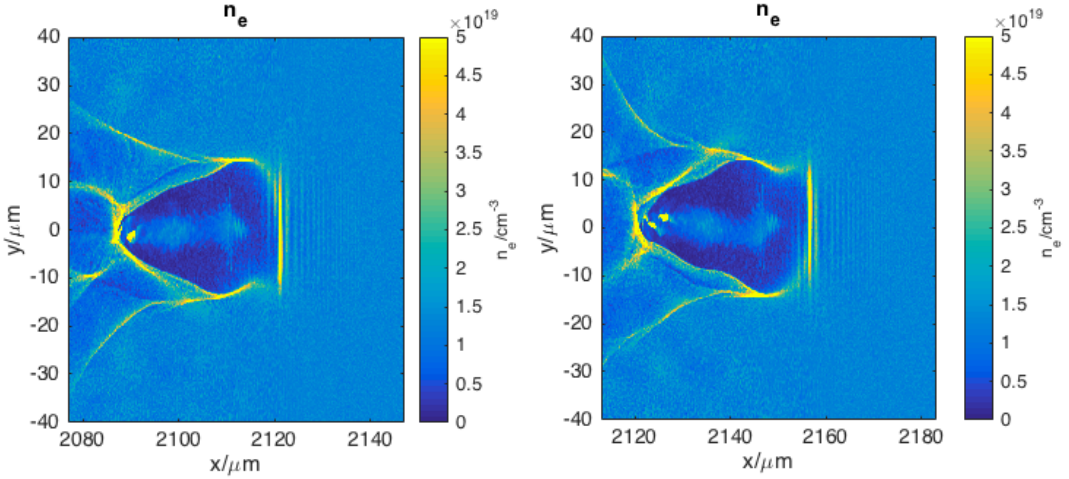


Figure 4.13: PIC simulations outputs, spaced by 0.5 ps, demonstrating bubble oscillations when the laser is polarised in the plane of the simulation.

cillations, shown in figure 4.13, which explains the difference in mean p_y seen in the II simulations.

The FWHM of each of the SI distributions is close to 4 mrad, so the polarisation direction of the laser does seem to affect transverse momentum of the electron distribution. This does not agree with the experimental observation. However the experimental beam profile measurements from SI were averaged over three shots only. For ionisation injection when the laser is polarised along y the FWHM of the dN/dp_y curve is 4.6 MeV, whereas when the laser is polarised along z it is 1.8 MeV. This is larger than what was observed in the experiment but it shows that electrons are picking up transverse momentum in the polarisation direction of the laser. The simulations showed that II electrons were injected in to the first bucket with relatively low transverse momentum: typically up to ~ 1 MeV for either polarisation compared with up to ~ 3 MeV for self-injected electrons. However because the laser pulse length was so mismatched to the plasma wavelength there was significant laser field throughout most of the bubble, shown in the simulation output in figure 4.14. This preferentially imparted momentum on to the electron beam in the polarisation direction. Clear evidence of the electron beam having interacted with the laser field can be seen in the plot of n_e at the top of this figure, as it appears to be modulated at the laser frequency. This was not the case for the self-injected electrons which were only seen to be injected in to the second bubble.

This cannot be a full description of what is happening in the cluster (methane) case because the elongation of the beam profile along the laser polarisation direction is in-

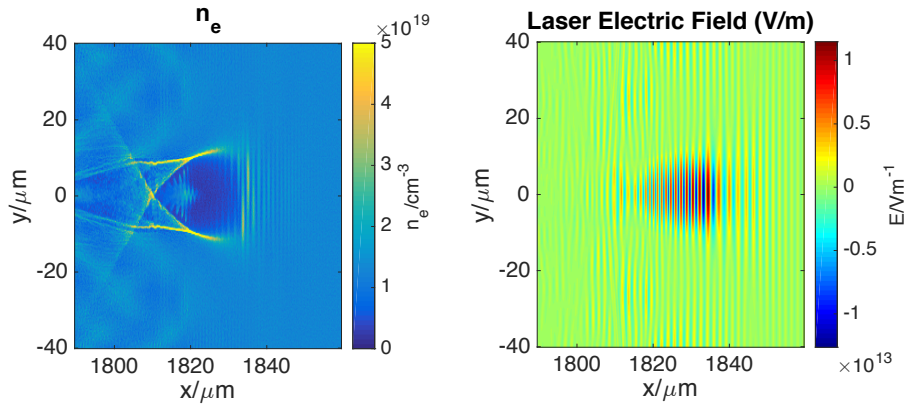


Figure 4.14: Simulation output showing the position of the bubble and the laser field.

creased even compared to ionisation injection. It has previously been found that the temperature of electrons from laser-cluster interactions exhibits a slight anisotropy, with higher temperatures being observed in the direction of laser polarisation [218]. To simulate this effect, an II simulation similar to those presented so far was run with the laser polarised along the y-axis and a plasma temperature of 1 keV in the y direction, and zero in the x and z directions. The FWHM of the dN/dp_y curve for the electrons exiting the plasma in this simulation was 4.8 MeV compared to 4.6 MeV for the cold plasma case, showing that a plasma temperature can increase the divergence of the electron beam. This is in agreement with previous work showing that the trapping threshold is reduced in a warm plasma [117], meaning that electrons with a higher initial transverse momentum can be trapped in a warm wakefield[1]. However this increase persisted in simulations with y polarisation and $T_z = 1$ keV, as shown in figure 4.15, demonstrating that this does not contribute further to the beam's transverse momentum anisotropy. It is noted that having the polarisation and plasma temperature aligned along the same axis causes slightly more charge to be injected.

It is not practical to simulate realistic clusters in a LWFA simulation because they are nanometre scale objects, meaning that they are of order 10^{-2} of the laser wavelength. Having a resolution of some fraction of this would require huge computational resources since the simulation box size must be at least a few λ_p, so 10's to 100 μm in size. However the ionisation injection simulations presented here may provide some insight in to the physics behind the extra elongation of the electron beam in the cluster case. In the experiment, both cluster and ionisation injected electrons had larger transverse momenta in the direction of laser polarisation than in the perpendicular direction. For ionisation

[1]Further simulations were run with a cold plasma but C^{4+} ions with temperatures of 1 keV and 100 keV in the polarisation direction. This made no difference to the transverse momentum distribution highlighting that this effect requires a hot electron plasma.

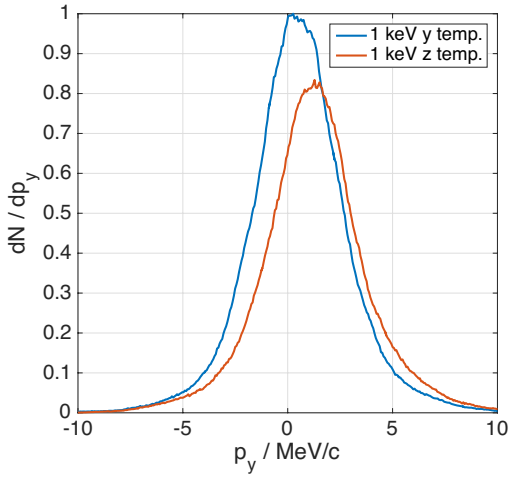


Figure 4.15: A comparison of dN/dp_y for a y polarised drive laser with a temperature anisotropy in the y and z directions.

injected beams this was shown by simulation to be a result of the laser field filling the bubble. In the cluster case the elongation was enhanced by the presence of the clusters, and the simulations demonstrated that this was not a temperature effect. One explanation could be from local electric field enhancement [219] that happens due to the generation of localised resonant surface plasmons on the clusters. It has been shown for two small solids (clusters are small collections of solid density material) placed 10's nm apart that the localised enhancement in the electric field can be very large, up to a factor of 10^3 over a small region of space between the objects [220]. This is one potential explanation of why a cluster medium might enhance the transverse momentum in one direction of some electrons in the electron beam. It may be possible to test this hypothesis in future by changing the size of the clusters at constant plasma density by changing the temperature of the gas. Another reason behind this elongation effect might come from the improved guiding of laser pulses in clustered media that has been reported in the literature [211]. Improved guiding would lead to an increase in the laser energy contained in the bubble, which in this case would increase the laser electric field strength throughout the bubble, increasing further the transverse momentum of electrons in the direction of laser polarisation. There is evidence that this may have been the case in the experiment from the exit mode diagnostic, which imaged the laser spatial profile as it exited the plasma. Figure 4.16 compares images of the exiting laser profile from six shots with a Helium plus 5% CO_2 target (for ionisation injection) at densities in the range $(1.12-1.32)\times10^{19}\,\mathrm{cm}^{-3}$ and six shots with methane at a plasma density of $(1.19\pm0.04)\times10^{19}\,\mathrm{cm}^{-3}$. Unfortunately a spatial scale was not available for this diagnostic. However it does show significantly better guiding in the case of the cluster target, with multiple shots showing an intense guided filament in the centre. This is good evidence that the increased transverse mo-

mentum of cluster injected electron beams is, at least in part, a result of improved laser guiding increasing the laser electric field throughout the bubble.

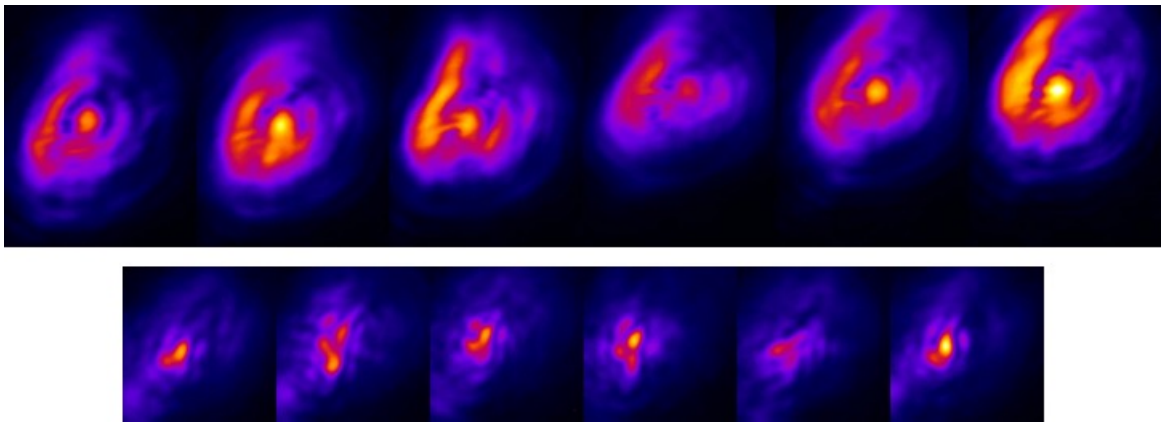


Figure 4.16: Comparison of exit mode images taken with a mixed gas target for ionisation injection (top) and a cluster target (bottom) on the same spatial scale.

4.5 Measurements of the Electron Energy Spectrum

The electron spectrometer allowed for the characterisation not only of the electron kinetic energy spectrum but also the vertical divergence and pointing fluctuation, and it was calibrated so that the total beam charge could be calculated. The low energy cut-off of the diagnostic was approximately 45 MeV. The methodology employed was to do so-called $P - z$ scans where a backing pressure (number density) scan would be carried out with the laser focussed at different distances in to the gas flow. The distance quoted is the distance between the focus and the front inside face of the nozzle. The laser focus was 1 mm above the top of the nozzle at all times.

The first thing this methodology allowed was a measurement of the injection threshold. A summary of the injection threshold versus distance focussed in to the nozzle is presented in table 4.3. Comparison to figure 4.11 suggests that the injection threshold is similar to what was found for self-injection.

Distance Focussed in to Nozzle	Injection Threshold Density / cm^{-3}
1.0 mm	$(8.0 \pm 0.3) \times 10^{18}$ cm^{-3}
1.5 mm	$(8.5 \pm 0.4) \times 10^{18}$ cm^{-3}
2.0 mm	$(9.2 \pm 0.4) \times 10^{18}$ cm^{-3}

Table 4.3: Injection threshold density with a methane target.

A typical electron energy spectrum is shown in figure 4.17. The raw image of the

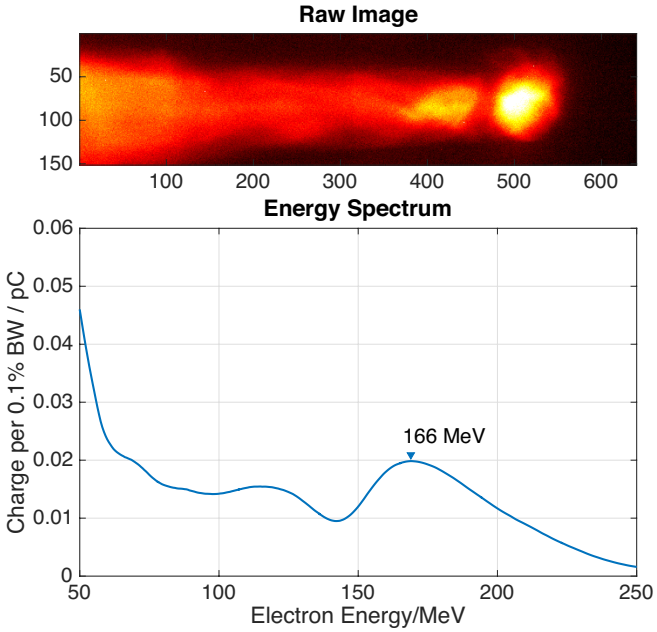


Figure 4.17: Example electron spectrometer image from a methane target (top, with high energies towards the right) and a graph of the energy spectrum (bottom).

screen is shown at the top and the energy spectrum is below. On this shot the plasma density was (1.02 ± 0.04) cm^{-3} and the laser was focussed 1 mm in to the plasma. This figure highlights a common feature of the electron beams from methane: that they are broadband but have a peak at high energy. This is good for applications as at the highest energy there is a large amount of charge per unit bandwidth[2]. The broad nature of the energy spectrum implies that electrons are being continuously injected in to the wakefield for a substantial length of plasma.

The energy of the high energy peak in the electron spectrum, the total beam charge above 45 MeV, the beam divergence and the beam pointing are shown as a function of density in figure 4.18.

This is for the laser focussed 1.0 mm, 1.5 mm and 2.0 mm in to the gas. Each point represents a single measurement and the solid lines are cubic smoothing splines fitted to the data. The vertical error bars on the peak energy points were calculated from the uncertainty in the Lanex screen position. No vertical error bars are plotted for the beam divergence or pointing because the error is suspected to be a few camera pixels, where each pixel represents approximately 0.1 mrad. The error in the beam charge is difficult

[2]For clarity, the peak energy of this shot would be reported as 166 MeV even though there is a tail going to beyond 200 MeV. This tail effect may in fact mostly be due to the finite beam divergence in the magnet's dispersion direction

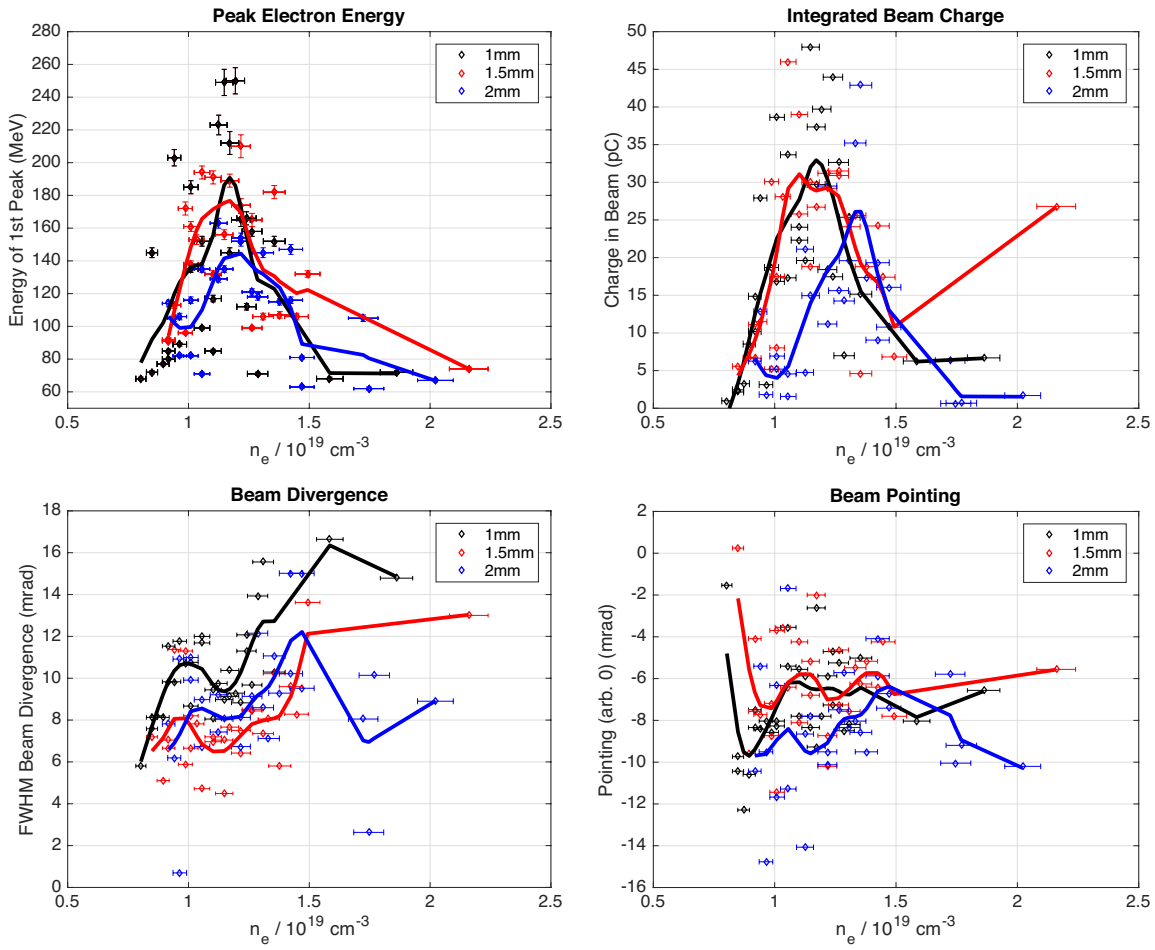


Figure 4.18: Electron spectrometer results from a $P - z$ scan in methane. The beam divergence and pointing is in the vertical direction only. Note that the zero position for pointing is arbitrary and that we are only looking for pointing fluctuations.

to estimate (see section 3.4.4) but all of the systematic errors relate to understanding of Lanex and image plate behaviour, so the trends in the beam charge plot are real but the absolute could be off by an, albeit small, multiplicative factor.

The peak energies are remarkably similar for each of the focal positions, and are largest at a density of close to 1.2×10^{19} cm^{-3}. For the maximum kinetic energy gain of approximately 190 MeV at this density, with the focus 1 mm in to the plasma, the Lu scaling from equation 2.116 suggests that the laser focusses within the plasma to a peak a_0 of 3.9, meaning that the dephasing length is approximately 600 μm. This suggests that the high energy electrons that were detected were injected close to the end of the plasma. It is unsurprising that this is the case because the laser pulse in this experiment was very mismatched: the matched spot size at 1.2×10^{19} cm^{-3} is 6.1 μm. Therefore a significant length of plasma would have been required for the pulse to evolve to an a_0 large enough

to drive a high amplitude wakefield that can trap electrons. The shape of the peak energy curves is then easily explained: at low densities there is not enough plasma left after the pulse evolution length and injection point to accelerate to the maximum energy achievable at that density, especially since the accelerating field $E_{max} \propto \sqrt{n_e}$. At high density the accelerating gradient is larger but the electrons quickly dephase. The optimal density is found where the acceleration length matches the dephasing length, which in this experiment was at 1.2×10^{19} cm^{-3}.

The highest charge beams were detected at almost exactly the same density as the maximum electron energies. Part of this effect is the low energy cut-off of the diagnostic but this is still encouraging from an applications perspective. In addition, at each focal position the divergence is relatively low at the optimum density. The fact that the electron energy and charge follow well defined curves is very encouraging for the use of clustered methane targets for LWFA's. The peak energy can be tuned simply by changing the density. The overlap of maximum electron energy, maximum beam charge and a low beam divergence would be ideal for light source applications.

Self-injected beams did not exhibit this level of tunability or consistency. This is demonstrated in figure 4.19, which shows the peak energy of self-injected beams as a function of plasma density. The laser was focussed 1 mm in to the plasma. At this focal position the highest electron peak energy observed on any shot with methane was (249 ± 8) MeV compared to (210 ± 7) MeV for SI. The highest charge beams detected were slightly higher for SI at $60 - 70$ pC compared to $45 - 50$ pC. It would, however, be fair to conclude that using a methane target produces electron beams of a similar energy and total charge to self-injection but with a much higher degree of tunability.

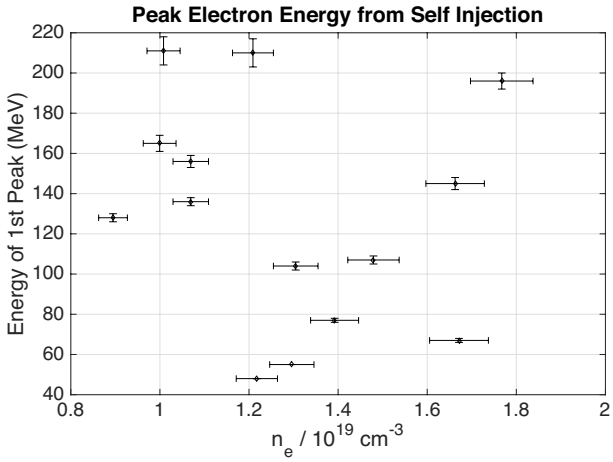


Figure 4.19: Peak electron energy from self-injection as a function of density, with the laser focussed 1 mm in to the gas jet.

4.6 Reproducibility

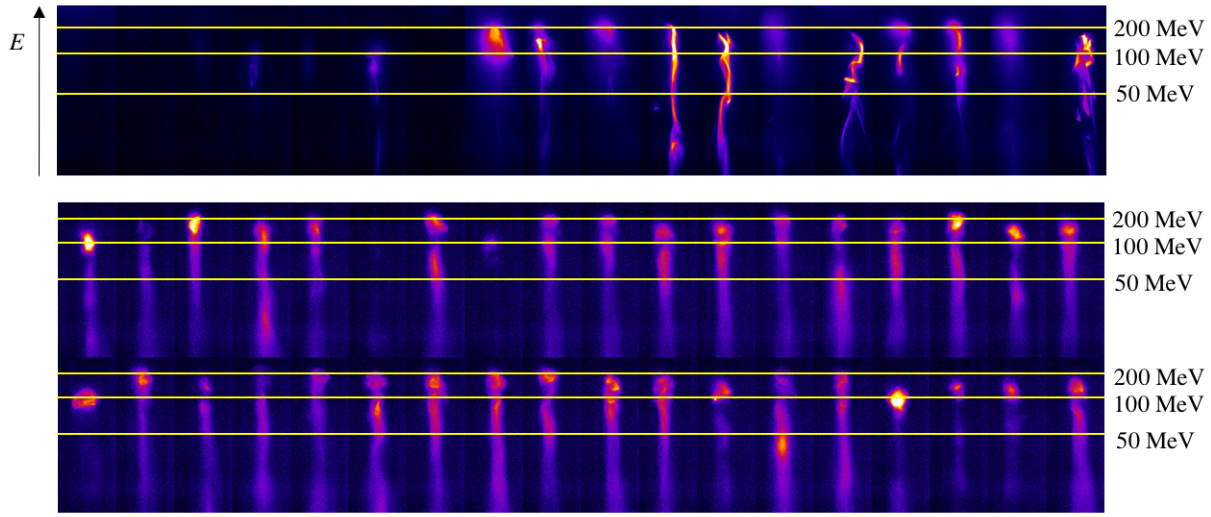


Figure 4.20: A comparison of electron spectrometer stability runs between a helium target (top) and methane target (bottom).

It has been shown that using methane as a gas target for a 10 TW LWFA experiment produces tunable electron beams with energies and charges close to those from self-injection. For this to be a practical source of energetic electrons it must also have good reproducibility, which will now be examined. At a density of $(1.22 \pm 0.04) \times 10^{19}$ cm^{-3} an electron beam was detected on the beam profile monitor on 43 out of 43 shots. At a very similar density of $(1.20 \pm 0.04) \times 10^{19}$ cm^{-3} an electron beam was detected on the electron spectrometer on 77 out of 79 shots. A subset of these shots is shown at the bottom of figure 4.20, where the top part shows a self-injection run at $n_e = (1.11 \pm 0.04) \times 10^{19}$ cm^{-3} for comparison. The probability of detecting an electron beam on any shot from self-injection is $\sim$ 76% compared to $\sim$ 98% for methane. In addition it is clear from the images that the structure of the electron beam is much more reproducible from methane. On almost all shots there is a high energy peak with a long tail. Additionally there is very little spatial structure transversely unlike in the SI case. Having a reproducible energy spectrum is important for applications. This is, therefore, an encouraging result that using a methane target produces electron beams with a more stable spectrum and spatial profile. The average properties of the electron beam as measured from the electron spectrometer screen in the 79 shot stability run are given in table 4.4. The graphs of these properties vs. shot number in figure 4.21 show a lack of very large deviations from the mean as there is for self-injection. The spectra typically exhibited multiple peaks as part (b) of this figure shows, where each line has been smoothed with a moving average filter. Interestingly there is a strong correlation between the energy of the first and second peaks. Re-plotting the electron beam parameters against laser energy, as done in figure

Quantity	Mean Value	Standard Deviation
Peak Electron Energy / MeV	173	41
Vertical Pointing / mrad	-	2
Vertical Divergence / mrad	8	1
Accelerated Charge / pC	27	9

Table 4.4: Electron beam parameters from a methane stability run.

4.22 shows no correlation between any electron beam parameter and the laser energy. Therefore an unmeasured parameter, such as the laser focal spot quality, must be causing the variation that is seen.

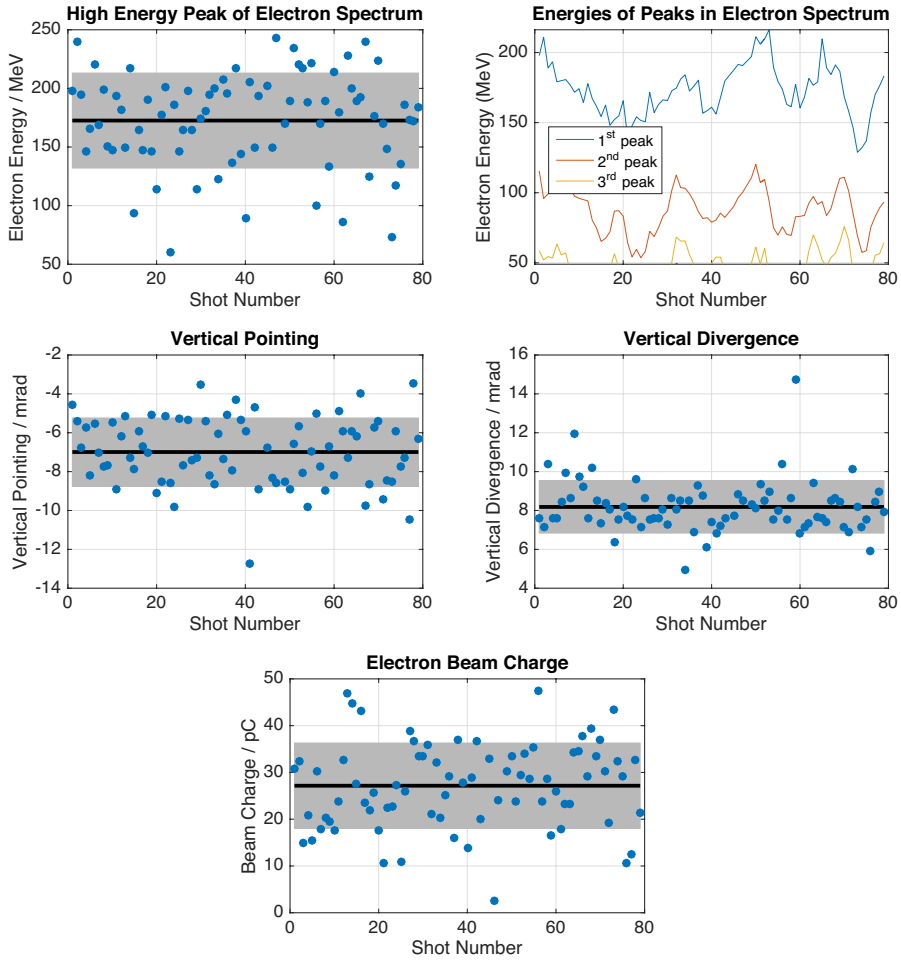


Figure 4.21: Stability of the accelerated electron beam from a methane target over a 79 shot run showing (a) the energy of the high energy peak of the electron spectrum, (b) the energy of multiple peaks in the spectrum (if present), (c) the vertical pointing fluctuation, (d) the vertical divergence and (e) the total charge in the beam above approximately 43 MeV, which was the low energy cut off of the electron spectrometer screen. Each point represents the result of one laser shot. The black line shows the mean the limits of the grey rectangles are the standard deviation of all of the shots.

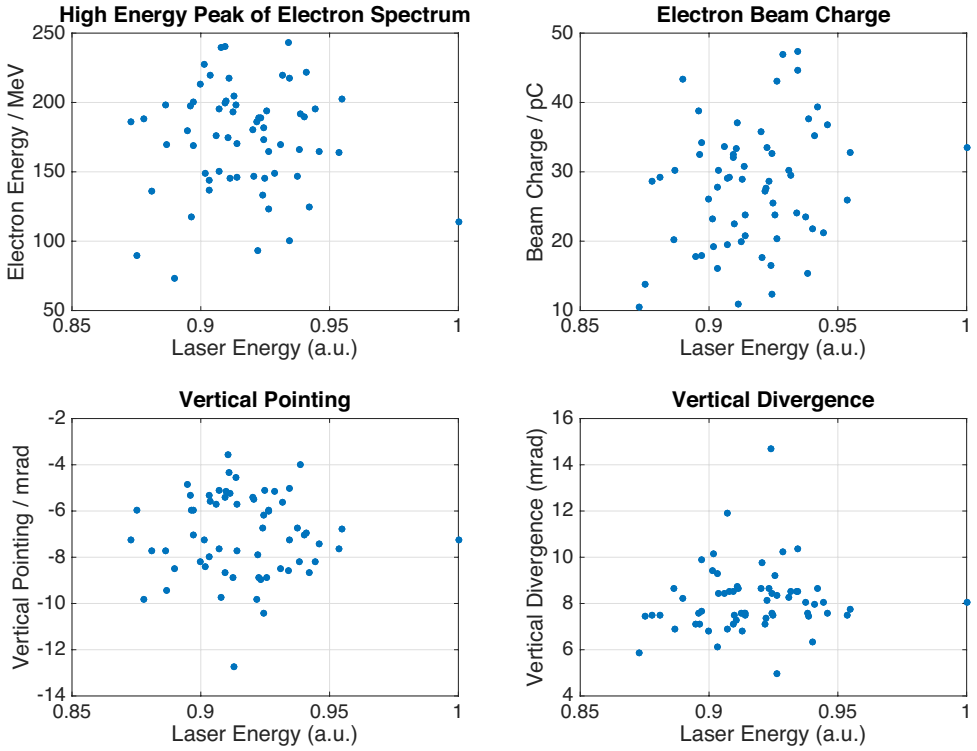


Figure 4.22: Stability of the accelerated electron beam from a methane target with respect to laser energy fluctuations. The laser energy was not measured directly on this day; the relative change in energy was inferred from a laser near field diagnostic. It is anticipated that a value of 1 here equates to approximately 0.4 J on target.

4.7 Summary and Outlook

This chapter has reviewed results from a $\sim$ 10 TW LWFA experiment. A 3 mm wide supersonic gas flow was used as the target, and the target gas was changed between pure helium, He + 5% CO_2 and clustered methane with a Hagena parameter of a few hundreds. Measurements of the beam profile from each gas allowed the properties of self-injected, ionisation injected and cluster injected beams to be compared. For SI and II the beam was slightly elongated in the direction of laser polarisation by a factor of approximately 1.5 and 1.8 respectively. This was increased to a factor of 3 for cluster injection at low densities which showed that this is a different injection mechanism. At higher densities the cluster injected beam persisted and was superposed on a higher charge, more divergent bunch that was believed to be from self-injection. 2D PIC simulations showed that ionisation injected electron beams have additional momentum in the direction of laser polarisation which was seen in the experimental results. The most likely cause of the enhanced divergence of electron beams from methane in the laser polarisation direction is

in the interaction of the laser with the nanometre scale clusters, which were much smaller than anything that could be reasonably simulated in a PIC simulation of LWFA.

Electron beams from clustered methane were shown to have similar beam charge and peak energies to those from self-injection but with significantly enhanced tunability and reproducibility. This makes methane a better source for applications because the required electron beam energy can be picked by simply changing the plasma density, and shot to shot fluctuations in the electron beam properties are reduced. The shape of the beams from cluster injection suggest that this could be a source of polarised betatron radiation which would be mostly polarised along the polarisation direction of the drive laser. Some of the highest energy beams from methane were produced at densities where the beam had a very elliptical profile (see figures 4.18 and 4.8). Therefore this is promising as a source of polarised, hard synchrotron light if these results can be repeated with few hundred TW laser systems capable of accelerating electrons to the GeV level. Strongly polarised (up to 80% polarisation degree) betatron radiation has been measured before [221], but the increased ellipticity of cluster injected beams compared to those from ionisation injection could improve further on this figure.

Chapter 5

Enhanced Betatron Radiation from a LWFA with an $f/40$ Focussing Optic

5.1 Motivation

One of the major goals of LWFA is to increase the energy gain of the electron beam in a single stage. Until high coupling efficiency through multiple stages can be demonstrated, increasing the single stage energy gain is the only method of making a LWFA suitable for some of its proposed applications, especially as a source for a compact X-FEL. In terms of betatron radiation, we saw in equation 2.166 that the total radiated x-ray energy $W_{tot} \propto \gamma^2 {K_\beta}^2 k_\beta = \gamma^4 {k_\beta}^3 r_\beta^2$, where $k_\beta = k_p/\sqrt{2\gamma}$. Assuming that the betatron oscillation radius doesn't scale strongly with γ, which is what we saw for large γ in figure 2.10, then the energy scales as $W_{tot} \propto \gamma^{5/2}$. Therefore by increasing single stage energy gain the brightness of betatron radiation can be significantly increased.

The highest energy gains reported to date have come from pre-formed plasma waveguides [61], which allow a large proportion of the laser pulse energy to be guided in a single filament, driving a strongly nonlinear wakefield over long distances. The disadvantage of these schemes is that the relatively complicated plasma target is easily destroyed by the unguided parts of the high intensity pulse. With this in mind it could be argued that experiments relying on a simple, robust gas target and self-guiding of the pulse offer a more reliable route to high repetition rate experiments in the future. Studies on how to increase the proportion of laser energy that is guided in a single filament [51] showed that long focal length geometries with spot size $w_0 > \lambda_p$ allowed more laser energy to be captured into this filament than short focal length ($w_0 < \lambda_p$) geometries. This energy was shown to be guided over a distance similar to the dephasing length which permits maximal energy gain from the wake. For this reason many recent experiments have used $f/20$ geometries or similar producing energy gains from self-guided LWFA of 100's MeV

to 1 GeV from 10's to 100's TW laser pulses. A summary of many papers from these experiments can be found in [222]. This is certainly the case at the Gemini laser where energy gains of ~ 1 GeV are routinely reported from this geometry [57] [33].

This chapter will detail an experiment that explored the effects of moving to an even longer focal length of 6 m using an $f/40$ focussing optic. The principle aim was to increase the maximum energy of the electron beam, although in this chapter the primary focus will be on how this affected the betatron beam properties. A review of published betatron characteristics can be found in [223], where experiments at laser systems at the few hundred TW level typically report of order 10^9 photons per shot with critical energies of $10 - 30$ keV. As this chapter will discuss how a change in focussing geometry from $f/20$ to $f/40$ can increase the brightness of the betatron beam, it is sensible to briefly review what has been achieved so far at the same laser system (the Gemini laser system) with an $f/20$ focussing geometry. In chapter 6, it will be reported that a (20.4 ± 0.8) keV critical energy betatron spectrum was produced with a peak brightness in the best conditions of $\sim 1.8 \times 10^{23}$ photons/s/mm^2/mrad^2/0.1%BW. This was from a ~ 1.6 μm diameter source, which was calculated from spectral measurements of the x-ray and electron beams. The highest brightness shot measured on Gemini happened during the experiment detailed in [33], where the critical energy was $E_c \approx 27$ keV and the brightness was $\sim 3.7 \times 10^{23}$ photons/s/mm^2/mrad^2/0.1%BW.

5.2 Experimental Set-up

The general experiment set-up is shown in figure 5.1. The laser was focussed using an $f/40$ spherical mirror and folded on to main beamline with an HR coated turning mirror. The optical aberrations, including the spherical aberration from the focussing optic, were corrected by the deformable mirror. The laser pulse energy on target was (5.6 ± 0.3) J including the 67% compressor efficiency and the 90% throughput from the entrance of the target chamber to the plasma target. The nominal FWHM pulse length was 47 fs. The FWHM spot size was $(54 \pm 2) \times (45 \pm 1)$ μm. (32 ± 3)% of energy was contained within the FWHM spot. Combining these values gives a peak focal intensity of $(2.5 \pm 0.2) \times 10^{18}$ W/cm^2, corresponding to an a_0 of 1.10 ± 0.03 for 800 nm light[1]. The 1σ pointing fluctuation was approximately 10 μm in both x and y. The total energy was limited by the damage threshold fluence on the final turning mirror. Some higher damage threshold mirrors became available later in the experiment and the on-target laser energy was increased to (9.4 ± 0.6) J, which is an a_0 at focus of 1.43 ± 0.05.

[1]This calculation has assumed that 32/50 of the energy was contained in the spot, as 50% is the theoretical maximum energy is contained within the FWHM for a gaussian.

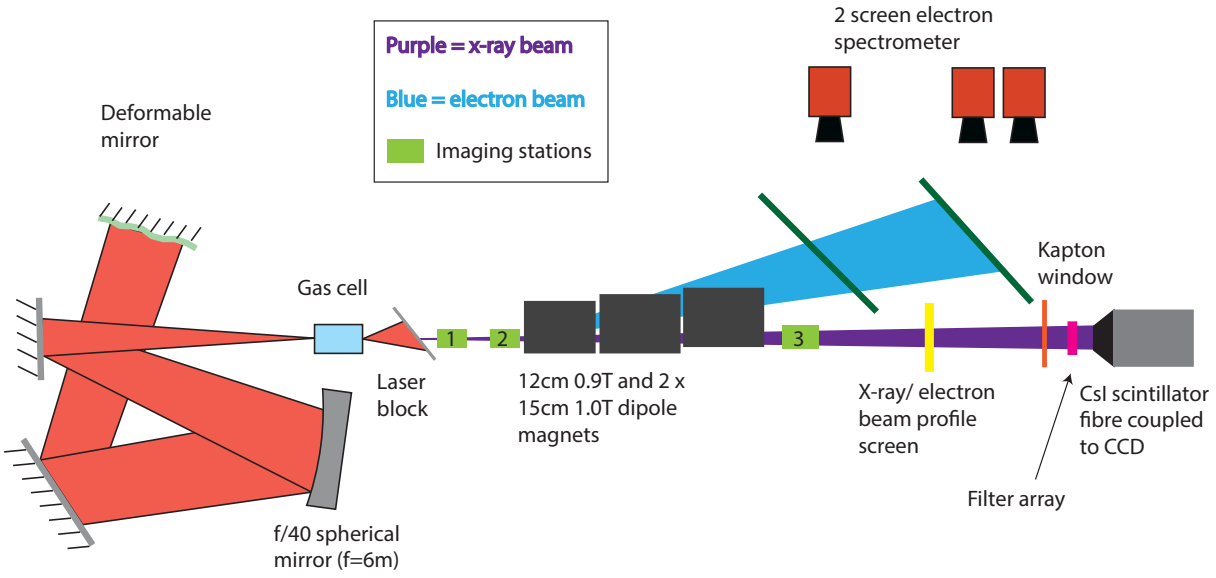


Figure 5.1: Diagram of the experimental set-up with the $f/40$ focussing optic.

The laser was focussed at the entrance hole of a helium filled single stage gas cell. The length of the cell, measured between cone tips, could be varied continuously between 3 mm and 42 mm. The plasma density was characterised using a ~ 50 fs FWHM probe beam transverse to the gas target that was timed to arrive just after the wakefield drive laser had exited the plasma. A Moiré interferometry diagnostic was used to find a conversion between backing pressure p and electron number density, which was $n_e\,[10^{18}\mathrm{cm}^{-3}] = (0.033 \pm 0.004)\,p\,[\mathrm{mbar}]$ [156]. The error comes from the fit to the data. The shot-to-shot backing pressure fluctuations were of order $1-2\%$. Shortly after the exit of the gas cell there was the option to block the transmitted laser light with a ~ 25 μm thick kapton tape that acted as a plasma mirror plus a 24 μm aluminium beam block that was used to shield any x-ray imaging targets that were on the laser axis. All shielding could be removed to allow the laser to be characterised by transmitted laser diagnostics, which are not detailed further here.

The electron beam was swept off-axis by an arrangement of permanent dipole magnets: first a 12 cm long magnet with a peak field of 0.9 T, followed by two 15 cm magnets with a peak field of 1.0 T. The height of the magnets increased slightly with distance from the source so that the highest energy electrons would experience the peak $\boldsymbol{B}$ field of each magnet for the longest amount of time to improve dispersion and therefore energy resolution at the highest energies. The electrons were detected on two Lanex regular screens which were imaged on to CCD cameras by TV lenses.

The principle x-ray detector was the Andor indirect detection camera detailed in section 3.5.2. To reach this detector, the x-rays passed through a 250 μm thick kapton

vacuum window that was shielded by 24 μm of aluminium foil as a final laser block. The x-rays then traversed (48 ± 1) cm of air to reach the detector. This allowed a small lead wall to be built up in front of the x-ray camera to reduce bremsstrahlung noise. The total distance from the source to the x-ray camera was 3.57 m. There were three x-ray imaging stations which are marked on figure 5.1. Imaging station 1 was ~ 12.7 cm after the source, meaning that the magnification was 29. This was where the JIMA target (appendix 8.10) was placed when it was imaged. Imaging station 2 was the location for the gold resolution target (also in appendix 8.10) and had a magnification of 10.7. Imaging station 3 was on a long rail, which allowed the magnification to be varied in the range ~ 2.0 to ~ 4.7. The x-ray beam profile 'screen' on this experiment was the 50×50 mm, 150 μm thick structured CsI scintillator that was usually used on the front of the Andor indirect detection camera. This was imaged on to an Andor iXon EMCCD camera.

5.3 Plasma Length Scans

The principle methodology used was to perform scans of the plasma length at a number of plasma densities, which were varied by changing the backing pressure on the gas cell. Plasma length scans are particularly revealing because they allow the electron beam properties to be studied either side of dephasing, giving a good insight in to the dynamics of the electron beam within the wakefield. This cannot be achieved in such a satisfactory way in a fixed length target. One could look at the electron beam properties either side of dephasing by performing a number density scan, but this also affects the laser focussing, the field strength in the wakefield and injection, so it paints a much more complicated picture of the dynamics. Additionally, data from length scans is relatively scarce in the literature because the gas target design needs to be slightly more advanced.

5.3.1 Electron Beam and X-ray Montages

Gas cell length scans were performed at constant plasma number densities of 1.9, 2.3, 2.6, 2.8, 3.3 and 5.7 $\times 10^{18}$ cm^{-3} to study the evolution of the accelerated electron beam. The error on the quoted densities is $\sim 10\%$, but it is a systematic error from the fitting of number density to backing pressure rather than a measure of the random fluctuation in density which was of order 1%. For this reason, horizontal error bars will rarely be plotted when discussing how parameters vary with plasma density. The laser energy on target for these runs was (5.6 ± 0.3) J. In this section the general behaviour of the electron and x-ray beams will be discussed. The electron and x-ray properties will then be discussed quantitatively in sections 5.3.2 and 5.3.3.

Figure 5.2 shows the raw electron spectra and betatron x-ray images from a scan of gas

cell length from 3 mm to 40 mm at a density of 2.3×10^{18} cm^{-3}. What we see over the first

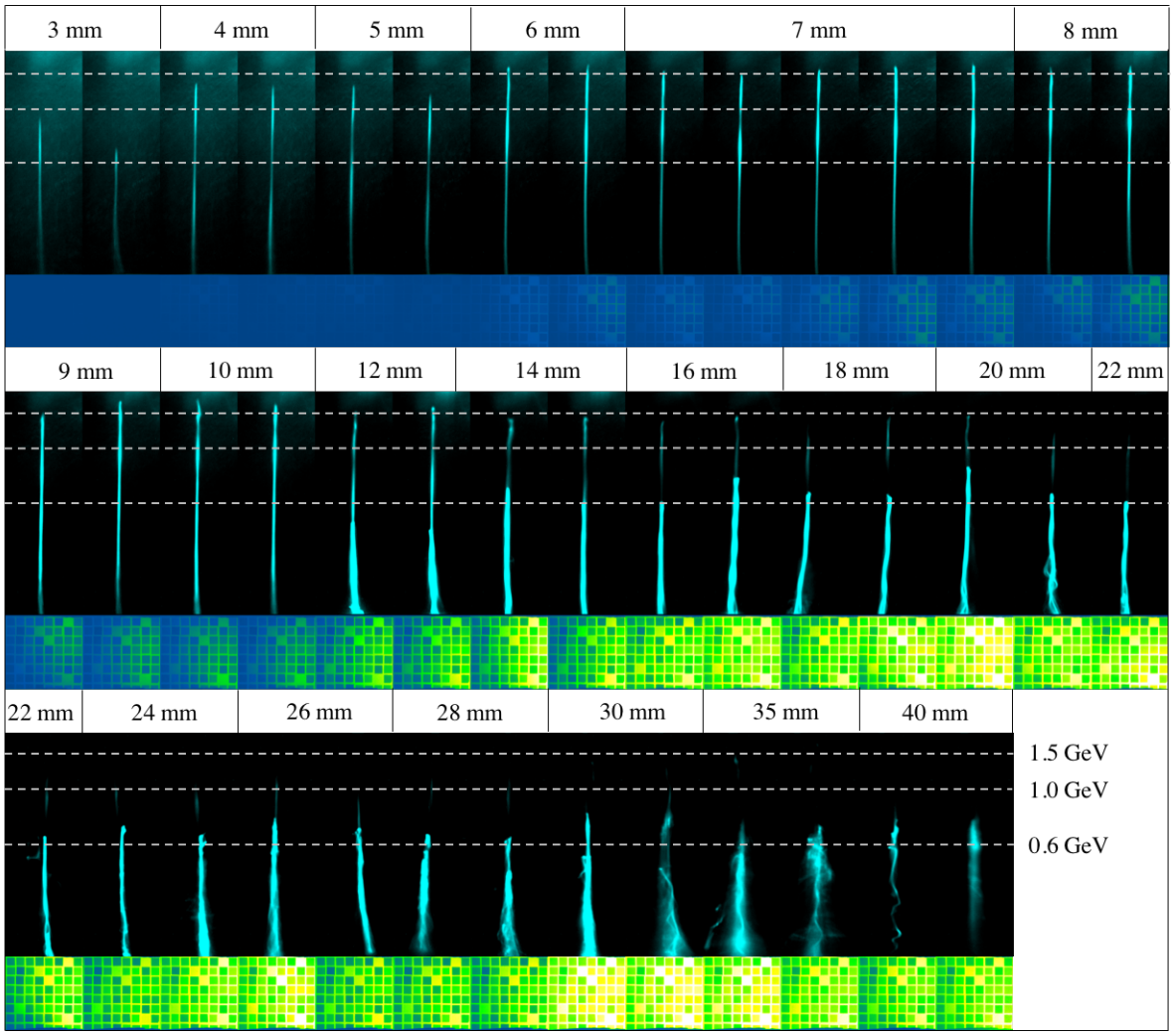


Figure 5.2: A montage of the electron spectrometer and x-ray camera images from a gas cell length scan. All electron spectra are shown on the same colour scale but the second injected bunch has been saturated so that the first bunch can still be seen. Likewise all x-ray images are on the same colour scale.

10 mm is an electron beam being continuously injected over some significant distance via the mechanism of self-injection. This semi-continuous injection is inferred from the 100% bandwidth of the beams. This first bunch is accelerated to energies beyond 1.5 GeV in the first 10 mm of plasma before it dephases. Once the gas cell length reaches 12 mm we see a second population of electrons has been injected that has significantly higher charge than the first bunch. Note that the colour scale in the figure has been saturated so that what remains of the first bunch can still be seen. The low energy cut-off of the diagnostic was 260 MeV, so the bunch will have been injected a little before 12 mm in to the plasma as it had to undergo some acceleration to appear on the electron spectrometer screen. Once this bunch has been injected it accelerates to sub-GeV levels. As the length of the

accelerator increases further the maximum energy of this second bunch does not vary much with length suggesting that the laser energy has depleted, causing a smaller bubble to be driven which has a smaller potential for electrons to gain energy from. The injection and acceleration of the second bunch seems to be correlated with the dephasing of the first bunch, which is losing charge from its highest energy part between $\sim 14 - 26$ mm, after which is disappears from the diagnostic completely.

Over the first 10 mm the x-ray intensity increases with cell length. This mirrors the fact that the electron number spectrum dN/dE is increasing in amplitude at the highest energies, which is to say that the peak electron energy is increasing and the number of electrons at high, say above 1 GeV, energies is also increasing. However the injection and acceleration of the second bunch is correlated with a significant increase in the number of detected x-rays between the lengths of approximately $12 - 22$ mm. After this there is relatively little variation in the detected x-ray intensity, and x-ray flux remains high independent of further increases in accelerator length.

A similar pattern for both the electron beam and the x-ray beam was seen at densities of 2.6, 2.8 and 3.3×10^{18} cm^{-3}. No injection of a second bunch was seen at the lower density of 1.9×10^{18} cm^{-3}, and at the high density of 5.7×10^{18} cm^{-3} the beams were so divergent that it was not possible to see such detail in them. When it was observed, the length at which the second bunch was injected was almost constant with plasma density: at 2.3, 2.6, and 3.3×10^{18} cm^{-3} it was at 12 mm and at 2.8×10^{18} cm^{-3} it was at 14 mm.

5.3.2 Study of the Electron Energy Spectrum

We start by comparing the spectrum of the initially injected bunch to the spectrum after the second bunch has been injected. Taking shots from 10 mm and 14 mm gas cell lengths at $n_e = 2.3 \times 10^{18}$ cm^{-3}, the spectra are compared in figure 5.3. The graphs of charge per 0.1% BW plotted against energy (calculated as $Q/0.1\%\text{BW} \approx 10^{-3} E \times dN/dE$) demonstrate the dramatic difference in injected charge between the first and second injected bunch. Between the two measurements the charge per 0.1% BW has increased from ~ 0.04 pC/0.1%BW at 600 MeV before the secondary injection happened to ~ 0.4 pC at just under 600 MeV after the second injection. It is interesting to note that what is being referred to as the 'first injection' actually appears to be the sum of at least 3 separate injections of charge. There is no significant change in beam divergence between the three bunches suggesting that each has the same injection mechanism. A comparison of the divergence of the first and second bunch is made in figure 5.4, showing that the divergence of the second bunch is only slightly larger than the first bunch.

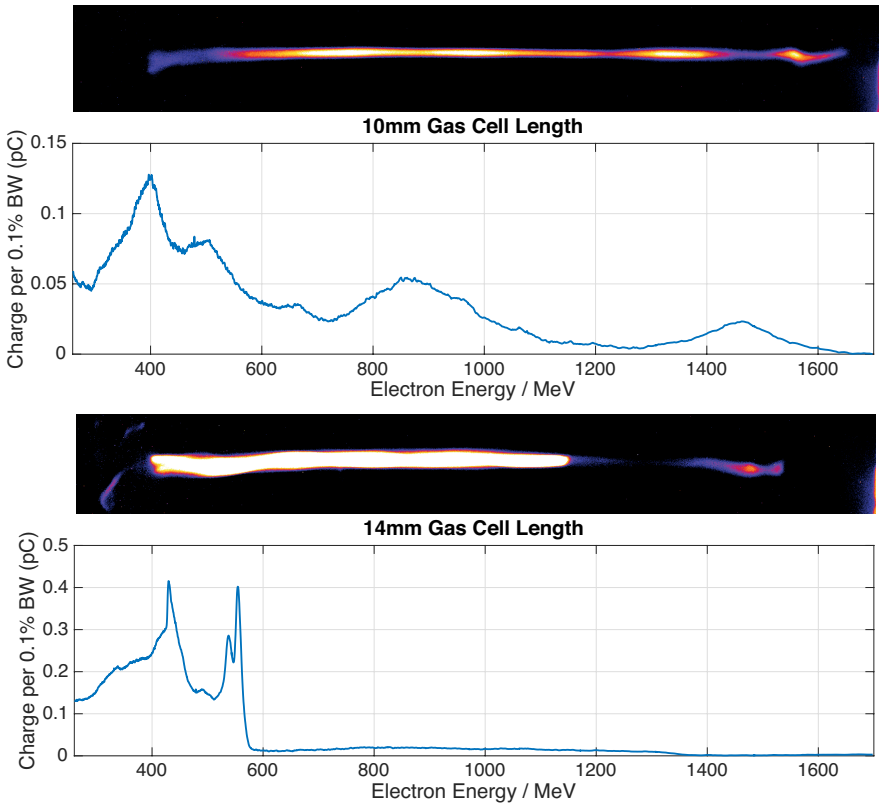


Figure 5.3: Comparison of the energy spectra of the first injected bunch just before dephasing (top image and graph) and the second injected bunch shortly after it was injected (bottom image and graph). The colour scale has been saturated in the lower image so that the high energy features can be seen.

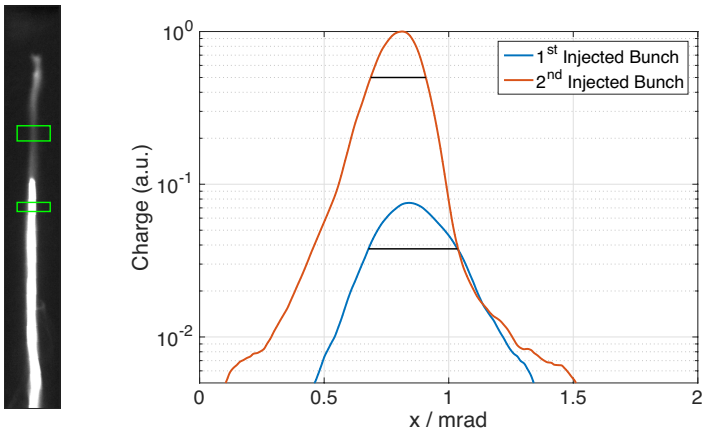


Figure 5.4: Comparison of the divergence of the first and second injected electron beams. The raw image is shown on the left. The divergence was found by summing along the columns inside the green rectangles. On the right is a graph of the charge as a function of the transverse x coordinate. The black lines indicate the FWHM width.

It looks more divergent in the images simply because it is much brighter. This is a strong indication that the injection mechanism is similar for both bunches. As the plasma target was uniform and free from impurities, the cause of the multiple injection events must be the evolution of the laser pulse, which is ultimately what is giving the bubble its properties. This would be an experimental realisation of the work in [126] and [127], which showed that laser driven bubble evolution can move electrons from untrapped to trapped orbits. Bubble contraction truncates the trapping, giving rise to quasi-monoenergetic electron spectra. Multiple bubble oscillations can, therefore, result in electron spectra similar to those shown in figure 5.3. The plasma wavelength at $n_e = 2.3 \times 10^{18}\,\mathrm{cm}^{-3}$ is $22\,\mu$m, meaning that the $\sim 50\,\mu$m FWHM focal spot used in this experiment was mismatched to the plasma. Therefore a lot of pulse evolution will have been necessary to drive a nonlinear wakefield and trap charge, lending further weight to this hypothesis. This interpretation is also backed up by PIC simulations [224].

Figure 5.5 shows the variation in the peak electron energy of the first and second bunches as a function of accelerator length. Almost all of the spectra had a peak in $Q/0.1\%$BW at high energy. The energy of the centre of this peak is what is reported as the peak energy. The errors were calculated from the uncertainties in the position of

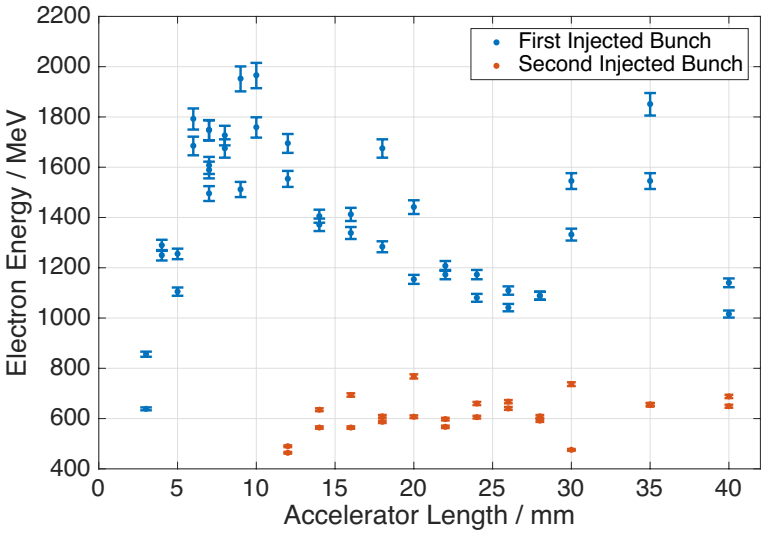


Figure 5.5: Peak energies of the first and second injected bunches.

the screen relative to the source, which were ± 1 mm in both height (y) and the axial direction (z). Particle tracking simulations showed that the uncertainty in the y position dominated the uncertainty in electron energy by a factor of approximately 10 over the uncertainty in z. Therefore the errors shown are from the uncertainty in the y position of the spectrometer screen only. This graph is just a quantitative summary of what we saw in figure 5.2. The first bunch of injected electrons are rapidly accelerated to almost

2 GeV over the first 10 mm, at which point they begin to dephase. After 10 mm we see two interesting phenomena occurring. There is the second bunch injection and also the dephasing of the first bunch. It is particularly noteworthy that the first bunch dephases over a much longer distance than it was accelerated over. This is not unrelated to the observation that the second bunch is only accelerated to ~ 600 MeV independent of accelerator length. Both of these phenomena can be described by the depletion of the driving pulse. As energy is transferred from the laser pulse to the plasma wave a_0 drops, which means that the bubble becomes smaller. This reduces the dephasing length and hence the maximum energy gain. As the bubble decreases in length the back of it catches up to the electron beam, rephasing it in the wake. The first injected bunch remains inside the decelerating part of the wakefield but much closer to the centre of the bubble, so the retarding field it faces is reduced, explaining the slow dephasing.

There is an unexpected increase in electron energy at the longest accelerator lengths. This is thought to be anomalous: looking back at figure 5.2 there is a decrease in x-ray intensity at the longest cell lengths. This should not be possible if the density is constant because what happens at the end of the accelerator can not affect what happens at the start. Therefore we must conclude that the gas flow in the gas cell was different at the longest lengths, and that this data does not make for a reliable comparison to shorter lengths.

Figure 5.6 shows how the charge contained in the first and second injected beams varies with accelerator length. It is necessary to be specific about how these charges are

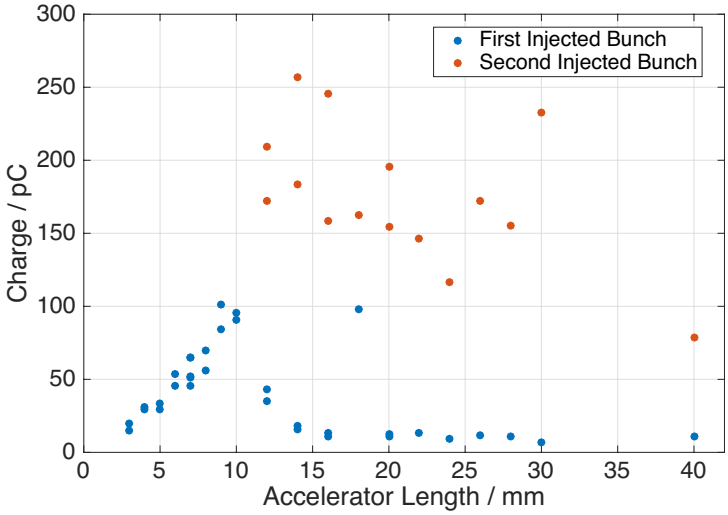


Figure 5.6: Charge contained within the first and second bunches.

defined. The charge quoted as being in the second bunch is all of the charge between

the low energy cut-off of the diagnostic ($\sim$ 260 MeV) and the peak energy of the second bunch. The charge quoted as being in the first bunch is all of the charge between the peak energy of the second bunch and high energy cut-off of the diagnostic. This means that the second bunch charge is an overestimate because it includes some of the charge from the first bunch, and consequently the charge in the first bunch is underestimated. Before the second injection happens the electron beam charge increases linearly with accelerator length, suggesting that charge is being continuously injected in to the wakefield or is being injected in multiple, closely spaced bunches as was suggested by figure 5.3. Indeed there is remarkably little fluctuation from the trend suggesting that self-injection from wakefield driven by a mismatched pulse is a stable and reproducible process. As soon as the second bunch is injected there is an immediate doubling in total charge, meaning that an almost equal amount of charge is injected in both the first and second phases, although there is a larger variation in the amount of charge injected in the second bunch.

5.3.3 X-ray Spectral Measurements

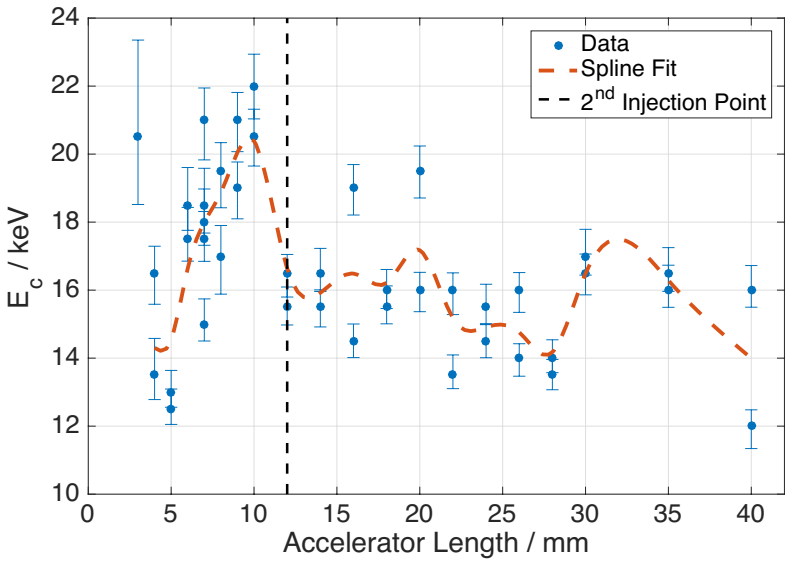


Figure 5.7: E_c as a function of accelerator length at $n_e = 2.3 \times 10^{18}$ cm^{-3}. The dashed red line is a spline fit, ignoring the anomalous first data point[2]. The length at which the second bunch injection is first seen is denoted by the black dashed line.

[2]The analysis code often over-estimates E_c when the signal level is low. This is because uncorrected noise becomes a significant part of the measured filter 'transmission', meaning that all filters have a similar apparent transmission, which would only physically be the case for a very hard x-ray spectrum.

Figure 5.7 shows how the critical energy changes as a function of accelerator length. As we saw in the previous section, the first injected electron bunch is rapidly accelerated to high energy. As one would expect this causes the critical energy of the x-ray spectrum to increase rapidly because of its strong γ^2 scaling. When the second bunch is injected at 12 mm accelerator length, marked on the graph by the black dashed line, there is a sudden decrease in the critical energy. This suggests that the second bunch, which has a much lower γ^2, is contributing significantly to the overall x-ray spectrum and reducing its apparent temperature. After the injection of the second bunch there is little change in the spectral shape. This too is what is expected from the electron results. Due to depletion of the driving laser very little acceleration of the second bunch occurs, independent of accelerator length, meaning that there is very little change in the spectrum of x-rays it emits.

Before the second injection happens the electron and x-ray spectral data can be combined to make an estimate of the betatron oscillation radius from the equation

$$E_c = \frac{3\hbar}{4c}\gamma^2 {\omega_p}^2 r_\beta \tag{5.1}$$

Figure 5.8 is a plot of r_β inferred from this equation as a function of accelerator length, up to a length of 10 mm. The errors are a combination of the uncertainties in the E_c measurement, the plasma density and the electron beam energy error from the uncertainty in the position of the electron spectrometer screen. As was seen in the theory section

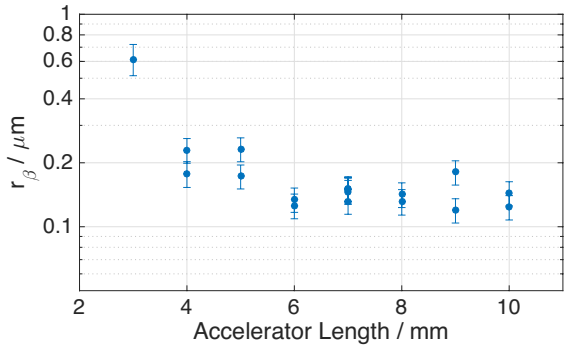


Figure 5.8: r_β as a function of accelerator length for the first injected bunch.

(section 2.4.2, particularly figure 2.10) the betatron oscillation radius rapidly decreases initially before varying very slowly at high electron γ factors. The measured radius of between 100 and 200 nm is smaller than the $r_\beta \gtrsim 0.5$ μm inferred from other works [90] [79] [88] [33] and also what has been found in an $f/20$ set-up at the Gemini laser (section 6.3.2 of this thesis) where $r_\beta = (800 \pm 200)$ nm was found. This adds to the suggestion that the injection mechanism in this $f/40$ experiment was not the standard transverse injection that is usually referred to as self-injection (see sections 2.3.4 and 2.3.5) because

of the dramatically lower trapped volume at similar laser powers and plasma densities. This supports the theory that injection was caused by bubble size changes driven by the evolution of a mismatched laser pulse. At the very least, it shows that injection in our case produces electron beams with much smaller r_β and therefore emittance.

By comparing the x-ray and electron spectra from just before and just after the second electron bunch was injected, i.e. at 10 mm and 12 mm, one can estimate the properties of the individual x-ray spectra emitted by each bunch. At 12 mm, where the first bunch has just started to dephase, the x-ray spectrum from the first bunch is assumed to be the same as that from 10 mm, where $(E_c = 21 \pm 1)\,\mathrm{keV}$. As shown in figure 5.10, there is approximately a tripling in the total number of x-ray photons when the second bunch is injected. When this happens the measured E_c, assuming a single on-axis synchrotron spectrum, falls to (16 ± 1) keV. This total spectrum can, therefore, be approximated by the sum

$$A\ S(E, 21\mathrm{keV}) + 2A\ S(E, E_{c2}) = 3A\ S(E, 16\mathrm{keV}) \tag{5.2}$$

A is related to the amplitude of the spectrum of the first injected bunch and S is the on-axis synchrotron spectrum. We now find E_{c2} from a range of trial values that minimises the squared difference between the integral over all energy of the left and right hand sides of this equation. This produces a best fit $E_{c2} \approx 7.3$ keV. Combining this with the peak electron energy from figure 5.5, of approximately 480 MeV, suggests a larger betatron radius of the second bunch of ~ 700 nm.

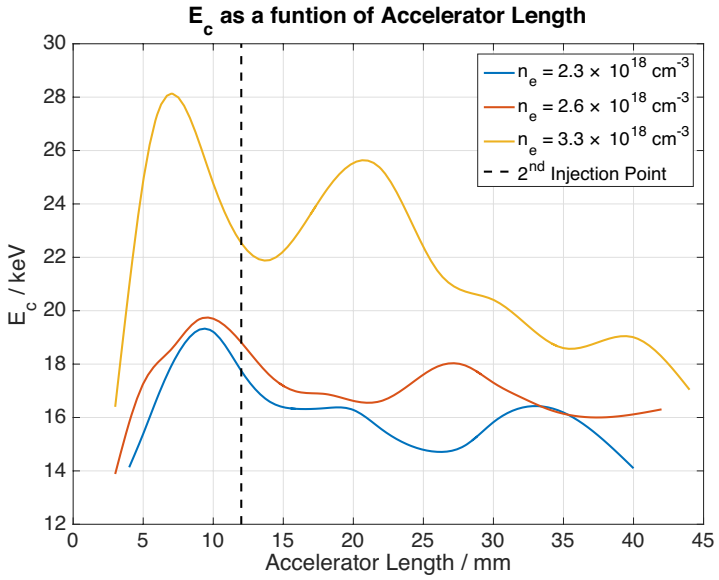


Figure 5.9: E_c as a function of accelerator length at a range of plasma densities. Only spline fits are shown for the sake of clarity.

Finally, the critical energy as a function of length is plotted for three different plasma densities in figure 5.9. For clarity only the spline fits are plotted. This data shows that the critical energy of the spectrum can be tuned at any length by changing the plasma density. Higher densities produce harder spectra, with an increased r_β being a likely candidate. This will be confirmed in section 5.4.

Now that we have a good understanding of the behaviour of the shape of the x-ray spectrum, attention will be turned to the number of photons emitted by, and therefore the brightness of, this source.

5.3.4 X-ray Brightness

Figure 5.10 shows the number of photons emitted by the source with an energy above 1 keV, assuming a FWHM beam divergence of 8 mrad from figure 5.13, at a plasma density of 2.3×10^{18} cm^{-3}. Within 3 mm of the second injection the total number of photons

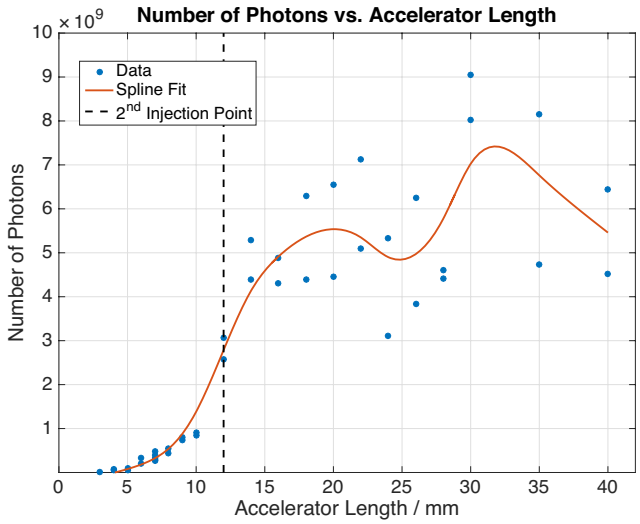


Figure 5.10: Total number of photons as a function of accelerator length at $n_e = 2.3 \times 10^{18}$ cm^{-3}. The black dotted line shows the length at which secondary injection was first observed.

increases five-fold. The reason for this lies in the energy emitted per betatron oscillation from equation 2.166,

$$W_{tot} = \frac{e^2}{6\epsilon_0} N_e N_\beta \gamma^2 K_\beta^2 k_\beta = \frac{e^2}{6\epsilon_0 c^3} N_e N_\beta {\omega_p}^3 \gamma^{5/2} {r_\beta}^2 \tag{5.3}$$

The number of electrons N_e is doubled by the second injection and r_β increases by a factor of $\sim 700/150 = 4.7$. The number of oscillations per electron $N_\beta \propto L/\lambda_\beta \propto \gamma^{1/2} L$ where L is the acceleration length. At, say, 20 mm acceleration length the first bunch has been

accelerated for ~ 20 mm and has $\gamma \sim 3000$ (see figure 5.5). The second bunch has been accelerated for ~ 8 mm to a $\gamma \sim 1200$. From this one can calculate that $N_{\beta 1} \sim 12$ and $N_{\beta 2} \sim 7$. Combining all of these factors in equation 5.3 results in the ratio of the total emitted energy by the second bunch to energy emitted by the first bunch of ~ 2.6. To convert this to a ratio of the number of photons, it is necessary to work out the mean photon energy of each spectrum. A 21 keV critical energy spectrum has a mean photon energy, of photons above 1 keV, of ~ 19 keV. A 7.3 keV critical energy spectrum has a mean photon energy above 1 keV of ~ 7.5 keV [3]. Therefore the ratio of the number of photons emitted by the second bunch to the first bunch is $\sim 2.6 \times (19/7.5) \approx 6.6$. Figure 5.10 shows an increase in photon number by a factor of $5-6$, which is in reasonable agreement with the estimate considering the number of approximations that have been made. This suggests that it is acceptable to assume for x-ray calculations the electron beam can approximated by a beam of its peak energy, and it gives more confidence in the very small source sizes of $100-200$ nm reported in the previous section. Figure 5.10 also highlights a trade-off between minimising the source size and maximising the number of photons. However for many conceivable betatron probing experiments, such as spectroscopic experiments, the source size is not important, so by acting to increase the amount of charge undergoing large betatron oscillations the number of photons, especially at moderate energies, can be dramatically increased.

Brightness as a function of accelerator length at $n_e = 2.3 \times 10^{18}$ cm^{-3} is plotted in figure 5.11. For lengths below 12 mm the source radius was taken from figure 5.8, and for lengths of 12 mm and above the source radius was assumed to be 0.5 μm. The maximum peak brightness on any shot was 2.8×10^{24} photons/s/mm^2/mrad^2/0.1%BW, a factor of ~ 7.5 increase on the highest reported brightness from an $f/20$ experiment. Furthermore, this is brighter than any previously reported betatron source. At short accelerator lengths, the increased brightness is due to a reduction in source size. At long accelerator lengths, it is driven by a large increase in the number of photons emitted. It is emphasised that the brightness of 3.7×10^{23} photons/s/mm^2/mrad^2/0.1%BW from an $f/20$ experiment was from a single shot. The average brightness taken over a number of shots in the same conditions was $\sim 1.8 \times 10^{23}$ photons/s/mm^2/mrad^2/0.1%BW. Figure 5.11 shows a grouping of three brightness measurements taken at 9 and 10 mm accelerator lengths with a brightness of $2.2-2.8 \times 10^{24}$ photons/s/mm^2/mrad^2/0.1%BW, meaning that taken over a number of shots the mean peak brightness of in this experiment was a factor of ~ 14 larger than from shorter focal length experiments.

[3] The mean energy of a 7.3 keV spectrum is of course less than the critical energy, although it has turned out to be higher here because we have ignored all photons with energies lower than 1 keV to stay consistent with the filter array analysis procedure.

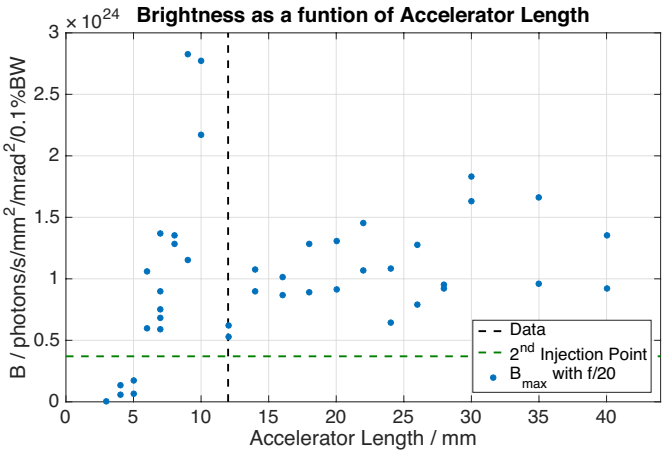


Figure 5.11: Brightness as a function of accelerator length at $n_e = 2.3 \times 10^{18}$ cm^{-3}. The black dotted line shows the length at which secondary injection was first observed. The green dashed line shows the highest brightness measured on a single shot in an $f/20$ geometry

5.4 X-ray Beam Profile

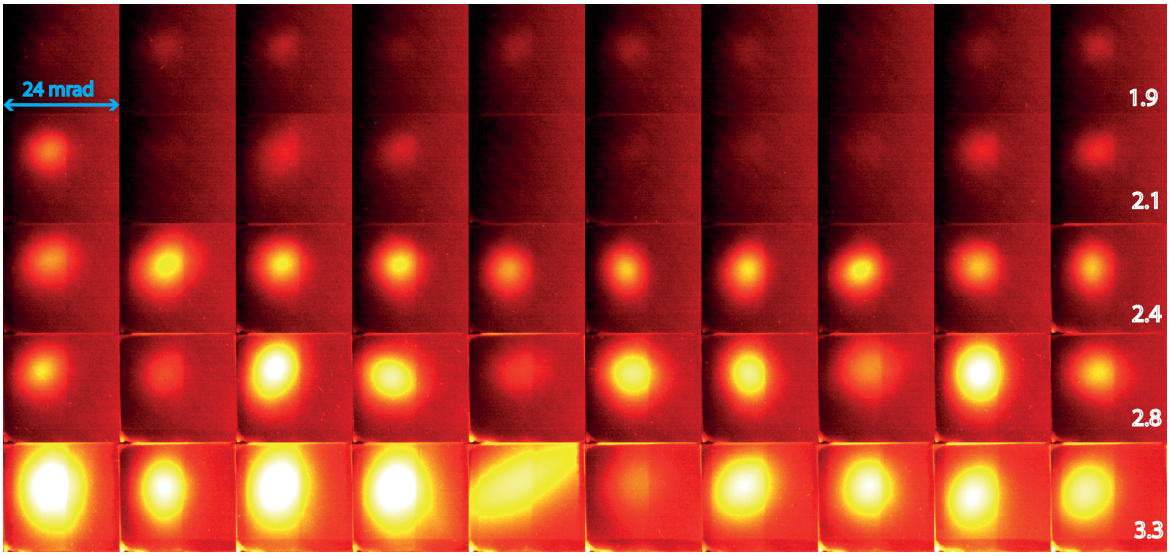


Figure 5.12: Montage of x-ray profile images showing variation as a function of plasma density. Each row is at the same plasma density, which is given in units of 10^{18} cm^{-3} in the white numbers on the right-hand side.

The x-ray beam profile was studied as a function of number density at a fixed gas cell length of 20 mm with a laser a_0 at focus of (1.43 ± 0.05). The density was varied between the limits $(1.5 \pm 0.2) \times 10^{18}$ cm^{-3} and $(3.3 \pm 0.4) \times 10^{18}$ cm^{-3}. The systematic error on the density is of order 10%, while the random error is $1 - 2\%$. While some electron acceleration was observed at $n_e = (1.5 \pm 0.2) \times 10^{18}$ cm^{-3} and $(1.7 \pm 0.2) \times 10^{18}$ cm^{-3}, the number of x-ray photons was below the detection limit of the diagnostic. The minimum

density at which x-rays were observed was $(1.9 \pm 0.2) \times 10^{18}\,\mathrm{cm}^{-3}$. A montage showing 10 x-ray profile images per density is displayed in figure 5.12. We see that the x-ray beams are close to being circular in almost all cases meaning that the distribution of electron beam momenta inside the wakefield is approximately the same width in both transverse directions. What this is also saying is that the shape of the beam is close to circular in the wakefield. There is an increase in beam divergence with n_e, which is shown more clearly in the graph in figure 5.13, where the errors are the standard error from 10 shots. The increase in divergence is approximately linear with n_e. At all densities, apart from $(3.2 \times 10^{18})\,\mathrm{cm}^{-3}$, the horizontal and vertical divergence is the same to within errors. Both the montage and the graph show that there is an optimal density for stability at $\sim 2.4 \times 10^{18}\,\mathrm{cm}^{-3}$, at which density it has a divergence of $(9.1 \pm 0.5) \times (9.2 \pm 0.2)\,\mathrm{mrad}$.

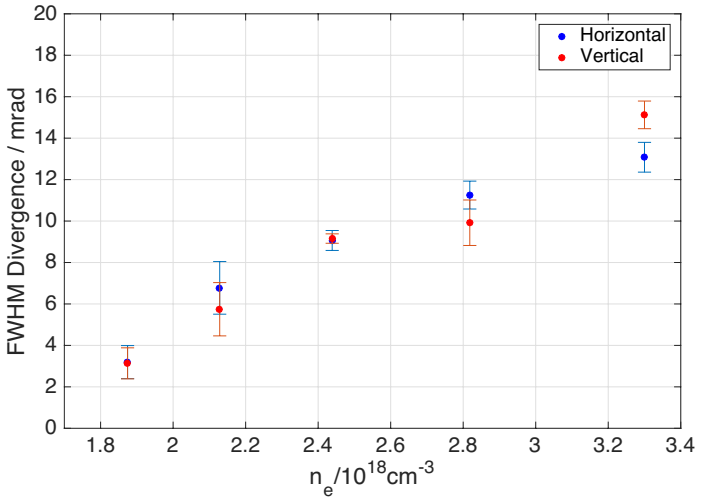


Figure 5.13: FWHM x-ray beam divergence as a function of plasma density in a 20 mm gas cell.

The x-ray intensity from the beam profile measurements as a function of n_e is shown in figure 5.14, showing a strong scaling. The intensity quoted is simply the sum of the counts in an image, averaged across 10 shots. To try to understand the properties of the x-ray beam profile, the electron beam maximum energy and total charge in the beam (above 260 MeV) were found, and these are plotted in figure 5.15.

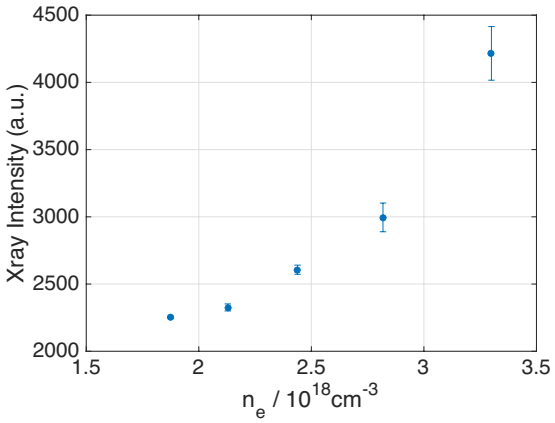


Figure 5.14: X-ray intensity as a function of plasma density in a 20 mm gas cell.

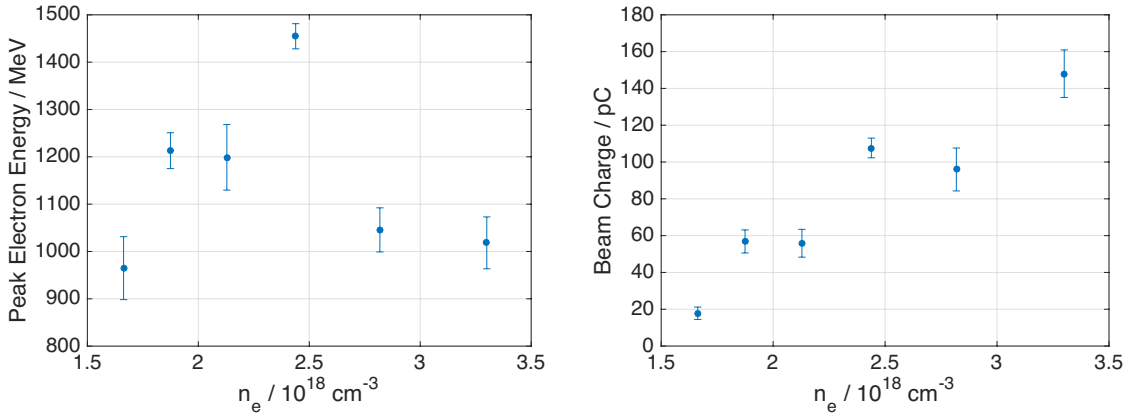


Figure 5.15: Peak electron energy (left) and total beam charge (right) from the run where the x-ray profile data was taken.

The electron energy increases with density up to close to 1.5 GeV at 2.5×10^{18} cm^{-3}. The dramatic decrease in electron energy after this is attributed to quicker dephasing in the lower velocity wakefield at higher density. The charge increases close to linearly with density, which is unsurprising given that the trapping threshold is lower at higher density. Comparing this also with the linear increase in beam divergence with density, figure 5.14, suggests that the transverse area of the trapped electron population increases with plasma density i.e. at higher densities r_β is higher. r_β can be calculated from the x-ray beam divergence as $\theta \approx K/\gamma = k_\beta r_\beta = \omega_p r_\beta/(\sqrt{2\gamma}c)$. Using the $1/e$ divergence as θ and the peak electron energy from the left-hand side of figure 5.15 allows r_β to be plotted as a function of n_e, which is done in figure 5.16. No points are shown after the electron beam is dephased because the measured electron energy will not be representative of the electron energy when the peak x-ray emission happened. This shows once again that sub-micron betatron source sizes are achievable and that by going to lower number densities

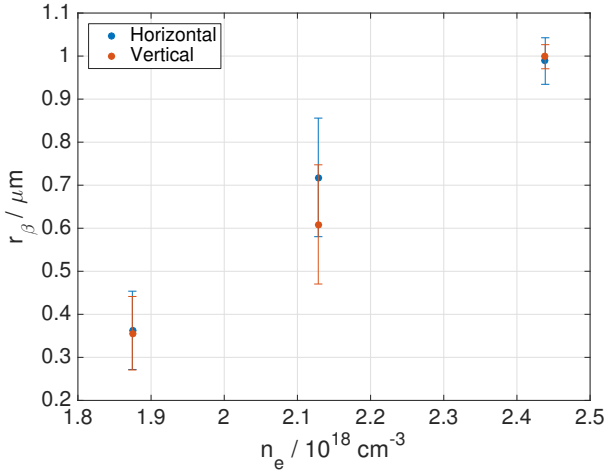


Figure 5.16: Betatron oscillation radius as a function of n_e measured from the x-ray beam divergence.

the transverse size of the trapped volume is reduced. Note that at these densities the electron beam energy was lowest for the smallest r_β, meaning that by scanning plasma density, the source size can be reduced but at the expense of critical energy and the number of photons (which we also saw in figure 5.12).

The pointing stability of the beam is quantified in figure 5.17, where zero is defined as being on the laser axis. The error bars show the standard deviation from 10 shots to give a

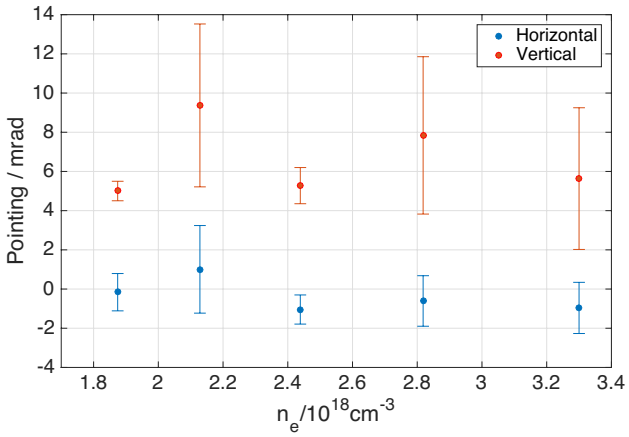


Figure 5.17: Horizontal and vertical x-ray beam pointing as a function of plasma density.

better idea of the fluctuations. Horizontally, within errors, there was very little deviation from the laser axis. Vertically there was an offset of $5 - 10$ mrad, that followed no real pattern with plasma density, and often with larger fluctuations than in the horizontal case. Practically speaking, from an x-ray imaging point of view, the absolute pointing

is of no great importance but pointing fluctuations should be minimised. Note that at $n_e = 2.4 \times 10^{18}$ cm^{-3}, the optimal density for beam divergence stability, the pointing stability is also best, or at least as good as for 1.9×10^{18} cm^{-3}. In the best conditions the 1σ pointing fluctuation was better than 1 mrad. The solid angle taken up by the x-ray camera chip, at 3.57 m from the source, was 7 mrad meaning that the best pointing fluctuation was not prohibitive to x-ray imaging.

5.5 Stability of the Betatron Spectrum

During this experiment a 533 shot run was completed taking a betatron x-ray tomography of an embryonic mouse, which is currently being written up for publication [225]. An example projection is shown in figure 5.18, although the point being highlighted here is that the imaging filter array (see appendix 8.9.3) allowed the critical energy to be measured on every shot. Therefore an extensive study of the stability of the betatron spectrum could be performed over significantly more shots than has been reported before.

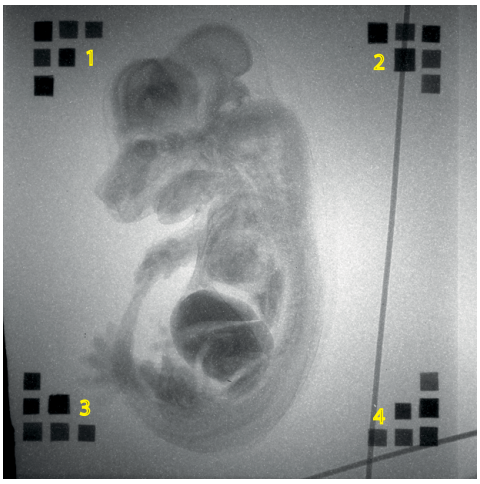


Figure 5.18: Betatron image of an embryonic mouse. The filter regions (labelled $1-4$) produced an on-shot measurement of the critical energy.

Figure 5.19 plots the critical energy as a function of shot number from the 533 shot run. The plasma density was held within the limits $n_e = (2.6 - 3.0) \times 10^{18}$ cm^{-3} and the mean laser energy delivered to target was (9.4 ± 0.6) J, corresponding to $a_0 = 1.43 \pm 0.05$. The figure shows that over the first $\sim 250 - 300$ shots the critical energy stayed almost constant. The critical energy measured by all 24 filters combined, $E_{c,tot}$ on the graph, was (18.1 ± 1.3) keV. The error here is the standard deviation to better highlight the fluctuation in E_c. The standard deviation is small at just 7% of the mean value. To obtain this, the calculation excluded a small number of points with a very bad fit, which can happen when the pointing fluctuation of the beam causes very low signal levels on one or more of the corners. This also explains the small number of points in the graph that lie

well above the curve. After shot number ~ 250, there is a fall off in critical energy which

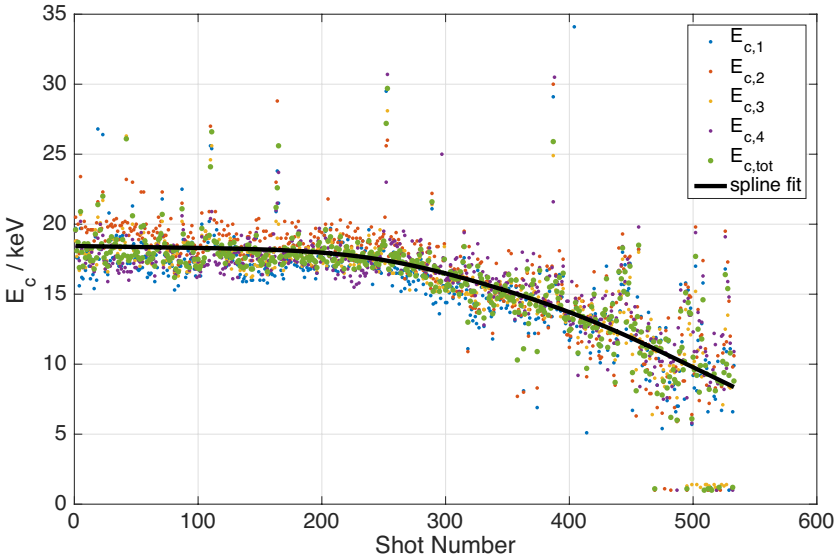


Figure 5.19: Critical energy as a function of shot number on the 533 shot stability run. The number in the legend subscripts denotes which filter region number the critical energy was retrieved from (see figure 5.18), and $E_{c,tot}$ takes in to account all filters. The black line is a cubic smoothing spline fit to $E_{c,tot}$.

was slow at first and became quite a rapid degradation towards the end. The critical energy is a function of three parameters: the electron beam energy (which depends on the plasma density and the laser a_0), the plasma frequency (which is related to the plasma density) and the betatron oscillation radius (which is dependent on the electron energy and the injection conditions, which themselves must be related to the plasma density and the laser a_0). Therefore the declining performance must be driven either by a change in the properties of the plasma source, i.e. the gas cell, or by a drop in the intensity of the laser, meaning that the laser energy declined, the temporal duration increased or the focal spot degraded, a sign of which would be a reduction in the proportion of energy contained within the FWHM, because energy contained far away from the centre of the pulse is likely to diffract away rather than contribute to driving the bubble. It is common for high power lasers to decline in performance over a long shot run (shot runs of this length take multiple hours) because of thermal changes or mechanical vibrations causing misalignments etc. in the system that are not self-correcting[4]. These issues will now be explored in relation to the experiment being reported here.

[4]This is not to say that correcting these long-term drifts would be an impossible task. Auto-alignment systems exist and are used in many laser systems, although most lasers currently used to drive LWFA's are themselves research systems, therefore auto-align systems have not been fully implemented in them yet.

The plasma target can degrade over time by unguided laser energy ablating the entrance and, especially, the exit cone. This causes more gas to escape from the gas cell meaning that the plasma density is lower than intended, because it is inferred during the run from the backing pressure that was applied to it. However as seen in figure 5.20 there is very little degradation of the exit cone over the run. As the left hand side of figure 5.20

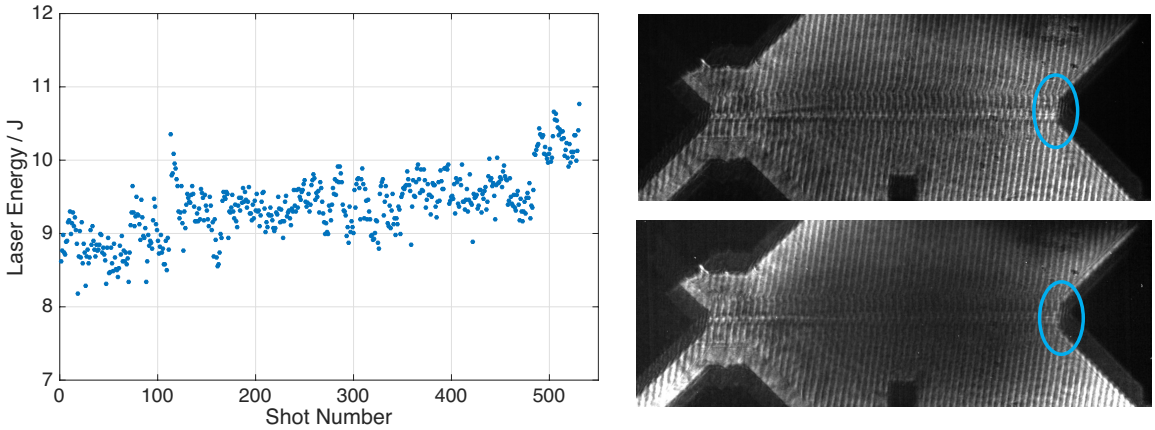


Figure 5.20: Laser energy (left) and gas cell condition (right) throughout the betatron stability run. The top image of the gas cell, which was taken with the moiré diagnostic, is from the first shot and the bottom image is from the 533'rd shot. The exit cone region, highlighted by the blue circle, barely changes throughout the whole run.

shows, the laser energy actually increased over the run: it was artificially raised to try to combat the decline in betatron performance. This means that the cause of the declining betatron performance over this extended run has to be something that was not measured on shot, with a likely candidate being the laser focal spot quality. While data was not taken on this run, focal spot data from a different day on the same experiment showed that over the course of approximately 8 hours and 318 shots the proportion of energy within the FWHM dropped from $(32 \pm 3)\%$ to $(26 \pm 1)\%$, representing a significant decline in focal spot quality. It should be noted that this was a degradation in the low power, not full power, focal spot. The capability to measure the full power Gemini focal spot did not exist at the time of this experiment, although it seems illogical that a poor quality low power spot could be amplified in to a high quality full power spot. A detailed study of the effects of poor focal spot quality on the electron beam, and hence x-ray production, would require a computationally very expensive parameter scan using 3 spatial dimensions in the simulations. 3D simulations would be required to model aberrations in the focal spot, and to capture these in full the shape of the full power wavefront close to focus would have to be known, and unfortunately this information was not available. However this is an issue that has been explored in the literature. Vieira et al. [226] showed via an analytic model that the presence of higher order Laguerre-Gaussian modes in the transverse laser

profile usually leads to lower energy gains from LWFA compared to a purely gaussian pulse. This result was backed up by 3D particle in cell simulations based on a realistic sum of modes that were used to approximate a real laser pulse from [57], showing a drop in electron energy by a factor of approximately 1/3. This would significantly reduce the critical energy of the x-ray beam and the total emitted x-ray energy through their γ^2 and $\gamma^{5/2}$ scalings respectively.

What this section has shown is that self-injected electrons accelerated in a self-guided LWFA can create a reproducible betatron spectrum. Considering that, at constant density, $E_c \propto \gamma^2 r_\beta$, and that electrons are being injected via a highly nonlinear process, this is quite a remarkable result. The fall-off in critical energy at later times seems to be driven by the laser properties. Therefore this experimental geometry and the gas cell target should be usable as a reproducible, ultrafast hard x-ray source for experiments with numbers of shots in the 1000's, if the laser reproducibility can be improved.

Coming to the x-ray intensity, the total number of counts on the x-ray camera is plotted as a function of shot number in figure 5.21. It is of particular interest to note that the number of x-ray counts appears to be anti-correlated with laser energy, which is an unexpected result.

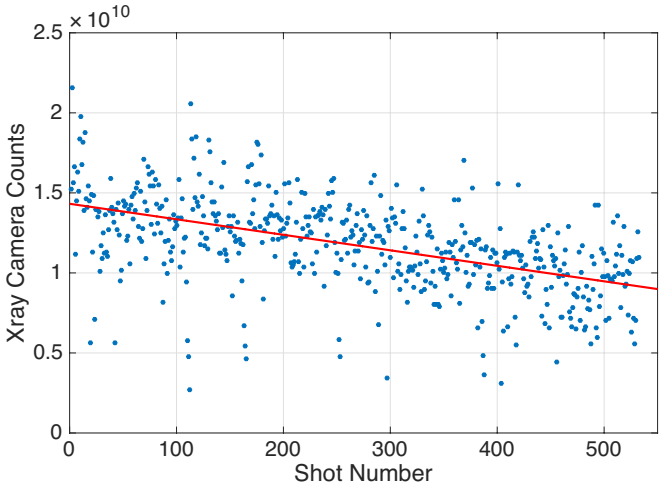


Figure 5.21: Number of x-ray camera counts vs. shot number for the betatron stability run. The blue dots are the data points and the red line is a linear fit.

5.6 Spatial Variation in the X-ray Spectrum

To make a measurement of how the spectrum changed across the beam, the imaging filter array was used in conjunction with the small 16 filter array (appendix 8.9.2) as shown in

figure 5.22. The x-ray beam was reasonably well centred on the 16 filter array on all of

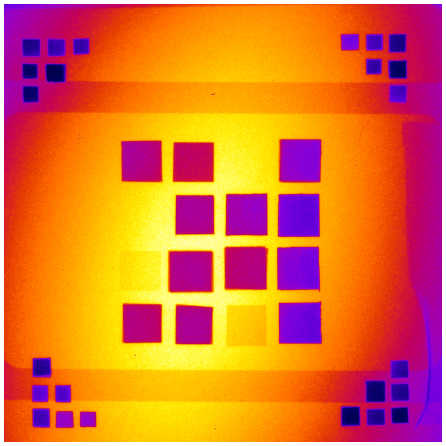


Figure 5.22: Method of analysing the spatial variation in the betatron spectrum.

the shots presented here. The spectrum was calculated from the centre 16 filters as well as each of the four corner arrays on the same shot. Assuming that the x-ray beam was centred on the 16 filter array then the corner arrays were $\sim 4.5\,\text{mrad}$ off-axis. So far in this thesis it has been assumed that the betatron spectrum is constant over the angular range taken up by the x-ray camera, typically around $8 - 10\,\text{mrad}$ full angle. This is in reasonable agreement with the findings in [227], where the peak x-ray energy was seen to drop by $\sim 15\%$ over the first $4 - 5\,\text{mrad}$ away from the centre of the beam, albeit with quite large errors. To check this assumption an on-axis synchrotron spectrum was fitted to each filter region, the results of which are shown in figure 5.23. These shots were taken at a density $n_e = (3.3 \pm 0.4) \times 10^{18}\,\text{cm}^{-3}$ and a laser energy on target of $(8.7 \pm 0.2)\,\text{J}$, corresponding to a focussed $a_0 = 1.37 \pm 0.05$. There is an apparent fall off in the measured E_c with this step off-axis from ~ 30 to $\sim 20\,\text{keV}$. While the errors on the fit are quite large, the fact that E_c is measured to be lower off-axis on every shot makes this a significant result. To describe this we consider the off-axis spectrum from equation 2.155. For this set of plasma and laser parameters $\gamma \sim 1900$ and the divergence from figure 5.13 suggests a wiggler parameter $K_\beta \sim 23$. Remembering to replace γ by the effective $\langle\gamma\rangle = \gamma/\sqrt{1 + {K_\beta}^2/2}$ in a plasma wiggler the observed results can be explained by figure 5.24. This plots the on-axis synchrotron spectrum with $E_c = 33\,\text{keV}$, as measured on shot 2 in figure 5.23, along with the off-axis spectrum for the same critical energy with $\theta = 4.5\,\text{mrad}$. The relative amplitude between these spectra is correct from the theory. On this shot the critical energies measured off-axis, with the naive assumption of an on-axis synchrotron spectrum, averaged to $\sim 22\,\text{keV}$. The black line on the graph plots this spectrum, where the amplitude has been normalised to the amplitude of the

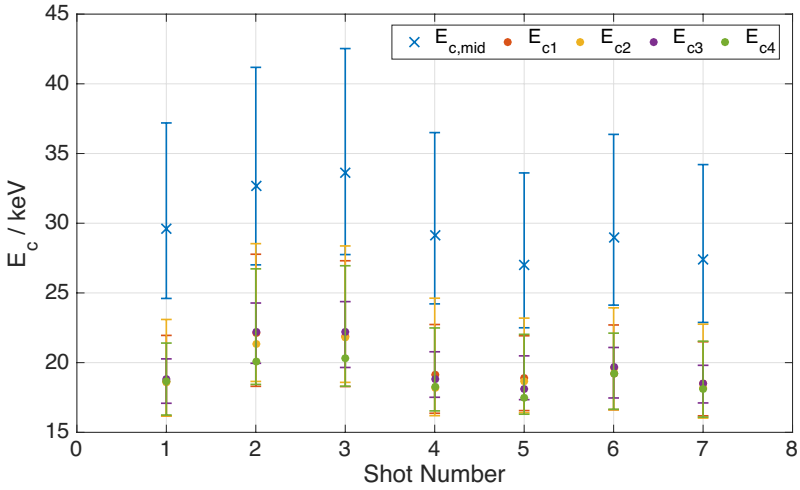


Figure 5.23: Spatial critical energy variation of the betatron x-ray beam for seven consecutive shots. $E_{c1}, E_{c2}, ...$ are the critical energies measured from each corner of the filter array, going top left, top right, bottom left, bottom right in figure 5.22. $E_{c,mid}$ was measured from the central 16 filter array.

off-axis spectrum[5]. The dashed lines are on-axis spectra for 19 and 25 keV to give an idea of how the errors on the measured value would affect this result. This graph shows that the measurements made in this section indicate that the betatron spectrum is well approximated by the off-axis synchrotron spectrum.

Considering that the critical energies reported earlier in this chapter from the full-chip 64 filter array assumed an on-axis spectrum, they are likely to be slight underestimates of the real E_c. One can approximately say that off-axis, the effective critical energy $E_c' \approx E_c / \left(1 + \langle\gamma\rangle^2 \theta^2\right)^{3/2}$. At 4.5 mrad off-axis for the parameters here, this is a reduction of ~ 1.4, which is in agreement with the measured values in figure 5.23. However since this is the extreme case (i.e. comparing on-axis to as far off-axis as we could detect), the measured critical energy from the 64 filter array would have been less than 1.4 times reduced from the real critical energy. Note that this also means that the reported r_β are also underestimated by a factor between 1 and 1.4, although even taking this in to account (which no comparable study has done) these would still be the smallest source sizes reported for betatron radiation.

[5]This is a consistent approach because the analysis code considers differences in filter transmission relative to the vacuum, so the absolute intensity makes no difference to the measured critical energy.

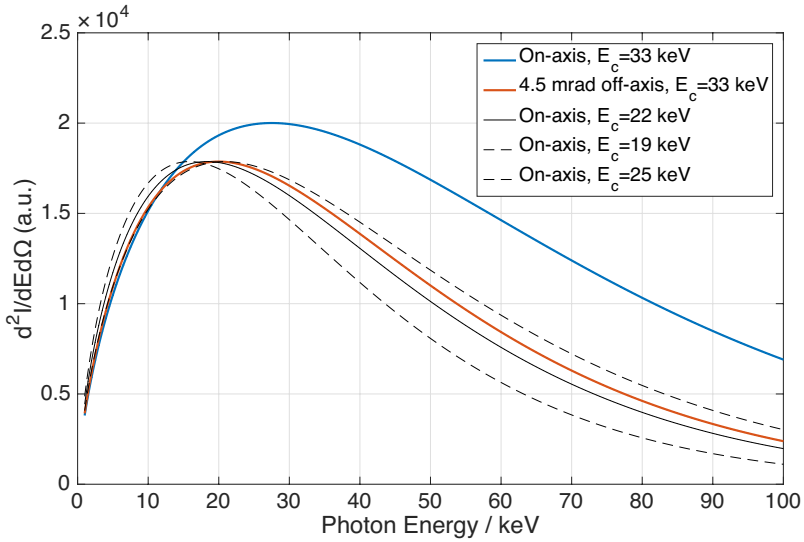


Figure 5.24: A comparison of on-axis and off-axis synchrotron spectra.

5.7 Measurements of the X-ray Imaging Resolution

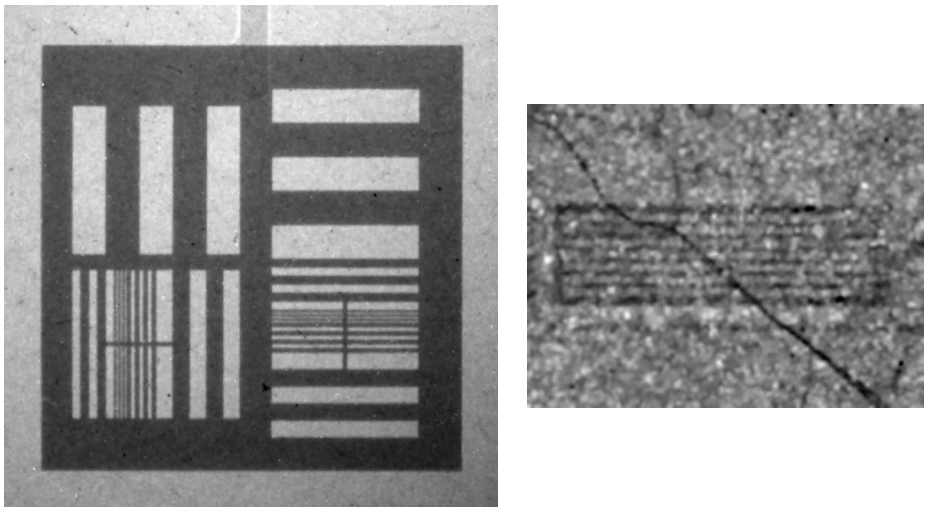


Figure 5.25: X-ray imaging resolution in the $f/40$ experiment. Left: image of the gold resolution target with a magnification of 10.7. The smallest bar spacing in the target was 10 μm. Right: 29 times magnified image of the 4 μm bars in the JIMA target, which was the smallest bar spacing that could be resolved.

Figure 5.25 shows that bar spacings of 10 μm can be resolved at a magnification of 10.7, suggesting that features spaced by $100 - 110\,\mu$m at the scintillator plane can be resolved. This image was taken using a 10 mm cell length at a density of $(2.6 \pm 0.3) \times 10^{18}$ cm^{-3}, with a laser $a_0 \sim 1.4$. The right-hand side of the figure shows that bar spacings of 4 μm can be resolved with a magnification of 29. This was with a 20 mm cell length, plasma density

$(2.3 \pm 0.3) \times 10^{18}\,\mathrm{cm}^{-3}$ and $a_0 \sim 1.1$. The $3\,\mu$m bars could not be resolved, implying that the resolution limit at the scintillator lies in the range $\sim 90 - 120\,\mu$m. Given the small source sizes reported in this chapter, of significantly less than $1\,\mu$m, then even for 29 times magnified objects the imaging resolution is limited by the scintillator MTF.

5.8 Summary and Outlook

This chapter has reviewed the results of a LWFA experiment driven by a slowly focussing $100 - 200\,$TW pulse focussed by an $f/40$ optic. The large, approximately $50\,\mu$m FWHM diameter, focal spot was mismatched to the plasma and had a relatively low initial a_0 of $1.1 - 1.4$. An accelerator length scan was performed which revealed that electrons were rapidly accelerated over the first 10 mm of the plasma to energies as high as 1900 MeV, after which they start to dephase. At an accelerator length of 12 mm an additional bunch of electrons was injected with a charge per unit bandwidth ten times higher than the first bunch, and approximately double the total charge. It is believed that the multiple injections are caused by evolution of the pulse in the plasma due to self-focussing and self-compression. Once injected the second bunch was accelerated to a maximum of $\sim 600\,$MeV, much lower than the first bunch, suggesting that significant laser depletion had happened by this time.

The second bunch injection was correlated with a large increase in the number of x-ray photons: the photon yield increased by a factor of 5 within less than 5 mm of the injection of the second electron bunch. It also caused an immediate drop in the critical energy. This was unsurprising considering the much lower γ^2 of this bunch. Comparing the spectra just before and just after the injection of this second bunch showed that the initial bunch radiated a spectrum with $E_c = (21 \pm 1)\,$keV and the second bunch had $E_c \approx 7.3\,$keV. Combining the critical energies and peak electron energies showed that the first bunch had a betatron oscillation radius $r_\beta \approx 150\,$nm whereas the second bunch had radius $r_\beta \approx 700\,$nm. This much increased oscillation radius explains the large increase in the number of photons produced, as total radiated energy scales with the square of r_β. Measurements of the x-ray beam profile showed that it was approximately circular, showing that with this injection mechanism there was no preferential oscillation plane for the electrons. By inferring the wiggler parameter from simultaneous measurements of the x-ray beam divergence and the electron energy spectrum, the source was again confirmed to be significantly below $1\,\mu$m in diameter. The critical energy of the betatron spectrum was shown to be stable to within $\sim 7\%$ over 250 consecutive shots, demonstrating that a self-guided, self-injecting LWFA can be a simple and stable source of reproducible, hard x-rays.

The brightness of the first injected bunch peaked at an accelerator length of 9 mm at 2.8×10^{24} photons/s/mm^2/mrad^2/0.1%BW, a factor of ~ 7.5 larger than the highest brightness measured from an $f/20$ geometry at the same laser system, and higher than any brightness reported so far in the literature. The main driver behind this brightness increase was the reduction in source size. At longer accelerator lengths the brightness was of order $1 - 1.5 \times 10^{24}$ photons/s/mm^2/mrad^2/0.1%BW, a factor of ~ 3 greater than anything measured with an $f/20$ set-up. This was driven by the large (factor of 5) increase in the number of photons, up to $5 - 6 \times 10^9$ per shot above 1 keV, while maintaining a relatively narrow divergence and small source size. This is also approximately 50 times more photons measured per shot that in [79]. The difference this makes will become apparent in chapter 6 where $f/20$ and $f/40$ x-ray imaging experiments are compared. This increase in the number of photons, will be useful not only for low noise x-ray imaging, but the increase in photons per eV will be helpful for ultrafast absorption spectroscopy experiments, XANES for example. It is also noted that the critical energy can be tuned at any accelerator length simply by changing the plasma density, with E_c increasing with plasma density.

Chapter 6

Betatron Imaging of Laser Driven Shock Waves in Solids

6.1 Motivation

The behaviour of solid density material in extreme states of pressure and temperature is fundamental to understanding in multiple fields of study, from the basic physics of condensed matter to meteorite impacts [228] [229], to material behaviour in planetary cores [230], to material failure mechanisms [231] [232]. Dynamic compression experiments, where a shock is driven in to a material by, for example, a pulsed laser or high velocity flyer are the only way to access states at very high energy densities. In the laboratory these states are very short lived because of the limited amount of energy that can be used to create them. Therefore diagnostics need excellent time resolution to probe the physics of the shock wave. Traditionally high speed photography and streak cameras, or surface velocity diagnostics such as VISAR have been used, but these have the disadvantage that the subsurface processes can not be diagnosed. This has driven the use of pulsed x-ray sources as an non-intrusive probe of rapidly evolving phenomena inside otherwise opaque materials [28], with some synchrotron facilities developing dedicated systems to further this field of study [233]. Such x-ray sources can be used for both absorption contrast and phase contrast imaging.

A further advantage of x-ray sources is that x-ray diffraction can be used to determine the crystal structure of the shocked material, and hence phase changes, at the same time as imaging of the bulk sample [234] [235]. Such experiments can provide vital information to aid with the theory and simulation of materials, and bring together the predictions of microscopic molecular dynamics codes and macroscopic fluid codes. The ultimate aim is to be able to describe how externally imposed conditions adjust the atomic potentials in a medium, and to then understand how this results in the observed behaviour in the bulk

medium. Judging from the increasing number of publications which use x-ray sources to answer related questions multiple groups believe that modern x-ray sources can move us towards this goal.

We will now consider what x-ray source parameters are required for these applications. To provide sufficient imaging contrast for solid density, moderate Z materials, the x-ray source must be hard (10's keV). It must also be bright, have a short temporal duration and be able to resolve small, preferably μm, scale features. For a shock wave travelling at 1 kms^{-1}, for example, to keep the motion blur in the image to less than 1 μm the x-ray pulse length must be sub-nanosecond. In addition it must be spatially coherent if phase contrast is necessary for a particular application. To produce an x-ray pulse with all of these characteristics light sources based on energetic, short pulse and low emittance electron beams are needed, namely synchrotron light sources or more recently x-ray free-electron lasers (X-FELs). In standard operational modes synchrotrons typically produce pulses with a duration of 10's to 100 ps [236] with peak brightness of order 10^{23} photons/s/mm^2/mrad^2/0.1%BW, while X-FELs produce pulses with lengths of a few 10's fs with a brightness of 10^{34} photons/s/mm^2/mrad^2/0.1%BW. The disadvantage of these devices is that they are large: 100m to 1km scale. This makes them expensive and also means that HEDP facilities must be built at them, which does not allow for good leverage of existing facilities. A compact source of bright synchrotron light such as a betatron source would be able to improve on this situation.

As we saw in section 1.4, betatron radiation is a source of hard, bright x-rays that emanates from a micron scale source, making it suitable for high resolution imaging. The inferred 10's fs pulse duration is significantly shorter than can be produced at a synchrotron source and is on a par with X-FELs. It has recently been shown that betatron radiation can be used to image mm thickness, moderate Z materials [33]. However despite its short pulse length, betatron radiation has never been used to image a rapidly evolving phenomenon. This chapter will present results of two experiments. The first is a proof-of-principle experiment to show that betatron radiation from an $f/20$ LWFA set-up can be used to image shock propagation in silicon. The second experiment took advantage large increase in x-ray brightness and number of photons from the $f/40$ set-up presented in chapter 5 of this thesis to increase the imaging quality to levels on a par with what has been done at conventional synchrotron sources.

6.2 $f/20$ Experiment Set-up

Figure 6.1 shows the layout of the $f/20$ shock physics experiment.

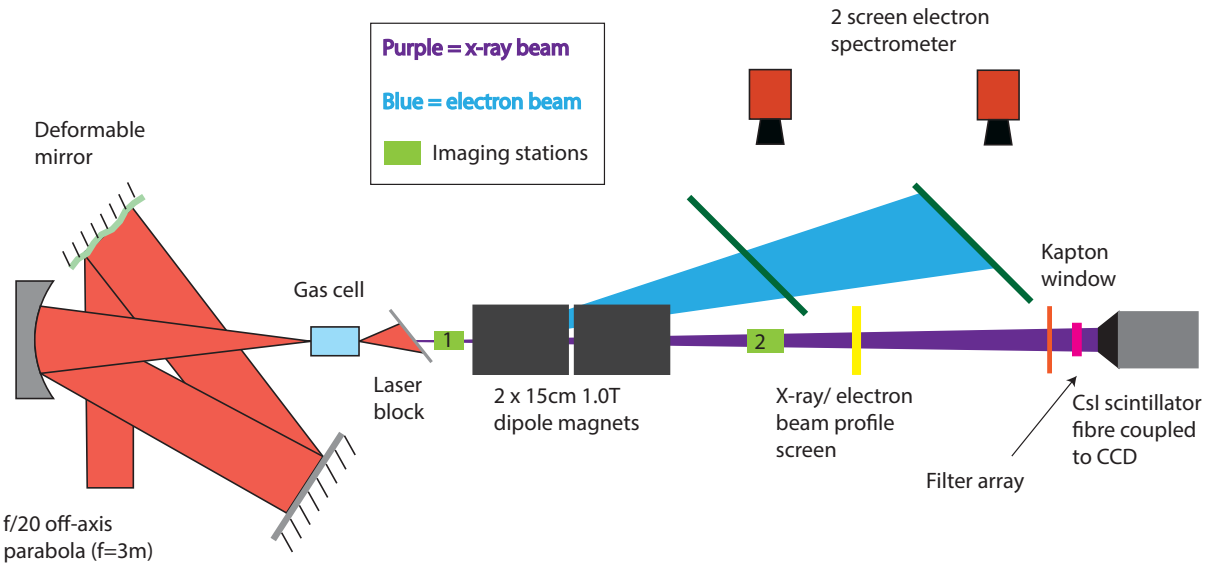


Figure 6.1: Diagram of the experimental set-up with the $f/20$ focussing optic.

The laser pulse was directed off a deformable mirror to correct the wavefront and on to a 3 m focal length $f/20$ off-axis parabolic mirror. The pulse energy on target was (10.5 ± 0.7) J with a pulse length of approximately 47 fs FWHM. This was focussed to a spot of FWHM size $(24 \pm 5) \times (15 \pm 1)$ μm. Due to the low bit depth of the available images a good measurement of the energy contained within the FWHM spot could not be made. Assuming that this was a maximum of 50%, the peak intensity at focus was at most $(2.4 \pm 0.5) \times 10^{19}$ W/cm^2, corresponding to a maximum a_0 of 3.4 ± 0.4. The pulse was focussed at the entrance hole of a 10 mm long gas cell filled with pure helium gas. The plasma electron number density was held in the range $n_e = (2.1 - 2.8) \times 10^{18}$ cm^{-3} for the data presented here. The random fluctuations in number density were approximately 4%.

The electron and betatron beams passed through a 12 μm kapton foil plus 12 μm aluminium foil that acted as a laser beam dump. The electrons were then deflected through two 15 cm long 1.0 T permanent magnets and on to a two screen electron spectrometer, consisting of two Lanex screens (type Lanex regular) each imaged by a CCD camera. The energy spectrum was prone to large fluctuations between shots. Typical spectra had 100% energy spread where $(dN/dE)/E$ was roughly constant as a function of energy. When the energy spectrum could be measured, the peak energy was always in the range $0.6 - 1$ GeV with 70% of shots having a peak in the range (700 ± 100) MeV. The total charge in the electron beam at energies greater than 200 MeV (approximately the low energy cut-off of this electron spectrometer diagnostic) was estimated to be at the $200 - 300$ pC level from similar experiments performed at this facility with a similar gas target and geometry.

The x-rays could either be detected on a Lanex screen (type DRZ plus) to measure the beam profile or could exit the vacuum chamber through a 250 μm kapton window for detection on the Princeton indirect detection camera (see section 3.5.2). The energy spectrum was characterised using the 64 filter array (appendix 8.9.1). Resolution targets were put at the imaging stations 1 and 2 marked on the setup diagram to determine the resolution of the x-ray imaging system. The line spread function of the imagining system was found by imaging the hard edge of a cleaved silicon crystal placed at imaging point 1. The total distance from the source to the camera was 3.70 m. The distance from the source to imaging point 2 was 53 cm giving a magnification of 8. The distance from the source to imaging point 1 was 14.8 cm so the magnification was 26. Further details on all of the x-ray properties can be found in the next section.

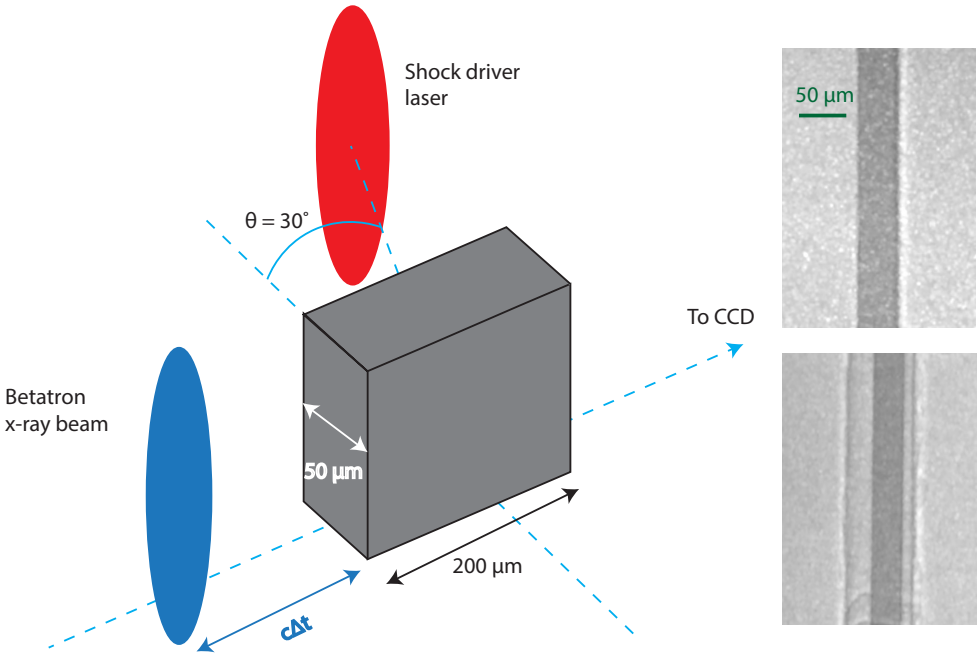


Figure 6.2: Geometry of the shock target interaction point. Inset right are 'cold' images of the shock targets with the tamped target at the bottom.

Imaging station 1 also doubled as the shock interaction point, the geometry of which is shown in figure 6.2. The shock target was single crystal silicon which was 50 μm thick in the shock propagation direction and 200 μm thick in the betatron probe direction. 200 μm thick silicon is 50% transmissive at a photon energy of 13.25 keV, which highlights the need for a hard x-ray source to perform this experiment. The experiment also explored the effect of having a 25 μm thick CH tamper layer on the shock driver side of the target. Tamper layers are commonly used to reduce ablation of the target from the front surface

which leads to a smoother interaction with the driving laser.

The uncompressed Gemini north beam was used to drive the shock. (14 ± 1) J were delivered in to the target chamber in approximately 1.5 ns, with a central wavelength of 800 nm. It was focussed by an $f/2$ off-axis parabolic mirror to a point just before the shock target. The defocussed beam at the surface of the shock target had a width of approximately 1.7 mm, and its intensity profile is shown in figure 6.3. The highest intensity part of the pulse had intensity $(1.2 \pm 0.1) \times 10^{13}$ W/cm^2. This shape allowed a single shot shock pressure scan to be performed.

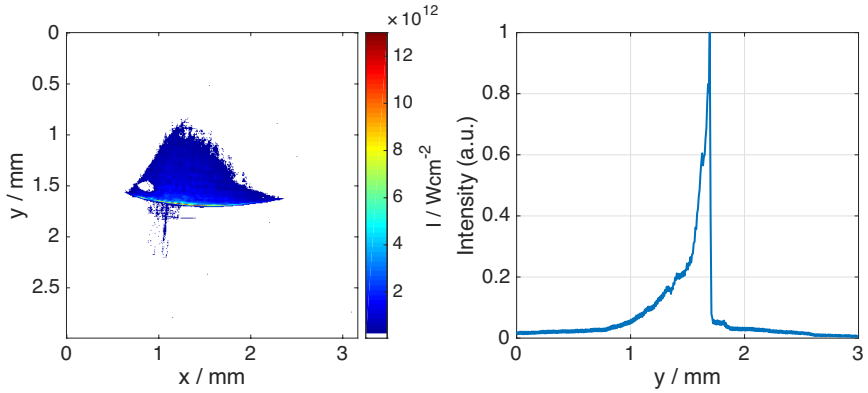


Figure 6.3: Left: Spatial profile of the shock driver pulse. Right: Integration over x of this profile.

6.3 $f/20$ Experiment X-ray Source Properties

6.3.1 Beam Divergence

X-ray beam profiles recorded at the same facility with the same general setup, using a 10 mm helium filled gas cell, produced elliptical x-ray beams which were elongated vertically, which was the direction of laser polarisation. An example of this is shown on the left hand side of figure 6.4. The right hand side of this figure shows how the divergence varied as a function of plasma density. From the linear fit, around 2.5×10^{18} cm^{-3} (the imaging density in this experiment) the beam divergence was approximately 22×10 mrad.

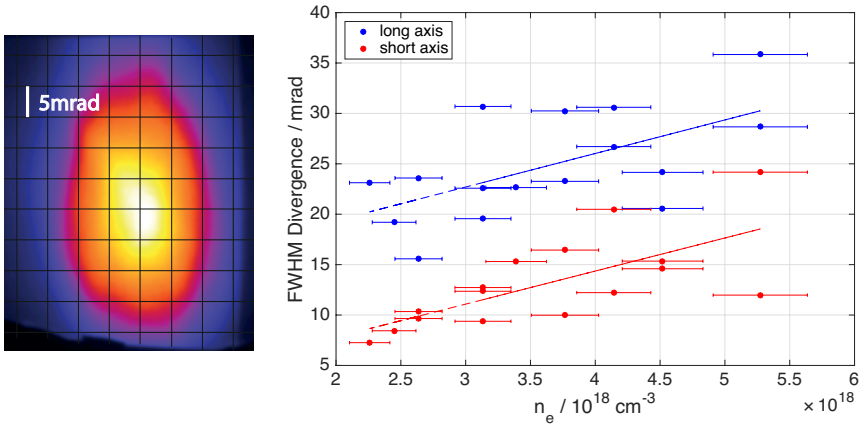


Figure 6.4: X-ray beam profile from the $f/20$ wakefield driver. Left: example beam profile image. Right: long and short axes of FWHM ellipse vs. plasma density.

6.3.2 Resolution and Source Size

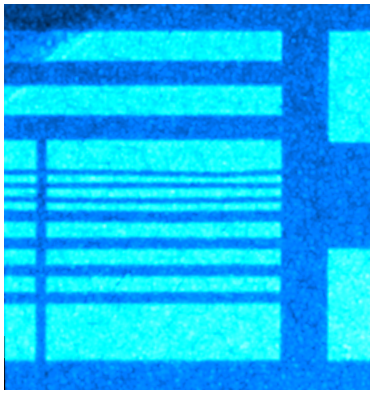


Figure 6.5: X-ray imaging resolution in the $f/20$ set-up, showing a 26 times magnified gold resolution target with a minimum bar spacing of 10 μm.

Figure 6.5 contains images of two targets that were used to characterise the resolution of the x-ray imaging system (betatron source plus scintillator plus camera). The left image shows the gold resolution target detailed in appendix 8.10, where the smallest spacing between the bars is 10 μm. The magnification here was 26. This shows that features separated by 260 μm at the scintillator can be very clearly resolved, or that features smaller than 10 μm in the shock target can be clearly resolved. To gain a better understanding of the the imaging resolution of the system the edge of a cleaved silicon crystal was imaged to measure the line spread function (LSF) and modulation transfer function (MTF) of the imaging system as described in section 3.5.6. These are plotted for one shot in figure 6.6. As no kicker magnet was used after the source in this experiment part of the electron beam will have hit the silicon. Bremsstrahlung photons from this contributed to an image

with a low signal to noise ratio, making this a challenging measurement.

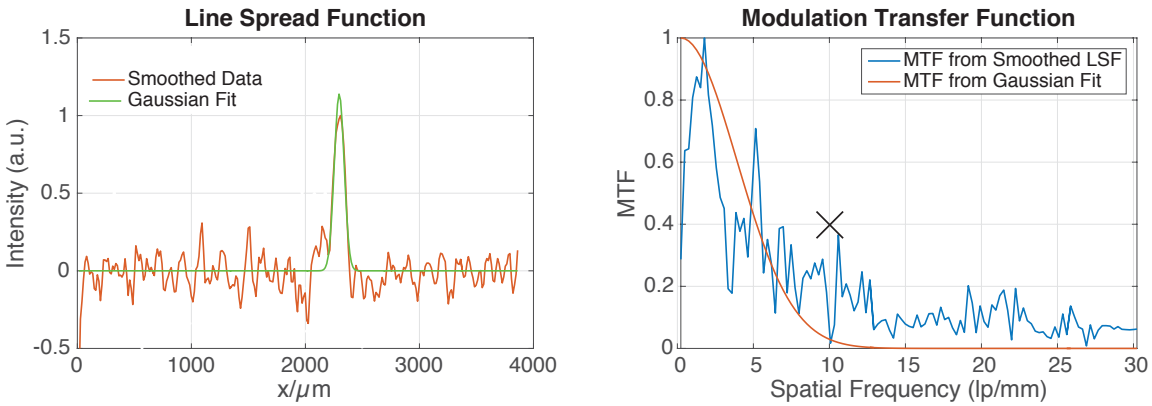


Figure 6.6: LSF and MTF of the x-ray imaging system in the $f/20$ shock physics experiment. The black cross on the MTF graph is the quoted MTF of the scintillator [173].

The LSF on this shot had a FWHM width of (120 ± 10) μm. We see that the MTF has almost dropped to zero at 10 lp/mm. The MTF of the scintillator [173], marked as the black cross on the MTF graph, suggests that the major limitation on the imaging resolution is the betatron source, although it is not entirely clear if this is a noise issue, a source size issue, or a combination of the two. Assuming that the LSF width is dominated by the source size gives an upper limit on the FWHM source size of (4.8 ± 0.4) μm. This was calculated using the geometry in figure 6.7. h_s is the source size. h_i is the size of the blurred projection of the point object (black circle), which was taken to be the FWHM of the gaussian fit to the LSF. Equating the two angles θ gives the expression $h_s = h_i u/v = h_i/(M-1)$ where M is the magnification of the imaging system.

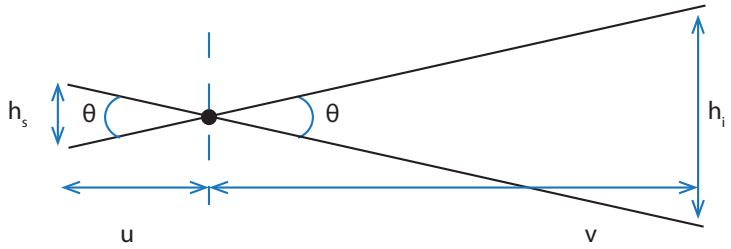


Figure 6.7: Geometry used to calculated the source size.

6.3.3 Spectrum

The x-ray spectrum was characterised on 42 shots during the run where the shocked silicon images were taken using the 64 filter array. The spectrum was successfully re-

trieved on 40 of these shots. On the two failed shots the x-ray intensity was too low to characterise with the filter array method. The plasma density was held within the limits $n_e = (2.3 \pm 0.2) \times 10^{18} - (2.6 \pm 0.2) \times 10^{18}$ cm^{-3}, and changing the density within these limits did not produce a statistically significant change in the critical energy. The mean critical energy was (20.4 ± 0.8) keV where the error is the standard error from 40 shots. E_c is plotted as a function of shot number on the left hand side of figure 6.8, which

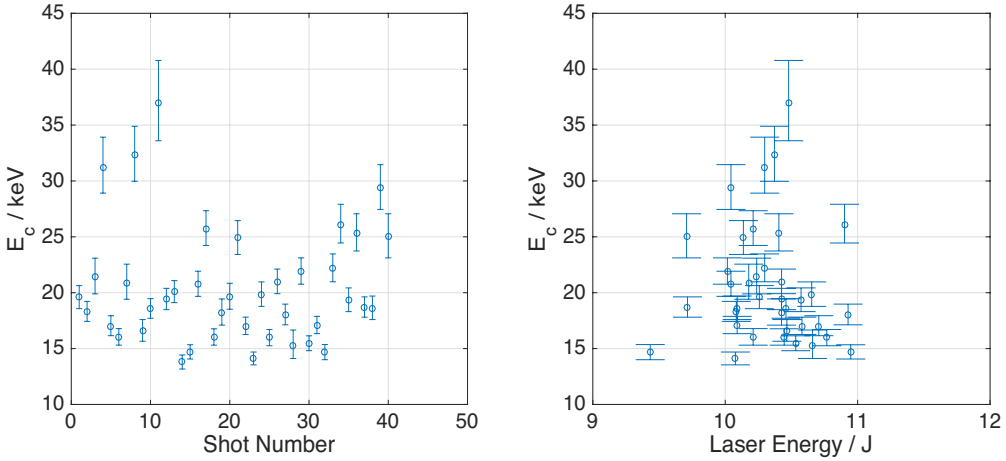


Figure 6.8: Critical energy measurements from the $f/20$ shock physics experiment.

shows that the shot-to-shot fluctuations in E_c were significant: much more than the error on the measurement. The only measured quantity that was varying during these shots was the laser energy, although as the right hand side of figure 6.8 shows there was no correlation between the laser energy and E_c (the linear correlation coefficient for these two parameters is 0.13). The conclusion of this is that the shot-to-shot variations in the spectral shape are being driven by a quantity we don't measure on-shot such as the focal spot quality, which we know had large variations from its characterisation at low power.

The total number of photons in the beam was found by taking the brightest pixel in the image (as discussed in section 3.5.7 for the brightness calculation) and from the deposited energy, with the measured spectrum, calculating the number of photons N_{max} that hit this pixel. The low energy cut-off for the number of photons was 1 keV. The photon number distribution as a function of space was assumed to be a 2D gaussian with amplitude N_{max} and FWHM widths 22×10 mrad, as discussed in section 6.3.1. Note that N_{max} is found in units of photons per square pixel so the FWHM should be written as 6030×2740 px. Integrating this gaussian over all space gives the total number of photons in the beam. This method underestimates the total number of photons if the peak of the gaussian is not in the diagnostic window. The mean number of photons per shot in this run was $(7 \pm 1) \times 10^9$, where the error is the standard error. The total number

of photons is plotted as a function of shot number in figure 6.9. We see a very large

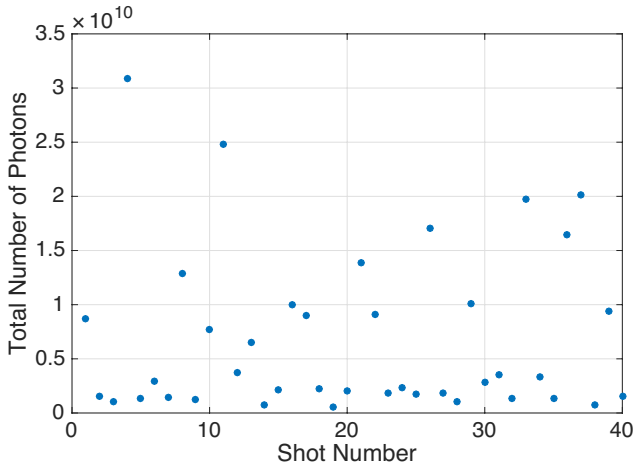


Figure 6.9: Measurements of the total number of photons.

shot-to-shot fluctuation in the total number of photons. While part of this might be due to the assumptions made in the calculation, inspection of the images show that the x-ray source was relatively bright only on a small number of shots. Again it seems likely that this is being driven by laser intensity fluctuations, mostly driven by the focal spot quality.

The shock target images presented in the next section were taken with the brightest x-ray source conditions, so with between 1 and 3×10^{10} photons per shot. Let us assume that there were 2×10^{10} photons on a shot. The FWHM beam area at the camera was approximately 9500 mm^2. The chip area was $27.6 \times 27.6 \approx 760$ mm^2, meaning that only around $2 \times 10^{10} \times (760/9500) \approx 1.6 \times 10^9$ photons with energy above 1 keV hit the camera per shot. The vacuum window, laser block and the beryllium window on the camera had a transmission of approximately 0.5 at 10 keV. Assuming then that only photons with energy above 10 keV contributed to the image the number of useful photons per shot was 9×10^8. This is approximately 210 useful photons per px, and so the estimated signal to noise ratio $SNR = 1/\sqrt{N} = 7\%$. Therefore it seems likely that on any shot the intrinsic signal to noise ratio (this is excluding bremsstrahlung photons and other noise sources) was in the range of $5 - 10\%$.

Figure 6.10 is a plot of the total number of photons against the critical energy. There is some correlation between these two parameters as shots with higher reported critical energies are much more likely to have a larger number of photons. Given that the electron peak energy fluctuations were quite small (the peak energy was (700 ± 100) MeV) it seems likely that both of these effects were being driven by an increase in r_β, meaning that the injection dynamics were unstable and contributed greatly to the shot-to-shot variation in the x-ray beam properties. It is unsurprising that the injection was so unstable given the

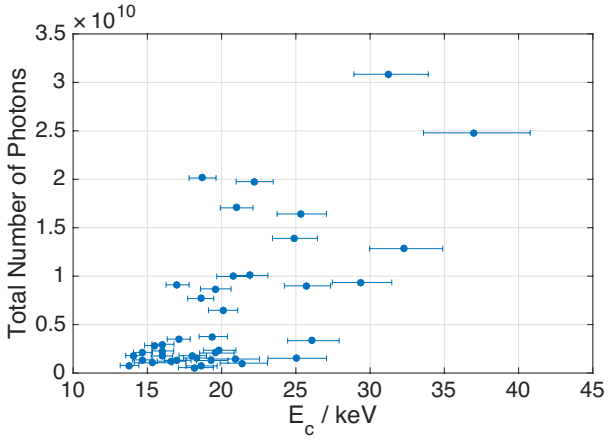


Figure 6.10: Total number of photons plotted against critical energy.

large shot-to-shot fluctuations in focused laser intensity in this experiment.

The brightness followed an almost identical pattern to the number of photons. The peak brightness averaged over all 40 shots, conservatively assuming that the source diameter was 4.8 μm, was $(1.3\pm0.3)\times10^{22}$ ph/s/mm^2/mrad^2/0.1%BW. The highest brightness recorded on any shot was $\sim 5\times10^{22}$ ph/s/mm^2/mrad^2/0.1%BW. These values may be significantly underestimated because of the very conservative source size used. Diffraction effects can lead to an overestimate of the source size from a hard edge because they cause the geometric optics approximation used in the source size calculation to break down. A better estimate of the source radius may come from the critical energy equation (see equation 2.161) which is

$$E_c = \frac{3\hbar}{4c}\gamma^2{\omega_p}^2 r_\beta \tag{6.1}$$

Calculating γ from the peak energy of the electron spectrum, which was reported in section 6.2 as (700 ± 100) MeV, gives an estimated $r_\beta = (0.8\pm0.2)$ μm. Assuming, then, a source diameter 1.6 μm the highest brightness recorded on any shot was $\sim 4.6\times10^{23}$ ph/s/mm^2/mrad^2/0.1%BW, and the mean peak brightness was $(1.2\pm0.2)\times10^{23}$ ph/s/mm^2/mrad^2/0.1%BW. Graphs of dI/dE and brightness (assuming a 1.6 μm source) as a function of photon energy are shown in figure 6.11. The errors were assumed to be dominated by the standard error in the total number of photons.

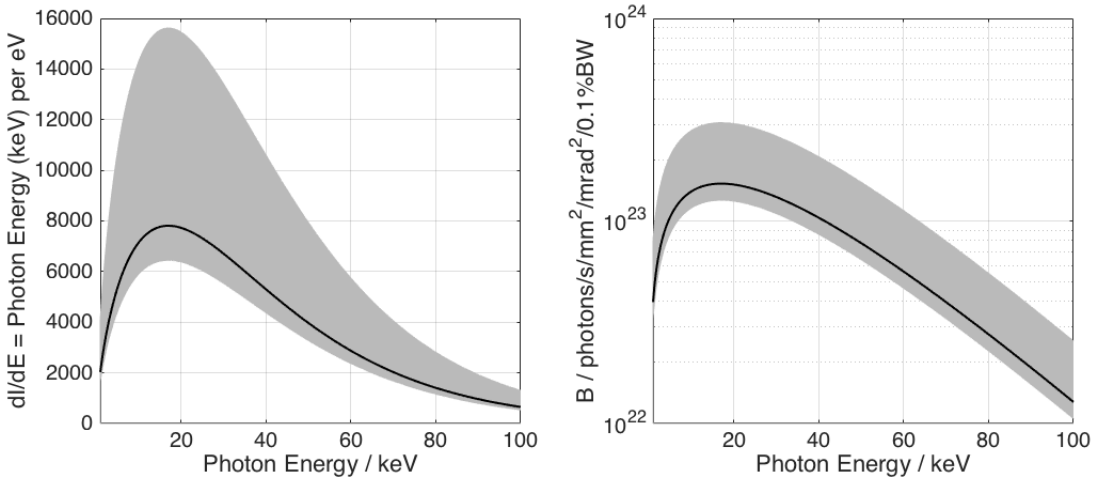


Figure 6.11: X-ray dI/dE (left) and brightness (right) as a function of photon energy. The black lines depict the mean and the grey areas the error bounds.

6.4 Shock Propagation in a Silicon Target

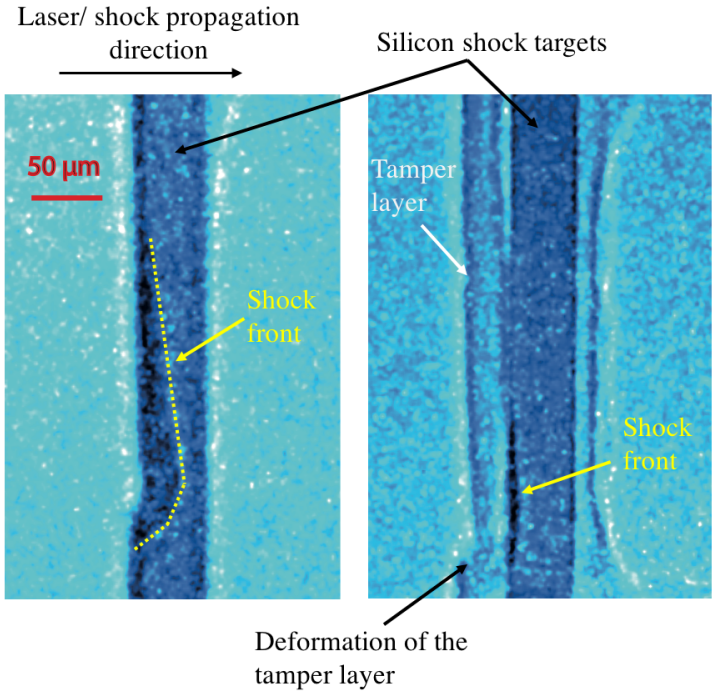


Figure 6.12: Betatron images of laser driven shocks in silicon. The shock driving laser travelled from left to right. The target in the right hand image had a 25 μm CH tamper layer on the front surface.

Figure 6.12 shows two betatron images of laser driven shocks propagating in single crystal silicon. The left hand image is of an untamped target 5.2 ns after the start of the laser-silicon interaction. The right hand image is of a tamped target taken 6.5 ns after the start of the interaction. These are the first images of a rapidly evolving phenomenon taken with betatron radiation. The images have been dark field and flat field corrected and have been filtered to reduce noise using a 2×2 background from minima filter in ImageJ. The shape of the shock in the untamped target is simply explained: it follows the intensity pattern of the drive laser, as shown in figure 6.13.

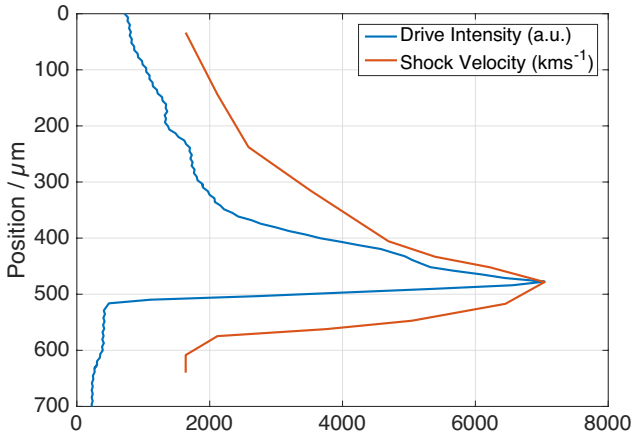


Figure 6.13: Shock velocity and laser intensity as a function of position. The shock velocity was inferred from the position of the shock front in the image taken at 5.2 ns. The peak of the intensity pattern was assumed to overlap with the position where the shock travelled most quickly.

It is immediately clear that the tamper layer had a large effect on the shock propagation. The shock drive laser was intense enough to drive a shock in to the tamper layer itself. After 6.5 ns this shock had only just travelled across the tamper layer and hit the silicon. This would not have been seen in conventional methods such as VISAR. This is only clear because of phase contrast imaging as the tamper layer was otherwise transparent to the x-rays.

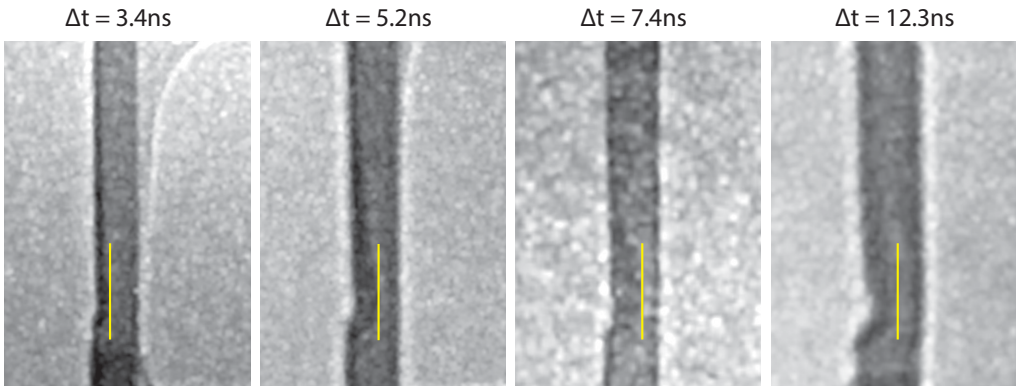


Figure 6.14: Time series of shock propagation in untamped silicon. The position of the shock front is denoted by the yellow bar. Δt is the time between the front of the shock driving pulse hitting the target and the arrival of the betatron probe.

A series of images of shocked, untamped silicon was taken with different betatron probe delays to study the evolution of the shock wave. This is shown in figure 6.14. Plotting the position of the shock front against time gives the graph shown in figure 6.15, where the full length of the error bar is the FWHM of the LSF of this system, which was 4.8 μm. Considering that the drive pulse was only 1.5 ns long it is possibly surprising that the shock velocity is constant for the first $\sim$ 8 ns, although part of this may be explained by the errors. The velocity inferred from the linear fit in the graph as 5.1 ± 0.8 kms^{-1}.

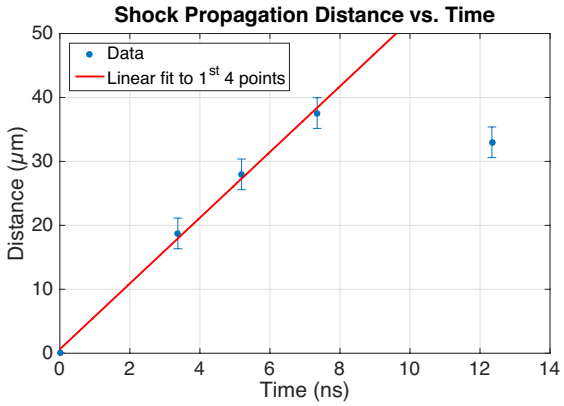


Figure 6.15: Shock propagation distance as a function of time in silicon.

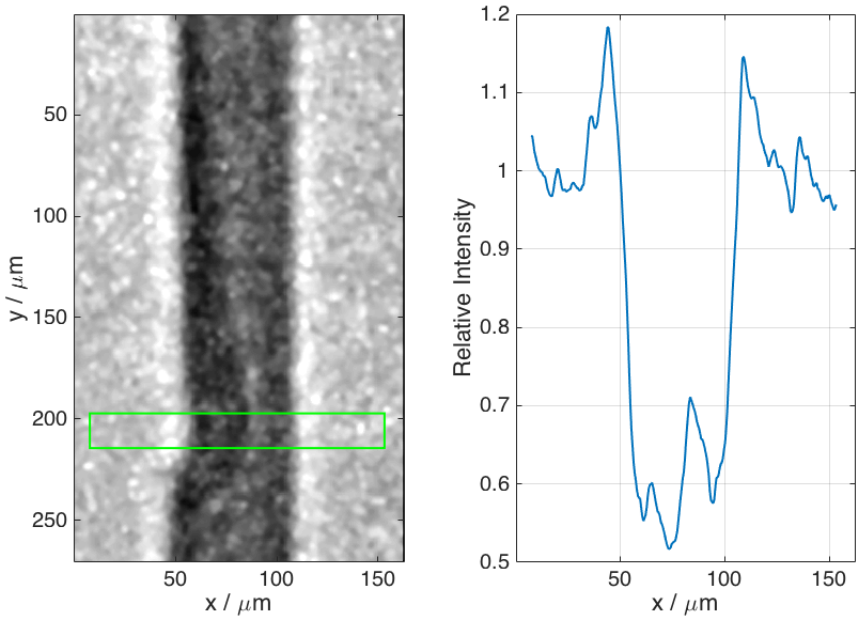


Figure 6.16: 'Lineout' of shock propagation in untamped silicon from the 5.2 ns delay shot. As the image had a high signal to noise ratio the part of the image inside the green rectangle was summed vertically to produce the plot of x-ray intensity on the right. 1 is the intensity of x-rays that did not pass through the target.

The right hand side of figure 6.16 shows a lineout of the image around the strongest part of the shock, where the intensity is relative to the x-ray intensity that did not pass through the silicon. The cold part of the silicon had a transmission of 0.69, equal to the transmission of silicon at 16 keV, meaning this can be taken as the effective x-ray photon energy on this shot. The phase contrast makes is a little more difficult to place an accurate value on the transmission through the shocked part of the target: it is the phase contrast in the image that is causing the intensity spikes in the lineout. Taking a value of 0.55 as the relative transmission through the shocked material the density of this material is 3.7 g/cm^3, which is a density increase by a factor of approximately 1.4 from silicon at standard pressure and temperature. This was calculated using the equation

$$\exp\left(-\frac{\mu}{\rho_0}\rho d\right) = 0.55 \tag{6.2}$$

This is simply the Beer-Lambert law where d is the material thickness, $\mu/\rho_0 = 7.96$ cm^2/g is the mass attenuation coefficient for silicon and ρ is the density of the shocked material. The Rankine-Hugoniot conditions, which describe some of a material's thermodynamic properties either side of a shock front, are written in a coordinate system moving with the shock as

$$\rho_0 u_s = \rho_1 \left(u_s - u_1\right) \tag{6.3}$$

$$P_1 - P_0 = \rho_0 u_s u_1 \tag{6.4}$$

$$e_1 - e_0 = \frac{1}{2}(P_0 + P_1)\left(\frac{1}{\rho_0} - \frac{1}{\rho_1}\right) \tag{6.5}$$

Quantities with subscript 0 are the upstream (unshocked) material properties. Quantities with subscript 1 are the downstream (shocked) material properties. The first equation describes the conservation of mass. ρ represents density, u is particle velocity and u_s is the shock velocity. Conservation of momentum gives the second equation where P is pressure. The final equation is a statement of conservation of energy where e is the specific (i.e. per unit mass) internal energy. For $u_s = (5.1 \pm 0.8)$ km/s (from the linear part of the graph in figure 6.15), $\rho_0 = 2.33$ g/cm^3 and $\rho_1 = 3.7$ g/cm^3, equation 6.3 gives the particle velocity u_1 as (1.9 ± 0.3) km/s. Assuming that the initial pressure $P_0 \sim 0$ the pressure behind the shock was 22 ± 5 GPa. However this may be slightly misleading, as there are a number of pressure-induced phase transitions in silicon between 11.7 and 38 GPa [237], which will have changed the density of the silicon, and meant that the fluid approximation used here was invalid. Nevertheless this has shown that betatron radiation can measure density changes and shock velocities, that in other cases could have been use to predict other material properties such as pressure.

At the laser intensities used here, the dominant mechanism by which a laser can drive a shock is material ablation, which dominates over radiation pressure. In the process of ablation, material is heated by the laser and flows away from the surface of the material. This is an example of the rocket effect, and by Newton's third law this applies a pressure to the remaining material which drives the shock. A simple form of the ablation pressure P_{abl} is given by Drake [238] as

$$P_{abl} = 800\ {I_{14}}^{2/3}\ {\lambda_\mu}^{-2/3}\ \text{GPa} \tag{6.6}$$

where I_{14} is the laser intensity expressed in units of 10^{14} W/cm^2 and λ_μ is the laser wavelength in microns. Using a peak intensity of 8×10^{12} W/cm^2, which was representative of the highest intensity part of the laser beam in this experiment (see figure 6.3) and the wavelength of 800 nm this equation can be used to estimate a shock pressure of ~ 170 GPa. This is much larger than the value estimated from the betatron radiographs of the shock, although this is unsurprising considering that the laser pulse length was 1.5 ns and the image was taken 5.2 ns after the arrival of the shock, meaning that the shock was unsupported at this time and therefore this equation does not strictly apply. To better model the experiment a 1D simulation was performed in the radiation-magnetohydrodynamics code HELIOS [239]. A planar geometry was used, and a gaussian laser pulse with an intensity peaking at 8×10^{12} W/cm^2 at time 0.75 ns, with a FWHM duration of 0.75 ns, was incident at 30° on to a 50 μm thick silicon target. This is an approximation to the real

pulse shape, which was broadly gaussian in time and with a total measurable duration of 1.5 ns. The simulation showed that the plasma pressure at 0.8 ns, just after the arrival of the peak of the laser pulse, was approximately 300 GPa. This is in agreement to within a factor of 2 with the simple Drake estimate. At 5.2 ns after the start of the interaction a peak pressure of ~ 33 GPa is found at a distance of approximately 10 μm in to the target. This is shown in figure 6.17. At a first glance this appears to be in good agreement with

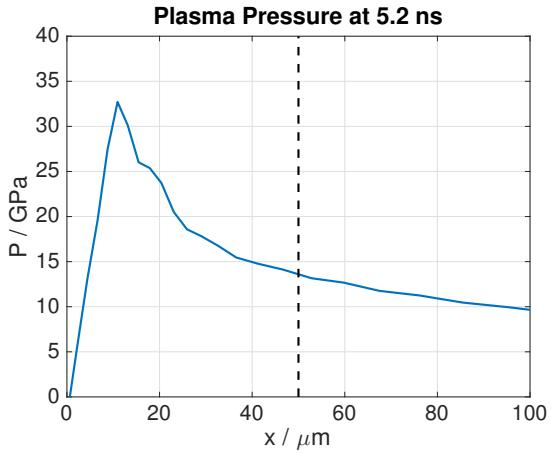


Figure 6.17: Pressure output from HELIOS 5.2 ns after the start of the interaction. The black dashed line shows the original position of the edge of the target.

the experimental data. Although as figure 6.18 shows the situation is more complicated, as the mass density plot taken at 1 ns shows that the simulated shock has almost reached the back of the target. This explains the long tail on the graph of plasma pressure vs.

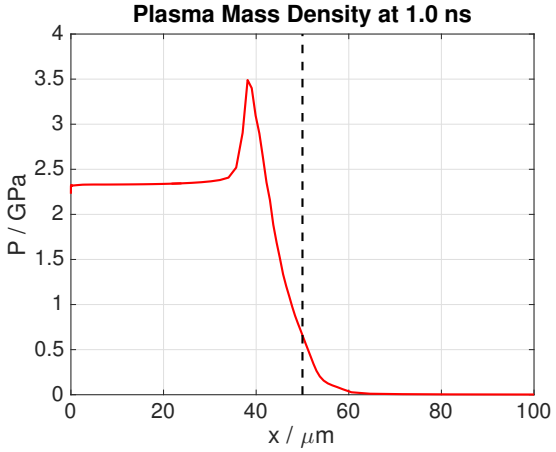


Figure 6.18: Mass density output from HELIOS 1.0 ns after the start of the interaction. The black dashed line shows the original position of the edge of the target.

position at 5.2 ns. No evidence of this shock breakout was seen in the betatron images,

with the rear side of the target appearing unperturbed, showing that this system was not well described by a 1D plasma. This is perhaps unsurprising given the complexity of the pulse shape and the fact that solids have properties such as strength, and experience phase changes, whereas plasmas do not.

In this section we have seen the first use of betatron radiation to image a rapidly evolving phenomenon, which was a laser driven shock wave propagating in silicon. This produced high resolution images and it has been shown that these can be used for basic quantitative measurements of the material properties. The main issue with these images was that the signal to noise was very high, which was caused by a combination of a high bremsstrahlung background and a low number of betatron photons hitting each pixel. To improve on this a similar shock imaging experiment was performed with the $f/40$ wakefield driver set-up which, as we saw in the previous chapter, gave an increase in brightness of a factor of 10. Additionally a small kicker magnet was introduced to divert the electron beam away from the shock target.

6.5 $f/40$ Experiment Set-up

6.5.1 General Set-up

The general experiment set-up for the $f/40$ experiment had many similarities to the $f/20$ set-up (figure 6.3), except for the wakefield driver pulse which used the $f/40$ spherical mirror geometry shown in figure 5.1. The exact set-up is shown in figure 6.19.

To reduce the bremsstrahlung noise a 2.5 cm long permanent kicker magnet with a peak field of 1.0 T was placed ~ 5 cm after the gas cell to deflect the electrons away from the shock target. Electron tracking simulations showed that, for electrons travelling along the laser axis, 2 GeV electrons would miss the shock target by over 200 μm. The wakefield driver pulse was the Gemini south beam. (11.3 ± 0.6) J was delivered to the target in a nominal FWHM pulse length of ~ 47 fs. This was focussed at the entrance of the gas cell to a FWHM spot size of $(58 \pm 1) \times (47 \pm 1)$, with 38% of energy contained within the FWHM. This gives a peak focussed intensity of $(5.5 \pm 0.4) \times 10^{18}$ W/cm^2, corresponding to a peak a_0 in vacuum of (1.61 ± 0.05). The 1σ pointing fluctuation was ~ 10 μm. The gas cell was filled with pure helium which produced a plasma with an electron number density in the range of $(3.5 - 3.9) \times 10^{18}$ cm^{-3}. The length of the gas cell, which was a single stage cell, was 16 mm in the best imaging conditions.

The laser beam dump consisted of a 27 μm thick kapton tape plus a 24 μm thick aluminium foil. The 250 μm kapton vacuum window was again used, which had a 92 μm

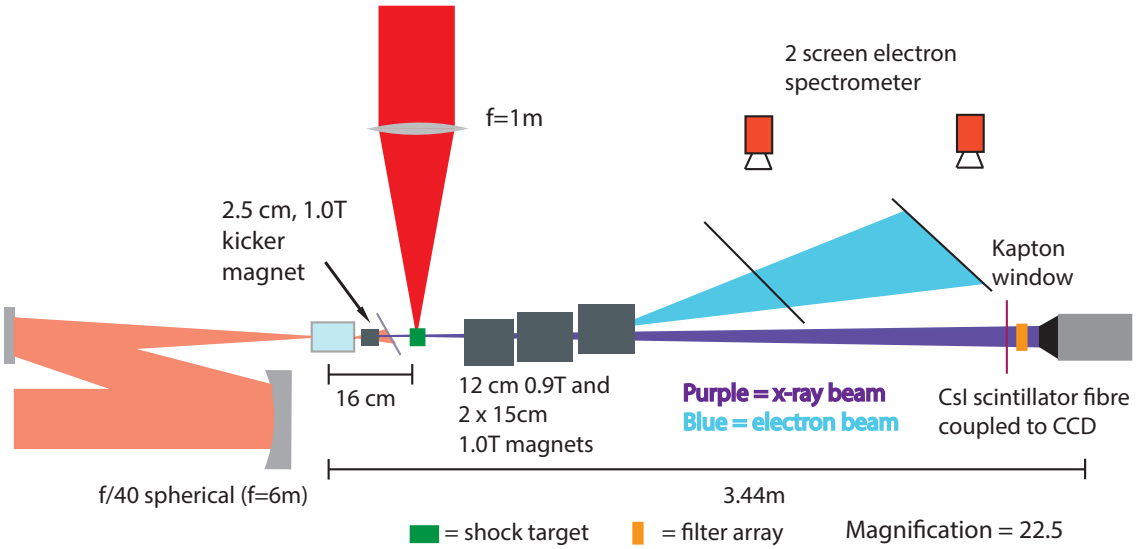


Figure 6.19: Diagram of the shock physics experiment setup with the $f/40$ focussing optic.

thick aluminium laser block in front of it. The x-rays were detected on the Andor indirect detection camera. The x-ray spectrum was characterised on-shot using the imaging filter array (see appendix 8.9.3). The 64 filter array was used at other times for better energy resolution and to produce a better estimate of the brightness. The x-ray source properties will be discussed later in this chapter. The magnification of the shock target in this experiment was 22.5.

6.5.2 Electron Beam Properties

This section will briefly describe the properties of the electron beam from the run where the shock images were taken. Almost all electron beams exhibited a strong peak at high energy followed by a long tail to low energies. An example spectrum is shown in figure 6.20, which had a peak at ~ 970 MeV with a FWHM $\Delta E/E \approx 1\%$. The spectrum shown is one of the higher quality ones, although 20 out of 42 shots exhibited a strong peak at the highest energy with a FWHM $\Delta E/E$ at the few per-cent level. The low energy cut-off was close to 500 MeV in this experiment because the kicker magnet caused electrons with a lower energy than this to hit the electron spectrometer magnets. This actually resulted in significantly less bremsstrahlung photons being detected by the x-ray camera than having the shock target in the electron beam, as there was 42 cm of iron to absorb energy from these electrons. The mean of the peak electron energies analysed over 42 shots was 940 ± 20 MeV, where the error is the standard error. To give a better representation of

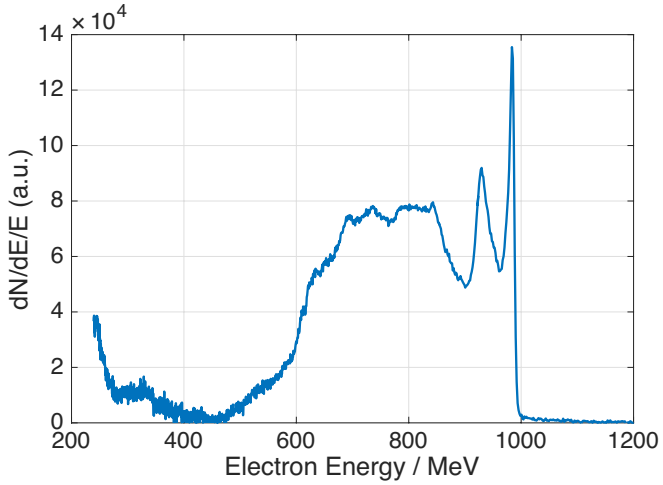


Figure 6.20: Example electron energy spectrum.

the peak electron energies throughout the run, figure 6.21 presents a histogram of peak electron energy in 50 MeV bins. It shows that most electron beams peaked between 900 and 1050 MeV. The total charge in the beam is estimated to be $\sim 200\,\mathrm{pC}$ from figure 5.6.

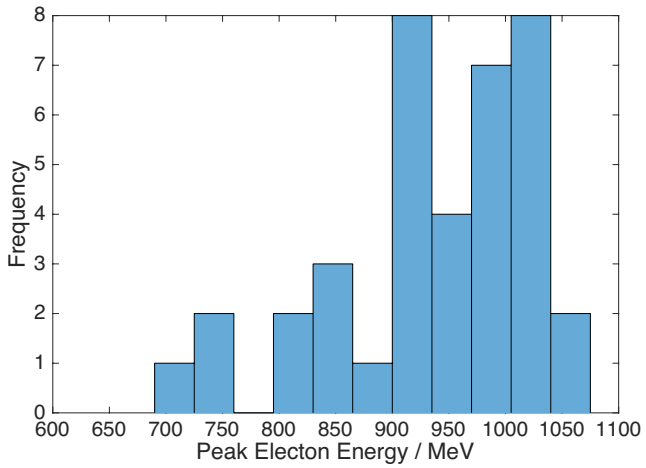


Figure 6.21: Histogram of peak electron energies

Finally the peak electron energy can be plotted against laser energy, which varied randomly during the run. This is done in figure 6.22, which shows no strong trend.

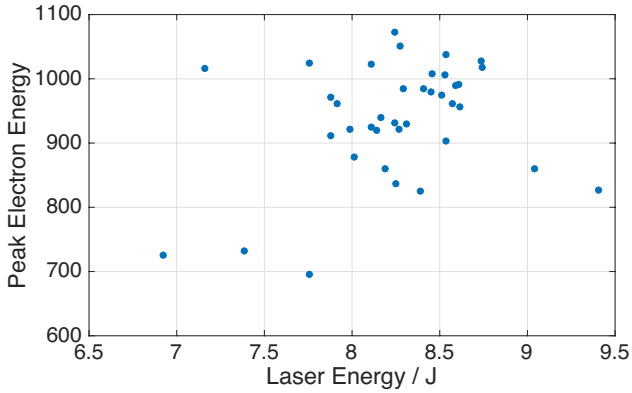


Figure 6.22: Peak electron energy plotted against wakefield driver laser energy.

6.5.3 Shock Target and Shock Driver

The form of the shock target is shown in figure 6.23 along with an example betatron radiograph of the unshocked target. The target was made of aluminium and was ap-

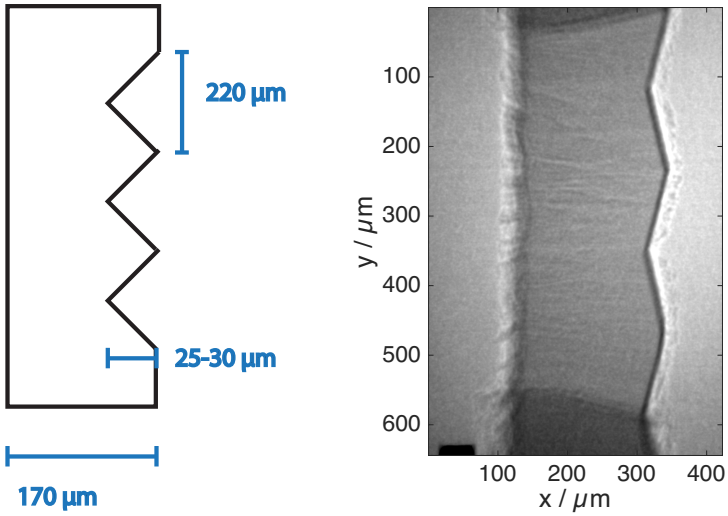


Figure 6.23: Left: design of the grooved aluminium target. The shock drive laser entered the picture from the left. Right: betatron x-ray image of an unshocked target.

proximately 200 μm thick in the betatron probe direction. The idea behind the grooved target was to study Richtmyer-Meshkov instability (RMI) growth, which can be used as a measure of material strength [240]. Unfortunately the targets were three times thicker than the design specification, so that by the time the shock had propagated through the material to the grooved surface it was no longer being supported by the laser driver. This

meant that there was very little RMI growth. It is also noted that the betatron image is able to identify defects in the target material, which were presumably created while manufacturing this shape of target.

The shock driver laser was a 30 J pulse of 1053 nm light, with a temporal profile shown in figure 6.24. The sharp rising edge was created by a Pockels cell, although a low intensity foot leading the pulse by $15 - 20$ ns persisted. The pulse was focussed on to a point just after the target by a 1 m focal length lens. The spatial profile of the defocussed pulse at the shock target surface was approximately a 2D gaussian with a FWHM width of 150 μm in x (out of the page in the shock images) and 180 μm in y (vertical in the shock images). The peak intensity on the shock target was $\sim 3.5 \times 10^{12}$ W/cm^2.

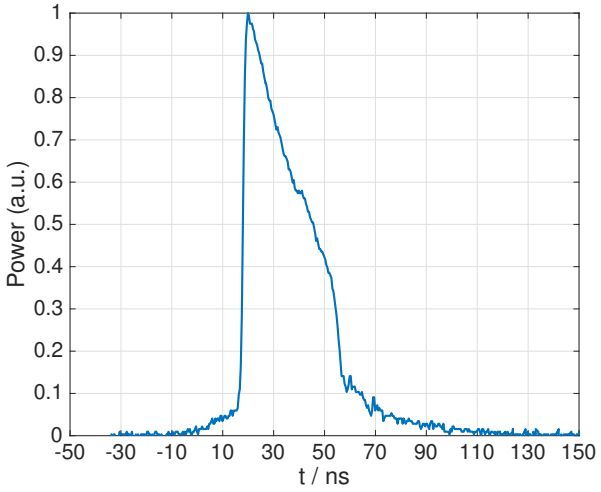


Figure 6.24: Temporal profile of the shock drive pulse.

6.6 $f/40$ Experiment X-ray Source Properties

6.6.1 Beam Divergence

The beam divergence was not directly measured on this experiment. It is assumed to follow the curve from figure 5.13 in the previous chapter. That data was also taken from a single stage helium filled gas cell, although at 20 mm length instead of the 16 mm length used here. Close to the operating plasma density in this experiment, at $(3.3 \pm 0.4) \times 10^{18}$ cm^{-3}, the beam divergence was (13 ± 2) mrad by (15 ± 2) mrad in the x and y directions respectively.

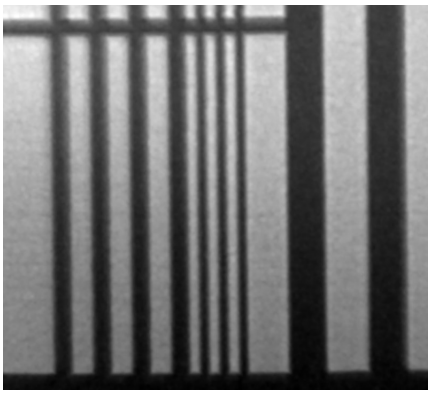


Figure 6.25: 22.5 times magnified image of the gold resolution target

6.6.2 Resolution and Source Size

An image of the gold resolution target, also taken with a magnification of 22.5, is shown in figure 6.25, where we see that the smallest bars with 10 μm spacing are very clearly resolved. Hence the resolution is significantly better than 10 μm. As discussed in section 5.7, images of the JIMA target in similar conditions, but with a slightly higher magnification of 25, showed that the resolution was limited to ~ 4 μm. This may have been an underestimate due to the noisy conditions and the low attenuation of the very thin tungsten bars on the JIMA target. Therefore it can be conservatively stated that the system resolution was $4\,\mu$m. This compares well to imaging experiments at synchrotron sources which had a stated resolution of $2-3$ μm [28] [29] [240].

6.6.3 Spectrum

During the shock imaging run the critical energy was characterised on 42 shots using the imaging filter array, with the same laser and plasma conditions that were used on the shock imaging shots. Only 10 filters were not obscured by the shock target and its holder, but these were close to the shock target so they will have given a good estimate of the spectrum going through the shock target. The critical energy as a function of shot number is shown on the left hand side of figure 6.26, where a single point was omitted due to low signal level. Note that the stability was much improved compared to the $f/20$ experiment. It is thought that this is at least in part related to the better focal spot size stability. The mean critical error of all of the shots was (18.0 ± 0.1) keV, where the error is the standard error. This is better quoted as (18.0 ± 0.6) keV because the error due to the filter thickness uncertainty can not be averaged out. In the right hand graph the critical energy has been plotted against laser energy. While the trend is not very strong, and seems to be dominated by the few points at low and high energy, there is an apparent decrease in critical energy with laser energy. This was taken at constant plasma electron density. This is particularly surprising given that figure 6.22 showed that the

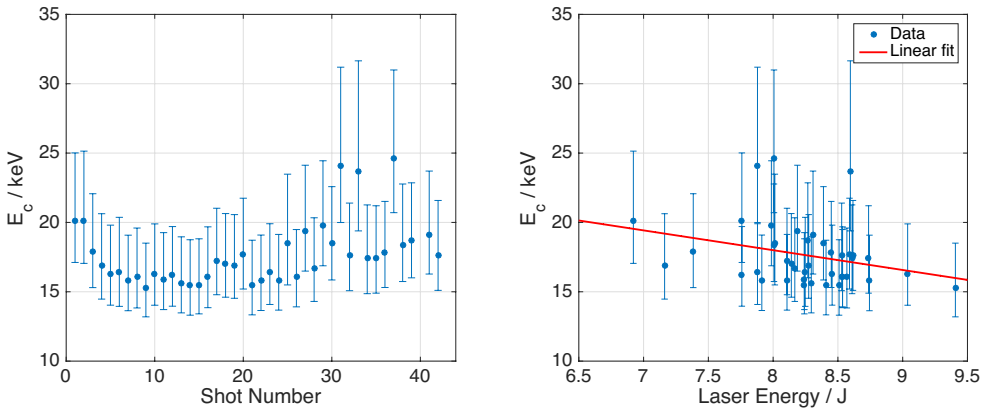


Figure 6.26: Critical energy as a function of shot number (left) and laser energy (right) for the aluminium shock imaging run.

peak electron energy was lowest at the lowest laser energies. This could be a dephasing effect because the nonlinear plasma wavelength is shorter, or it could be that via some means electrons have larger betatron oscillation radius with slightly reduced a_0. In any case, it highlights the fact that for the most reproducible results it is crucial to minimise fluctuations in the laser parameters. This was something that was strongly highlighted in the $f/20$ set-up where there were large random fluctuations in laser spot size.

Spectral measurements from the 64 filter array were taken in similar conditions but on a different day. A density scan was performed to find the critical energy as a function of number density, which is plotted in figure 6.27. At our familiar operating density

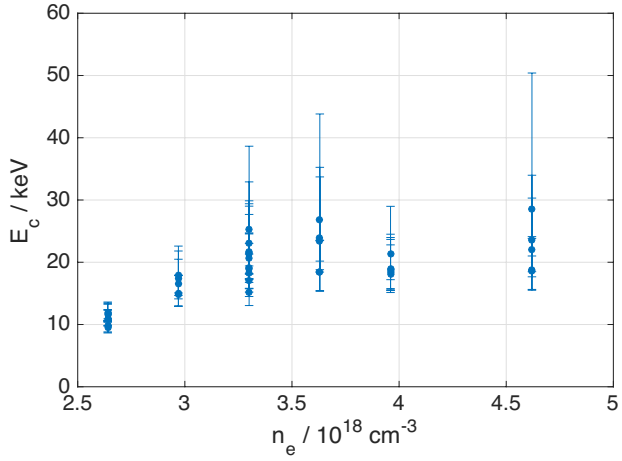


Figure 6.27: Critical energy as a function of electron number density

of $(3.5 - 3.9) \times 10^{18}$ cm^{-3}, E_c is slightly above 20 keV here, which is not too different from what was measured during the shock imaging run. The total number of photons in the beam and the brightness, again assuming a 1 μm source diameter, are plotted as

a function of n_e in figure 6.28. At the imaging density, which coincided with the peak

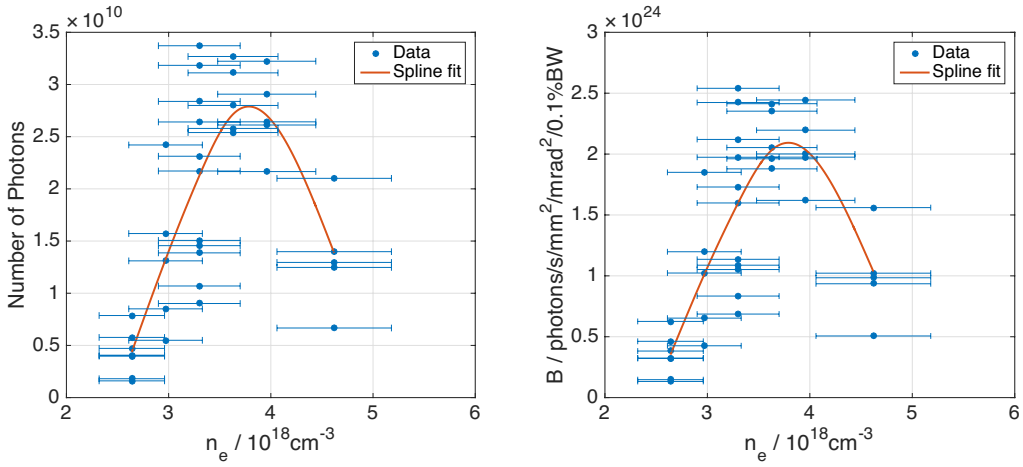


Figure 6.28: Number of photons (left) and peak brightness (right) as a function of number density. The brightness was calculated assuming a 1 μm source diameter.

photon flux, approximately 3×10^{10} photons were contained within the whole beam. This is only a factor of 1.5 larger than what was found in the best conditions in the $f/20$ experiment but crucially the beam divergence was smaller, meaning that more photons were detected per pixel. At $n_e = 3.5 \times 10^{18}$ cm^{-3} an average of $(4.6 \pm 0.6) \times 10^9$ photons hit the camera, compared to $\sim 1.6 \times 10^9$ in the best conditions in the $f/20$ experiment. This is an increase by a factor of approximately 3. It also suggests a narrower beam divergence than discussed in section 6.6.1. The mean peak brightness from the $f/20$ and $f/40$ experiments from this chapter are plotted in figure 6.29 which shows the significant increases made in x-ray flux in the $f/40$ experiment, which we anticipate will lead to much higher quality images. For the $f/40$ experiment a 0.8 ± 0.1 μm source diameter was used, double the r_β found using the same method as in section 6.3.3.

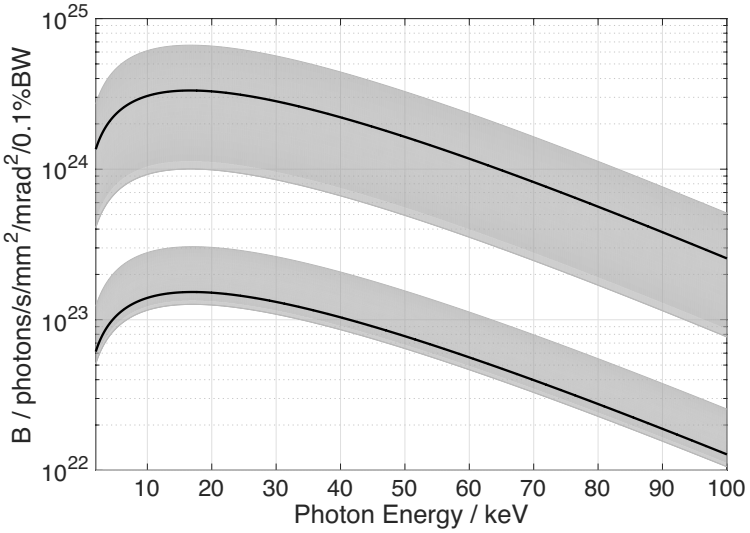


Figure 6.29: Comparison of mean peak brightness between the $f/20$ (lower curve) and $f/40$ (upper curve) shock physics experiments. The grey shaded areas denote the standard error.

6.7 Shock Propagation in an Aluminium Target

A scan was performed varying the betatron probe delay relative to the arrival of the shock driver laser at the surface of the aluminium target. This allowed the dynamics of the shock propagation to be seen. The images from this timing scan are shown in figure 6.30. We immediately see that as a consequence of the higher number of photons per pixel and the addition of the kicker magnet the signal to noise ratio has improved greatly compared to figure 6.15. To remove the small amount of noise that there was a 2×2 background from minima filter was applied in ImageJ. The relatively small laser spot drove a roughly spherical shock wave in to the target, which can be tracked through each of the images, apart from the one at 70 ns which seems to be something of an anomaly. It seems likely that the pulse foot at early times had a significant impact on the experiment. The image taken at 30 ns delay is enlarged in figure 6.31, where we see a low amplitude shock wave has already traversed most of the material as the main shock wave has a long way still to go. This may be why we see a significant amount of spall just ahead of the high density bulk of the material. In the images taken at 60 ns and 80 ns the beginnings of jet growth can be seen from the positions which started off as concave parts of the target rear surface. This confirms that betatron radiation would be well suited to making a measurement of material strength from RMI growth if the conditions of foot-free laser driver and correct target thickness could be put together.

This shot taken with a 30 ns delay is analysed further with the help of figure 6.32.

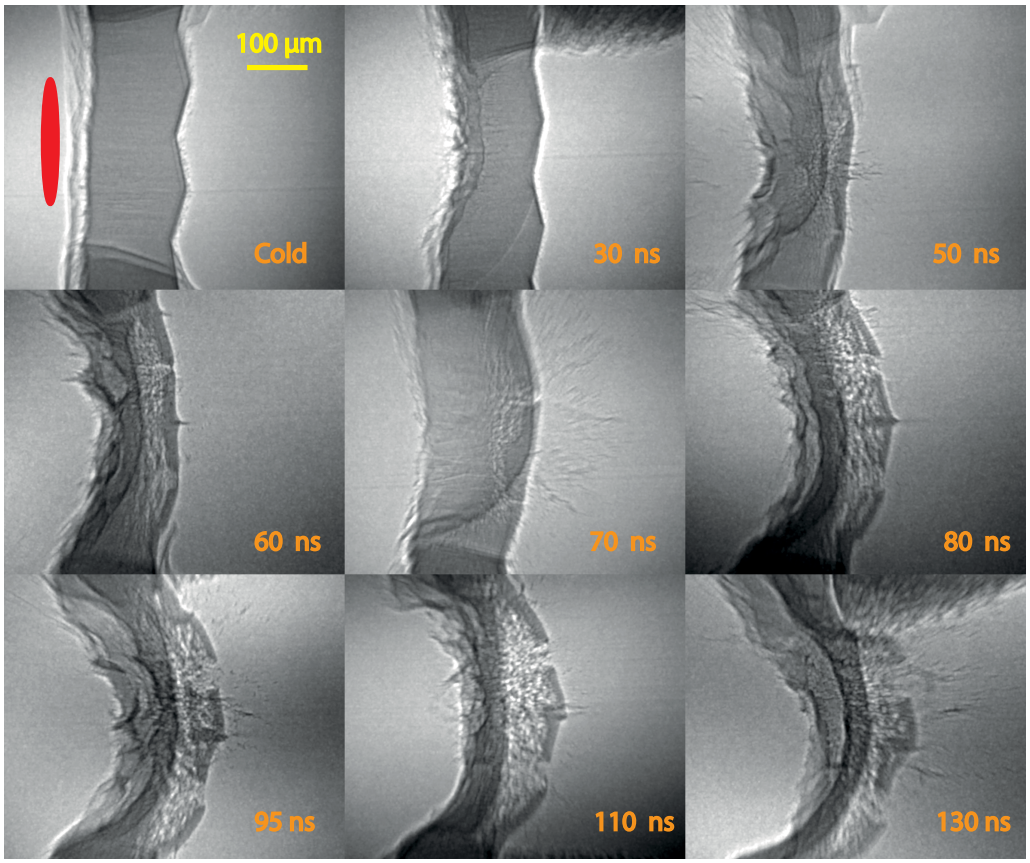


Figure 6.30: Betatron x-ray images of shocks travelling through aluminium taken at a range of delays. The red ellipse in the top left image shows the FWHM size of the drive laser spot. The orange numbers are the delay between the arrival of the shock drive laser and the betatron probe.

Note that the delay refers to the length of time between the arrival of the front of the foot of the pulse at the surface of the target and the arrival of the betatron beam, so that the most intense part of the pulse does not arrive at the target until approximately 20 ns after the beginning of the interaction. To quantify the density change caused by the small shock driven by the foot of the pulse, first three rectangles were drawn within the green lines: one inside the shocked material, one in the unshocked material and one in vacuum. The mean intensity value of the pixels within these rectangles is related to the optical depth of aluminium via the Beer-Lambert law. To eliminate the effects of phase contrast (this analysis requires an absorption contrast image) the rectangles were positioned away from the shock front and material edges. A standard feature of phase contrast imaging is clear in figure 6.32: at sharp density gradients there is a dark/ light fringe that enhances the edge. This is, therefore, to be avoided in this method. Comparison of the x-ray transmission through the unshocked aluminium and the vacuum suggested an effective photon energy of 20.2 keV on this shot. The transmission of the shocked material relative to the unshocked material was 0.988. Following the same procedure as section 6.4 it was

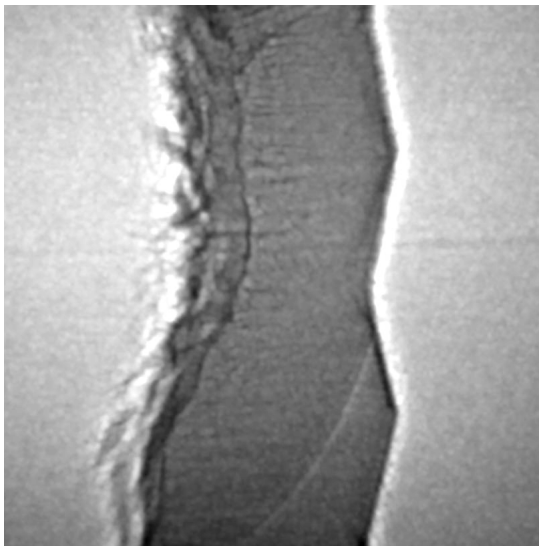


Figure 6.31: Enlarged image of the shock in Al with 30 ns betatron delay. Near the bottom right of the target there is a shock front, enhanced by phase contrast, which has been driven in to the material by the pulse foot.

calculated that the density of the material behind the shock was $2.73\,\mathrm{g/cm^3}$, compared to $2.70\,\mathrm{g/cm^3}$ in the cold case. This has arisen simply from the difference in x-ray transmission between the two regions of the target and the application of the Beer-Lambert law. This demonstrates that betatron radiographs can resolve differences in material density of just over 1%.

The properties of the main shock, bounded by the blue lines, can be analysed in the same way. The transmission through the shocked region relative to the unshocked region was 0.754. Following the same analysis as for the weak shock detailed above, the density of the material was found to increase to $4.2\,\mathrm{g/cm^3}$ behind the main shock. The diagram shows that the main shock front has propagated $86\,\mu\mathrm{m}$ in the 10 ns since the arrival of the sharp peak of the main pulse (refer back to figure 6.24), implying a shock velocity of $8.6\,\mathrm{kms^{-1}}$. The Rankine-Hugoniot conditions (equations 6.3 and 6.4) reveal that the particle velocity behind the shock $u_1 \approx 3.1\,\mathrm{km/s}$, implying that the pressure was 71 GPa. Drake's equation, equation 6.6, estimates a shock pressue of 82.7 GPa for a drive intensity of $3.5 \times 10^{12}\,\mathrm{W/cm^2}$, which is in good agreement with the experimentally deduced value. 1D HELIOS simulations were run using an approximation to the real temporal pulse shape impacting at normal incidence on a $170\,\mu\mathrm{m}$ thick sample of aluminium. The simulation revealed a pressure a few microns behind the shock, as measured on the experimental image, in the range $30 - 40\,\mathrm{GPa}$, within a factor of ~ 2 of the experimental value. It also overestimated the shock velocity- predicting that the shock would have travelled $135\,\mu\mathrm{m}$ in to the material, and it underestimated the density compared to the experiment, which reached a peak of $3.6\,\mathrm{g/cm^3}$ compared to the measured value of $4.2\,\mathrm{g/cm^3}$. Again the 1D

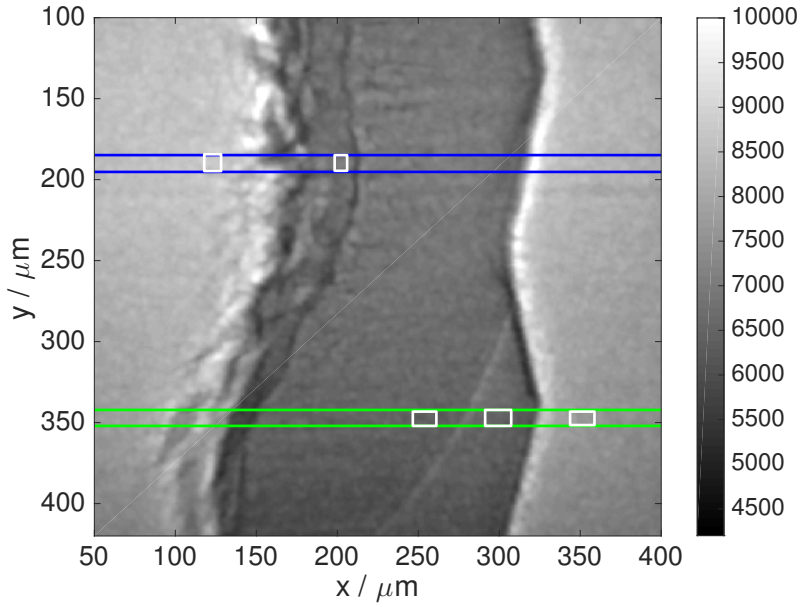


Figure 6.32: Diagram depicting the analysis method for the shocked aluminium 30 ns after the start of the interaction.

radiation-hydrodynamics simulation was a very simple approximation to the experiment, where the target was initially solid aluminium and the laser had spatial variations in intensity as well as temporal variations.

6.8 Summary and Outlook

In this chapter two experiments were undertaken using ~ 20 keV betatron radiation to image shock propagation in silicon and grooved aluminium targets. The major result was that the increase in x-ray flux with the long focal length ($f/40$) wakefield driver geometry, which was reported in chapter 5, led to a large improvement in the quality of images. The imaging resolution was comparable with what has been achieved in recent experiments at conventional synchrotron light sources. The images of the aluminium targets with the improved signal to noise ratio are comparable in quality to those taken recently at synchrotron [241] [28] [232] and X-FEL [242] sources. This was all done in a significantly more compact facility with a fraction of the cost. It was shown that betatron x-ray radiographs can be used to make quantitative statements about the properties of a material in shocked conditions, and that it can resolve differences in density as small as $\sim 1\%$.

While there has been a lot of talk about using betatron radiation as a compact source of hard x-ray radiation, there have been very few uses of it to probe current scientific problems. This work shows that betatron radiation had advanced to a level where it can

make an impact in the field of HEDP science. It is currently the case that high power, short pulse laser facilities are generally not equipped to meet the demands of the shock physics community, especially when it comes to providing the ideal flat-top temporal pulse profile for the shock driver. Likewise many HEDP facilities do not have a compact source of brilliant x-rays, meaning that only experiments relying on portable shock driver equipment can be done at x-ray facilities. It seems likely that in the future these issues can be resolved by the installation of a LWFA facility at a permanent HEDP facility, allowing a broader range of users to reap the benefits of bright, hard, pulsed synchrotron light.

With this scenario in mind, the possibility of imaging non-laser driven shocks with betatron radiation will now be discussed. A common method of driving a shock is to use a high velocity (of order $1\,\mathrm{kms}^{-1}$) flyer, accelerated by a gas gun, impacting on a sample. Typical sample diameters range from 20 mm [243] to 100 mm or more [244]. Figure 6.33 shows the intensity transmission through aluminium in this range of material thickness for an 18 keV critical energy betatron spectrum. For reference the transmission through 200 μm aluminium, which was the thickness for the images presented in this chapter, is 0.76. The graph shows that, especially for the $\sim$ 18 keV energy spectra pre-

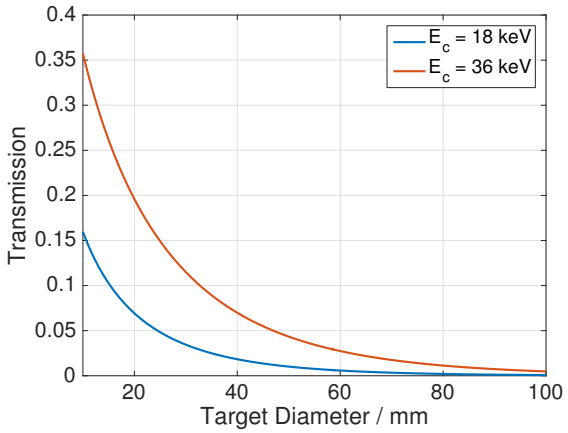


Figure 6.33: Transmission of the betatron beam through thicknesses of aluminium relevant to gas gun experiments.

sented in this chapter, imaging through very thick (many 10's mm) targets is not viable. For 10 mm thick aluminium targets the transmission is reduced by a factor 5, meaning that it should be just about viable to image through them with this betatron source. If the critical energy could be doubled from its current value while only keeping constant the x-ray beam intensity, images of 10 mm aluminium could be taken with a factor of 2 reduction in transmitted intensity compared to those presented in this chapter. This would still produce high quality images. If a factor of 5 reduction is acceptable, 25 mm thick targets could be imaged. Note that for such large targets, very little magnification would be possible meaning that the resolution will be worse, and probably close to the

intrinsic resolution of the scintillator. Due to rapidly increasing x-ray absorption with the atomic number, betatron imaging, or even synchrotron x-ray imaging in general, is not likely to be applicable to subsurface imaging of thick, high Z targets in the near future.

We have seen that betatron imaging may be applicable to mechanical impact driven shocks for relatively small samples of low Z materials. It is better suited to laser driven shocks which can be created in smaller samples of material. In this case future increases in critical energy from more powerful laser systems could be used to extend the range of materials this can be applied to. There are in fact many long pulse laser systems in the world that are used to drive shock physics experiments, and these are likely to benefit most from betatron imaging if a short pulse laser system can be installed at such a facility. By keeping the target size small the magnification of the target can be large, which combined with the small source size of betatron radiation means that high resolution images can be taken in a relatively compact geometry, especially compared to the very long beamlines found at synchrotrons.

Figure 6.34 shows the number of photons per eV from the betatron source reported in section 6.6.3, with a critical energy of 18.0 keV and a total of 3×10^{10} photons in the whole beam above 1 keV. Up to ~ 20 keV there are more than 5×10^5 photons/eV in the whole

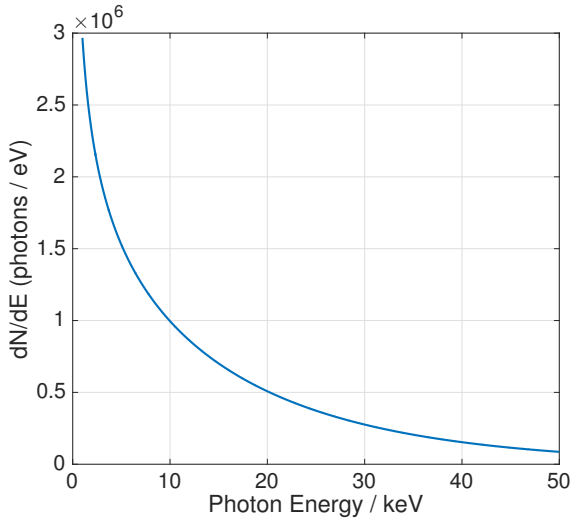


Figure 6.34: Photons per eV from the betatron source.

beam. This suggests that it should be possible to do hard x-ray diffraction experiments with betatron radiation, although it may require detectors that are single photon sensitive and are well shielded from noise. If a demonstration of dynamic diffraction from a target could be made with a betatron source, which seems to be possible, then it could be considered to really have capabilities equal to current third generation light sources.

Chapter 7

Conclusions

This thesis has mostly been concerned with the production, characterisation and application of hard betatron x-ray radiation from laser wakefield accelerators. By driving a wakefield with a large spot $w_0 \sim 2\lambda_p$, and a moderate $a_0 = 1.1$, it was shown that an electron bunch with a very small transverse source size could be self-injected. This was accelerated to a maximum peak energy of 1.9 GeV, meaning that it produced a very high brightness source of x-rays: a peak brightness of 2.8×10^{24} photons/s/mm^2/mrad^2/0.1%BW with a critical energy of (21 ± 1) keV was measured. This is a similar critical energy to what has been found in shorter focal length experiments ($f/20$) but the brightness is approximately 7 times larger, driven by the smaller source size: the source diameter was ~ 300 nm. This is the highest brightness reported from a betatron source. By extending the length of the accelerator at constant plasma density it was seen that a second electron bunch was injected with a similar charge, at ~ 100 pC, to the first bunch. Due to laser depletion this bunch was accelerated only to 600 MeV energies, independent of accelerator length, meaning that it had a much higher charge per unit bandwidth than the initial bunch. The injection of the second bunch caused a large (factor of 5) increase in the number of photons emitted by the source, but only at moderate energies as the overall temperature of the spectrum fell to ~ 16 keV. The increased number of photons was driven by an increase in the betatron oscillation radius, and the cooling off in the spectrum was due to the limited energy gain of the electrons. The source brightness dropped slightly to $1 - 1.5 \times 10^{24}$ photons/s/mm^2/mrad^2/0.1%BW as a result of the increased r_β, however this is likely to be a more useful mode for applications because of the large number of photons. These high brightness betatron results are currently being written up for publication. Future betatron experiments are likely to take advantage of the large increase in number of photons from this move to a longer focal geometry. One immediate advantage is that the quality of x-ray images taken with betatron radiation can be improved. Later in the very same experiment this was already achieved: a high quality tomogram of an embryonic mouse sample was taken, which is currently being written up for publication in correspondence with the author. The brightness increase may also make it possible

to move to source-size limited imaging resolutions at hard ($> 10\,\text{keV}$) photon energies because a thinner scintillator could be used and still produce enough light to create a high signal-to-noise ratio image. It will also be much easier to perform single shot experiments probing dynamic structure changes in warm dense matter, using techniques such as XANES or EXAFS. From the nature of laser wakefield accelerators, this would be at a pulse length comparable to an X-FEL. Indeed it has been estimated that high quality single shot XANES spectra could be obtained with a flux greater than 10^6 photons/eV [94]. The brightest spectrum reported in this thesis had approximately 1.4×10^6 photons/eV at 6-8 keV, close to the iron k-edge, meaning that single shot, low noise XANES data could be collected with a well designed experiment.

To demonstrate the applicability of betatron radiation as a tool for solving modern science problems, two experiments were performed where betatron images of shock propagation in solids were taken. The first of these was with an $f/20$ geometry, and the second with an $f/40$. By using a slightly larger $a_0 \approx 1.4$ in this $f/40$ experiment it was shown that up to 3.5×10^{10} photons could be produced per shot, from a $0.8\,\mu$m diameter source, corresponding to a peak brightness of 2.5×10^{24} photons/s/mm^2/mrad^2/0.1%BW. This was an increase on the number of photons from the $f/20$ experiment by a factor of approximately 1.5, but crucially the beam divergence was smaller meaning that the x-ray intensity was boosted by a factor of 3. The images taken with the $f/40$ geometry were of a similar quality to those that have been taken at synchrotron and x-ray sources, with similar few micron resolution and good signal to noise levels. In addition, it was demonstrated that betatron radiation can be used to make quantitative measurements of density and shock velocity. Calculations showed that the source has in excess of 5×10^5 photons/eV at photon energies up to $\sim 20\,\text{keV}$, suggesting that with sufficiently sensitive diagnostics it should be possible to perform hard x-ray diffraction experiments to probe ultrafast phase changes. Therefore this is a promising source for compact installation at existing, mainly long pulse[1] laser based, facilities performing HEDP experiments, allowing them to benefit from this bright x-ray source. At the time of writing, experiments involving diffraction of betatron radiation from a temporally evolving sample and spectroscopic measurements of warm dense matter are being planned by U.K. groups, including the Imperial College group, to be performed at the Gemini laser system. Thanks to the work presented in this thesis, these will almost certainly be taking advantage of the increase in photons/mrad^2 from a LWFA in a long focal length geometry. The results of shock propagation in silicon are being written up for publication currently. The large increase in imaging quality in the long focal length geometry, in the particular case of shock imaging, is worthy of report in its own right. However work is ongoing to understand the shock physics further before publication.

[1]Long pulse here refers to nanosecond timescales.

It was also shown that by using a clustered LWFA target, rather than a more conventional gas monomer target, it was possible to inject beams in to a wakefield with 3 times more transverse momentum in the laser polarisation direction than in the perpendicular direction. This was shown to be an electron source with greater reproducibility and tunability than those based on self-injection, without compromising the maximum energy or amount of charge that was accelerated. This could, then, be a future reliable source of hard, polarised betatron x-rays. These results are currently being combined with further data taken by the Imperial College London group, although not the author, which compare data from clustered methane with unclustered methane in a gas cell. This will allow a clearer picture to be formed of the mechanics of clusters in laser wakefield accelerators. The experiment reported in this thesis inspired further investigations of methane clusters taken using the Gemini TA3 (few hundred TW) laser beam, the results of which are currently being analysed. This data will also be published in the near future.

Chapter 8

Appendix

8.1 Maxwell's Equations

The underpinning of any work on electromagnetism are Maxwell's equations

$$\boldsymbol{\nabla}.\boldsymbol{E} = \frac{\rho}{\epsilon_0} \tag{8.1}$$

$$\boldsymbol{\nabla}.\boldsymbol{B} = 0 \tag{8.2}$$

$$\boldsymbol{\nabla} \times \boldsymbol{E} = -\frac{\partial \boldsymbol{B}}{\partial t} \tag{8.3}$$

$$\boldsymbol{\nabla} \times \boldsymbol{B} = \mu_0 \boldsymbol{J} + \mu_0 \epsilon_0 \frac{\partial \boldsymbol{E}}{\partial t} \tag{8.4}$$

Maxwell's equations describe how the electric field $\boldsymbol{E}$ and magnetic field $\boldsymbol{B}$ change in relation to electric charges and currents, and indeed each other. ρ represents the charge density, $\boldsymbol{J}$ the current density and μ_0 and ϵ_0 are the permeability and permittivity of free space. Typically in electrostatics the $\boldsymbol{E}$ field is written as the gradient of some potential i.e. $\boldsymbol{E} = -\boldsymbol{\nabla}\phi$. Combined with equation 8.1, this yields the familiar Poisson equation

$$\nabla^2 \phi = -\frac{\rho}{\epsilon_0} \tag{8.5}$$

Similarly a potential for $\boldsymbol{B}$, $\boldsymbol{A}$, can be defined such that $\boldsymbol{B} = \boldsymbol{\nabla} \times \boldsymbol{A}$, meaning that equation 8.2 is automatically fulfilled. Examining Faraday's equation 8.3 and substituting for $\boldsymbol{B}$, one is left with the equation

$$\boldsymbol{\nabla} \times \left(\boldsymbol{E} + \frac{\partial \boldsymbol{A}}{\partial t} \right) = 0 \tag{8.6}$$

Mathematically some $\boldsymbol{\nabla} f$, where f is a scalar function, can be added to the term in brackets and the equality still holds, explicitly

$$\boldsymbol{\nabla} \times \left(\boldsymbol{E} + \frac{\partial \boldsymbol{A}}{\partial t} + \boldsymbol{\nabla} f \right) = 0 \tag{8.7}$$

This is known as gauge invariance. Comparing 8.7 to Poisson's equation the identification $f = \phi$ is made. This ensures that equation 8.3 is always fulfilled by our definitions of the potentials ϕ and $\boldsymbol{A}$:

$$\boldsymbol{B} = \boldsymbol{\nabla} \times \boldsymbol{A} \tag{8.8}$$

$$\boldsymbol{E} = -\frac{\partial \boldsymbol{A}}{\partial t} - \boldsymbol{\nabla} \phi \tag{8.9}$$

Inserting these equations in to Maxwell's equations 8.1 and 8.4, one derives Maxwell's equations in terms of the potentials:

$$-\nabla^2 \phi - \frac{\partial}{\partial t} \boldsymbol{\nabla}.\boldsymbol{A} = \frac{\rho}{\epsilon_0} \tag{8.10}$$

$$\boldsymbol{\nabla} \left(\boldsymbol{\nabla}.\boldsymbol{A} \right) - \nabla^2 \boldsymbol{A} = \mu_0 \boldsymbol{J} - \mu_0 \epsilon_0 \frac{\partial^2 \boldsymbol{A}}{\partial t^2} - \mu_0 \epsilon_0 \boldsymbol{\nabla} \frac{\partial \phi}{\partial t} \tag{8.11}$$

These are neither the most tractable nor beautiful equations to deal with. They can however be simplified by a choice of gauge. An initially 'obvious' choice is the Coulomb gauge where one sets $\boldsymbol{\nabla}.\boldsymbol{A} = 0$ yielding the equations below. This has the advantage that the potential ϕ is the familiar scalar potential defined by Poisson's equation. In this gauge Maxwell's equations are

$$\nabla^2 \phi = -\frac{\rho}{\epsilon_0} \tag{8.12}$$

$$-\nabla^2 \boldsymbol{A} = \mu_0 \boldsymbol{J} - \mu_0 \epsilon_0 \frac{\partial^2 \boldsymbol{A}}{\partial t^2} - \mu_0 \epsilon_0 \boldsymbol{\nabla} \frac{\partial \phi}{\partial t} \tag{8.13}$$

Another common choice of gauge is the Lorenz gauge

$$\boldsymbol{\nabla}.\boldsymbol{A} + \mu_0 \epsilon_0 \frac{\partial \phi}{\partial t} = 0 \tag{8.14}$$

This reduces Maxwell's equations in terms of potentials to the equations

$$\mu_0 \epsilon_0 \frac{\partial^2 \phi}{\partial t^2} - \nabla^2 \phi = \frac{\rho}{\epsilon_0} \tag{8.15}$$

$$\mu_0 \epsilon_0 \frac{\partial^2 \boldsymbol{A}}{\partial t^2} - \nabla^2 \boldsymbol{A} = \mu_0 \boldsymbol{J} \tag{8.16}$$

It is often argued that this is the natural gauge because of the symmetry of these equations, the fact that ϕ and $\boldsymbol{A}$ are uncoupled and the fact that these equations are quite simple: they are wave equations driven by charge and current densities. However through the

choice of gauge we have made some sacrifice. ϕ is no longer the familiar scalar potential as waves of ϕ defined here can propagate in the absence of a source. The propagation is at the speed of light $c = 1/\left(\mu_0 \epsilon_0\right)^{\frac{1}{2}}$

8.2 Normalised Units

The normalised units used in this thesis are detailed in the table below.

Physical Quantity	Description	Normalised Quantity
$\boldsymbol{v}$	Velocity	$\boldsymbol{\beta} = \boldsymbol{v}/c$
$\boldsymbol{p}$	Momentum	$\tilde{\boldsymbol{p}} = \boldsymbol{p}/m_e c = \gamma\boldsymbol{\beta}$
$\boldsymbol{A}$	Vector Potential	$\boldsymbol{a} = e\boldsymbol{A}/m_e c$
$\boldsymbol{u}$	Generalised Momentum	$\tilde{\boldsymbol{u}} = \boldsymbol{u}/m_e c$
ϕ	Scalar Potential	$\tilde{\phi} = e\phi/m_e c^2$
H	Hamiltonian	$\tilde{H} = H/m_e c^2$

Table 8.1: Summary of normalised units

8.3 The Relativistic Ponderomotive Force

We start with the Lagrangian for an electron subjected to some external field $\boldsymbol{a}$ which is repeated here for convenience

$$L = -m_e c^2 \sqrt{1-\beta^2} - m_e c \boldsymbol{v}.\boldsymbol{a} \tag{8.17}$$

Applying the Euler-Lagrange equations leads to the equation of motion

$$\frac{d\tilde{\boldsymbol{u}}}{dt} = -\boldsymbol{v}.\boldsymbol{\nabla}\boldsymbol{a} = -c\frac{\tilde{\boldsymbol{p}}}{\gamma}.\boldsymbol{\nabla}\boldsymbol{a} \tag{8.18}$$

This is written in the normalised units (section 8.2). $\tilde{\boldsymbol{p}}$ is the normalised linear momentum and $\tilde{\boldsymbol{u}}$ is the normalised canonical momentum. Making the substitution $\tilde{\boldsymbol{p}} = \tilde{\boldsymbol{u}} + \boldsymbol{a}$ this can be re-written as

$$\frac{d\tilde{\boldsymbol{u}}}{dt} = -\frac{c}{\gamma}\tilde{\boldsymbol{u}}.\boldsymbol{\nabla}\boldsymbol{a} - \frac{1}{2}\frac{c}{\gamma}\boldsymbol{\nabla}a^2 \tag{8.19}$$

As we are interested only in the slowly varying part of the motion we now take the time average of this equation

$$\left\langle \frac{d\tilde{\boldsymbol{u}}}{dt} \right\rangle = -\frac{1}{\Delta t}\int_t^{t+\Delta t} \left(\frac{c}{\gamma}\tilde{\boldsymbol{u}}.\boldsymbol{\nabla}\boldsymbol{a} + \frac{c}{2\gamma}\boldsymbol{\nabla}a^2 \right) dt' \tag{8.20}$$

The second term in this integral depends on a^2 which is always positive therefore its time average will be non-zero. The first term can be integrated by parts as done in the integral

$$I = \int_t^{t+\Delta t} \left(\frac{c}{\gamma} \tilde{\boldsymbol{u}} . \boldsymbol{\nabla} \boldsymbol{a} \right) dt' = \left[\frac{c}{\gamma} \tilde{\boldsymbol{u}} . \boldsymbol{\nabla} \left\langle \boldsymbol{a} \right\rangle \right]_t^{t+\Delta t} - \int_t^{t+\Delta t} c \boldsymbol{\nabla} \left\langle \boldsymbol{a} \right\rangle . \frac{\partial}{\partial t} \left(\frac{\tilde{\boldsymbol{u}}}{\gamma} \right) dt' \tag{8.21}$$

Both terms in this integral depend on $\langle \boldsymbol{a} \rangle$ which is approximately equal to zero if the laser envelope is slowly varying. Therefore the relativistic ponderomotive force, which is a generalised force because it is the time rate of change of the generalised momentum, can be written as

$$\left\langle \frac{d\tilde{\boldsymbol{u}}}{dt} \right\rangle = -\frac{1}{2} c \left\langle \frac{1}{\gamma} \boldsymbol{\nabla} a^2 \right\rangle \tag{8.22}$$

8.4 The Wave Frame

When dealing with any wave equation i.e. one with two spatial and two time derivatives, the 1D solution typically has the form $f(z - vt)$ where f is some function that can be differentiated at least twice with respect to time and space. v is the velocity of the wave. To work with solutions of this form, of which there are a number in this work, it is easier to work in the wave frame. This has coordinates $\xi = z - vt$ and $\tau = t$. Since we are dealing with light waves $v = v_g \approx c$. The derivatives transform as

$$\frac{d}{dz} = \frac{\partial \tau}{\partial z} \frac{d}{d\tau} + \frac{\partial \xi}{\partial z} \frac{d}{d\xi} = \frac{d}{d\xi} \tag{8.23}$$

$$\frac{d}{dt} = \frac{\partial \tau}{\partial t} \frac{d}{d\tau} + \frac{\partial \xi}{\partial t} \frac{d}{d\xi} = \frac{d}{d\tau} - c \frac{d}{d\xi} \tag{8.24}$$

Often the quasi-static approximation is used where processes are assumed to vary slowly in the frame of the wave. In this case $\frac{d}{d\tau} = 0$.

8.5 General Equations for Radiation from a Moving Charge

From appendix 8.1, equations 8.15 and 8.16 we have Maxwell's equations written in terms of the potentials $\boldsymbol{A}$ and ϕ, repeated here for convenience.

$$\mu_0 \epsilon_0 \frac{\partial^2 \phi}{\partial t^2} - \nabla^2 \phi = \frac{\rho}{\epsilon_0} \tag{8.25}$$

$$\mu_0 \epsilon_0 \frac{\partial^2 \boldsymbol{A}}{\partial t^2} - \nabla^2 \boldsymbol{A} = \mu_0 \boldsymbol{J} \tag{8.26}$$

This is using the Lorenz gauge $\left(\boldsymbol{\nabla}.\boldsymbol{A} + \mu_0\epsilon_0\frac{\partial\phi}{\partial t} = 0\right)$. The general solution to these equations for the fields $\boldsymbol{E}$ and $\boldsymbol{B}$ from a moving charge are the Liénard-Wiechert fields

$$\boldsymbol{E}\left(\boldsymbol{r},t\right) = \frac{e}{4\pi\epsilon_0}\left[\frac{\hat{\boldsymbol{n}}-\boldsymbol{\beta}}{\gamma^2R^2\left(1-\boldsymbol{\beta}.\hat{\boldsymbol{n}}\right)^3} + \frac{\hat{\boldsymbol{n}}\times\left[\left(\hat{\boldsymbol{n}}-\boldsymbol{\beta}\right)\times\dot{\boldsymbol{\beta}}\right]}{cR\left(1-\boldsymbol{\beta}.\hat{\boldsymbol{n}}\right)^3}\right]_{ret} \tag{8.27}$$

$$\boldsymbol{B}\left(\boldsymbol{r},t\right) = \frac{\hat{\boldsymbol{n}}\times\boldsymbol{E}}{c} \tag{8.28}$$

The vector $\boldsymbol{R} = \boldsymbol{r} - \boldsymbol{r}_0\left(t_{ret}\right)$ is the vector pointing from the position of the charge $\boldsymbol{r}_0$ at the retarded time t_{ret} to the observer at position $\boldsymbol{r}$ at time t. The distance from the charge at t_{ret} to the observer is $R = |\boldsymbol{R}|$ and the unit vector pointing in this direction is $\hat{\boldsymbol{n}} = \boldsymbol{R}/R$. The retarded time $t_{ret} = t - R/c$ where t is the observation time. Note that the fields at position $\boldsymbol{r}$ and time t are written entirely in terms of the charge position, velocity and acceleration at the retarded time. Setting $\boldsymbol{\beta} = 0$ and $\dot{\boldsymbol{\beta}} = 0$ reduces $\boldsymbol{E}$ to Coulomb's law and leaves $\boldsymbol{B} = 0$.

Looking back at the form of equation 8.27, the fields are split in to two parts. The left hand part depends on the particle velocity and is known as the velocity field or generalised Coulomb field. The term on the right depends on the acceleration of the charge and is referred to as the acceleration field or radiation field. We note that the velocity field scales as $1/(\gamma^2R^2)$ while the acceleration field scales as $1/R$. Far away from the source, the $\boldsymbol{E}$ field from equation 8.27 reduces to

$$\boldsymbol{E}\left(\boldsymbol{r},t\right) = \frac{e}{4\pi\epsilon_0}\left[\frac{\hat{\boldsymbol{n}}\times\left[\left(\hat{\boldsymbol{n}}-\boldsymbol{\beta}\right)\times\dot{\boldsymbol{\beta}}\right]}{cR\left(1-\boldsymbol{\beta}.\hat{\boldsymbol{n}}\right)^3}\right]_{ret} \tag{8.29}$$

The $\boldsymbol{B}$ field can still be written as equation 8.28. By using the definition of the vector triple product and noting that $\boldsymbol{E}.\hat{\boldsymbol{n}} = 0$, the Poynting vector $\boldsymbol{S} = \frac{1}{\mu_0}\boldsymbol{E}\times\boldsymbol{B} = \frac{1}{c\mu_0}\boldsymbol{E}\times\hat{\boldsymbol{n}}\times\boldsymbol{E}$ can be written as

$$\left[\boldsymbol{S}.\hat{\boldsymbol{n}}\right]_{ret} = \frac{e^2}{16\pi^2c\epsilon_0}\left[\frac{1}{R^2}\left|\frac{\hat{\boldsymbol{n}}\times\left[\left(\hat{\boldsymbol{n}}-\boldsymbol{\beta}\right)\times\dot{\boldsymbol{\beta}}\right]}{\left(1-\boldsymbol{\beta}.\hat{\boldsymbol{n}}\right)^3}\right|^2\right]_{ret} \tag{8.30}$$

This is the energy per unit area per unit time detected by the observer at time t. Following Jackson [100], the total energy radiated by the charge due to its acceleration between times $t' = T_1$ and $t' = T_2$ is:

$$E = \int_{t=T_1+|R(T_1)/c|}^{t=T_2+|R(T_2)/c|}\left[\boldsymbol{S}.\hat{\boldsymbol{n}}\right]_{ret}dt = \int_{t'=T_1}^{t'=T_2}\left(\boldsymbol{S}.\hat{\boldsymbol{n}}\right)\frac{dt}{dt'}dt' \tag{8.31}$$

t' is the particle's own (i.e. retarded) time, and t is the observation time. From this we note that the power emitted per unit solid angle, as a function of the charge's own time t', is

$$\frac{dP(t')}{d\Omega} = R^2 \left(\boldsymbol{S}.\hat{\boldsymbol{n}}\right) \frac{dt}{dt'} = \frac{e^2}{16\pi^2 c\epsilon_0} \frac{\left|\hat{\boldsymbol{n}} \times \left[(\hat{\boldsymbol{n}} - \boldsymbol{\beta}) \times \dot{\boldsymbol{\beta}}\right]\right|^2}{\left(1 - \boldsymbol{\beta}.\hat{\boldsymbol{n}}\right)^5} \tag{8.32}$$

This has used $\frac{dt}{dt'} = (1 - \boldsymbol{\beta}.\hat{\boldsymbol{n}})$, which can be calculated from the definition $t' = t - R(t')/c$. Relativistic effects enter this equation through the $(1 - \boldsymbol{\beta}.\hat{\boldsymbol{n}})^{-1}$ term. The fact that this is raised to the fifth power in the $\frac{dP(t')}{d\Omega}$ equation means that as $\beta \to 1$ the emitted radiation becomes confined to a tight angle in the forwards direction. Integration over all angles [100] gives the total power radiated as

$$P = \frac{e^2}{6\pi c\epsilon_0} \gamma^6 \left[\left|\dot{\boldsymbol{\beta}}\right|^2 - \left|\boldsymbol{\beta} \times \dot{\boldsymbol{\beta}}\right|^2\right] \tag{8.33}$$

8.6 Lanex

Lanex, while a trademark of the Kodak company, is used as an umbrella term in this thesis and throughout the field for a powdered (∼10-12 μm grain size [245]) terbium doped gadox (Gd_2O_2S:Tb) scintillator deposited on to a plastic support layer. The peak emission wavelength of this scintillator is 546 nm [246] with a relaxation time on the order of 1 ms [168] [247]. There is a lack of consensus in the literature on the angular emission of scintillation light from Lanex screens. Glinec [168] writes that the distribution is close to Lambertian referencing Giakoumakis [245], who reports in his/ her paper that deviations of 5-25% from a Lambertian are found! Buck [246] finds deviations of a few per-cent. It is clear at least that some care should be taken if one should need to rely on this assumption.

The brand names of the Lanex available for use in experiments were Kodak Lanex Fine, Lanex Regular and Lanex Fast, and Mitsubishi Chemical DRZ-STD, DRZ-PLUS and DRZ-HIGH. A table summarising some of their properties [248] [249] [168] [250] is displayed in 8.2. Since light output is generally increased by using a thicker scintillator there is a trade-off between sensitivity and resolution, which is quantified in the table by the Modulation Transfer Function (MTF, section 3.5.6). Typically DRZ-STD was used for the electron beam profile screen and Lanex Regular was used for the electron spectrometer screens, meaning that 0.25 mm sized features are reasonably well resolved. DRZ-HIGH or DRZ-PLUS was used for the x-ray profile screen, necessitated by the low light levels. 0.25 mm features were about the smallest that could be resolved.

Glinec [168] performed Monte-Carlo simulations of energy deposition by relativistic electrons in to the active layer of Lanex Fine using GEANT4 [251]. The result, figure

Name	Areal Density of Active Layer	Relative Brightness	MTF at 1 lp/mm	MTF at 2 lp/mm
Lanex Fine	36 mg/cm^2	25%	-	-
Lanex Regular	50 mg/cm^2	100%	0.77	0.43
DRZ-STD	68 mg/cm^2	145%	0.8	0.49
DRZ-PLUS	100 mg/cm^2	173%	0.72	0.36
DRZ-HIGH	145 mg/cm^2	229%	0.44	0.16

Table 8.2: Summary of the properties of different types of Lanex screen. The relative brightness for Lanex Fine was inferred from figure 1 in [250]. Comparable MTF data for Lanex Fine could not be found, however this same figure states that Lanex Regular can resolve 6 lp/mm at 10% contrast while Lanex Fine can resolve ∼12 lp/mm at 10% contrast.

1 in his paper, is shown in figure 8.1. We see that beyond around 1 MeV energy deposition is independent of incident electron energy. This is not an issue for the electron spectrometer but could be for the electron beam profile screen. NIST's ESTAR database [252] calculates the range of an energetic electron in matter using the continuous slowing down approximation (CSDA). In aluminium the range of a 1 MeV electron is 2.1 mm. Some attempt to block MeV electrons was made for the electron profile screen by putting 0.5 mm of aluminium on the front surface but this will, at best, have only partially mitigated the problem. The number of MeV electrons travelling in the forward direction from a GeV LWFA is unknown. Therefore it is safer to make measurements of the electron beam charge from the electron spectrometer diagnostic.

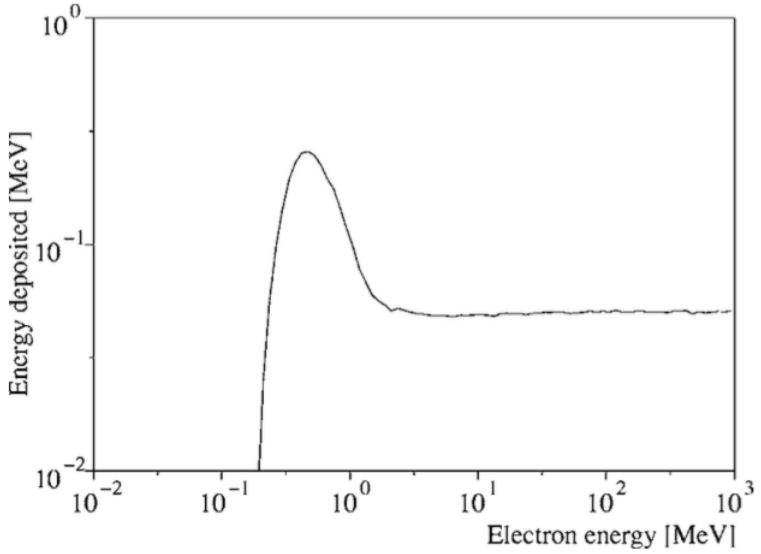


Figure 8.1: Amount of energy deposited in Lanex Fine as a function of incident electron energy. Taken from [168].

Buck et al. [246] show experimentally that the number of scintillation photons from Lanex Fine and Regular (amongst others) is constant with charge density (pC/mm^2) over many orders of magnitude. However it is possible to saturate Lanex. Buck defines a saturation density ρ_{sat} where the charge density detected by the scintillator ρ_{scint} drops to 95% of the physical charge density ρ_{phys}. For Lanex Fine this is >100 pC/mm^2 and for Lanex Regular this is 66 ± 33 pC/mm^2. This is higher than anything that is usually measured in LWFA experiments and so this effect will be very small. The form of this fall-off in detected charge density follows Birk's law

$$\rho_{scint} = \frac{\rho_{phys}}{1 + B\rho_{phys}} \tag{8.34}$$

where B is some constant to be determined.

8.7 Image Plate

Fujifilm Imaging Plate, often just called Image Plate, is commonly used as a detector for x-rays and energetic charged particles. It is popular because it has a large area detector (∼30×15 cm sheets are available) that is highly sensitive, versatile and can achieve good spatial resolution. Its popularity has driven a number of scientific studies in which it has been thoroughly characterised.

Image Plate (IP) is a $BaFBr_{0.85}I_{0.15}$:Eu^{2+} phosphor on a plastic support layer with a magnetic base. Several varieties are available. The types used in this work were BAS-MS and BAS-TR. Their compositions are summarised in table 8.3 [253]. Upon interaction

Layer	BAS-MS	BAS-TR
Protective	6 μm	0 μm
Sensitive	115 μm	50 μm
Support	190 μm	250 μm
Magnetic	160 μm	160 μm

Table 8.3: Composition of Image Plate types BAS-MS and BAS-TR [253].

with x-rays or energetic charged particles the Eu^{2+} is excited to Eu^{3+}. This photoelectron is then captured in a lattice defect called an F centre which is a metastable state [254]. This spontaneously decays slowly and can be stimulated to decay by optical light. This decay releases a 400 nm wavelength photon [255]. This is the working principle of an IP scanner: a 632 nm laser scans across the surface of the IP and the stimulated decay photons are collected by a photo-multiplier tube. In this way an image of deposited energy as a function of space is built up. To deal with the high dynamic range of IP the

scanner employs a logarithmic data amplifier. The measured decay photon signal, the photo-stimulated luminescence (PSL), is related to the scanner output image which is stored in units of Quantum Level (QL) by the equation

$$PSL = \left(\frac{R}{100}\right)^2 \left(\frac{4000}{S}\right) 10^{L\left(\frac{QL}{G}-\frac{1}{2}\right)} \tag{8.35}$$

R is the scanner resolution in μm (which is specified by the user), S is a scanner dependent sensitivity which is equal to 5000 for the FLA-5100 scanner used here. $L = 5$ for this scanner. G is the bit depth of the scan i.e. $G = 65535$ for 16 bit scans. To see low intensity features the QL image should be used but for quantitative analysis PSL should be used because this is proportional to the deposited energy. The resolution with the FLA-5000 range of scanners is reasonable: features at 6 lp/mm have a contrast transfer function of 20% [254] i.e. one can expect to resolve features of around 80 μm. BAS-TR has a blue pigment (BAS-MS is white) which absorbs stray laser light, improving resolution. Now we have had a brief overview of what IP is and what its uses are we will move on to factors affecting its usage in LWFA experiments.

8.7.1 Spontaneous Decay Rate

As mentioned the metastable state that the excited electron finds itself in decays spontaneously. This has been studied for image plate types BAS-MS and BAS-SR (not used in this work) in [256] and [257]. A graph from [256] summarising the results of both studies is shown in figure 8.2. The spontaneous decay of BAS-TR has not been studied in the literature, however it has the same composition as BAS-MS i.e. $BaFBr_{0.85}I_{0.15}:Eu^{2+}$ compared to $BaFBr:Eu^{2+}$ for BAS-SR, so it would be expected to have the same decay rate as BAS-MS. There is a worrying discrepancy between the two studies for BAS-SR type IP. However in this thesis the decay curve shown for BAS-MS will be used. The image plates were usually scanned between 20 and 30 minutes after exposure resulting in a reduction in PSL value of 0.93 to 0.90.

8.7.2 Conversion of PSL to Electron Number

This is the most crucial piece of information to know if IP is to be used for to determine the charge of the electron beam. Two questions must be answered: how much energy must be deposited in a pixel to produce 1 PSL and how much energy is deposited by an energetic electron. PSL scales linearly with electron beam charge [256]. For BAS-MS Kneip [258] reports that 1 PSL is equivalent to 50 electrons passing through the IP with energies 1-100 MeV. He also reports that 1 PSL corresponds to an energy deposition of 7 MeV in BAS-TR. It has been found for the scanner used in the experiments detailed here that 1 PSL corresponds to 7.9 MeV of deposited energy [259] which is the figure that

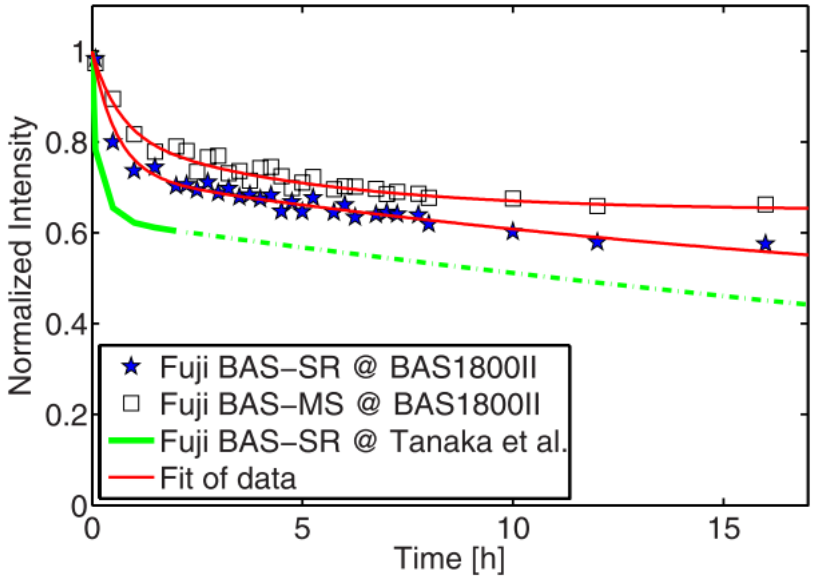


Figure 8.2: Measured signal on the IP scanner image as a function of the time between electron exposure and scanning taken from [256], who used 100 MeV electrons from a conventional accelerator (squares and stars). [257] used ^{147}Pm β decay as the source (green line). BAS1800II is a type of IP scanner.

will be used. GEANT4 simulations [260] show that one electron above 1 MeV deposits 20 keV in to the active layer of BAS-TR, meaning that it takes 350 electrons to produce 1 PSL. It should be noted that these simulations showed that the $PSL/electron$ was constant with electron energy. The issue of PSL variation with electron energy will be discussed next.

8.7.3 Energy Dependence

The $PSL/electron$ recorded on IP as a function of incident electron beam energy has been measured up to 1 GeV in two studies [257] [261]. A graph summarising the results is shown in figure 8.3. This was for IP type BAS-SR and scanned using scanner type BAS1800II. The amplitude of this graph will not be suitable for converting PSL to electron number here because it is a different type of image plate and a different scanner was used. It should be the correct shape of curve for BAS-MS and BAS-TR because the photoelectrons produced in the interaction are from the Eu^{2+} to Eu^{3+} transition for all types of IP. Much like Lanex there is a strong peak below ~1 MeV. These energies are not detected by any of the electron spectrometers used here. There is a significant decrease in sensitivity between electron energies of 100-1000 MeV which would need to be accounted for in the charge calibration (section 3.4.4). These experimental results disagree with the modelling mentioned in the previous section and the modelling performed in [257] who

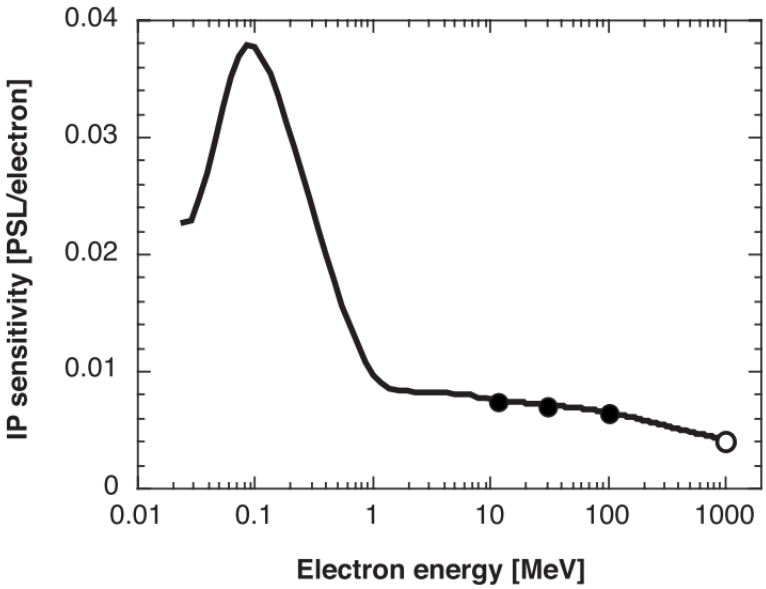


Figure 8.3: Measured $PSL/electron$ recorded using BAS-SR Image Plate vs. Incident Electron Energy, taken from [261].

also saw constant energy deposition with electron energy. For the charge calibration it has been assumed that energy deposition is constant with electron energy above 1 MeV because the GEANT4 code is widely used and well tested, and extrapolation of the curve in 8.3 to beyond 1 GeV would cause it to fall to zero rapidly, which is not intuitive. However this is an area of scientific debate in need of further clarification!

8.7.4 Saturation of Image Plate

When a high charge density electron beam passes through a pixel in the IP the image can be saturated meaning that the QL value recorded exceeds 65535 for 16 bit images. This does not mean that the IP was physically saturated (i.e. all of the available metastable states were occupied), merely that the logarithmic data amplifier saturated the image to preserve the low intensity features. A common method is to perform multiple scans to reduce the image intensity in a way that can be calibrated [262]. This is not recommended because the IP scanner only samples the IP so misalignments (even on the order of 10's μm) between scans means that unscanned regions can be exposed to the laser on a later scan, which can artificially produce higher than expected PSL values [263]. To get around this problem the charge calibrations performed in this thesis used only unsaturated IP regions from the first scan.

8.8 Quantum Efficiency of the X-ray Cameras

The QE of the three cameras used (section 3.5.2) is shown as a function of photon energy in figure 8.4. For the Andor DD camera this data was taken from [170] and extended

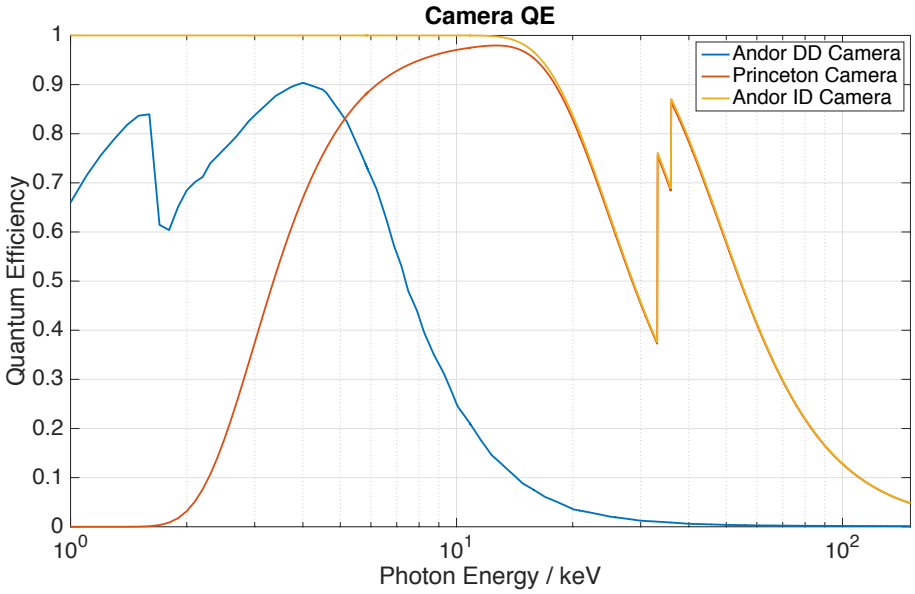


Figure 8.4: The quantum efficiency of the x-ray cameras.

beyond 30 keV using the mass attenuation coefficients from the NIST x-ray mass attenuation database [177]. This was for 40 μm thick silicon [170]. For the Andor ID detection the QE curve shown is simply the QE curve for 150 μm thick CsI. It differs from the Princeton camera at low photon energies because the Princeton camera has a 250 μm Beryllium window in front of of the scintillator. There is a subtlety here: for the ID cameras this is the QE of the CsI scintillator. There is not a 100% conversion of x-ray energy in to scintillation light, and not all scintillation light is detected by the CCD. This is taken care of by the camera calibration in section 3.5.5.

8.9 X-ray Filter Arrays

8.9.1 64 Filter Array

Figure 8.5 shows the composition of the 64 filter array[1]. Like all of the filter array diagrams in this section, this is drawn as it is seen on the x-ray image (back to front, if you like). The whole arrangement was mounted by the edges to a plastic holder which was held a few cm in front of the x-ray camera (i.e. with magnification $M \sim 1$.) Figure 8.6 shows

[1]This was designed by Michael Bloom, formerly of Imperial College London.

the transmission of the different filter materials. Note that there are a number of Ross filter pairs: 50 μm Mo with 50 μm Sn, 50 μm Gd with 50 μm Yb, and 25 μm W with 40 μm Bi.

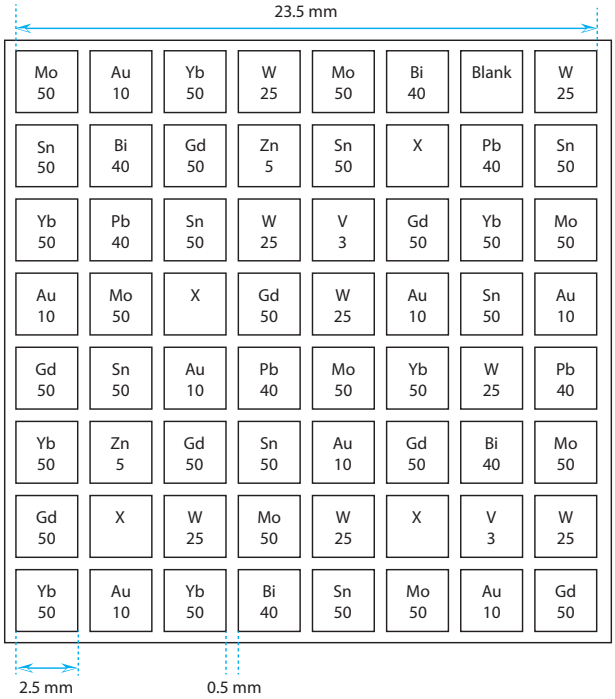


Figure 8.5: Diagram of the 64 filter array. Shown are the elemental symbols and the filter thickness in μm's. The backing material was 2 layers of 6 μm Mylar with a flash coating of Al. Filter X changed between 40 μm Pr, 20 μm Ag and nothing.

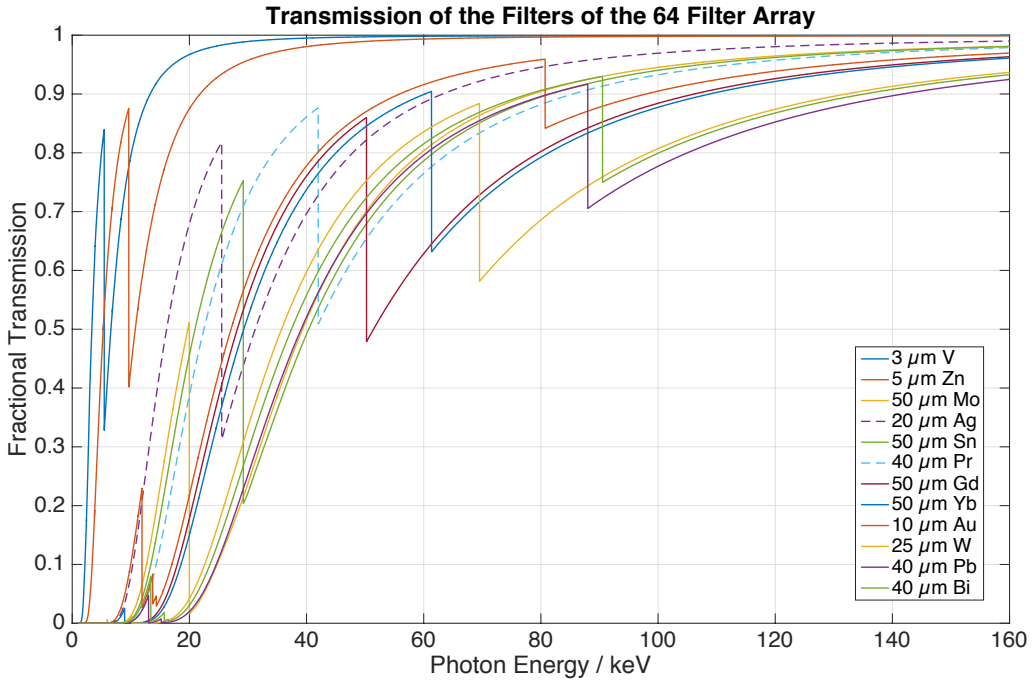


Figure 8.6: Transmission of the filters of the 64 filter array including the effect of absorption in the backing material.

8.9.2 16 Filter Arrays

Figure 8.5 shows the composition of the 16 filter array[2]. The whole arrangement was

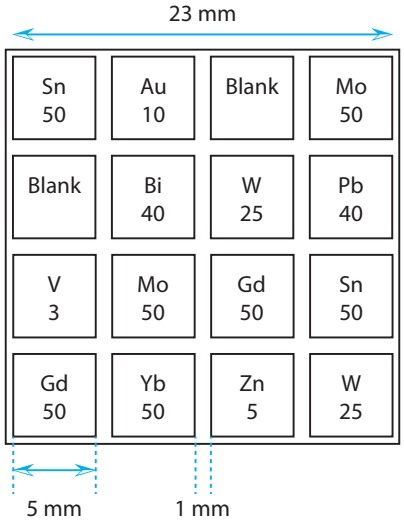


Figure 8.7: Diagram of the 16 filter array. Shown are the elemental symbols and the filter thickness in μm's. The backing material was 2 layers of 6 μm Mylar with a flash coating of aluminium.

[2]This was designed by Michael Bloom, formerly of Imperial College London.

mounted by the edges to a plastic holder, which was also held a few cm in front of the x-ray camera. There were two of these: one as shown and one shrunk by a factor of 2 (the thicknesses of filter materials were the same). The smaller one could be used with the Andor DD camera which had a smaller chip. The materials are the same as for the 64 filter array so the transmission curves can also be seen in figure 8.6

8.9.3 Imaging Filter Array

It is desirable to obtain an on-shot estimate of the x-ray spectrum while imaging. To do this the filter pack shown in figure 8.8 [3] was used which left most of camera chip area free for imaging. The transmission of these filters is shown in figure 8.9. This design has preserved the three Ross pairs from the 64 filter array as well as maintaining reasonably well spaced k-edges. The thin V and Zn filters were not used because very few x-rays with energies less than approximately 5 keV would have been transmitted through the laser dump materials and vacuum window.

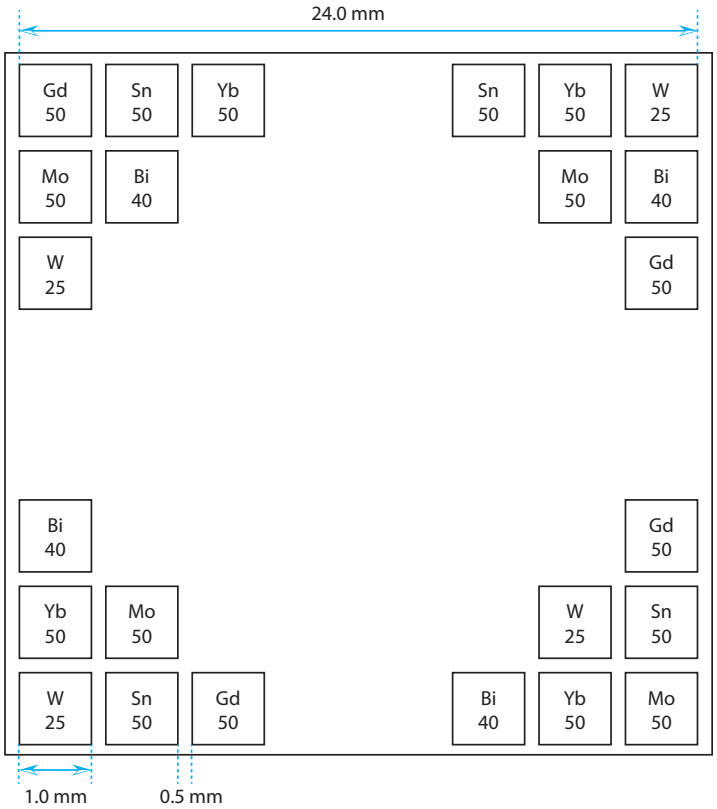


Figure 8.8: Diagram of the imaging filter array (not to scale). Shown are the elemental symbols and the filter thickness in μm's. The backing material was 2 layers of 6 μm Mylar with a flash coating of aluminium.

[3]Designed by the author.

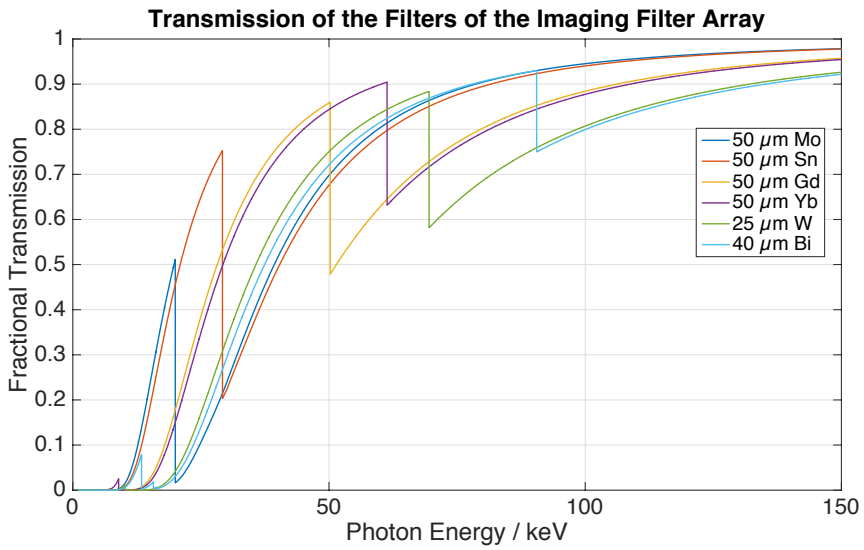


Figure 8.9: Transmission of the filters of the imaging filter array. This includes the effect of absorption in the backing material.

8.10 Resolution Targets

Figure 8.10 is a diagram of the JIMA resolution target [264]. This consists of alternating 1.1 μm thick SiO_2 and 1 μm thick W bars deposited with a lithographic technique on to a base of 60 μm thick Si. The front surface is covered by a 0.1 mm thick polycarbonate protective layer.

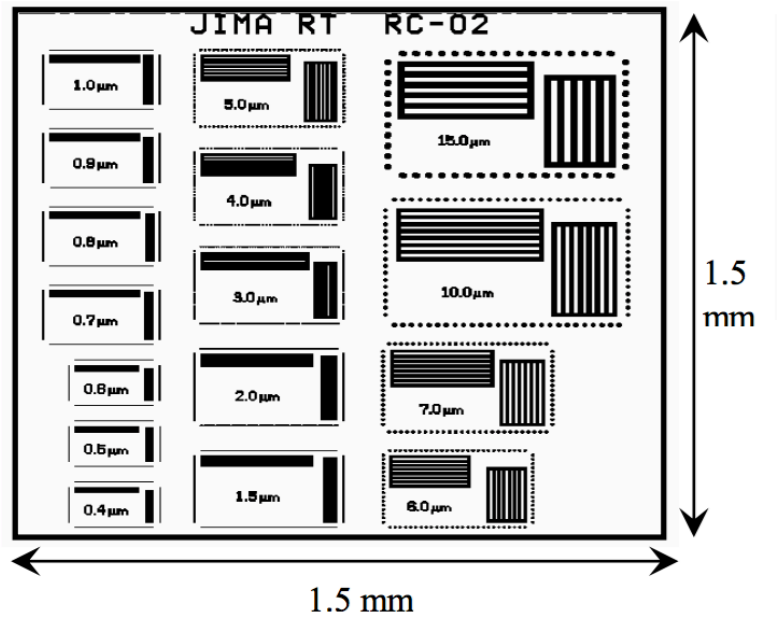


Figure 8.10: Diagram of the JIMA resolution target from [264].

Figure 8.11 is a high magnification optical image of the gold x-ray resolution target. The horizontal and vertical bars have widths of approximately 160, 80, 40, 20 and 10 microns and are spaced by these distances also. The target is made from 20 μm thick gold and was bought from Agar Scientific.

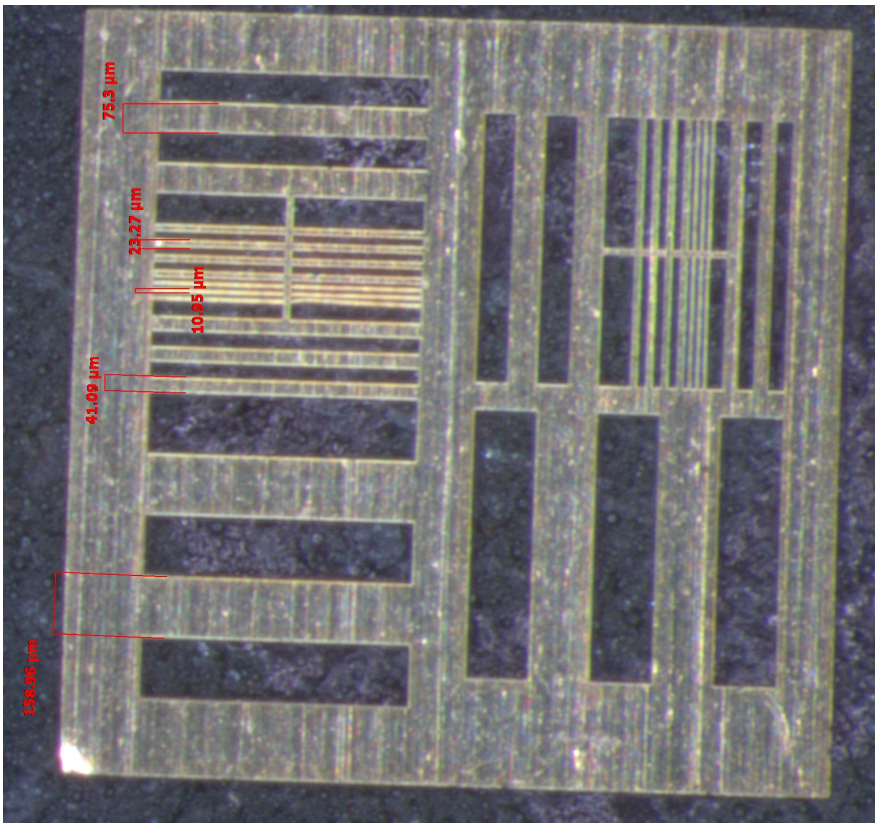


Figure 8.11: Optical image of the gold resolution target taken by Christopher Spindloe at the Rutherford Appleton Laboratory.

Bibliography

[1] C.M.S. Collaboration. *Phys. Lett. B.* 716, pp. 30–61. 2012. "Observation of a new boson at a mass of 125 GeV with the CMS experiment at the LHC"
(Cited on p. 16).

[2] ATLAS Collaboration. *Phys. Lett. B.* 716, pp. 1–29. 2012. "Observation of a new particle in the search for the Standard Model Higgs boson with the ATLAS detector at the LHC"
(Cited on p. 16).

[3] M. Kado. *Results with the Full 2015 Data Sample from the ATLAS Experiment.* CERN Special Seminar 15 December 2015 (Cited on p. 16).

[4] A. Knapp. *How Much Does It Cost To Find A Higgs Boson?* Published on 05.07.2012. Accessed on 22.04.2016. URL: http://www.forbes.com/sites/alexknapp/2012/07/05/how-much-does-it-cost-to-find-a-higgs-boson (Cited on p. 16).

[5] CERN. *LHC Aerial View.* Accessed on 27.04.2016. URL: http://est-div-lea-at.web.cern.ch/est-div-lea-at/atlas_lhcpicturesAERIAL.htm (Cited on p. 17).

[6] E. S. Reich. *Physicists plan to build a bigger LHC.* Nature News 12.11.2013. Accessed on 27.04.2016. URL: http://www.nature.com/news/physicists-plan-to-build-a-bigger-lhc-1.14149 (Cited on p. 17).

[7] CERN. *The FCC-ee design study Machine Parameters.* Accessed on 25/07/2016. 2016. URL: http://tlep.web.cern.ch/content/machine-parameters (Cited on p. 17).

[8] M. Aicheler et al. *A Multi-TeV Linear Collider based on CLIC Technology: CLIC Conceptual Design Report.* Tech. rep. 2012 (Cited on p. 17).

[9] J. E. Clendenin et al. *SLAC-PUB.* 5049. August. 1989. "The High-Gradient S-Band Linac for Intitial Acceleration of the SLC Intense Positron Bunch"
(Cited on p. 18).

[10] J. Wang et al. *SLAC-PUB.* 7684. October, p. 28. 1997. "Field Emission and RF Breakdown in High-Gradient Room-Temperature Linac Structures"
(Cited on p. 18).

[11] T. Behnke et al. *ILC Technical Design Report Volume 1: Executive Summary.* Tech. rep. 2013, pp. 1–60. arXiv: 1306.6327. URL: http://arxiv.org/pdf/1306.6327v1.pdf (Cited on p. 18).

[12] *Lightsources of the World.* Accessed on 27.04.2016. URL: http://www.lightsources.org/regions (Cited on p. 18).

[13] CC BY-SA 3.0. *File:Undulator.png.* Accessed on 02.05.2016. URL: https:commons.wikimedia.org/w/index.php?curid=537945 (Cited on p. 19).

[14] R. Fitzgerald. *Phys. Today.* 53. 7, pp. 23–26. 2000. "Phase-sensitive x-ray imaging"
(Cited on p. 20).

[15] V. Mocella et al. *Nat. Commun.* 6. April, p. 5895. 2014. "Revealing letters in rolled Herculaneum papyri by X-ray phase-contrast imaging."
(Cited on p. 20).

[16] Hammamatsu Photonics K.K. *Microfocus X-ray Source Series*. Accessed on 28.04.2016. URL: http://www.hamamatsu.com/resources/pdf/etd/MFX_TXPR1007E.pdf (Cited on p. 20).

[17] S. W. Wilkins et al. *Nature*. 384. 6607, pp. 335–338. 1996. "Phase-contrast imaging using polychromatic hard X-rays"
(Cited on p. 21).

[18] T. Weitkamp et al. *Optics Express*. 13. 16, pp. 6296–6304. 2005. "X-ray phase imaging with a grating interferometer."
(Cited on p. 21).

[19] F. Pfeiffer et al. *J. Appl. Phys.* 105. 10, pp. 1–4. 2009. "X-ray dark-field and phase-contrast imaging using a grating interferometer"
(Cited on p. 21).

[20] B Verman et al. *Rigaku J.* 19. 1, pp. 4–13. 2002. "Microfocusing source and multilayer optics based x-ray diffraction systems"
(Cited on p. 21).

[21] M. Cornacchia. *SLAC-PUB-8053*. 1999. "The LCLS X-ray FEL at SLAC"
(Cited on p. 21).

[22] Emil Espes et al. *Liquid-Metal-Jet X-ray Tube Technology for Nanoelectronics Characterisation and Metrology*. Poster. Accessed on 02.05.2016. URL: http://www.nist.gov/pml/div683/conference/upload/12_espes.pdf (Cited on p. 21).

[23] Paul Scherrer Institut. *TOMCAT - X02DA: Tomographic Microscopy*. Accessed on 28.04.2016. URL: https://www.psi.ch/sls/tomcat/tomcat (Cited on p. 21).

[24] Y. S. Chu et al. *Appl. Phys. Lett.* 92. 10. 2008. "Hard-x-ray microscopy with Fresnel zone plates reaches 40 nm Rayleigh resolution"
(Cited on p. 21).

[25] G. C. Yin et al. *Appl. Phys. Lett.* 88. 24, pp. 86–89. 2006. "Energy-tunable transmission x-ray microscope for differential contrast imaging with near 60 nm resolution tomography"
(Cited on p. 21).

[26] A. Wagner et al. *J. Phys. Chem. A*. 106. 28, pp. 6581–6590. 2002. "Structure and charge density of a C60-fullerene derivative based on a high resolution synchrotron diffraction experiment at 100 K"
(Cited on p. 21).

[27] D. E. Eakins et al. *Rev. Sci. Instrum.* 85. 123708. 2014. "X-ray imaging of subsurface dynamics in high-Z materials at the Diamond Light Source"
(Cited on p. 22).

[28] B. J. Jensen et al. *AIP Adv.* 2. 1. 2012. "Ultrafast, high resolution, phase contrast imaging of impact response with synchrotron radiation"
(Cited on p. 22, 164, 185, 191).

[29] S. N. Luo et al. *Rev. Sci. Instrum.* 83. 7. 2012. "Gas gun shock experiments with single-pulse x-ray phase contrast imaging and diffraction at the Advanced Photon Source"
(Cited on p. 22, 185).

[30] C. S. Yoo et al. *Science (80-.).* 270, p. 1473. 1995. "Phase Diagram of Iron by in Situ X-ray Diffraction: Implications for Earth's Core"
(Cited on p. 22).

[31] J Amann et al. *Nat. Photonics*. 6. 10, pp. 693–698. 2012. "Demonstration of self-seeding in a hard-X-ray free-electron laser"
(Cited on p. 22).

[32] L. B. Fletcher et al. *Nat. Photonics*. 9. 4, pp. 274–279. 2015. "Ultrabright X-ray laser scattering for dynamic warm dense matter physics"
(Cited on p. 23).

[33] J. M. Cole et al. *Sci. Rep.* 5, p. 13244. 2015. "Laser-wakefield accelerators as hard x-ray sources for 3D medical imaging of human bone"
(Cited on p. 23, 30, 138, 147, 165).

[34] H. Loos. *SLAC-PUB*. 15422. 2013. "LCLS accelerator operation and measurement of electron beam parameters relevant for the x-ray beam"
(Cited on p. 23).

[35] T. Ishikawa et al. *Nat. Photonics*. 6. June, pp. 540–544. 2012. "A compact X-ray free-electron laser emitting in the sub-ångström region"
(Cited on p. 23).

[36] S. M. Vinko et al. *Nat. Commun.* 6, p. 6397. 2015. "Investigation of femtosecond collisional ionization rates in a solid-density aluminium plasma"
(Cited on p. 23).

[37] J. M. Martin-Garcia et al. *Arch. Biochem. Biophys.* 8. 2016. "Review: Serial femtosecond crystallography: A revolution in structural biology"
(Cited on p. 23).

[38] L. F. Gomez et al. *Science*. 345. 6199, p. 906. 2014. "Shapes and vorticities of superfluid helium nanodroplets"
(Cited on p. 23).

[39] S Gerber et al. *Sciencexpress Reports.* 350, pp. 1–8. 2015. "Three-dimensional charge density wave order in YBa2Cu3O6.67 at high magnetic fields."
(Cited on p. 23).

[40] M. P. Minitti et al. *Phys. Rev. Lett.* 114. 25, pp. 1–5. 2015. "Imaging Molecular Motion: Femtosecond X-Ray Scattering of an Electrocyclic Chemical Reaction"
(Cited on p. 23).

[41] McCarthy, Joanne. *ESRF Facility & User Program Overview*. Presented at 3-Way Meeting, APS, 2013: User Services Workshop- ESRF Facility Overview (Cited on p. 24).

[42] Stanford Linear Accelerator Center. *Project Execution Plan for the Linac Coherent Light Source, Revision 1*. p. 12 (Cited on p. 24).

[43] SLAC National Accelerator Laboratory. *Major Upgrade Will Boost Power of World's Brightest X-ray Laser*. Accessed on 11.07.2016. URL: `https://www6.slac.stanford.edu/news/2016-04-04-major-upgrade-will-boost-power-worlds-brightest-x-ray-laser.aspx` (Cited on p. 24).

[44] *LCLS-II Final Design Report DRAFT*. December 21, 2014 (Cited on p. 24).

[45] Pellegrini, C. *Making X-rays: bright times ahead for FELs*. CERN Courier. Accessed on 09/08/2016. URL: `http://cerncourier.com/cws/article/cern/44357` (Cited on p. 24).

[46] Ginter, P. *ESRF: The storage ring of the European Light Source (ESRF) in Grenoble.* Accessed on 29/05/2016. URL: `http://www.eiroforum.org/media/photo_galleries/esrf/index.html` (Cited on p. 24).

[47] ESRF. *ESRF in brief and key figures.* Accessed on 29/05/2016. URL: `http://www.esrf.eu/about/press-room/intro-esrf-journalists` (Cited on p. 24).

[48] *Astra Gemini laser area.* Accessed on 30/05/2016. URL: `http://www.clf.stfc.ac.uk/CLF/resources/image/jpg/gemini_laser_area_02.jpg` (Cited on p. 25).

[49] T. Tajima et al. *Phys. Rev. Lett.* 4. 4, pp. 267–270. 1979. "Laser Electron Accelerator"
(Cited on p. 26, 61).

[50] W. Mori. *IEEE J. Quantum Electron.* 33. 11, pp. 1942–1953. 1997. "The physics of the nonlinear optics of plasmas at relativistic intensities for short-pulse lasers"
(Cited on p. 26, 38).

[51] A. G. R. Thomas et al. *Phys. Rev. Lett.* 98. 095004, pp. 1–4. 2007. "Effect of Laser-Focusing Conditions on Propagation and Monoenergetic Electron Production in Laser-Wakefield Accelerators"
(Cited on p. 26, 47, 137).

[52] R. Wagner et al. *Phys. Rev. Lett.* 78. 16, pp. 3125–3128. 1997. "Electron Acceleration by a Laser Wakefield in a Relativistically Self-Guided Channel"
(Cited on p. 26).

[53] J. Faure et al. *Phys. Rev. Lett.* 95. 20, p. 205003. 2005. "Observation of Laser-Pulse Shortening in Nonlinear Plasma Waves"
(Cited on p. 26, 45).

[54] A. Pukhov et al. *Appl. Phys. B Lasers Opt.* 74. 4-5, pp. 355–361. 2002. "Laser wake field acceleration: the highly non-linear broken-wave regime"
(Cited on p. 26, 54, 63).

[55] W. Lu et al. *Phys. Rev. Lett.* 96. 16, p. 165002. 2006. "Nonlinear Theory for Relativistic Plasma Wakefields in the Blowout Regime"
(Cited on p. 26, 54, 63).

[56] W. P. Leemans et al. *Nat. Phys.* 2. 10, pp. 696–699. 2006. "GeV electron beams from a centimetre-scale accelerator"
(Cited on p. 27, 46, 82).

[57] S. Kneip et al. *Phys. Rev. Lett.* 103. 3, p. 035002. 2009. "Near-GeV Acceleration of Electrons by a Nonlinear Plasma Wave Driven by a Self-Guided Laser Pulse"
(Cited on p. 27, 47, 82, 138, 158).

[58] C. Clayton et al. *Phys. Rev. Lett.* 105. 10, p. 105003. 2010. "Self-Guided Laser Wakefield Acceleration beyond 1 GeV Using Ionization-Induced Injection"
(Cited on p. 27, 82).

[59] H. T. Kim et al. *Phys. Rev. Lett.* 111. 16, p. 165002. 2013. "Enhancement of Electron Energy to the Multi-GeV Regime by a Dual-Stage Laser-Wakefield Accelerator Pumped by Petawatt Laser Pulses"
(Cited on p. 27, 82, 112).

[60] X. Wang et al. *Nat. Commun.* 4. 1988. 2013. "Quasi monoenergetic laser plasma acceleration of electrons to 2 GeV"
(Cited on p. 27, 82, 112).

[61] W. P. Leemans et al. *Phys. Rev. Lett.* 113. 24, p. 245002. 2014. "Multi-GeV Electron Beams from Capillary-Discharge-Guided Subpetawatt Laser Pulses in the Self-Trapping Regime"
(Cited on p. 27, 46, 112, 137).

[62] O. Lundh et al. *Nat. Phys.* 7. 3, pp. 219–222. 2011. "Few femtosecond, few kiloampere electron bunch produced by a laser plasma accelerator"
(Cited on p. 27, 30, 86).

[63] E. Brunetti et al. *Phys. Rev. Lett.* 105. November, pp. 3–6. 2010. "Low emittance, high brilliance relativistic electron beams from a laser-plasma accelerator"
(Cited on p. 27, 86).

[64] S. P. D. Mangles et al. *Nature.* 431, pp. 535–538. 2004. "Monoenergetic beams of relativistic electrons from intense laser plasma interactions"
(Cited on p. 27, 112).

[65] C. Geddes et al. *Nature*. 431. September, pp. 538–541. 2004. "High-quality electron beams from a laser wakefield accelerator using plasma-channel guiding"
(Cited on p. 27, 46, 112).

[66] J Faure et al. *Nature*. 431. September, pp. 541–544. 2004. "A laser plasma accelerator producing monoenergetic electron beams"
(Cited on p. 27, 112).

[67] S. P. D. Mangles et al. *Phys. Rev. Spec. Top. - Accel. Beams*. 15. 1, p. 011302. 2012. "Self-injection threshold in self-guided laser wakefield accelerators"
(Cited on p. 27, 58).

[68] S. P. D. Mangles et al. *Phys. Plasmas*. 14. 5, pp. 1–7. 2007. "On the stability of laser wakefield electron accelerators in the monoenergetic regime"
(Cited on p. 27).

[69] C. McGuffey et al. *Phys. Rev. Lett.* 104. 2, p. 025004. 2010. "Ionization Induced Trapping in a Laser Wakefield Accelerator"
(Cited on p. 27, 112, 113).

[70] A. Pak et al. *Phys. Rev. Lett.* 104. 2, p. 025003. 2010. "Injection and Trapping of Tunnel-Ionized Electrons into Laser-Produced Wakes"
(Cited on p. 27, 113).

[71] C. Geddes et al. *Phys. Rev. Lett.* 100. 21, p. 215004. 2008. "Plasma-Density-Gradient Injection of Low Absolute-Momentum-Spread Electron Bunches"
(Cited on p. 27, 83).

[72] K. Schmid et al. *Phys. Rev. Spec. Top. - Accel. Beams*. 13. 9, pp. 1–5. 2010. "Density-transition based electron injector for laser driven wakefield accelerators"
(Cited on p. 27, 112).

[73] J. Faure et al. *Nature*. 444. 7120, pp. 737–9. 2006. "Controlled injection and acceleration of electrons in plasma wakefields by colliding laser pulses."
(Cited on p. 27, 86, 112).

[74] X. L. Xu et al. *Phys. Rev. Spec. Top. - Accel. Beams*. 17. 6, p. 061301. 2014. "Low emittance electron beam generation from a laser wakefield accelerator using two laser pulses with different wavelengths"
(Cited on p. 27).

[75] W. Leemans et al. *Phys. Today*. 62. 3, p. 44. 2009. "Laser-driven plasma-wave electron accelerators"
(Cited on p. 28).

[76] C. B. Schroeder et al. *Phys. Rev. Spec. Top. - Accel. Beams*. 13. 10, p. 101301. 2010. "Physics considerations for laser-plasma linear colliders"
(Cited on p. 28).

[77] S. Steinke et al. *Nature*. 2016. "Multistage coupling of independent laser-plasma accelerators"
(Cited on p. 28).

[78] A. R. Maier et al. *Phys. Rev. X*. 2. 3, p. 031019. 2012. "Demonstration Scheme for a Laser-Plasma-Driven Free-Electron Laser"
(Cited on p. 28).

[79] S. Kneip et al. *Nature Physics*. 6. 12, pp. 980–983. 2010. "Bright spatially coherent synchrotron X-rays from a table-top source"
(Cited on p. 28–30, 92, 96, 97, 112, 147, 163).

[80] E. Esarey et al. *Phys. Rev. E*. 52. 5, pp. 5443–5453. 1995. "Laser acceleration of electrons in vacuum"
(Cited on p. 29).

[81] M. Thévenet et al. *Nat. Phys.* advance on. December. 2015. "Vacuum laser acceleration of relativistic electrons using plasma mirror injectors"
(Cited on p. 29).

[82] E. A. Peralta et al. *Nature.* 503. V, pp. 91–94. 2013. "Demonstration of electron acceleration in a laser-driven dielectric microstructure."
(Cited on p. 29).

[83] I. Blumenfeld et al. *Nature.* 445. 7129, pp. 741–4. 2007. "Energy doubling of 42 GeV electrons in a metre-scale plasma wakefield accelerator."
(Cited on p. 29).

[84] M. Litos et al. *Nature.* 515. 7525, pp. 92–95. 2014. "High-efficiency acceleration of an electron beam in a plasma wakefield accelerator"
(Cited on p. 29).

[85] A. Rousse et al. *Physical Review Letters.* 93. 13, pp. 1–4. 2004. "Production of a keV X-Ray Beam from Synchrotron Radiation in Relativistic Laser-Plasma Interaction"
(Cited on p. 29, 92).

[86] E. Esarey et al. *Phys. Rev. E.* 65. 5, p. 056505. 2002. "Synchrotron radiation from electron beams in plasma-focusing channels"
(Cited on p. 29, 63, 64, 74).

[87] S Fourmaux et al. *New Journal of Physics.* 13. 3, p. 033017. 2011. "Demonstration of the synchrotron-type spectrum of laser-produced Betatron radiation"
(Cited on p. 30, 72).

[88] M. Schnell et al. *Phys. Rev. Lett.* 108. 7, pp. 1–5. 2012. "Deducing the electron-beam diameter in a laser-plasma accelerator using x-ray betatron radiation"
(Cited on p. 30, 147).

[89] L. M. Chen et al. *Sci. Rep.* 3, p. 1912. 2013. "Bright betatron X-ray radiation from a laser-driven-clustering gas target."
(Cited on p. 30).

[90] K. Ta Phuoc et al. *Physical Review Letters.* 97. 22, p. 225002. 2006. "Imaging Electron Trajectories in a Laser-Wakefield Cavity Using Betatron X-Ray Radiation"
(Cited on p. 30, 147).

[91] S. Kneip et al. *Applied Physics Letters.* 99. 9, p. 093701. 2011. "X-ray phase contrast imaging of biological specimens with femtosecond pulses of betatron radiation from a compact laser plasma wakefield accelerator"
(Cited on p. 30, 111).

[92] S Fourmaux et al. *Opt. Lett.* 36. 13, pp. 2426–2428. 2011. "Single shot phase contrast imaging using laser-produced Betatron x-ray beams."
(Cited on p. 30, 111).

[93] J. Wenz et al. *Nature Communications.* 6. May, p. 7568. 2015. "Quantitative X-ray phase-contrast microtomography from a compact laser-driven betatron source"
(Cited on p. 30, 111).

[94] F Albert et al. *Plasma Phys. Control. Fusion.* 56. 8, p. 084015. 2014. "Laser wakefield accelerator based light sources: potential applications and requirements"
(Cited on p. 30, 195).

[95] M. Fuchs et al. *Nat. Phys.* 5. 11, pp. 826–829. 2009. "Laser-driven soft-X-ray undulator source"
(Cited on p. 30).

[96] S. Chen et al. *Phys. Rev. Lett.* 110. 15, p. 155003. 2013. "MeV-Energy X Rays from Inverse Compton Scattering with Laser-Wakefield Accelerated Electrons"
(Cited on p. 30).

[97] N. D. Powers et al. *Nat. Photonics*. 8. January, pp. 28–31. 2014. "Quasi-monoenergetic and tunable X-rays from a laser-driven Compton light source"
(Cited on p. 30).

[98] G. Sarri et al. *Phys. Rev. Lett.* 113. 22, pp. 1–5. 2014. "Ultrahigh brilliance multi-MeV γ-ray beams from nonlinear relativistic thomson scattering"
(Cited on p. 30).

[99] K. Khrennikov et al. *Phys. Rev. Lett.* 114. 19, pp. 1–5. 2015. "Tunable all-optical quasimonochromatic Thomson X-ray source in the nonlinear regime"
(Cited on p. 30).

[100] Jackson, John David. *Classical Electrodynamics, 3rd Edition, Section 12.1, Wiley, 2014* (Cited on p. 33, 70, 71, 201, 202).

[101] Chang, William S. C. Chang. *Principles of Lasers and Optics, Section 2.1.6., Cambridge University Press, 2005* (Cited on p. 39).

[102] P. Gibbon. *Short Pulse Laser Interactions with Matter: An Introduction*. Imperial College Press, 2005 (Cited on p. 40, 41).

[103] H. A. Bethe et al. *Quantum Mechanics of One- and Two-Electron Atoms*. 1957 (Cited on p. 40).

[104] M. V. Ammosov et al. *Sov. Phys. JETP*. 64. December 1986, pp. 1191–1194. 1986. "Tunnel ionization of complex atoms and of atomic ions in an alternating electromagnetic field"
(Cited on p. 41).

[105] J. Schreiber et al. *Phys. Rev. Lett.* 105. 23, p. 235003. 2010. "Complete Temporal Characterization of Asymmetric Pulse Compression in a Laser Wakefield"
(Cited on p. 45).

[106] J. T. Mendonça et al. *Phys. Rev. E*. 49. 4, pp. 3520–3523. 1994. "Regular and stochastic acceleration of photons"
(Cited on p. 45).

[107] C. D. Murphy et al. *Phys. Plasmas*. 13. 3, p. 033108. 2006. "Evidence of photon acceleration by laser wake fields"
(Cited on p. 45).

[108] J. M. Dias et al. *Phys. Rev. Spec. Top. - Accel. Beams*. 1. 031301, pp. 1–8. 1998. "Photon acceleration versus frequency-domain interferometry for laser wakefield diagnostics"
(Cited on p. 45).

[109] P. Sprangle et al. *Phys. Rev. Lett.* 69. 15, pp. 2200–2203. 1992. "Propagation and guiding of intense laser pulses in plasmas"
(Cited on p. 46).

[110] P. Sprangle et al. *IEEE Trans. Plasma Sci.* 15. 2, pp. 145–153. 1987. "Relativistic self-focusing of short-pulse radiation beams in plasmas"
(Cited on p. 47).

[111] E. Esarey et al. *Rev. Mod. Phys.* 81. 3, pp. 1229–1285. 2009. "Physics of laser-driven plasma-based electron accelerators"
(Cited on p. 49).

[112] J. Dawson. *Phys. Rev.* 113. 2, p. 383. 1959. "Nonlinear Electron Oscillations in a Cold Plasma"
(Cited on p. 49).

[113] L. Gorbunov et al. *Zh. Eksp. Teor. Fiz.* 93, pp. 509–518. 1987. "Excitation of plasma waves by an electromagnetic wave packet"
(Cited on p. 50).

[114] E. Esarey et al. *Phys. Plasmas.* 2. 5, p. 1432. 1995. "Trapping and acceleration in nonlinear plasma waves"
(Cited on p. 51, 56, 57).

[115] E. Esarey et al. *Rev. Mod. Phys.* 81. 3, p. 1234. 2009. "Physics of laser-driven plasma-based electron accelerators"
(Cited on p. 52).

[116] A. I. Akhiezer et al. *JETP Lett.* 3. 5, pp. 696–705. 1956. "Theory of Wave Motion of an Electron Plasma"
(Cited on p. 52).

[117] T. Katsouleas et al. *Phys. Rev. Lett.* 61. 1, pp. 90–93. 1988. "Wave-Breaking Amplitude of Relativistic Oscillations in a Thermal Plasma"
(Cited on p. 53, 127).

[118] V. I. Berezhiani et al. *Phys. Lett. A.* 148. 6-7, pp. 338–340. 1990. "Relativistic wake-field generation by an intense laser pulse in a plasma"
(Cited on p. 53).

[119] W. Lu et al. *Phys. Rev. Spec. Top. - Accel. Beams.* 10. 6, p. 061301. 2007. "Generating multi-GeV electron bunches using single stage laser wakefield acceleration in a 3D nonlinear regime"
(Cited on p. 53, 55, 60, 61, 114).

[120] J. Vieira et al. 2016. "Multidimensional Plasma Wake Excitation in the Non-linear Blowout Regime"
(Cited on p. 54).

[121] W. Lu et al. *Phys. Plasmas.* 13. 5. 2006. "A nonlinear theory for multidimensional relativistic plasma wave wakefields"
(Cited on p. 54, 55).

[122] F. S. Tsung et al. *Phys. Rev. Lett.* 93. 18, pp. 1–4. 2004. "Near-GeV-energy laser-wakefield acceleration of self-injected electrons in a centimeter-scale plasma channel"
(Cited on p. 58, 59).

[123] S. Y. Kalmykov et al. *New J. Phys.* 12. 2010. "Numerical modelling of a 10-cm-long multi-GeV laser wakefield accelerator driven by a self-guided petawatt pulse"
(Cited on p. 58).

[124] C. Benedetti et al. *Phys. Plasmas.* 20. 10, pp. 0–11. 2013. "Numerical investigation of electron self-injection in the nonlinear bubble regime"
(Cited on p. 58).

[125] A. G. R. Thomas. *Phys. Plasmas.* 17. 5, p. 056708. 2010. "Scalings for radiation from plasma bubbles"
(Cited on p. 58).

[126] S. Kalmykov et al. *Phys. Rev. Lett.* 103. 13, pp. 1–4. 2009. "Electron self-injection and trapping into an evolving plasma bubble"
(Cited on p. 58, 144).

[127] S. A. Yi et al. *Plasma Phys. Control. Fusion.* 53. 1, p. 014012. 2011. "Hamiltonian analysis of electron self-injection and acceleration into an evolving plasma bubble"
(Cited on p. 58, 144).

[128] M. Chen et al. *Phys. Plasmas.* 19. 3. 2012. "Theory of ionization-induced trapping in laser-plasma accelerators"
(Cited on p. 59).

[129] S. Gordienko et al. *Phys. Plasmas.* 12. 4, p. 043109. 2005. "Scalings for ultrarelativistic laser plasmas and quasimonoenergetic electrons"
(Cited on p. 61).

[130] C. D. Decker et al. *Phys. Plasmas.* 3. 5, p. 2047. 1996. "The evolution of ultra-intense, short-pulse lasers in underdense plasmas"
(Cited on p. 61).

[131] A. G. R. Thomas. *Phys. Plasmas.* 17. 5, p. 056708. 2010. "Scalings for radiation from plasma bubbles"
(Cited on p. 63).

[132] Y. Glinec. "Propagation d'une impulsion laser ultra-intense dans un plasma sous-dense: Génération de faisceaux d'électrons quasi monoénergétiques et développment d'applications." PhD thesis. L'École Polytechnique, 2006 (Cited on p. 65).

[133] C. Pellegrini et al. *Rev. Mod. Phys.* 88. 1, p. 015006. 2016. "The physics of x-ray free-electron lasers"
(Cited on p. 66).

[134] B. M. Kincaid. *J. Appl. Phys.* 48. 7, pp. 2684–2691. 1977. "A short-period helical wiggler as an improved source of synchrotron radiation"
(Cited on p. 67).

[135] D. Strickland et al. *Opt. Commun.* 56. 3, pp. 219–221. 1985. "Compression of Amplified Chirped Optical Pulses"
(Cited on p. 77).

[136] STFC Central Laser Facility. *Oscillator and Pre-Amplifier.* Accessed on 29.06.2016. URL: `http://www.clf.stfc.ac.uk/Facilities/Astra/Astra%20Laser/13891.aspx` (Cited on p. 77).

[137] Hooker, C. *New front end for the Gemini facility.* Tech. rep. Central Laser Facility Annual Report 2013-14 (Cited on p. 77).

[138] Langley, A. J. *The Development of a Multi-Terawatt Femtosecond Laser Facility - Astra.* Tech. rep. Central Laser Facility Annual Report 1999-2001, pp. 196–200 (Cited on p. 77).

[139] E. J. Divall. *Laser performance data analysis tool, Central Laser Facility Annual Report.* Tech. rep. 2008, pp. 220–222 (Cited on p. 78).

[140] R Trebino. *Frequency-Resolved Optical Gating: The Measurement of Ultrashort Laser Pulses.* Kluwer Academic Publishers, 2000 (Cited on p. 79).

[141] D. J. Kane et al. *IEEE J. Quantum Electron.* 29. 2, pp. 571–579. 1993. "Characterization of Arbitrary Femtosecond Pulses Using Frequency-Resolved Optical Gating"
(Cited on p. 79).

[142] C Iaconis et al. *Opt. Lett.* 23. 10, pp. 792–794. 1998. "Spectral phase interferometry for direct electric-field reconstruction of ultrashort optical pulses."
(Cited on p. 79).

[143] M. E. Anderson et al. *Laser Phys. Lett.* 5. 4, pp. 256–266. 2008. "SPIDER: A decade of measuring ultrashort pulses"
(Cited on p. 79).

[144] A. Monmayrant et al. *J. Phys. B At. Mol. Opt. Phys.* 43. 10, p. 103001. 2010. "A newcomer's guide to ultrashort pulse shaping and characterization"
(Cited on p. 79).

[145] O. Gal. *fit_ellipse.m.* MATLAB code written on 31/03/2003, updated on 02/10/2003. Accessed on 08.06.2016. URL: `http://www.mathworks.com/matlabcentral/fileexchange/3215-fit-ellipse` (Cited on p. 81).

[146] D. J. Spence et al. *Phys. Rev. E.* 63, 015401(R). 2001. "Investigation of a hydrogen plasma waveguide"
(Cited on p. 82).

[147] A Butler et al. *Phys. Rev. Lett.* 89. 18, p. 185003. 2002. "Guiding of high-intensity laser pulses with a hydrogen-filled capillary discharge waveguide."
(Cited on p. 82).

[148] S. Semushin et al. *Rev. Sci. Instrum.* 72. 7, p. 2961. 2001. "High density gas jet nozzle design for laser target production"
(Cited on p. 82).

[149] B. B. Pollock et al. *Physical Review Letters.* 107. 4, p. 045001. 2011. "Demonstration of a Narrow Energy Spread, ∼0.5 GeV Electron Beam from a Two-Stage Laser Wakefield Accelerator"
(Cited on p. 83).

[150] O. Kononenko et al. *Nucl. Instruments and Methods Phys. Res. Sect. A*, pp. 1–5. 2016. "2D hydrodynamic simulations of a variable length gas target for density down-ramp injection of electrons into a laser wakefield accelerator"
(Cited on p. 83).

[151] O. F. Hagena et al. *J. Chem. Phys.* 56. 5, p. 1793. 1972. "Cluster Formation in Expanding Supersonic Jets: Effect of Pressure, Temperature, Nozzle Size, and Test Gas"
(Cited on p. 84, 85).

[152] J. Wörmer et al. *Chem. Phys. Lett.* 159. 4, pp. 321–326. 1989. "Fluorescence excitation spectroscopy of xenon clusters in the VUV"
(Cited on p. 84, 85).

[153] J. Farges et al. *J. Chem. Phys.* 84. 6, p. 3491. 1986. "Noncrystalline structure of argon clusters. II. Multilayer icosahedral structure of ArN clusters 50<N<750"
(Cited on p. 85).

[154] R. A. Smith et al. *Rev. Sci. Instrum.* 69. 11, p. 3798. 1998. "Characterization of a cryogenically cooled high-pressure gas jet for laser/cluster interaction experiments"
(Cited on p. 85).

[155] K. Bockasten. *J. Opt. Soc. Am.* 51. 9, p. 943. 1961. "Transformation of Observed Radiances into Radial Distribution of the Emission of a Plasma"
(Cited on p. 85).

[156] J. M. Cole. "Diagnosis and Application of Laser Wakefield Accelerators". PhD thesis. Imperial College London, 2016 (Cited on p. 85, 139).

[157] I Glatt et al. *Opt. Lasers Eng.* 8, pp. 277–320. 1988. "Moire Deflectometry - Ray Tracing lnterferometry"
(Cited on p. 85).

[158] Y. Song et al. *J. Opt. Soc. Am. A.* 26. 4, pp. 882–889. 2009. "Theoretical analysis for moire deflectometry from diffraction theory"
(Cited on p. 85).

[159] J Ruiz-Camacho et al. *J. Phys. D. Appl. Phys.* 40. 7, pp. 2026–2032. 2007. "Comparison of sensitivities of Moiré deflectometry and interferometry to measure electron densities in z -pinch plasmas"
(Cited on p. 85).

[160] C. Rechatin et al. *New J. Phys.* 12. 2010. "Characterization of the beam loading effects in a laser plasma accelerator"
(Cited on p. 86).

[161] A. D. Debus et al. *Phys. Rev. Lett.* 104. 8, pp. 1–4. 2010. "Electron bunch length measurements from laser-accelerated electrons using single-shot thz time-domain interferometry"
(Cited on p. 86).

[162] M. Zhang. *Fermilab-TM.* 1988. "Emittance Formula for Slits and Pepper-pot Measurement"
(Cited on p. 86).

[163] S. Fritzler et al. *Phys. Rev. Lett.* 92. 16, p. 165006. 2004. "Emittance Measurements of a Laser-Wakefield-Accelerated Electron Beam"
(Cited on p. 86).

[164] S Corde et al. *Nat. Commun.* 4, p. 1501. 2013. "Observation of longitudinal and transverse self-injections in laser-plasma accelerators."
(Cited on p. 86).

[165] S. Kneip et al. *Phys. Rev. Spec. Top. - Accel. Beams.* 15. 2, p. 021302. 2012. "Characterization of transverse beam emittance of electrons from a laser-plasma wakefield accelerator in the bubble regime using betatron x-ray radiation"
(Cited on p. 86).

[166] R. Weingartner et al. *Phys. Rev. Spec. Top. - Accel. Beams.* 15, pp. 1–5. 2012. "Ultralow emittance electron beams from a laser-wakefield accelerator"
(Cited on p. 86).

[167] Contaldi, Carlo R. *Computational Physics Section 4: Methods for Integrating ODE systems.* University Lecture. 2010 (Cited on p. 88).

[168] Y. Glinec et al. *Rev. Sci. Instrum.* 77. 10, p. 103301. 2006. "Absolute calibration for a broad range single shot electron spectrometer"
(Cited on p. 90, 202, 203).

[169] ANDOR. *High Energy Detection Solutions Beyond The Visible.* Product brochure. Accessed on 14/06/2016. URL: `http://www.andor.com/pdfs/literature/Andor_High_Energy_Detection_Brochure.pdf` (Cited on p. 93).

[170] ANDOR. *ANDOR iKon-M SO.* Datasheet. Accessed on 14/06/2016. (Cited on p. 93, 208).

[171] Princeton Instruments X-ray Group. *PIXIS-XF: 2048.* Datasheet. Accessed on 14/06/2016. (Cited on p. 93).

[172] ANDOR. *ANDOR iKon-L Series.* Datasheet. Accessed on 14/06/2016. (Cited on p. 93).

[173] Hamamatsu. *X-ray Scintillator.* Datasheet. Accessed on 14/06/2016. 2014. URL: `https://www.hamamatsu.com/resources/pdf/etd/FOS_ACS_GPXS_ALS_TXPR1024E.pdf` (Cited on p. 93, 170).

[174] Saint-Gobain. *CsI(Tl), CsI(Na) Cesium Iodide Scintillation Material.* Datasheet. Accessed on 14/06/2016. (Cited on p. 93).

[175] Princeton Instruments. *PIXIS-XF System.* User Manual. 2011 (Cited on p. 94).

[176] F Albert et al. *Plasma Phys. Control. Fusion.* 50. 12, p. 124008. 2008. "Full characterization of a laser-produced keV x-ray betatron source"
(Cited on p. 96).

[177] NIST. *Tables of X-Ray Mass Attenuation Coefficients and Mass Energy-Absorption Coefficients from 1 keV to 20 MeV for Elements Z = 1 to 92 and 48 Additional Substances of Dosimetric Interest.* Accessed on 14.06.2016. URL: `http://www.nist.gov/pml/data/xraycoef/` (Cited on p. 96, 208).

[178] M. Sanchez del Rio et al. *SPIE Proceedings.* 8141, p. 814115. 2011. "Status of XOP: v2.4: recent developments of the x-ray optics software toolkit"
(Cited on p. 96).

[179] GoodFellow. *Index of Materials - Foil.* Accessed on 06.07.2016. URL: `http://www.goodfellow.com/E/Foil.html` (Cited on p. 99).

[180] Blake and Boughton. *Micro Analytical Balances BM Series.* Accessed on 05.01.2017. URL: `http://www.blakeandboughton.co.uk/BM.pdf` (Cited on p. 100).

[181] AEA Technology. *Sources.* Datasheet provided with the source. 2011 (Cited on p. 102).

[182] Brookhaven National Laboratory. *NuDat 2.6*. Accessed on 23.06.2016. URL: http://www.nndc.bnl.gov/nudat2/ (Cited on p. 102, 103).

[183] Whitbread, S. *Private Communication*. 2016 (Cited on p. 102).

[184] J. Smith et al. *J. Appl. Phys.* c. 1954, pp. 519–527. 1954. "Generalized Off-Axis Distributions from Disk Sources of Radiation"
(Cited on p. 103).

[185] J. T. Conway. *Nucl. Instruments Methods Phys. Res. Sect. A Accel. Spectrometers, Detect. Assoc. Equip.* 589. 1, pp. 20–33. 2008. "Calculations for a disk source and a general detector using a radiation vector potential"
(Cited on p. 104).

[186] T. J. Davis et al. *Phase-contrast imaging of weakly absorbing materials using hard X-rays*. 1995. DOI: 10.1038/373595a0. URL: http://www.nature.com/doifinder/10.1038/373595a0 (Cited on p. 110).

[187] V. N. Ingal et al. *J. Phys. D. Appl. Phys.* 28. 11, pp. 2314–2317. 1995. "X-ray plane-wave topography observation of the phase contrast from a non-crystalline object"
(Cited on p. 110).

[188] Y. Suzuki et al. *J. Synchrotron Radiat.* 9. 3, pp. 160–165. 2002. "X-ray refraction-enhanced imaging and a method for phase retrieval for a simple object"
(Cited on p. 110).

[189] S. W. Wilkins et al. *Nature*. 384. 6607, pp. 335–338. 1996. "Phase-contrast imaging using polychromatic hard X-rays"
(Cited on p. 110).

[190] M Born et al. *Principles of Optics: Electromagnetic Theory of Propagation, Interference and Diffraction of Light*. 7th ed. Cambridge University Press, 1999 (Cited on p. 110).

[191] R. Paschotta. *Noise in Laser Technology Part 3: Beam Pointing Fluctuations*. Published 2010. Accessed on 12.01.2017. URL: https://application.wiley-vch.de/berlin/journals/op/10-01/OP1001_S55-S57.pdf (Cited on p. 112).

[192] R. Paschotta. *Noise in Laser Technology Part 1: Intensity and Phase Noise*. Published June 2009. Accessed on 12.01.2017. URL: https://application.wiley-vch.de/berlin/journals/op/09-02/OP0902_S48-S50.pdf (Cited on p. 112).

[193] R. Paschotta. *Noise in Laser Technology Part 2: Fluctuations in Pulsed Lasers*. Published 2009. Accessed on 12.01.2017. URL: https://application.wiley-vch.de/berlin/journals/op/09-03/OP0903_S45-S47.pdf (Cited on p. 112).

[194] RP Photonics Encyclopedia. *Lamp-pumped Lasers*. Accessed on 12.01.2017. URL: https://www.rp-photonics.com/lamp_pumped_lasers.html (Cited on p. 112).

[195] S. Bulanov et al. *Phys. Rev. E.* 58. 5, R5257–R5260. 1998. "Particle injection into the wave acceleration phase due to nonlinear wake wave breaking"
(Cited on p. 112).

[196] A. J. Gonsalves et al. *Nat. Phys.* 7. 11, pp. 862–866. 2011. "Tunable laser plasma accelerator based on longitudinal density tailoring"
(Cited on p. 112).

[197] T. Rowlands-Rees et al. *Phys. Rev. Lett.* 100. 10, pp. 1–4. 2008. "Laser-Driven Acceleration of Electrons in a Partially Ionized Plasma Channel"
(Cited on p. 112).

[198] F. G. Desforges et al. *Phys. Plasmas*. 21. 12, pp. 1–6. 2014. "Dynamics of ionization-induced electron injection in the high density regime of laser wakefield acceleration"
(Cited on p. 113).

[199] N. Bourgeois et al. *Phys. Rev. Lett.* 111. 15, pp. 1–5. 2013. "Two-pulse ionization injection into quasilinear laser wakefields"
(Cited on p. 113).

[200] B. Hidding et al. *Phys. Rev. Lett.* 108. 3, pp. 1–5. 2012. "Ultracold electron bunch generation via plasma photocathode emission and acceleration in a beam-driven plasma blowout"
(Cited on p. 113).

[201] L.-L. Yu et al. *Phys. Rev. Lett.* 112. 12, p. 125001. 2014. "Two-Color Laser-Ionization Injection"
(Cited on p. 113).

[202] J. S. Liu et al. *Phys. Rev. Lett.* 107. 3, p. 035001. 2011. "All-Optical Cascaded Laser Wakefield Accelerator Using Ionization-Induced Injection"
(Cited on p. 113).

[203] G Golovin et al. *Phys. Rev. Spec. Top. - Accel. Beams.* 18, p. 011301. 2015. "Tunable monoenergetic electron beams from independently controllable laser-wakefield acceleration and injection"
(Cited on p. 113).

[204] M. Zeng et al. *Phys. Plasmas.* 21. 3, p. 030701. 2014. "Self-truncated ionization injection and consequent monoenergetic electron bunches in laser wakefield acceleration"
(Cited on p. 113).

[205] M Mirzaie et al. *Sci. Rep.* 5, p. 14659. 2015. "Demonstration of self-truncated ionization injection for GeV electron beams"
(Cited on p. 113).

[206] C Kamperidis et al. *Plasma Phys. Control. Fusion.* 56. 8, p. 084007. 2014. "Low energy spread electron beams from ionization injection in a weakly relativistic laser wakefield accelerator"
(Cited on p. 113).

[207] T. Ditmire et al. *Phys. Rev. Lett.* 78. 14, pp. 2732–2735. 1997. "High Energy Ion Explosion of Atomic Clusters: Transition from Molecular to Plasma Behavior"
(Cited on p. 113).

[208] Y. Fukuda et al. *Phys. Rev. Lett.* 103. 16, pp. 1–4. 2009. "Energy increase in multi-MeV ion acceleration in the interaction of a short pulse laser with a cluster-gas target"
(Cited on p. 113).

[209] R. C. Issac et al. *Phys. Plasmas.* 11. 7, pp. 3491–3496. 2004. "Ultra hard x rays from krypton clusters heated by intense laser fields"
(Cited on p. 113).

[210] L. M. Chen et al. *Phys. Rev. Lett.* 104. 21, pp. 1–4. 2010. "Intense high-contrast femtosecond K-shell x-ray source from laser-driven Ar clusters"
(Cited on p. 113).

[211] I Alexeev et al. *Phys. Rev. Lett.* 90. 10, p. 103402. 2003. "Self-Focusing of Intense Laser Pulses in a Clustered Gas"
(Cited on p. 113, 128).

[212] V. Kumarappan et al. *Phys. Rev. Lett.* 2005. "Guiding of Intense Laser Pulses in Plasma Waveguides Produced from Efficient, Femtosecond End-Pumped Heating of Clustered Gases"
(Cited on p. 113).

[213] M. Mori et al. *Phys. Rev. Spec. Top. - Accel. Beams.* 12. 8, pp. 1–5. 2009. "Generation of stable and low-divergence 10-MeV quasimonoenergetic electron bunch using argon gas jet"
(Cited on p. 114).

[214] Y. Fukuda et al. *Phys. Lett. Sect. A Gen. At. Solid State Phys.* 363, pp. 130–135. 2007. "Ultrarelativistic electron generation during the intense, ultrashort laser pulse interaction with clusters"
(Cited on p. 114).

[215] L. Zhang et al. *Appl. Phys. Lett.* 100. 1, pp. 2010–2013. 2012. "Electron acceleration via high contrast laser interacting with submicron clusters"
(Cited on p. 114).

[216] M. Mirzaie et al. *Plasma Phys. Control. Fusion.* 58. 3, p. 034014. 2016. "Laser acceleration in argon clusters and gas media"
(Cited on p. 114).

[217] T. D. Arber et al. *Plasma Physics and Controlled Fusion.* 57. 11, pp. 1–26. 2015. "Contemporary particle-in-cell approach to laser-plasma modelling"
(Cited on p. 124).

[218] T. Fennel et al. *Phys. Rev. Lett.* 98. 14, pp. 1–4. 2007. "Plasmon-enhanced electron acceleration in intense laser metal-cluster interactions"
(Cited on p. 127).

[219] J Vieira et al. Private Communication. February 2015 (Cited on p. 128).

[220] S. S.-w. S. S.-W. S. S.-W. Kim et al. *Nature.* 453. 7196, pp. 757–60. 2008. "High-harmonic generation by resonant plasmon field enhancement"
(Cited on p. 128).

[221] A. Doepp et al. *arXiv*, pp. 1–12. 2015. "Stable and polarized Betatron x-ray radiation from a laser plasma accelerator in ionization injection regime"
(Cited on p. 136).

[222] S. P. D. Mangles. *Proceedings of the CAS-CERN Accelerator School: Plasma Wake Acceleration*, pp. 289–300. 2016. "An Overview of Recent Progress in Laser Wakefield Acceleration Experiments"
(Cited on p. 138).

[223] F. Albert et al. *Plasma Phys. Control. Fusion.* 58. 10, p. 103001. 2016. "Applications of laser wakefield accelerator-based light sources"
(Cited on p. 138).

[224] Sahai, Aakash A. Private Communication. September 2016 (Cited on p. 144).

[225] J. M. Cole et al. *To be published.* 2016 (Cited on p. 155).

[226] J. Vieira et al. *Plasma Phys. Control. Fusion.* 54. 5, p. 055010. 2012. "Influence of realistic parameters on state-of-the-art laser wakefield accelerator experiments"
(Cited on p. 157).

[227] F. Albert et al. *Phys. Rev. Lett.* 111. 23, p. 235004. 2013. "Angular Dependence of Betatron X-Ray Spectra from a Laser-Wakefield Accelerator"
(Cited on p. 159).

[228] H. J. Melosh. *Icarus.* 59. 2, pp. 234–260. 1984. "Impact ejection, spallation, and the origin of meteorites"
(Cited on p. 164).

[229] C. A. Trepmann. *Earth Planet. Sci. Lett.* 267. 1-2, pp. 322–332. 2008. "Shock effects in quartz: Compression versus shear deformation - An example from the Rochechouart impact structure, France"
(Cited on p. 164).

[230] M. G. Kanatzidis et al. 287. February, pp. 1027–1031. 2000. "Physics of Iron at Earth' s Core Conditions"
(Cited on p. 164).

[231] M. Hudspeth et al. *J. Dyn. Behav. Mater.* 1. 1, pp. 55–64. 2015. "In Situ Visual Observation of Fracture Processes in Several High-Performance Fibers"
(Cited on p. 164).

[232] K. J. Ramos et al. *J. Phys. Conf. Ser.* 500. 14, p. 142028. 2014. "In situ investigation of the dynamic response of energetic materials using IMPULSE at the Advanced Photon Source"
(Cited on p. 164, 191).

[233] B. J. Jensen et al. *Rev. Sci. Instrum.* 84. 1, p. 013904. 2013. "Impact system for ultrafast synchrotron experiments"
(Cited on p. 164).

[234] M. Hudspeth et al. *J. Synchrotron Radiat.* 22. 1, pp. 49–58. 2015. "Simultaneous X-ray diffraction and phase-contrast imaging for investigating material deformation mechanisms during high-rate loading"
(Cited on p. 164).

[235] S. N. Luo et al. *Rev. Sci. Instrum.* 83. 7, p. 073903. 2012. "Gas gun shock experiments with single-pulse x-ray phase contrast imaging and diffraction at the Advanced Photon Source"
(Cited on p. 164).

[236] Bartolini, R. *Accelerator Physics Challenges in 3rd Generation Synchrotron Light Sources*. J.A.I. Particle Physics Seminar, 19 February 2008 (Cited on p. 165).

[237] S. J. Turneaure et al. *Phys. Rev. Lett.* 117. 4, pp. 1–5. 2016. "Real-Time Examination of Atomistic Mechanisms during Shock-Induced Structural Transformation in Silicon"
(Cited on p. 178).

[238] R. P. Drake. *High-Energy-Density Physics: Fundamentals, Inertial Fusion, and Experimental Astrophysics*. Springer, 2006, p. 303 (Cited on p. 178).

[239] J. J. MacFarlane et al. *J. Quant. Spectrosc. Radiat. Transf.* 99. 1-3, pp. 381–397. 2006. "HELIOS-CR - A 1-D radiation-magnetohydrodynamics code with inline atomic kinetics modeling"
(Cited on p. 178).

[240] B. J. Jensen et al. *J. Appl. Phys.* 118. 19, p. 195903. 2015. "Jet formation in cerium metal to examine material strength"
(Cited on p. 183, 185).

[241] J. D. Yeager et al. *Compos. Part A Appl. Sci. Manuf.* 43. 6, pp. 885–892. 2012. "High-speed synchrotron X-ray phase contrast imaging for analysis of low-Z composite microstructure"
(Cited on p. 191).

[242] A. Schropp et al. *Sci. Rep.* 5, p. 11089. 2015. "Imaging Shock Waves in Diamond with Both High Temporal and Spatial Resolution at an XFEL"
(Cited on p. 191).

[243] A. H. Jones et al. *J. Appl. Phys.* 37. 9, pp. 3493–3499. 1966. "Measurement of the very-high-pressure properties of materials using a light-gas gun"
(Cited on p. 192).

[244] R. E. Winter et al. *Shock Waves*. 26. 4, pp. 395–401. 2016. "Generation of ramp waves using variable areal density flyers"
(Cited on p. 192).

[245] G. E. Giakoumakis et al. *Phys. Med. Biol.* 30. 1, pp. 21–29. 1985. "Light angular distribution of fluorescent screens excited by x-rays"
(Cited on p. 202).

[246] A Buck et al. *Rev. Sci. Instrum.* 81. 3, p. 033301. 2010. "Absolute charge calibration of scintillating screens for relativistic electron detection."
(Cited on p. 202, 204).

[247] A. Glendinning et al. *Phys. Med. Biol.* 46. 517. 2001. "Measurement of the response of Gd2O2:Tb phosphor to 6 MV x-rays"
(Cited on p. 202).

[248] Mitsubishi Chemical Holdings Group. *X-ray Scintillator Screen "DRZ ^{TM}" Characteristics*. Accessed on 09.06.2016. URL: http://www.m-kagaku.co.jp/english/products/business/electron/ddm/details/1195241_3373.html (Cited on p. 202).

[249] MCI Optonix LLC. *DRZ Screens*. Accessed on 09.06.2016. URL: http://www.mcio.com/Products/drz-screens.aspx (Cited on p. 202).

[250] G. C. Tyrrell. *Nucl. Instruments and Methods Phys. Res. Sect. A*. 546. 1-2, pp. 180–187. 2005. "Phosphors and scintillators in radiation imaging detectors"
(Cited on p. 202, 203).

[251] S. Agostinelli et al. *Nucl. Instruments and Methods Phys. Res. Sect. A*. 506. 3, pp. 250–303. 2003. "Geant4-A simulation toolkit"
(Cited on p. 202).

[252] NIST. *ESTAR: stopping-power and range tables for electrons*. Accessed on 09.06.2016. URL: http://physics.nist.gov/PhysRefData/Star/Text/ESTAR.html (Cited on p. 203).

[253] T Bonnet et al. *Response function of Imaging Plates to protons and alphas : experimental results and modelisation*. Presentation. 2012 (Cited on p. 204).

[254] S. G. Gales et al. *Rev. Sci. Instrum.* 75. 10, p. 4001. 2004. "Image plates as x-ray detectors in plasma physics experiments"
(Cited on p. 204, 205).

[255] I. J. Paterson et al. *Meas. Sci. Technol.* 19. 9, p. 095301. 2008. "Image plate response for conditions relevant to laser-plasma interaction experiments"
(Cited on p. 204).

[256] K Zeil et al. *Rev. Sci. Instrum.* 81. 1, p. 013307. 2010. "Absolute response of Fuji imaging plate detectors to picosecond-electron bunches."
(Cited on p. 205, 206).

[257] K. A. Tanaka et al. *Rev. Sci. Instrum.* 76. 1, p. 013507. 2005. "Calibration of imaging plate for high energy electron spectrometer"
(Cited on p. 205, 206).

[258] S. Kneip. "Laser Plasma Accelerator and Wiggler". PhD thesis. Imperial College London, 2010 (Cited on p. 205).

[259] Rusby, Dean. Private Communication. October 2015 (Cited on p. 205).

[260] Poder, Kristjan. Private Communication. November 2015 (Cited on p. 206).

[261] N Nakanii et al. *Rev. Sci. Instrum.* 79. 6, p. 066102. 2008. "Absolute calibration of imaging plate for GeV electrons."
(Cited on p. 206, 207).

[262] B Hidding et al. *Rev. Sci. Instrum.* 78. 8, p. 083301. 2007. "Novel method for characterizing relativistic electron beams in a harsh laser-plasma environment."
(Cited on p. 207).

[263] Wood, J.C. *Decay of Image Plate Signal with Number of Scans*. Tech. rep. Unpublished report. 2013 (Cited on p. 207).

[264] Japan Inspection Instruments Manufacturers Association. *Micro Resolution Chart for X-ray: Resolution Test-patterns for micro-focus X-ray images*. Datasheet. 2006 (Cited on p. 212).